Processing, Mechanical Properties and Elevated Temperature Formability of Automotive AA6xxx and AA7xxx Sheet Materials with High Recycle Content

By Cedric Yeshan WU, B.A.Sc, P.Eng.

A Thesis Submitted to the School of Graduates Studies in Partial Fulfilment of the Requirements for the Degree of Master of Applied Science

Master of Applied Science (2017) **McMaster University**

Hamilton, Ontario

TITLE: **Processing, Mechanical Properties and Elevated Temperature Formability of Automotive AA6xxx and AA7xxx Sheet Materials with High Recycle Content**

AUTHOR: **Cedric Yeshan Wu**

SUPERVISOR: **Professor Mukesh Jain**

NUMBER OF PAGES: **xv, 160**

ABSTRACT

In modern society, car manufactures are actively pursuing vehicle light weighting under both stricter government regulations due to environmental concerns and consumers' demand for better fuel economy. Under such circumstances, OEMs are using more parts using aluminum alloys to replace parts made with steel. New forming processes are being developed to produce structural components to achieve higher in-service strength using higher strength aluminum alloys. Two of the commonly used high strength aluminum alloys, AA6111 and AA7075, are being considered for elevated temperature sheet forming applications. With more aluminum applications in vehicle and good recyclability of aluminum components, there is a concern of contamination from transition metals such as Fe, Mn and Cr from vehicle end of life scraps getting into aluminum scrap stream. Such impurity elements can have profound impact on aluminum alloy's mechanical properties, performance and formability at room and elevated temperatures. This study is focused on variants of AA6111 and AA7075 alloys with increased recycling content, and thus higher amounts of the above transition metals. The objective is to investigate the effect of impurity alloying elements on final microstructure, mechanical properties and formability of the above sheet materials. Formability is studied in terms of sheet bendability and elevated temperature forming limit diagrams (FLDs) using a hot gas bulge tester.

ACKNOWLEDGEMENTS

I would like to express my gratitude to my supervisor Dr. Jain for his expertise, guidance and support throughout the course of this thesis. I would also like to thank all the staff in McMaster Automotive Research Center (MARC), Dr. Mike Bruhis for the assistance he has provided to ensure the success of my research, a senior year undergraduate student, Aaron Bruinsma and post-doctoral fellow, Dr. Anantheswara Kommunje.

I would also like to thank my manager Mr. Duane Bendzinski for his support and encouragement to me in perusing my continuous education. I would also like to thank Dr. Rajeev Kamat from Novelis GRTC for his technical input and suggestions. In addition, I would also like to thank my colleagues from Novelis GRTC, Tracey McDaniel, Raj Talla, Kevin Starks, Bill Lightell, Paul Nolan, Richard Burrows, David Anderson and Tianyu Yu for their help with rolling, sample preparation, training technical expertise they provided related to the project.

Beside the technical support I received from the above individuals, I would also like to thank my family for their moral support and my dear friends Bernie Ting, Zongshu Li and Alan Tsung, who welcomed me to stay in their home during my visits to McMaster University (Hamilton) from Atlanta.

Lastly, I would like to express my gratitude to Novelis Inc. for their financial support and permission to publish this work.

1. TABLE of CONTENTS

ABSTRACT ii
ACKNOWLEDGEMENTS iii
List of Figures vii
List of Tables xv
1. Introduction 1
1.1 Application of Aluminum in Automotive Industry 3
1.2 Vehicle end of life and recycling strategy 7
1.3 Forming limit curve 10
1.4 Elevated temperature forming and formability 18
2. Project Objectives 21
3. Literature Review 23
3.1 Effect of high recycling content on microstructure of 6xxx alloys 23
3.2 Effect of transition metals addition on microstructure of 7xxx alloys 28
3.3 Methods of evaluating formability at high temperature 31
4. Experimental Methodology 37
4.1 Microstructure evaluation 37
4.1.1 Metallurgical Mount Preparation 38
4.1.2 Optical and Electron Optical Imaging 39
4.2 Mechanical testing 39
4.2.1 Room temperature tensile test 39
4.2.2 Elevated temperature tensile test 39
4.2.3 Wrap bend test sample preparation and test apparatus 41
4.3 High temperature formability testing 42
4.3.1 Sample perpetration 42
4.3.2 High Temperature Forming Test 43
4.3.3 Sample imaging 46
4.3.4 Image analysis with Argus 48
4.4 Fractography 49

5. Sample casting and processing 51
5.1 6xxx 51
5.2 7xxx 52
6. Results and Discussion 55
6.1 6xxx Series Alloys 55
6.1.1 Microstructures 55
6.1.1.1 As-cast Microstructures 58
6.1.1.2 Homogenization and Homogenized Microstructures 60
6.1.1.3 T4 Microstructures 64
6.1.1.4 T82 Microstructures 68
6.1.2 Mechanical Properties 72
6.1.2.1 Room Temperature Tensile Properties 72
6.1.2.2 Wrap Bend Test of AA6111 Variant 74
6.1.2.3 Elevated Temperature Tensile Test Results 78
6.1.3 Microstructural Characterization Using SEM Feature Detection and Count 80
6.1.4 Warm Forming Characteristics of AA6111 Sheet Materials 83
6.1.5 Fractography of equi-biaxial bulge samples of AA6111 and HRC6111 tested at 300ºC 88
6.2 7xxx Series Alloys 101
6.2.1 Microstructures 101
6.2.1.1 As-cast Microstructures 104
6.2.1.2 Homogenization Process and Homogenized Microstructures 105
6.2.1.3 T6 Microstructures 108
6.2.2 Mechanical Properties 112
6.2.2.1 Room Temperature Tensile Properties 112
6.2.2.2 High Temperature Tensile Test Results 112
6.2.3 Hot Forming Characteristics of AA7075 Alloys 114
6.2.3.1 FLC of AA7075 variants at 470ºC 115
6.2.3.2 FLC of AA7075 variants at 425ºC 117

6.2.4 Fractography of Equi-biaxial Bulge Test Samples of AA7075, MRC7075 and HRC7075 at 470ºC 119
6.2.5 Elevated temperature FLCs using interrupted hot gas bulge tests 136
6.2.6 Hot Gas Forming FLC of AA7075 sheet at 425ºC with in-situ 2-Camera Aramis System..... 138
6.2.7 Comparison of FLCs of different AA7075 sheets at 425ºC and 470ºC 142
6.3 Comparison of 7xxx and 6xxx series aluminum alloys. 143
7. Summary and Conclusions 144
8. Future Work 148
9. References 150
10. Appendix 153

List of Figures

Figure 1-1 WARDSAUTO, automotive trend benchmark study. (WARDSAUTO, 2014) . 2

Figure 1-2 Automotive industry survey on approach for vehicle light weighting approach. (WARDSAUTO, 2015)..... 3

Figure 1-3 Direct mass saving and market penetration of automotive aluminum. (Ducker, 2012). 4

Figure 1-4. Example of aluminum application in Audi A8 construction. (Audi). 5

Figure 1-5. A Hot Formed B-pillar reinforcement using Novelis' 7075 aluminum. 7

Figure 1-6. Typical end- of- life vehicle recycling process. (Cui, et al., 2010)..... 9

Figure 1-7. A general schematic of the forming limit curve. (Anderson, 2016). 10

Figure 1-8. A schematic of Nakajima geometry. (Nakazima, et al., 1968). 12

Figure 1-9. A schematic of Marciniak geometry. (Marciniak, et al., 1967). 13

Figure 1-10. Overview of FLC geometries used at Novelis Inc. (Anderson, 2016). 14

Figure 1-11. Specimen geometries and elliptical dies used in hot gas forming FLC. (Mitukiewicz, et al., 2014)..... 15

Figure 1-12. Overview of a CGA network showing original pattern, deformed pattern and fractured pattern. (Cikmis, et al., 2010) 16

Figure 1-13. Overview of a speckle pattern used for DIC at Novelis Inc. 17

Figure 1-14. A schematic of incoming material - warm forming- final product route. 18

Figure 1-15 A schematic of incoming material- hot forming- final product route..... 19

Figure 3-1. Changes in number density and peak hardness with (a) Mn and (b) Fe content. (Shumei Wang, 2012) 23

Figure 3-2. Metallography of 0.2% addition of transition metals that reduces the grain size. (Wang, et al., 2011). 24

Figure 3-3. Evolution of (a) cube; (b) goss and (c) P* components of the recrystallized texture as a function of the Fe content. (Haiou, et al., 2005). 25

Figure 3-4. Maximum bend angle in longitudinal (L) and transverse (T) rolling direction with different Fe content level in AA6111. (Lievers, 2003). 26

Figure 3-5. Correlation between bendability and the reduction in thickness in the case of AA6111. (Sarkar, et al., 2004). 27

Figure 3-6. Fatigue fractured sample showing Al_7Cu_2Fe particles at the fractured interface. (Rometsch, et al., 2013). 28

Figure 3-7. SEM Image of 7475 T7651 alloy after corrosion test with Al_7Cu_2Fe particles adjacent to pitting corrosion. (Chemin, et al., 2014). 29

Figure 3-8. AA7150 with different cooling rate showing grain boundary precipitation induced by chromium dispersoids. (Rometsch, et al., 2013). 30

Figure 3-9. Effects of forming temperature on FLD for AA6111-T4. (Li, et al., 2004). ... 32

Figure 3-10. Profiles of hydro formed AA6061 at different temperature. (S. Mahabunphachai, 2010)..... 32

Figure 3-11. Deep drawability of AA7020-T6 and 7075-T6 alloys; (a) photos of a cross-shaped deep drawn component at room temperature and 200ºC, and (b) LDR and LDD values at elevated temperature. (M. Kumar, 2014). 33

Figure 3-12. Yield strength plotted as function of heat treatment temperature with and without paint bake for AA7075-T6 sheet. (Wang Hui, 2012). 34

Figure 3-13. FLDs of 7075-T6 aluminum alloy sheet obtained at various temperatures. (Hua, et al., 2010)..... 35

Figure 3-14. Predicted FLDs of AA7075-T6 sheet, (a) FLC for 7075 at various temperatures at 0.1 s^{-1} strain rate, and (b) FLC at 420ºC with different strain rates. (Weimin, et al., 2014). 36

Figure 4-1. Typical macro segregation profile in a round DC cast aluminum ingot. (Beckermann, 2001)..... 38

Figure 4-2. Gleeble thermo-mechanical test system for high temperature tensile test and overview of the Gleeble specimen..... 40

Figure 4-3. A photograph of Gleeble tensile test specimen with a thermocouple welded for elevated temperature test. 40

Figure 4-4. Photographs of the wrap bend tester and the mandrel region. 42

Figure 4-5. Photographs of electrochemical etching set-up (left) and an etched and deformed test sample (right). 43

Figure 4-6. Photograph and a schematic of the hot gas bulge test system. 44

Figure 4-7. Schematics of the clamping and bulging process steps for a hot gas bulge specimen..... 45

Figure 4-8. Photographs of the dies with elliptical openings for hot gas bulge test. 45

Figure 4-9. Hardware of Argus optical strain measurement system for surface strain mapping of bulge samples. 47

Figure 4-10. Schematic of the images taken with two 360ºC rotations and with two levels of tilt..... 48

Figure 4-11. Strain mapping and limit strain determination proceure with Argus optical strain measurement system for bulged specimens. 49

Figure 4-12. Schematic of sample location for fractography using SEM. 49

Figure 4-13. A photograph of the cut region of the test specimen. 50

Figure 5-1. 6000 alloys' process flow of the ingot from DC cast to final gauge/temper. 52

Figure 5-2. Photographs of an ingot sample and the resulting hot band plates from 4 ingots..... 53

Figure 5-3. Process flow of 7075 alloys from ingot to final gauge/temper. 54

Figure 6-1. Phase predictions of baseline AA6111 alloy from JMet Pro. 56

Figure 6-2. Phase predictions of HRC 6111 alloy from JMet Pro. 57

Figure 6-3. As cast microstructure of AA6111 from quarter location. 58

Figure 6-4. As cast microstructure of HRC6111 from quarter location. 58

Figure 6-5. SEM (BSE) image of AA6111 alloy in the as-cast condition and various EDX plots showing matrix and two different constituent particles. 59

Figure 6-6. SEM (BSE) image of HRC 6111 in as cast condition and various EDX plots showing different constituent particles..... 60

Figure 6-7. Differential Scanning Calorimetric (DSC) traces of both 6xxx alloys after homogenization showing no sign of eutectic melting. 61

Figure 6-8. Microstructure of AA6111 after homogenization. 62

Figure 6-9. Microstructure of HRC 6111 after homogenization. 62

Figure 6-10. SEM (BSE) image of AA6111 in homogenized condition with EDX plots of different constituent particles. 63

Figure 6-11. SEM (BSE) image of HRC6111 in homogenized condition with EDX plots of different constituent particles. 64

Figure 6-12. AA6111-T4 (200x). Figure 6-13. HRC AA6111-T4 (200x). 65

Figure 6-14. BSE image of AA6111-T4 sample with EDX plots of constituent particles. 66

Figure 6-15. BSE image of HRC6111 T4 sample with EDX plots of particles. 67

Figure 6-16. Microstructure of baseline AA6111 in T82 condition. 68

Figure 6-17. Microstructure of HRC AA6111 in T82 condition. 68

Figure 6-18. Grain size comparison between AA6111 and HRC 6111-T82 sheets. 69

Figure 6-19. SEM (BSE) of AA6111-T82 sheet and EDX plots of the constituent particles. 70

Figure 6-20. SEM (BSE) of HRC 6111-T82 sheet and EDX plots of particles. 71

Figure 6-21 Stress Strain Curve of AA6111 and HRC6111 in T4 and T82. 72

Figure 6-22. Optical micrograph of AA6111-T4 bent sample tested with r=0.02 in mandrel. 75

Figure 6-23. Optical micrograph of HRC 6111-T4 bent sample tested with r=0.024 in mandrel. 76

Figure 6-24. A comparison of microstructures of bend specimens of AA6111-T4 and HRC 6111-T4 from tests conducted with different bending mandrel radii. 78

Figure 6-25. Stress-strain curves of AA6111-T82 and HRC 6111-T82 sheets at RT and 300ºC. 79

Figure 6-26. An SEM image of AA6111 alloy showing α and β particles and Mg_2Si precipitates. (G. Mrowka-Nowotnik, 2007) 80

Figure 6-27. FDC plots of area fractions of α and β in AA6111. 81

Figure 6-28. FDC plots of area fractions of α and β in HRC 6111. 82

Figure 6-29. A comparison of burst pressures of AA6111-T82 and HRC 6111-T82 sheets. 84

Figure 6-30. A typical AA6111-T82 balanced bi-axial tension bulge sample and strain map at 300ºC. 85

Figure 6-31. Major and minor forming limit strain measurement by Argus optical system. 85

Figure 6-32. Necking observed at the bottom radius area in samples from Geometry 1 die and corresponding strain map. 86

Figure 6-33. Experimentally determined biaxial tension side of FLC for AA6111-T82 and HRC 6111-T82 sheets at 300ºC. 87

Figure 6-34. FLC of AA6111 T4 at room temperature. 88

Figure 6-35. SEM image of equi-biaxial AA6111 T82 bulge specimen fracture surface showing ductile void damage. 89

Figure 6-36. SEM image of the fractured surface of equi-biaxial AA6111 T82 sample fractured at 300ºC showing void formation around constituent particles. 90

Figure 6-37. EDX spectrum of constituent particles found at the fractured surface of AA6111-T82 sheet. 90

Figure 6-38. SEM image of Bi-axial HRC6111-T82 fractured surface. 91

Figure 6-39. SEM image of fracture surface of equi-biaxial bulge sample of HRC6111-T82 sheet fractured at 300ºC. 92

Figure 6-40. Optical micrographs of AA6111 T82 biaxial hot gas bulge sample fractured at 300ºC (50x and 200x). 93

Figure 6-41. Back scattered SEM image of AA6111 T82 biaxial hot gas bulge sample fractured at 300ºC. 93

Figure 6-42. Back-scatterd SEM image of AA6111 hot gas bulge specimen fracture region at 300ºC. 94

Figure 6-43. Higher magnification BSE image of AA6111 in the vicinity of fractured location showing void formmation adjacent to intermetallic particles. 95

Figure 6-44. High magnification BSE of AA6111, showing nacent void formation in the matrix adjacent to the Fe and Mn containing intermetallic particles. 96

Figure 6-45. Optical mcrographs of HRC6111 biaxial bulge sample fractured at 300ºC (50x and 200x). 97

Figure 6-46. Back scattered SEM image of HRC6111 hot gas bulge specimen in the fracture region. 98

Figure 6-47. Back Scatterd SEM image of HRC6111 hot gas bulge specimen in the fractured region. 98

Figure 6-48. High magnification BSE image of HRCA6111 in the vicinity of fractured location showing void formmation adjacent to intermetallic particles. 99

Figure 6-49 High magnification BSE of HRC6111, showing nacent void formation in the matrix adjacent to the Fe and Mn containing intermetallic particles. 100

Figure 6-50. Baseline 7075 alloy phase predictions using ThermalCalc software. 103

Figure 6-51. MRC 7075 alloy phase predictions using Thermal Calc software. 103

Figure 6-52. HRC 7075 phase predictions using ThermalCalc software. 104

Figure 6-53. As-cast optical micrographs from quarter location of baseline 7075, MRC 7075 and HRC 7075 alloys. 105

Figure 6-54. DSC scans of baseline 7075, MRC and HRC in as-cast condition showing eutectic melting. 106

Figure 6-55. DSC scans of baseline and HRC Ingots after homogenization. 106

Figure 6-56. Optical micrographs of baseline 7075, MRC7075 and HRC 7075 after homogenization. 107

Figure 6-57. Optical micrographs in T6 condition of baseline 7075, MRC 7075 and HRC 7075 sheets. 108

Figure 6-58. SEM (BSE) of AA7075-T6 sheet and EDX plots of the constituent particles. 109

Figure 6-59. SEM (BSE) of MRC7075 sheet and EDX plots of the constituent particles. 110

Figure 6-60. SEM (BSE) of HRC 7075 sheet and EDX plots of the constituent particles. 111

Figure 6-61. Elevated temperature tensile stress-strain curves of baseline 7075 at 400ºC, 425 ºC, 450 ºC and 475 ºC respectively. 113

Figure 6-62. Tensile stress strain curves of AA7075 at elevated temperatures (Weimin, et al., 2014). 114

Figure 6-63. Burst pressures of 7xxx sheet materials at 425º and 470ºC. 115

Figure 6-64. Baseline 7075 hot gas bulge samples and corresponding strain map at 470ºC. 116

Figure 6-65. Right side of FLC for baseline 7075, MRC 7075 and HRC 7075 sheet materials at 470ºC. 117

Figure 6-66. Right side of FLC for baseline 7075, MRC 7075 and HRC 7075 sheet materials at 425ºC. 118

Figure 6-67. MRC 7075 hot gas bulge sample and corresponding major strain map at 425ºC. 119

Figure 6-68. SEM image of equi-biaxial AA7075 fractured surface. 120

Figure 6-69. SEM image of equi-biaxial 7075 fractured surface. 121

Figure 6-70. EDX spectrum showing composition of precipitates in 7075. 121

Figure 6-71. SEM image of fractured surface of an equi-biaxial bulge sample of MRC7075 sheet. 122

Figure 6-72. High mag SEM image of fractured surface of an equi-biaxial bulge sample of MRC7075 sheet. 123

Figure 6-73. EDX spectrum showing Fe containing particles found in MRC7075. 123

Figure 6-74. SEM image of fractured surface of equi-biaxial bulge specimen of HRC7075 sheet. 124

Figure 6-75. High mag SEM image of fractured surface of equi-biaxial bulge specimen of HRC7075 sheet. 125

Figure 6-76. EDX spectrum from fractured surface of equi-biaxial bulge specimen of HRC7075 sheet showing Fe, Cr and Mn containing particles. 125

Figure 6-77. Through-thickness optical micrographs at two different magnifications of a AA7075 equi-biaxial hot gas bulge sample tested to fracture at 470ºC. 126

Figure 6-78. Lower magnification BSE Image of AA7075 biaxial hot gas bulge sample taken to fracture at 470ºC. 127

Figure 6-79. Higher magnification BSE image of AA7075 biaxial hot gas bulge sample taken to fracture at 470ºC. 128

Figure 6-80. High magnification of AA7075 biaxial hot gas bulge sample fractured at 470ºC with EDX identification of the matrix and constituent phases. 129

Figure 6-81. Through-thickness optical micrographs at two different magnifications of a MRC7075 equi-biaxial hot gas bulge sample tested to fracture at 470ºC. 130

Figure 6-82. BSE Image of MRC7075 biaxial hot gas bulge sample tested to fracture at 470ºC. 131

Figure 6-83. Higher magnification BSE image of MRC7075 biaxial hot gas bulge sample tested to fracture. 131

Figure 6-84. Higher magnification of MRC7075 biaxial hot gas bulge sample tested to fracture at 470ºC with EDX identification of the matrix and constituent phases. 132

Figure 6-85. Through-thickness optical micrographs at two different magnifications of a HRC7075 equi-biaxial hot gas bulge sample tested to fracture at 470ºC. 133

Figure 6-86. BSE image of a HRC7075 biaxial hot gas bulge sample taken to fracture at 470ºC. 133

Figure 6-87. Large magnification BSE image of HRC7075 biaxial hot gas bulge sample taken to fracture at 470ºC. 134

Figure 6-88. Still larger magnification of HRC7075 biaxial hot gas bulge sample taken to fracture at 470ºC with EDX identification of the matrix and constituent phases. 135

Figure 6-89. Photographs of a bulge test specimen and the pressure profile from interrupted bulge test. 136

Figure 6-90. Comparison of baseline AA7075 equi-biaxial bulge specimens obtained using continuous and interrupted test methods. 137

Figure 6-91. Comparison of major strain maps from last 2 images at the end of the test from baseline AA7075 equi-biaxial bulge specimen tested at 425ºC using the interrupted test method. 138

Figure 6-92. Photographs of two bulged samples of baseline 7075 sheet tested at 425ºC using Macrodyne press. 139

Figure 6-93. Major strain maps of baseline 7075 bulged samples from Macrodyne press at 425ºC. 140

Figure 6-94 Effective stress and strain calculated for AA7075, MRC7075 and HRC7075. 141

Figure 6-95. Comparison of FLCs of baseline 7075, MRC 7075 and HRC 7075 FLC at 425ºC and 470ºC. 142

Figure 10-1. Photographs and corresponding Argus major strain maps of various hot as bulge sample of baseline AA6111 sheet. 154

Figure 10-2. Photographs and corresponding Argus major strain maps of various hot as bulge sample of baseline HRC6111 sheet. 155

Figure 10-3. Photographs and corresponding Argus major strain maps of various hot as bulge sample of baseline AA7075 sheet at 470ºC. 156

Figure 10-4. Photographs and corresponding Argus major strain maps of various hot as bulge sample of MRC 7075 sheet at 470ºC. 158

Figure 10-5. Photographs and corresponding Argus major strain maps of various hot as bulge sample of HRC 7075 sheet at 470ºC. 159

Figure 10-6. Photographs and corresponding Argus major strain maps of various hot as bulge sample of baseline AA7075 sheet at 425ºC. 160

Figure 10-7. Photographs and corresponding Argus strain maps of various hot as bulge sample of MRC 7075 sheet at 425ºC. 161

Figure 10-8. Photographs and corresponding Argus strain maps of various hot as bulge sample of HRC 7075 sheet at 425ºC. 162

Figure 10-9. A sequence of Aramis major strain maps from interrupted hot gas bulge tests showing the development of strain at the pole of the bulge up to fracture. 163

List of Tables

Table 1. Typical wrought aluminum alloy used in automotive application and their chemical composition (Association, 2009). 6

Table 2. Hot Rolling Pass Schedule (RPS) of AA6111 variants. 51

Table 3. Hot Rolling Pass Schedule (RPS) of 7075 and its variants. 53

Table 4. Actual Compositions of Baseline 6111 and HRC 6111. 55

Table 5. Room temperature mechanical properties of both variants of 6111 sheet in T4 and T82 conditions. 73

Table 6. Bendability in terms of R/T values from Wrap bend test. The symbols R and T refer to the bend mandrel radius and sheet thickness respectively. 74

Table 7. Uniaxial tensile properties of AA6111-T82 and HRC 6111-T82 at 300ºC..... 79

Table 8. Particle data for AA6111-T82. 82

Table 9. Particle data for HRC 6111 T82. 83

Table 10. Chemical compositions of AA7075 baseline, MRC7075 and HRC 7075 alloys. 101

Table 11. Room temperature tensile test results for baseline 7075-T6, MRC 7075-T6 and HRC 7075-T6 sheets..... 112

1. Introduction

In modern society, global warming and other environmental concerns are being addressed by governments and manufacturing industries worldwide. In December 2015, representatives from 196 countries had participated and debated in the 21st conference of the UNFCCC and signed a mutual agreement to deal with increasing greenhouse gas emissions. This agreement, known as the “Paris Agreement” now have 195 committed members. The primary goal is to limit the increase in global average temperature to below 2ºC, through lower greenhouse gas emission. One of the main source of greenhouse gas by human activity is automotive emission. Governments have set legislative target to reduce greenhouse gas emission. One of such regulation is so called “Corporate Average Fuel Economy (CAFÉ) Standards” by United States. Phase 2 of the standard is to improve fuel efficiency and cut carbon pollution, by up to 2 billion barrels of oil and reduce CO_2 emissions by up to 1.1 billion metric tons over the lifetimes of MY 2018-2029 Vehicles (NHTSA, 2016). Original Equipment Manufacturers (OEMs) are responsible to reduce emission on a fleet wide basis, the reduction target set was 163 g/mile of CO_2, by model year 2025, which is equivalent to 54.5 mpg (4.3L/ 100km). OEMS exploit various ways to achieve the emission requirement such as introducing smaller engine, improvement in transmission technology and development of zero emission vehicles such as electric vehicle (EV) or hybrid vehicles.

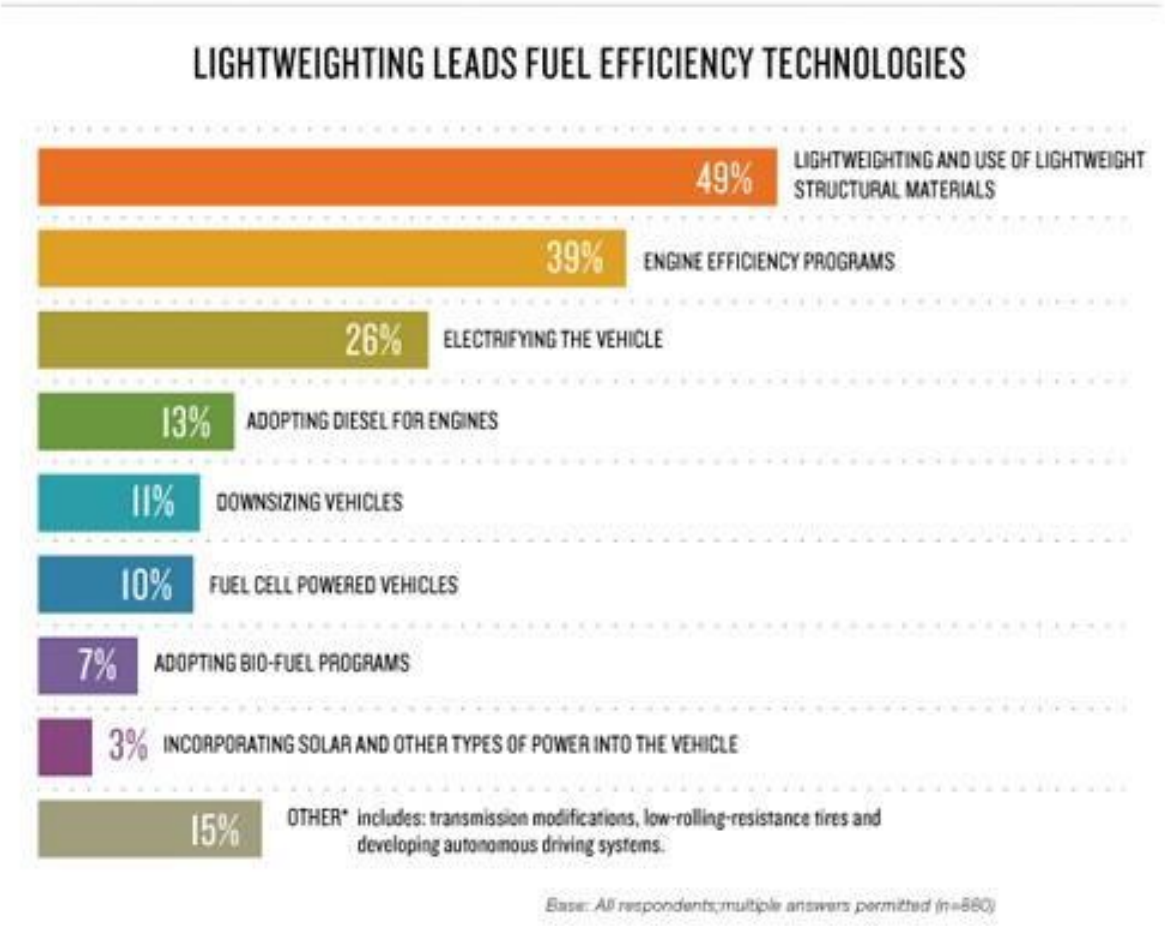

Figure 1-1 WARDSAUTO, automotive trend benchmark study. (WARDSAUTO, 2014)

According to an industrial survey conducted by WARDSAUTO in 2014, one of the most efficient way to reduce greenhouse gas emission is through vehicle light weighting. (Figure 1-1) Furthermore, automotive industry has overwhelmingly agreed that aluminum is the most efficient way for vehicle light weighting. (see Figure 1-2)

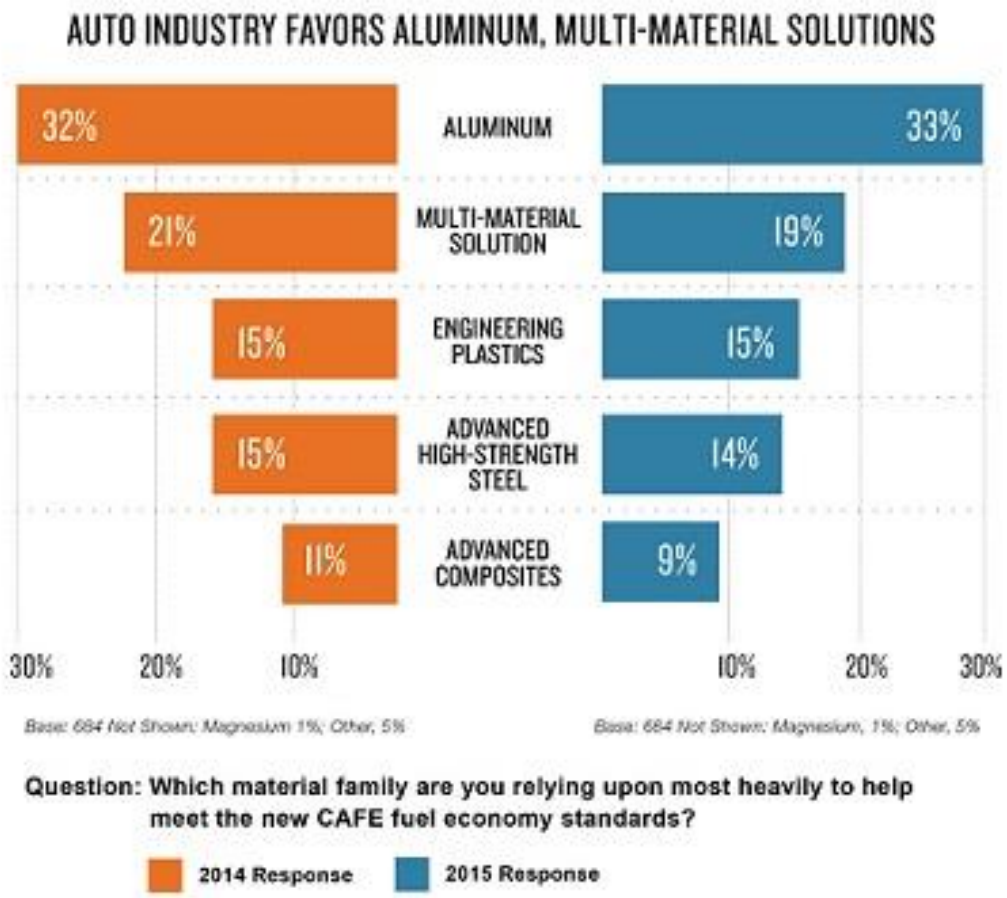

.

Figure 1-2 Automotive industry survey on approach for vehicle light weighting approach. (WARDSAUTO, 2015).

1.1 Application of Aluminum in Automotive Industry

Aluminum alloys offer good strength to weight ratio and much better corrosion resistance compared to steel. Aluminum is considered to be more environmental friendly. It was reported that to use 1 kg of aluminum in a car could reduce CO_2 emission by 19 kg during its whole life cycle. In addition, 5-7% fuel saving can be achieved for every 10% weight reduction by substituting aluminum. (Cui, et al., 2010). Aluminum in automotive industry can be incorporated in the following systems:

1. Power-train system (engine, fuel system, liquid lines), transmission housing and radiators
2. Chassis and suspension: steering system, suspension and wheels
3. Car body (BIW) and hang-on parts: Doors, hoods, structural component such as B Pillars and bumpers etc.

Aluminum alloys can be used in automotive components in various forms such as extruded shapes, castings, forgings and formed sheet components depending on the application. For instance, power train system such as engine blocks are mostly aluminum casting, wheels are typically forged aluminum. Hang-on parts such as doors, hoods use stamped aluminum sheet materials. Figure 1-3 shows the amount of mass saving by using aluminum and market penetration. Among the different categories, engine and transmission parts, chassis and suspension parts and hang on parts would provide the highest absolute mass saving.

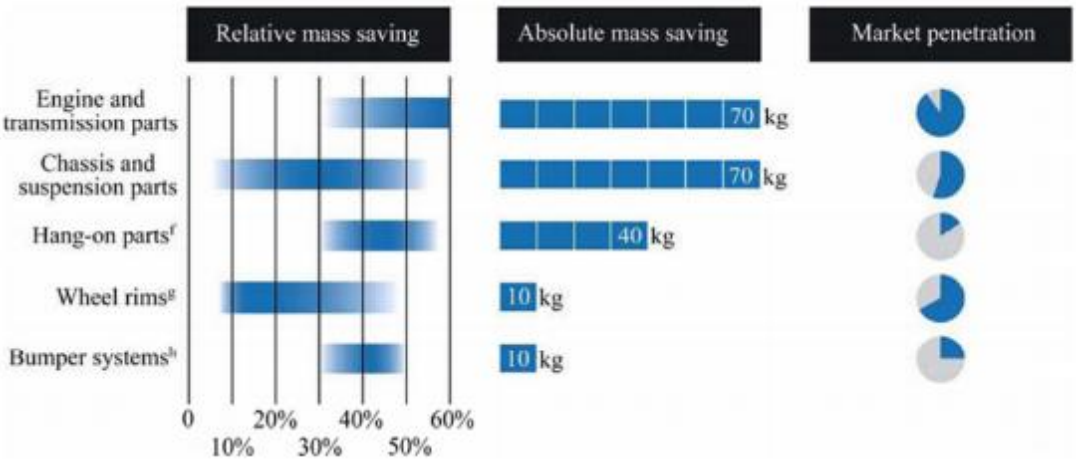

Figure 1-3 Direct mass saving and market penetration of automotive aluminum. (Ducker, 2012).

High strength wrought aluminum sheet metal, the focus of this study, is primarily used in the structural and hang on parts. Different grades of aluminum and gauge are used depending on the application. For example, 5xxx series aluminum are typically used for parts that require high formability such as door inners; 6xxx series aluminum are typically used for skin sheets where class A surface finish, good corrosion resistance and dent resistance is required; high strength 6xxx and 7xxx alloys are used for structural parts, where their high strength and high energy absorption is desired during a crash scenario to safeguard the occupant. Figure 1-4 shows the Audi A8 (D2, type 4D) with full aluminum body and various aluminum alloys used for various applications.

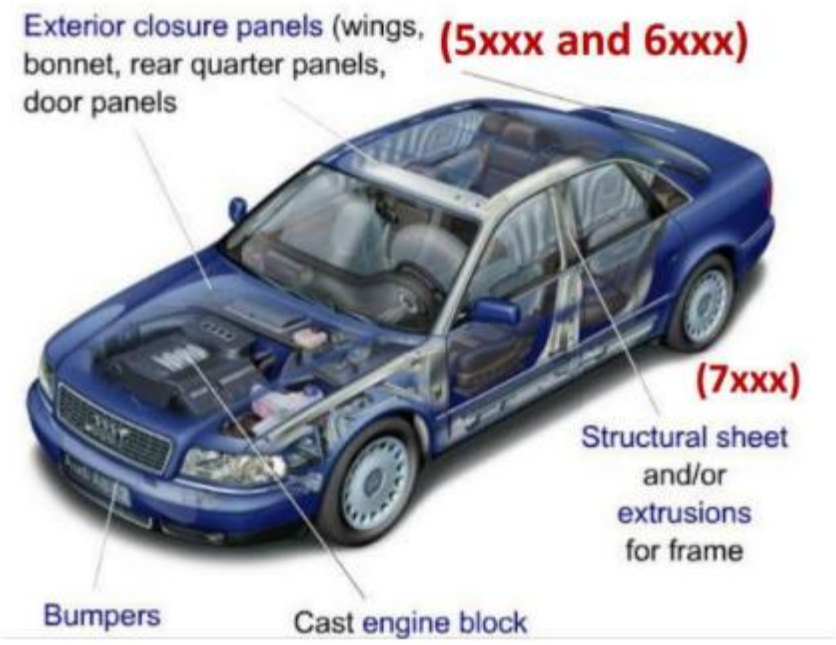

Figure 1-4. Example of aluminum application in Audi A8 construction. (Audi).

Depending on the application, the aluminum sheet materials are typically utilized in the thickness range from 0.8 to 4.0 mm. The 6xxx and 7xxx precipitation hardening alloy sheets are typically aged to different tempers in order to meet the different strength and

corrosion requirements by the OEM. Some of the commonly used aluminum temper used for high strength, heat treatable aluminum alloys are as follows:

- F: As fabricated, hot rolled and cold rolled
- T4: Solution heat treated and natural aged
- T6: Solution heat treated and artificially aged to peak strength
- T8: Solution heat treated, cold worked and then artificially aged
- T7: Solution heat treated and then stabilized

Table 1 shows the typical grades and alloy compositions of wrought aluminum sheet materials, published by the Aluminum Association, that are used in the automotive industry.

Table 1. Typical wrought aluminum alloy used in automotive application and their chemical composition (Association, 2009).

Alloy	Si	Fe	Cu	Mn	Mg	Cr	Zn
5182	0.2	0.35	0.15	0.2-0.5	4.0-5.0	0.1	0.25
5754	0.4	0.4	0.1	0.5	2.6-3.6	0.3	0.2
6014	0.3-0.6	0.35	0.25	0.05-0.2	0.4-0.8	0.2	0.1
6016	1-1.5	0.5	0.2	0.2	0.25-0.6	0.1	0.2
6111	0.6-1.1	0.4	0.5-0.9	0.1-0.45	0.5-1	0.1	0.15
6451	0.1-1	0.4	0.4	0.05-0.4	0.4-0.8	0.1	0.15
6061	0.4-0.8	0.7	0.15-0.4	0.15	0.8-1.2	0.04-0.35	0.25
7021	0.25	0.4	0.25	0.1	1.2-1.8	0.05	5.0-6.0
7075	0.4	0.5	1.2-2.0	0.3	2.1-2.9	0.18-0.28	5.1-6.1

Figure 1-5. A Hot Formed B-pillar reinforcement using Novelis' 7075 aluminum.

1.2 Vehicle end of life and recycling strategy

The production of primary aluminum is an energy intensive process which consumes large amount of electricity using the Bayer process, by electrolytic extract aluminum from alumina. It is reported that 113 GJ of energy is required to produce one ton of primary aluminum. In contrast, the amount of energy used is reduced by 88%, equivalent of 13.6 GJ per ton when it comes to re-melt and recycle aluminum scrap (Rombach, 1998). Therefore, re-melt and recycle path would reduce the amount of solid waste disposal and provide an energy efficient way to reuse aluminum. A "close looped recycling" strategy has been implemented by OEMs, stampers and material suppliers where the run around scrap from material production and stamping are properly separated and transported back to the cast house for re-melt and recycling. This strategy, similar to aluminum can recycling, is relatively simple to implement and would minimize the amount of cross-contamination from different grades of alloys. But this process would become more complicated, if one decides to recycle the aluminum at the end of life of a vehicle, more

specifically aluminum intensive vehicles. There have been quite a few aluminum intensive vehicles developed by OEMs over the years, such as the smaller volume vehicle: Audi A2, A8, Honda NSX, Jaguar XJ to large volume cars such as the latest Ford F-150 pickup truck. The 2002 Jaguar XJ has 30000 cars/year production volume and the Ford F-150 has production volume of 700000 trucks/year. (Hirsch, 2014) . With more Aluminum intensive and mix material cars coming into the market, it is obvious that scrapping these vehicles would generate a large amount of scrap aluminum that could be potentially recycled at the end of the vehicle life. To recycle this mix-scrap aluminum would bring much benefit such as reduced greenhouse gas emission and energy use from production of primary aluminum, reduce land fill waste and reduce cost of new aluminum alloy by using low cost scrap. Modern automotive recyclers uses a number of efficient process to recover valuable materials as illustrated in Figure 1-6.

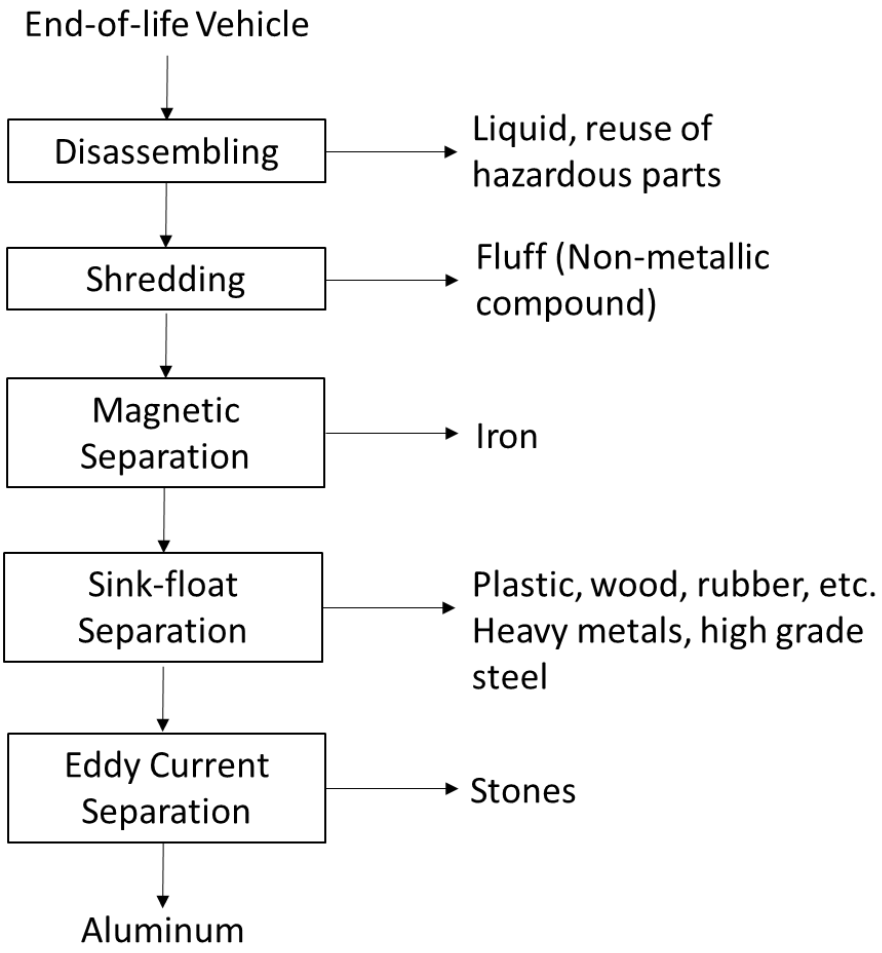

Figure 1-6. Typical end- of- life vehicle recycling process. (Cui, et al., 2010).

Though the ferrous and non-ferrous materials could be separated using magnetic and sink-flotation methods, smaller components such as fasteners, rivets and metal shavings could get mixed into the aluminum scrap stream. During the re-melt of scrap aluminum, the transition elements such as Fe, Mn, and Cr from ferrous components can cause a profound impact on the aluminum alloys' properties as they are typically considered to be impurities. Thus, it is important to study the impact of these elements and establish boundaries for maximum tolerance.

1.3 Forming limit curve

A forming limit curve (or FLC) is a quantitative method used to define the maximum plastic deformation of sheet materials prior to sheet necking during a stamping process. Sometimes the diagram constructed with the curve is also referred to as a forming limit diagram (FLD). The curve is often used in numerical forming simulation software to predict thinning and determine if the component is within the “safe” regime during the forming process. The forming limit curve typically provides two principle surface strains, i.e., ε_1 and ε_2, also called major and minor strain respectively. The concept of FLC originated from the work of Keeler and Backofen back in 1964. (Keeler, et al., 1964)

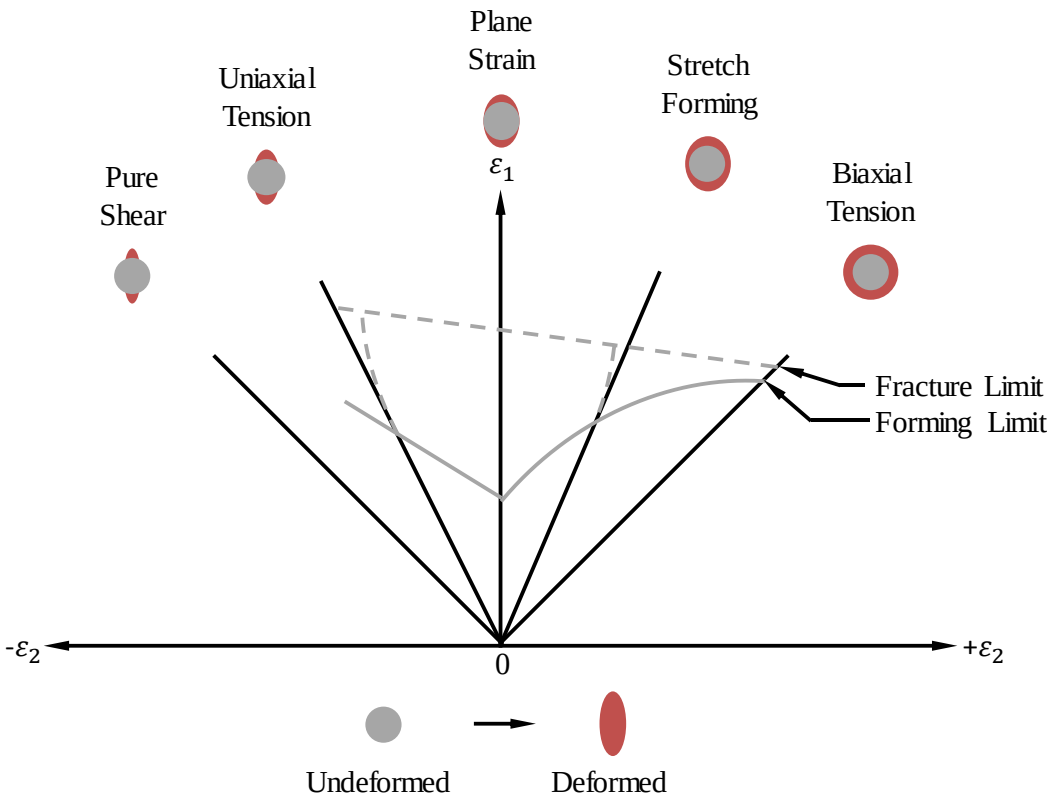

Figure 1-7. A general schematic of the forming limit curve. (Anderson, 2016).

Figure 1-7 shows a general schematic of FLD. The diagram is divided into two sides. The left hand side (LHS) represents the drawing conditions and the right hand side represents the stretching condition. The left hand side undergoes uniaxial tension state ($\varepsilon_2 = -0.5\ \varepsilon_1$) and pure shear state ($\varepsilon_2 = -\ \varepsilon_1$). The right hand side undergoes tension-tension and up to the equi-biaxial tension state ($\varepsilon_2 = \varepsilon_1$). The dashed line in the figure represents the fracture limit of the materials. It is the strain at which the materials finally fractures. The strain path also has a pronounced effect on the fracture limit of the material. Fracture limit of most ductile material continuously decreases as the strain path is changed from simple tension to biaxial tension. The solid grey line represent the FLC and the solid black lines represent several different strain paths on the left and right sides of FLD. The limit strain (ε_1 and ε_2) point corresponds to the onset of necking for each of the strain paths, and the locus of the different limit strains points for different strain paths is the FLC. The area (major and minor strain states) below the FLC is considered to be safe from a forming perspective. The area above the FLC is considered to be un-safe where significant necking/thinning would occur. The red circle represents the deformation of the grey circle would experience for each idealized strain path.

There are standards such as ISO 12004-2 and ASTM E2218-15 for determination of forming limit curves of metallic sheet materials. Standards describe in much detail the test method to generate a FLC.

The most accepted method to obtain a FLC involves use of a hemispherical punch to stretch sheet specimens of various geometrical configurations, a method pioneered by Nakajima et al., and illustrated in Figure 1-8. (Nakazima, et al., 1968) The sheet specimen is clamped between two dies and uses a hemispherical punch to deform the sheet metal

until the onset of necking or failure (if necking cannot be captured due to the precipitous nature of failures for some sheet materials). It is the most commonly used technique as it is easy to perform and can accommodate a wide range of sheet thicknesses. However, due to the hemispherical punch geometry and out-of-plane deformation, it is susceptible to bending and friction at the punch specimen interface, which could lead to some non-linearity in the strain paths.

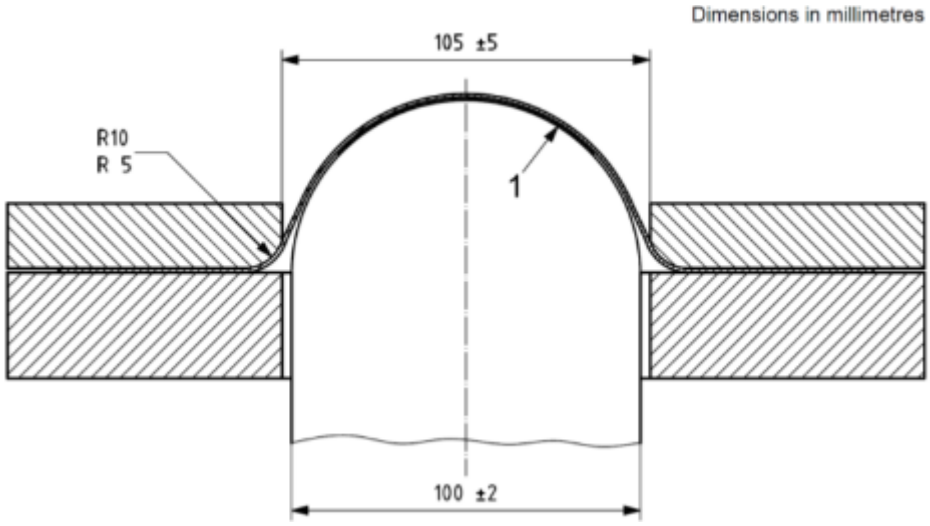

Figure 1-8. A schematic of Nakajima geometry. (Nakazima, et al., 1968).

Another commonly used test was developed by Marciniak et al., and illustrated in Figure 1-9. (Marciniak, et al., 1967). This test is similar to the Nakazima test but utilizes a flat cylindrical punch and involves a pair of sheet materials, the test material at the top and a carrier blank typically made of a more ductile sheet material than the test blank with a central hole of the same size at the bottom. The carrier blank enables necking of the test specimen in the top flat (or in-plane) region where both surfaces of the test blank remain free of punch contact, and therefore in a frictionless condition. Hence, compared to

Nakajima, no bending is introduced into the neck region of the specimen resulting in nearly linear strain paths for a point in the neck region.

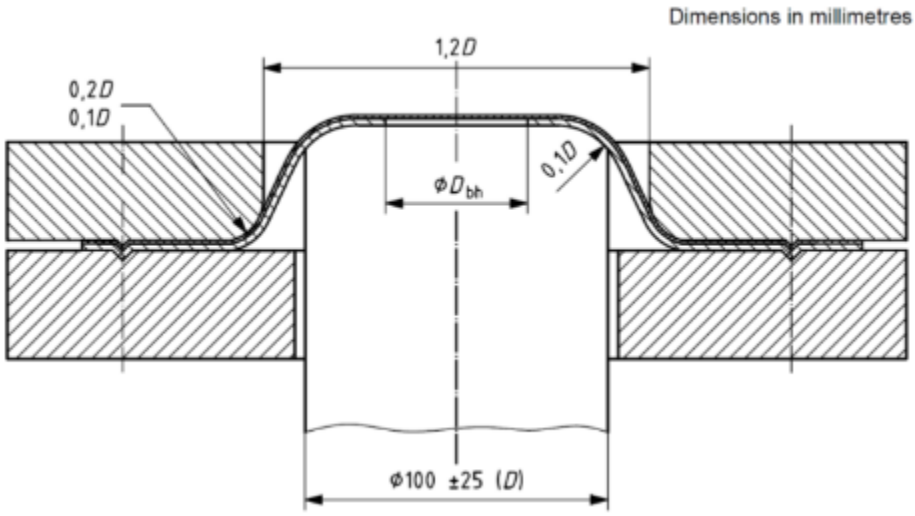

Figure 1-9. A schematic of Marciniak geometry. (Marciniak, et al., 1967).

Specialized specimen geometry is used for Nakajima and Marciniak tests in order to achieve different strain paths. The standards mentioned above suggest specimen geometries, starting with a circular specimen for the bi-axial tension strain paths on the most right hand side of the forming limit curve, followed by the specimen with decreasing width until pure shear state which is the most left hand side of the forming limit curve. A set of specimen geometries to achieve different strain paths are shown in Figure 1-10. The number represents the width of the specimen in millimeters.

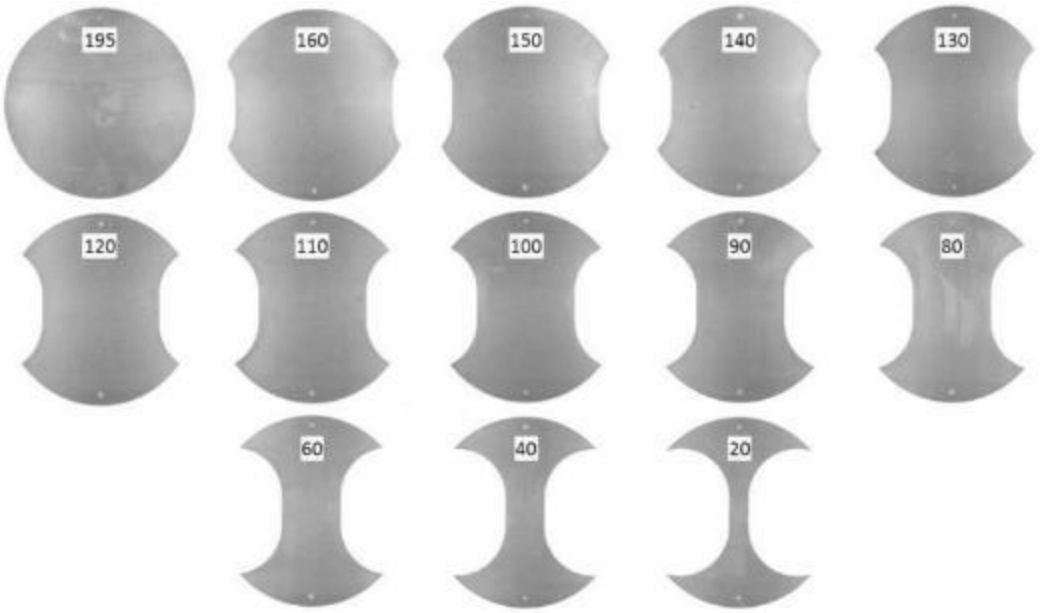

Figure 1-10. Overview of FLC geometries used at Novelis Inc. (Anderson, 2016).

Another recently developed method involves the use of hot gas forming to generate both the left and right sides of FLC, first demonstrated by Mitukiewicz et al. (Mitukiewicz, et al., 2014) See Figure 1-11. Pressurized and heated gas is used to deform the specimen instead of a physical punch or fluid. Strain paths on the right hand side of FLD are achieved using elliptical dies of different aspect ratios. However, a carrier blank is required to obtain the strain paths on the left side of FLD by providing a sealed conditions for gas pressurization. This is the method used in the current study. There are limitations with the hot gas forming test compared to physical punch, such as thick and high strength alloy may be challenging due to equipment bulge pressure limitations. However, this method to produce high temperature FLC for sheet gauge material is quite promising. It can measure FLC without the need of a physical punch and it also eliminates the use of lubrication, which for high temperature application, is another challenge by itself.

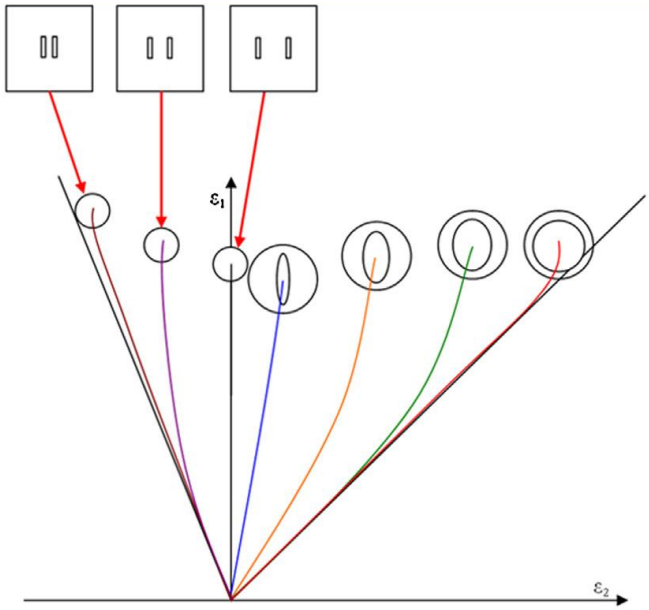

Figure 1-11. Specimen geometries and elliptical dies used in hot gas forming FLC. (Mitukiewicz, et al., 2014)

There are two primary methods used to measure surface strains. First method, called the Circle Grid Analysis (CGA), is a traditional method based on deformed grid measurements after the specimens has been tested. Second, a more recent method based on continuous full-field strain mapping technique of Digital Image Correlation (DIC), is an on-line strain measurement method that provides both the strain path and the limit strains for each path by acquiring continuous digital images of the deforming test specimen. CGA uses a network of spherical pattern with fixed diameter and spacing that are electrolytic etched onto the specimen surface as illustrated in Figure 1-12.

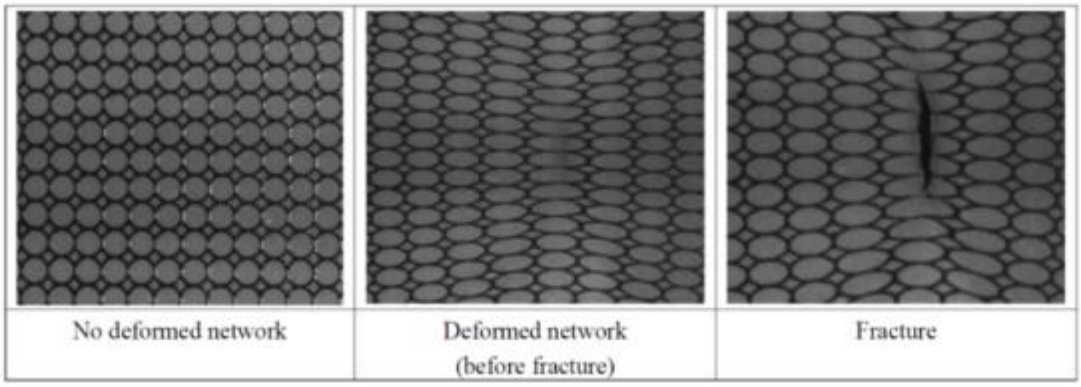

Figure 1-12. Overview of a CGA network showing original pattern, deformed pattern and fractured pattern. (Cikmis, et al., 2010)

The advantage of CGA is the ability to measure full panels enclosed in process dies and the ability to measure both sides of the panel and it would provide easy visualization of strain state on a formed part. However, it can only measure the initial and final state of deformation unless one utilizes a rather tedious interrupted test scheme to remove the test specimen from the forming system at different stages of punch stroke to record and analyze the deformed grids. In contrast, DIC uses a random black speckle pattern instead of circular grid. A white layer is first applied onto the metal surface to prevent bright spots that are typically present on shiny aluminum dome surfaces when incident light beam falls upon them. This is followed by a fine blank speckle pattern using an ink nozzle sprayer. A typical resulting flat sheet surface prior to dome stretching is shown in Figure 1-13.

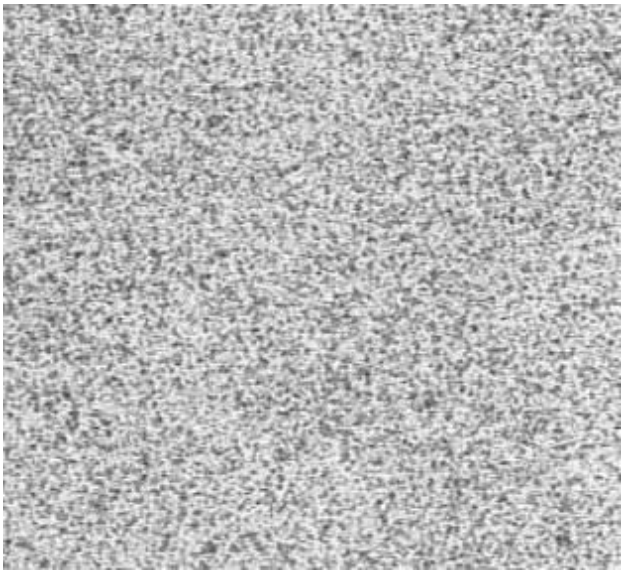

Figure 1-13. Overview of a speckle pattern used for DIC at Novelis Inc.

The DIC software utilizes the acquired set of images and converts each images of the deformed speckle pattern into displacement field and subsequently a strain map of the entire dome surface. The advantages of DIC is the strain history up to failure can be determined, since two cameras continuously record the deforming dome surface during the test. However, the down side of DIC is it tends to be more expensive with hardware and software and a large number of images must be efficiently processed. More importantly, it has limitations when testing at high temperature with large deformation, where the paint will suffer from the heat input and damage/peel during the final stage of deformation. CGA method was mostly utilized to perform the strain analysis. Some hot gas bulging tests were also carried out with continuous strain field measurements using the DIC methodology.

1.4 Elevated temperature forming and formability

Conventionally, aluminum alloys are stamped at room temperature. With stricter safety requirement for automobiles, alloys with higher strength and toughness are developed and employed to improve safety for occupants. The drawback of high strength alloys is that the higher strength typically comes with a drop in elongation and formability as well as spring back issues. Some of the high strength alloys, 7000 series aluminum sheet for example, is very difficult to form at room temperature in T6 temper. As a result, more sophisticated forming techniques are being developed to improve the formability of such high strength alloys in order to create more complex shapes not feasible with conventional stamping process methods. One of the techniques commonly used by the industry is elevated temperature forming. Depending on the forming temperature, it could be categorized into warm forming and hot forming.

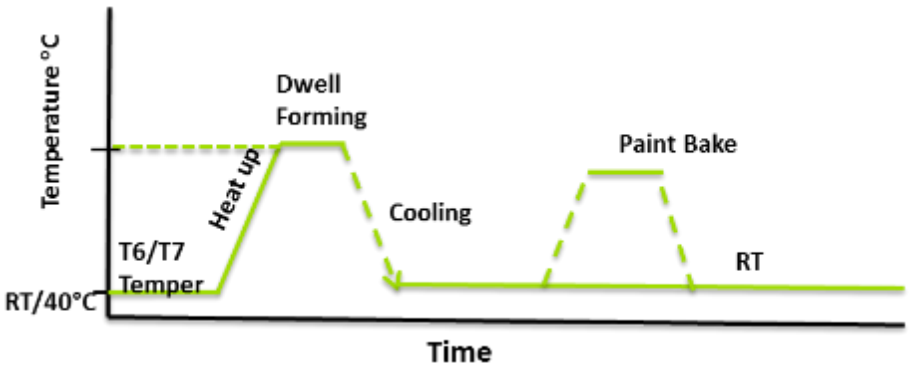

Figure 1-14. A schematic of incoming material - warm forming- final product route.

A warm forming process (Figure 1-14) is for metal heated to an elevated temperature that is below the recrystallization temperature of the alloy. One of the advantages of a warm forming process is that the final temper, such as T6 and T8 tempers, could be used as incoming material and could avoid the post-forming artificial aging that need to be carried

out in a hot forming process. However, one should be cautious that, with warm forming, the material properties could potentially be decreased. This is due to the precipitate coarsening at higher temperature. Springback, a change in the shape of the part after removal from the forming die, can also be present with warm forming process.

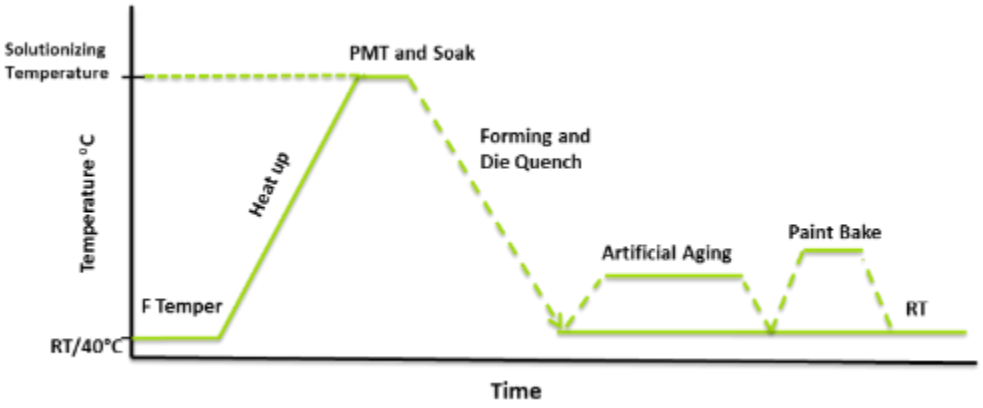

Figure 1-15 A schematic of incoming material- hot forming- final product route.

A hot forming process (see Figure 1-15) on the other hand, involves heating the incoming sheet to its solutionising temperature. This step is typically performed just prior to the hot forming process. After the material had been fully solutionised in the furnace, the blank is transferred into the press followed by forming at high temperature with immediate die quench. Therefore, the incoming material could be F temper and the springback is typically negligible with the hot forming process. The drawback is a very tight process control of solutionising, forming and die quenching conditions (quench rate) to above a critical threshold in order to ensure adequate properties in the final temper. A separate artificial aging process is needed to age the component to the final temper. Since the hot forming temperature is above most hydrocarbon based lubricant's operating temperatures, special type of lubricant such as Boron Nitride or Graphite are often used.

Another advantage of the aluminum hot forming process is that some of the existing hot forming line used for press hardening steel (PHS) could be modified and used for hot forming aluminum. However, due to aluminum's higher emissivity compared to steel, the heat up rate for aluminum using a conventional furnace is not optimized.

Similar to room temperature forming, high temperature FLCs are very useful and need to be developed for aluminum elevated temperature forming. In conjunction with the vehicle end of life recycling strategy mentioned previously, elevated temperature FLDs are important to aid evaluation of the formability of the aluminum alloys with high recycle content. Such FLDs are currently unavailable.

2. Project Objectives

The objective of this project is to investigate the effect of compositional impurities on the formability and performance of baseline automotive aluminum alloys, AA6111 and AA7075. The impurities were introduced through vehicle end of life recycling and mixed scrap stream. Both of the alloys investigated are high strength alloys which could potentially replace steel component in body in white (BIW). Therefore, the effect of material processing on consequent tensile properties such as strength, elongation and formability, including high temperature formability, are investigated in this study.

Impact of adding impurities to the alloy's baseline composition in terms of its microstructure, room temperature mechanical properties, wrap bend performance and warm temperature formability are examined. The right hand side of FLC (representing plane strain to equi-biaxial tension modes of forming) for baseline and high recycling content (HRC) version of AA6111 are obtained and compared at various warm forming temperatures. For baseline AA7075, two recycle content variants with increasing minor element from high recycle content are similarly investigated. The alloy's microstructure, mechanical properties in T6 temper are compared. Ultimately, the right hand side of the FLC curve at two targeted hot forming temperatures are constructed and compared for all three variants. Finally, the results from mechanical and formability tests are related to un-deformed and deformed microstructural and damage characteristics of the above sheet materials. The following specific objectives have been studied in the present work.

[1]. Characterization of microstructures of baseline and recycle compositions of AA6111 and AA7075 alloys from the various processing steps in the automotive sheet production process.

[2]. Qualitative correlation of microstructure in terms precipitates and constituent particles and resulting tensile mechanical properties and bendability of 6xxx alloys at room temperature.

[3]. Qualitative correlation of microstructure in terms precipitates and constituent particles and resulting tensile mechanical properties and forming limits of 6xxx alloys at elevated temperature and select tempers.

[4]. Qualitative correlation of microstructure in terms precipitates and constituent particles and resulting tensile mechanical properties and forming limits of 7xxx alloys at elevated temperature and select temper states.

[5]. Assessment of different methods of formability testing and forming limit measurement at elevated temperatures.

3. Literature Review

3.1 Effect of high recycling content on microstructure of 6xxx alloys

Transition metals such as Fe, Cr, Mn, Co have been added into Al-Mg-Si alloys and typically result in a decrease in the grain size of the alloys' in the as-cast condition compared to base alloys (Wang, et al., 2011). Moreover, small Fe and Mn additions in to Al-Mg-Si alloy increases the number density of the precipitates and further increase the peak hardness of the alloy. It is reported that the addition of Fe and Mn would enhance the formation of Mg-Si-Mn-vacancy or Mg-Si-Fe-vacancy, and the diffusion of the solute atoms in the matrix. They are effective cluster for the homogeneous nucleation of GP zones and also increase the number density of the precipitates in the alloys. It was found that with Mn level above 0.25% and Fe level above 0.2% could lead to formation of constituent particles and decreased the age-hardening ability in 6xxx alloys (Figure 3-1) (Shumei Wang, 2012).

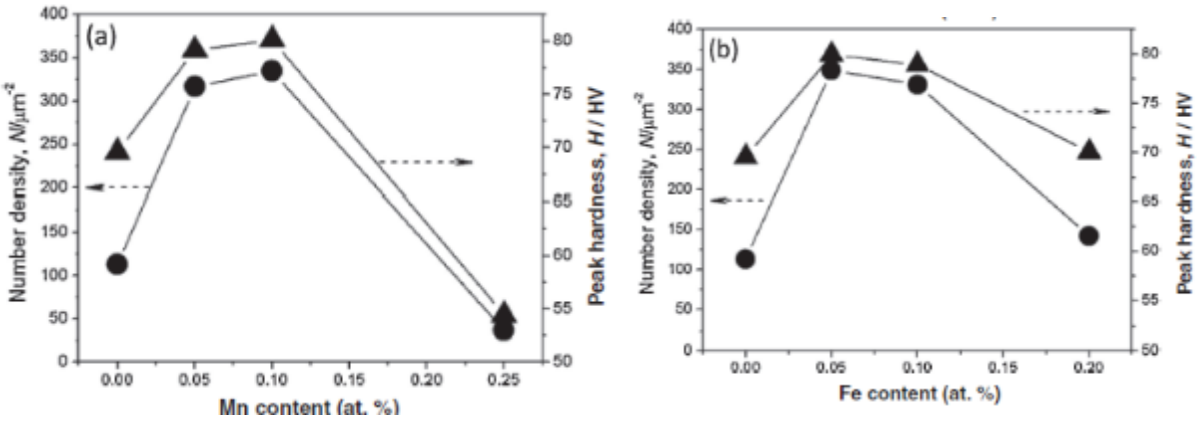

Figure 3-1. Changes in number density and peak hardness with (a) Mn and (b) Fe content. (Shumei Wang, 2012)

The types of constituents formed is also related to the Mg/Si ratio in 6xxx alloys. The α Al-Fe-Si phase is formed first with high Mg/Si ratio or balanced ratio in Al-Mg-Si alloys but β Al-Fe-Si phase is formed if Si is in excess (C.W.Fulton, 1968). Addition of transition metals also have a tendency to decrease the grain size in 6000 series. With Mn having the most significant impact, followed by Cr and Fe. (Wang, et al., 2011)

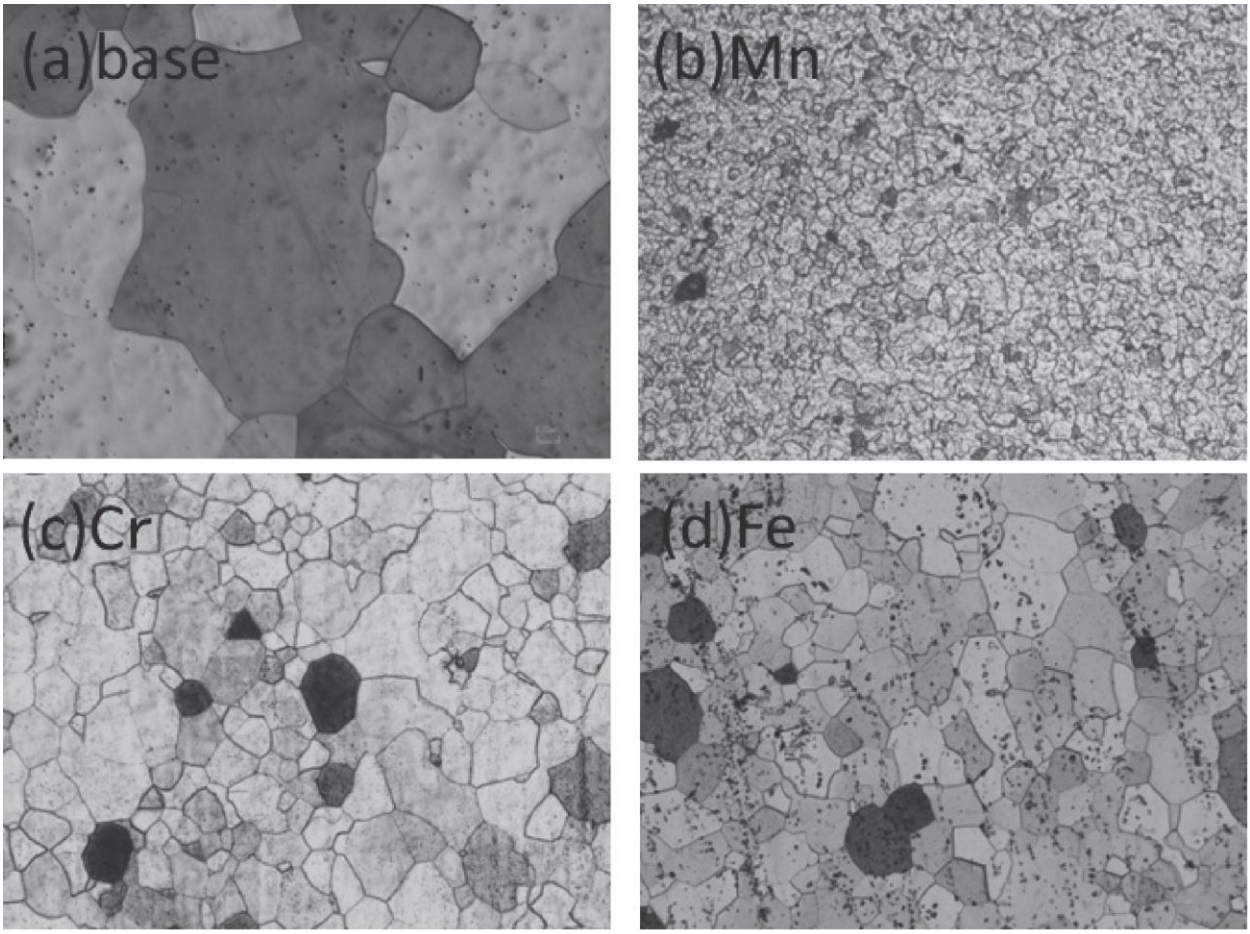

Figure 3-2. Metallography of 0.2% addition of transition metals that reduces the grain size. (Wang, et al., 2011).

Increasing Fe may also change the texture components which could have an effect on the formability in room temperature. Haiou et al. found that, with increasing Fe content, goss and other texture components become significantly weaker after solutionising. But

Fe content up to 0.75% did not have a significant influence on roping of AA6111 (Haiou, et al., 2005) .

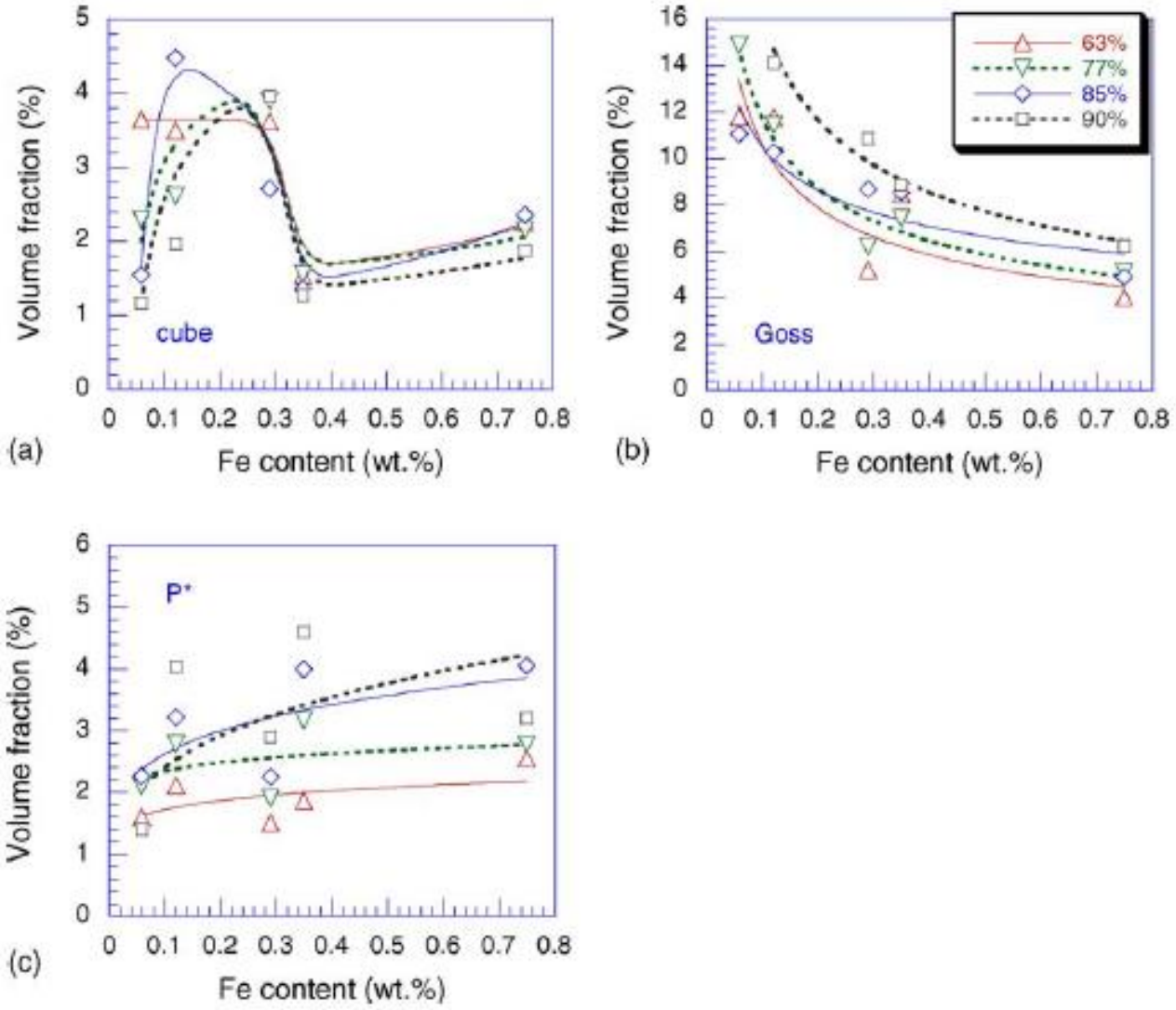

Figure 3-3. Evolution of (a) cube; (b) goss and (c) P* components of the recrystallized texture as a function of the Fe content. (Haiou, et al., 2005).

A study by Lievers et al. found that the bendability of AA6111 sheet decreases with increasing Fe content, up to 0.68% using an instrumented cantilever bend test. Higher Fe variant of AA6111 appears to have more Fe base particles and also form stingers oriented along the rolling direction, Figure 3-4.

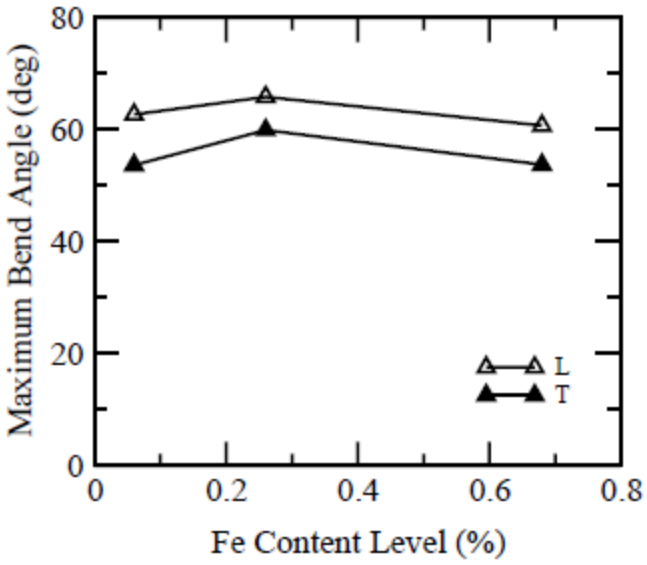

Figure 3-4. Maximum bend angle in longitudinal (L) and transverse (T) rolling direction with different Fe content level in AA6111. (Lievers, 2003).

A study by Sarkar et al. also looked into the effect of increasing Fe content (from 0.06% to 0.68%) on sheet bendability in terms of the r/t values of AA6111. A significant decrease in ductility was observed as the iron level was increased. Both the low and high iron-containing alloys failed in a shear mode due to void sheeting. During bending, small pre-existing micro-cracks, initial surface roughness and hard particles at or near the tensile surface all aid the development of shear bands. At sufficiently high Fe levels, strain localization contributes to damage initiation in the form of voiding at Fe-containing particles. Such damage in unstable in these microstructures and triggers the rapid development of shear cracks that propagate by a combination of void sheeting and intergranular fracture. (Sarkar, et al., 2004).

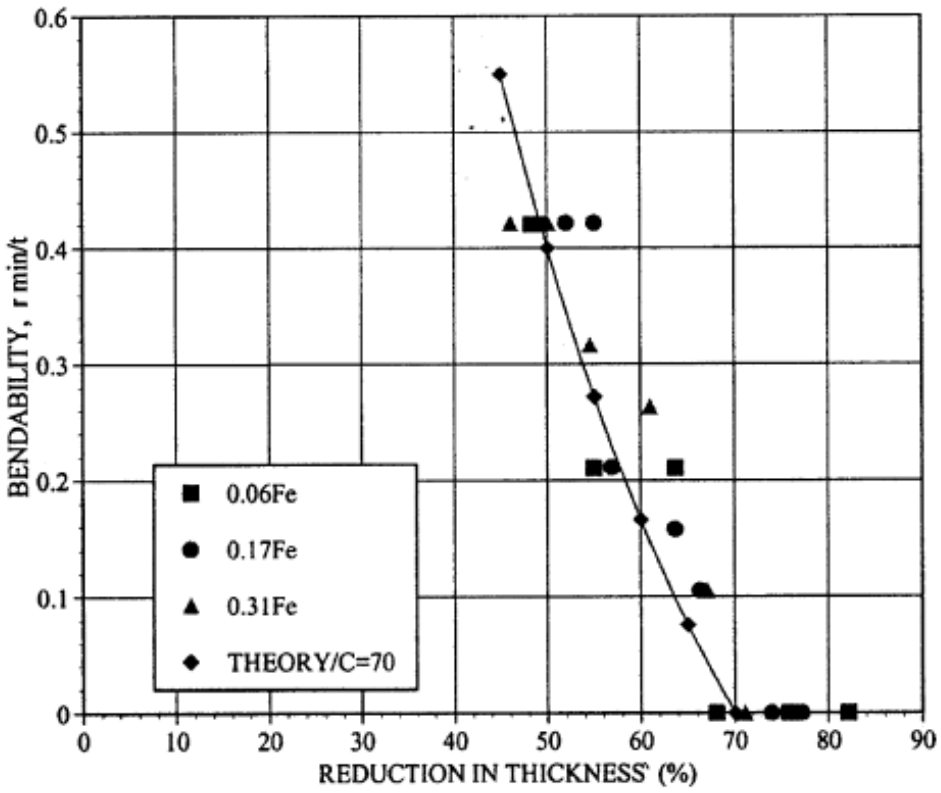

Figure 3-5. Correlation between bendability and the reduction in thickness in the case of AA6111. (Sarkar, et al., 2004).

The addition of Cr forms a chromium containing dispersoids (Al_7Cr) which is incoherent with the aluminum matrix. It increases the mechanical properties of Al-Mg-Si alloys slightly due to solid solution hardening. The addition of Cr also increases corrosion resistance by diminishing inter-crystalline attack and promoting pitting. Chromium content of 0.1% in an Al-Mg-Si alloy made stress corrosion worse but 0.25% Cr did not affect stress corrosion. (C.W.Fulton, 1968)

In summary, the addition of transition metals such as Fe, Mn and Cr is expected to reduce the grain size of 6xxx alloys, could potentially increase strength of the alloy due to solid solution hardening. However, such additions cause formation of constituent particles and hence a decrease in bendability.

3.2 Effect of transition metals addition on microstructure of 7xxx alloys

Iron addition into 7xxx series forms constituent particles such as Al_7Cu_2Fe, which are insoluble during the homogenization process and subsequent solution heat treatment. These hard intermetallic constituent particles were found to have a profound impact on the fatigue performance in the case of AA7150. (Rometsch, et al., 2013)

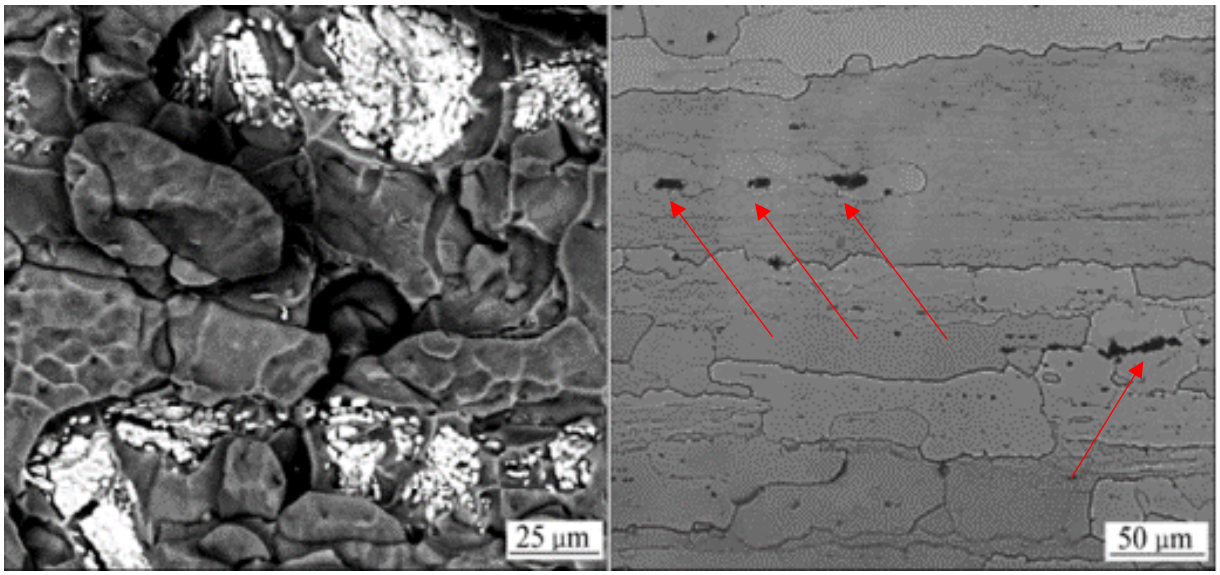

Figure 3-6. Fatigue fractured sample showing Al_7Cu_2Fe particles at the fractured interface. (Rometsch, et al., 2013).

Al_7Cu_2Fe particles were also found in 7075 T6 alloy causing a strong galvanic connection with matrix, which resulted in high corrosion potential values, indicating that passive film fracture and pitting corrosion occurred simultaneously. Pitting corrosion was found to have evolved around these Al_7Cu_2Fe particles. (Chemin, et al., 2014)

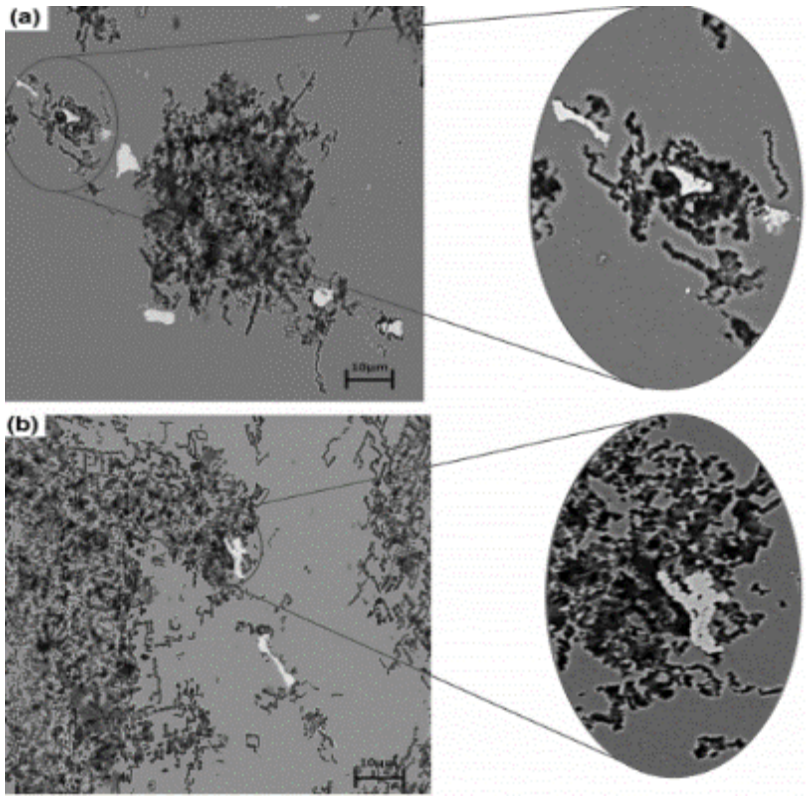

Figure 3-7. SEM Image of 7475 T7651 alloy after corrosion test with Al_7Cu_2Fe particles adjacent to pitting corrosion. (Chemin, et al., 2014).

Chromium had been used in AA7075 to form dispersoids. The Cr containing dispersoids can pin grain boundaries. Hence hinder the recrystallization and inhibit grain growth. Cr reduces the ability of Al-Zn-Mg alloys to age harden through precipitation of $Cr_2Mg_3Al_{18}$ during solution heat treatment. However, adding chromium also increases the quench sensitivity of AA7075. Since the Cr containing dispersoids are typically located at the grain boundaries, when quench rate is not adequate, a nucleation of $MgZn_2$ onto Cr phase particles occurs at the grain boundaries, thus reducing the age hardenability of the alloy. (Rometsch, et al., 2013)

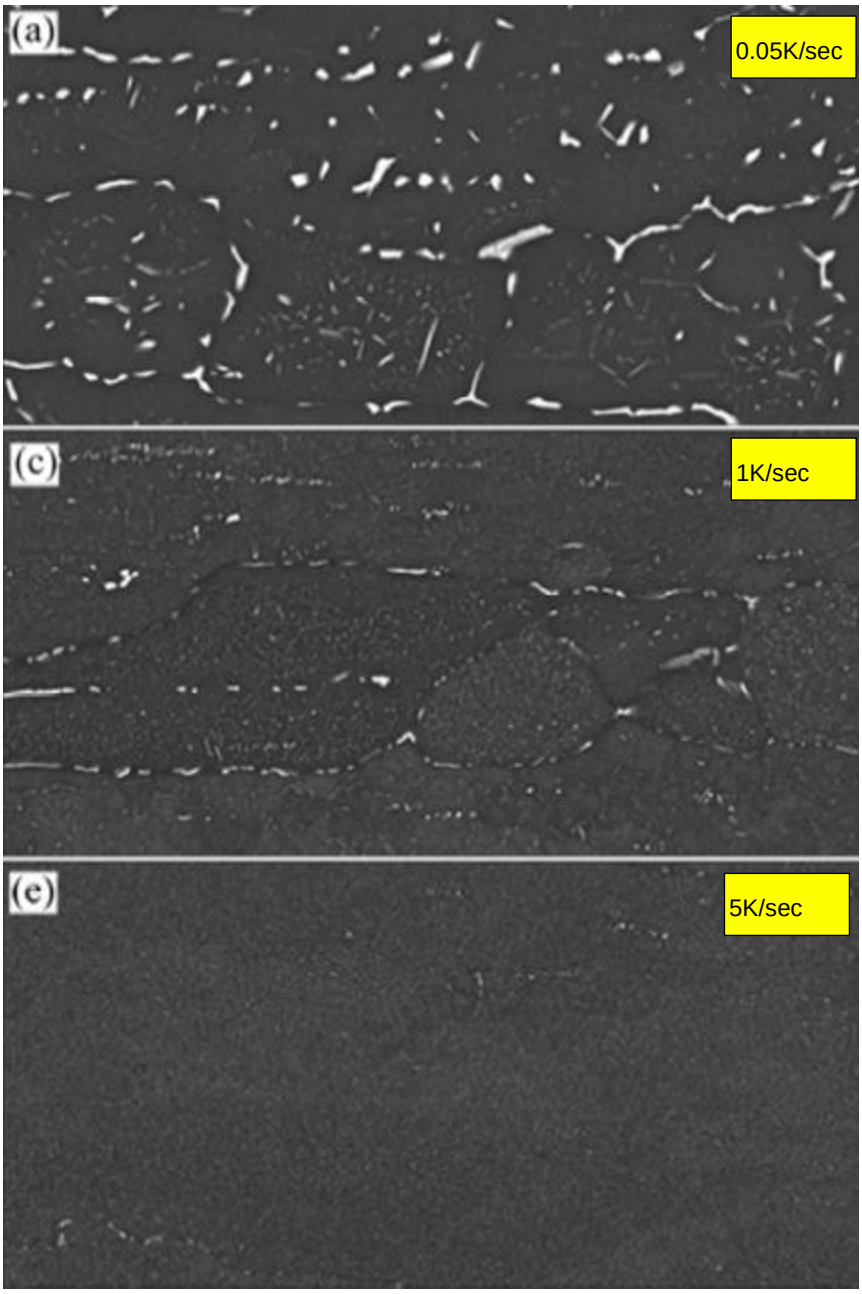

Figure 3-8. AA7150 with different cooling rate showing grain boundary precipitation induced by chromium dispersoids. (Rometsch, et al., 2013).

It is to be noted that the Cr-based dispersoids also bring some beneficial effect in terms of stress corrosion cracking. Cr containing dispersoids raise the grain boundary potential to help prevent corrosion. In fact, 0.15-0.25% Cr in Al-Zn-Mg-Cu alloys is used to improve the resistance to corrosion and stress corrosion. (C.W.Fulton, 1968). Conventionally, 7000 series alloys have high strength and mostly used in aerospace industries. Thus the fatigue was the main focus of the most of the studies related to 7xxx. But the fatigue behavior would be much different for automotive applications. Therefore, there have been very few studies on the effect of transition metals such as Fe and Mn on mechanical properties of automotive grade 7xxx alloys.

3.3 Methods of evaluating formability at high temperature

Due to its long history in automotive applications, the FLD of AA6111 in T4 temper is readily available (Graf, et al., 1993). Studies related to warm forming of high strength aluminum alloys are relatively recent. Li et al. investigated the warm forming behavior of 5754, 5185 and AA6111 T4 in the warm forming temperature range of 200-350ºC range and in strain rate range of 0.015-1.5s^{-1}. (Figure 3-9). They found that all alloys exhibited a significant improvement in their formability in the biaxial warm forming in these temperatures and are comparable to those of A-K steels formed at room temperature. The optimum warm forming window for these alloys at 200-350ºC may not cause drastic loss in strength level of the formed part. (Li, et al., 2004)

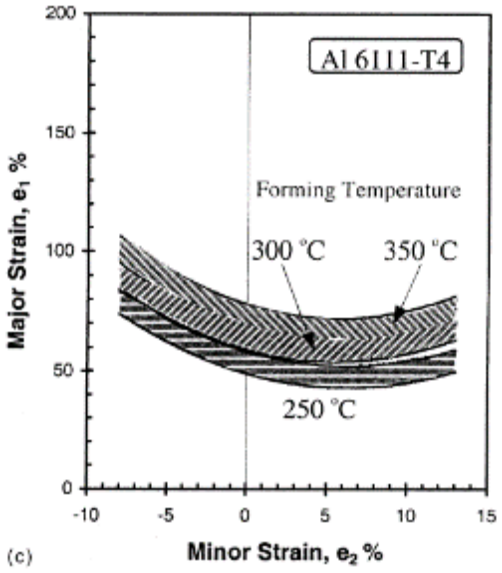

Figure 3-9. Effects of forming temperature on FLD for AA6111-T4. (Li, et al., 2004).

Similar trend in the increase in formability with increasing temperature was also obtained by Mahabunphachai et al. on 5052 and 6061 sheet alloys (S. Mahabunphachai, 2010) on hydro formed parts at elevated temperature. (Figure 3-10)

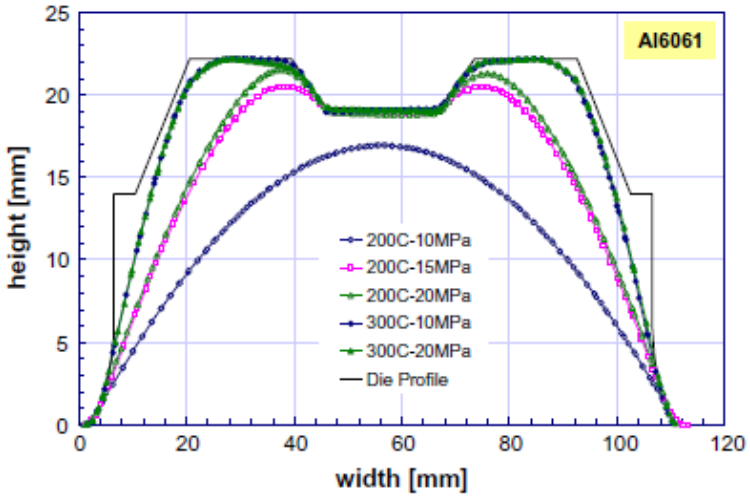

Figure 3-10. Profiles of hydro formed AA6061 at different temperature. (S. Mahabunphachai, 2010).

As for 7xxx series aluminum, since the elongation is very low at room temperature in T6 temper, there is very little value in getting the FLD at room temperature. However, warm forming and hot forming FLDs have been determined by several researchers. Kumar et al. studied warm forming behavior of 7020 T6 sheet and found the alloy is temperature and strain rate dependent. Limiting draw ratio (or LDR) and Limiting drawing depth (or LDD) increases with increasing temperature above 150ºC. However, there was a 30% loss in UTS and YS when 7020 T6 was warm formed at temperature between 200ºC and 250ºC due to coarsening of precipitates. (M. Kumar, 2014).

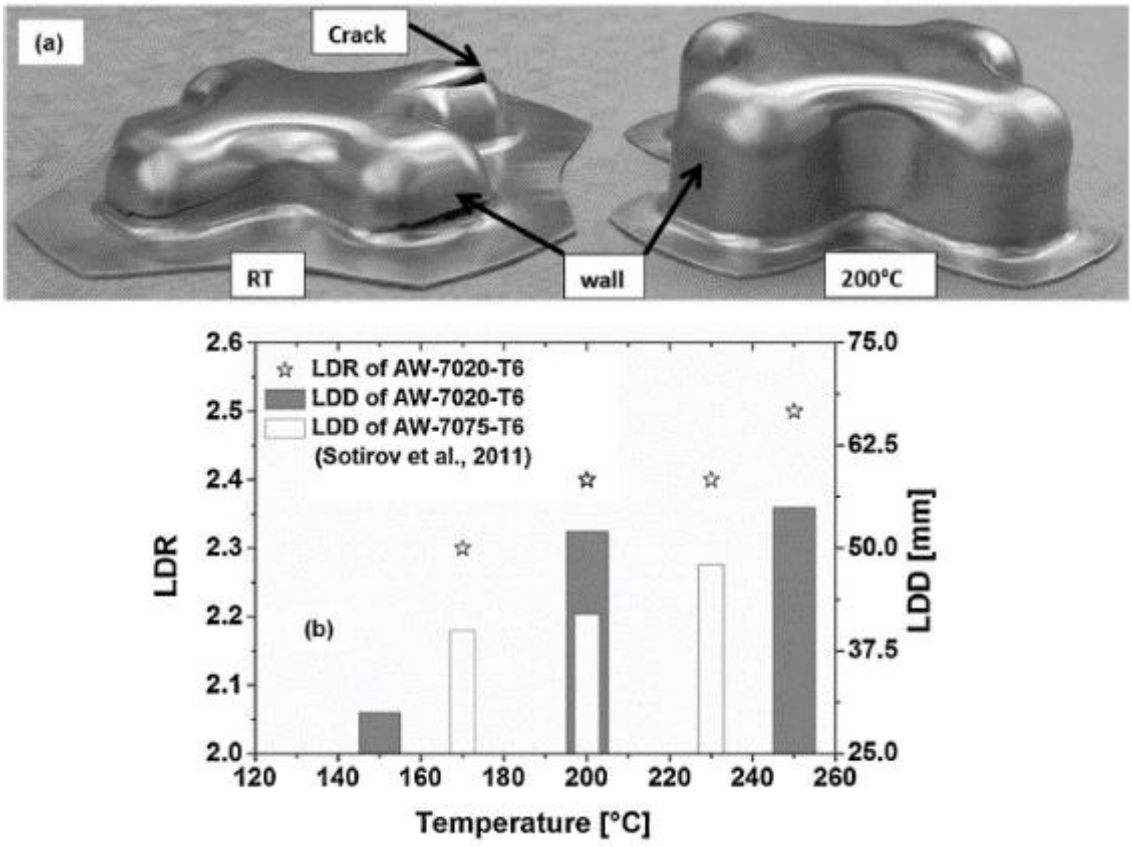

Figure 3-11. Deep drawability of AA7020-T6 and 7075-T6 alloys; (a) photos of a cross-shaped deep drawn component at room temperature and 200ºC, and (b) LDR and LDD values at elevated temperature. (M. Kumar, 2014).

Similar trend of decreasing mechanical properties after warm forming simulation of 7075 T6 sheet were observed and reported by Wang et al., in 2012. At 140ºC and below, there was no effect on the mechanical properties. However, when the samples were exposed to temperatures over 220ºC, a significant loss of strength was observed. The best deep drawing formability was found at 180ºC and the best stretch formability was at 220ºC for AA7075-T6 sheet. (Wang Hui, 2012)

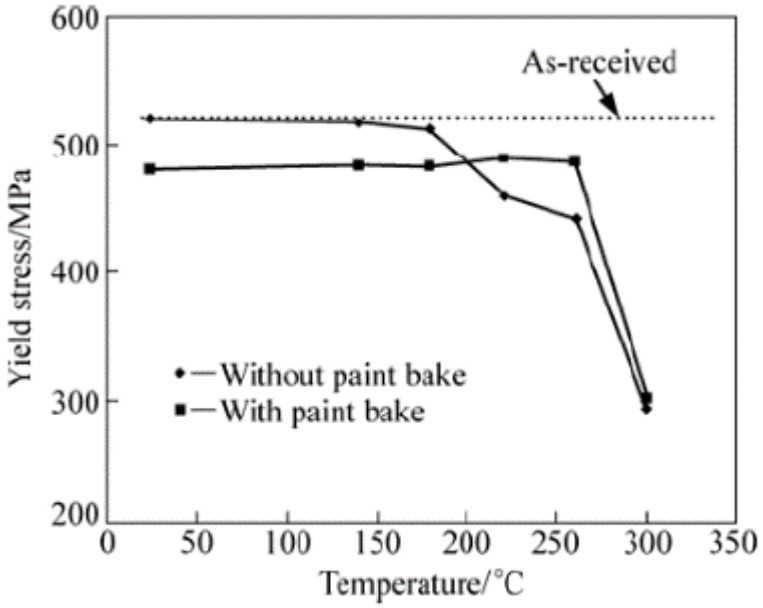

Figure 3-12. Yield strength plotted as function of heat treatment temperature with and without paint bake for AA7075-T6 sheet. (Wang Hui, 2012).

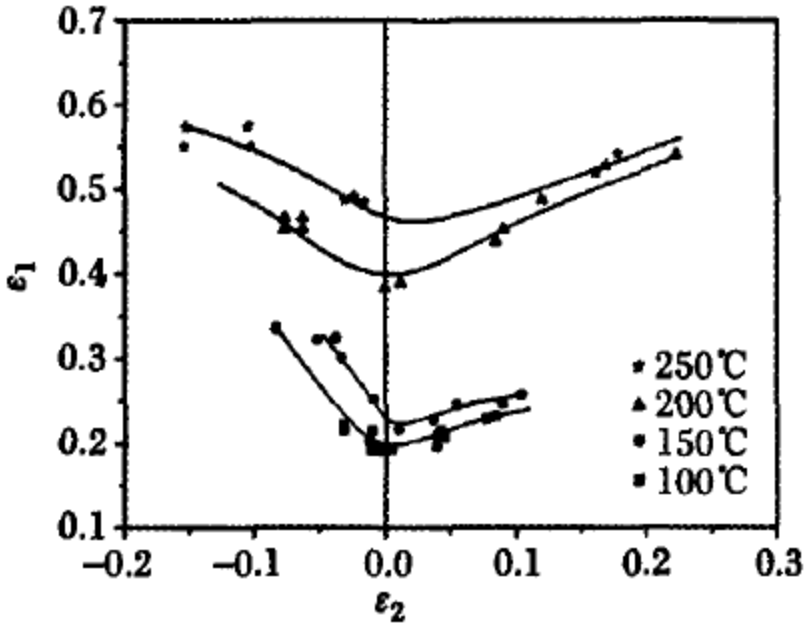

Figure 3-13. FLDs of 7075-T6 aluminum alloy sheet obtained at various temperatures. (Hua, et al., 2010).

Elevated temperature FLD of AA7075-T6 were obtained by Huang et al. (see Figure 3-13). The FLDs shift upwards towards larger limits with increase in temperature between 100ºC to 250ºC. There is a larger unexplained shift between 150ºC and 200ºC (Hua, et al., 2010). FLD for AA7075 at hot stamping temperature were predicted by Weimin et al. The predicted FLDs, as shown in Figure 3-14, reached a plane strain limit of about 1 at 420ºC. Also, the FLDs obtained were very strain rate dependent at high temperatures with lower limit strains at higher strain rates (Weimin, et al., 2014). However, predicted FLDs were not validated with experiments.

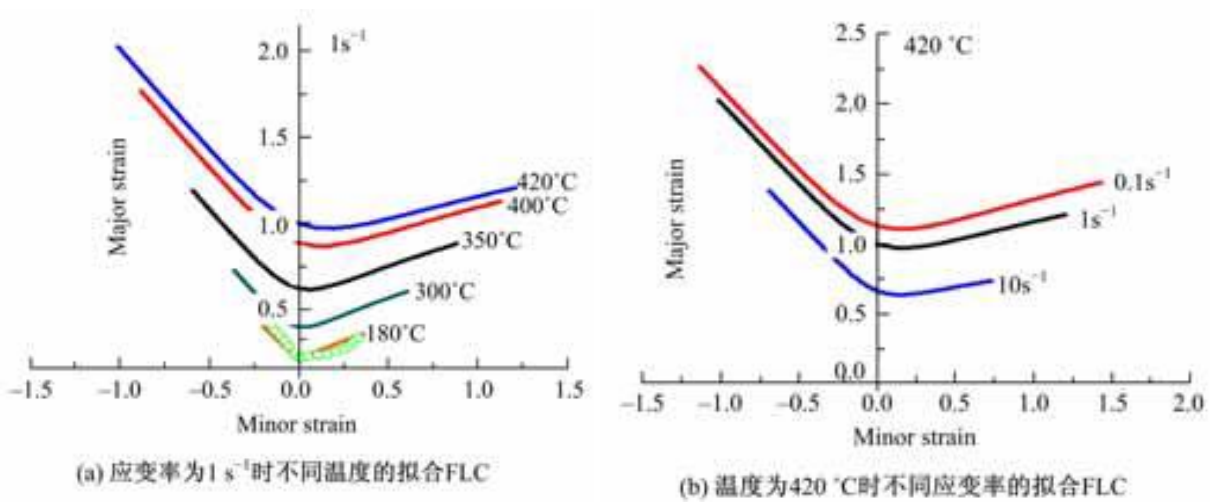

Figure 3-14. Predicted FLDs of AA7075-T6 sheet, (a) FLC for 7075 at various temperatures at 0.1 s^{-1} strain rate, and (b) FLC at 420ºC with different strain rates. (Weimin, et al., 2014).

4. Experimental Methodology

4.1 Microstructure evaluation

In a conventional DC cast aluminum ingot, macro-segregation is a common phenomenon. It could occur in the range of several millimeters in small ingots to even hundreds of centimeters in the case of a full size ingot. The macro-segregation is caused by relative movement (or flow) of segregated liquid and solid during solidification. Since the solubility of elements is lower in a solid than in a liquid, the center of the ingot typically solidifies first and its element content is lower than in the regions away from the center. The edge of the ingot also solidifies first due to increased heat transfer to the ambient air. Consequently, in the present work, regions of the ingot between the center and the periphery at about the quarter thickness location were the richest in elemental constituents. Figure 4-1 shows a typical DC cast ingot macro-segregation where the surface with the cortical zone had the highest macro- segregation. However, the ingot surface was scalped off prior to the rolling process. Thus, all of the samples for metallography and DSC work were taken from the quarter thickness location.

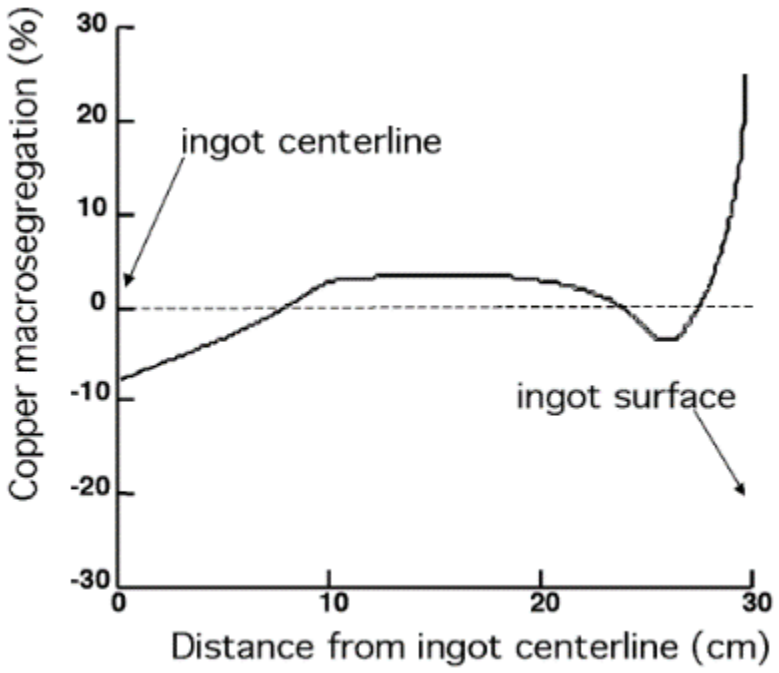

Figure 4-1. Typical macro segregation profile in a round DC cast aluminum ingot. (Beckermann, 2001).

4.1.1 Metallurgical Mount Preparation

Metallurgical samples were cut from quarter locations of the ingot and cold mounted using epoxy resin. The samples were then ground using silicon carbide paper with grit sizes of 240, 320, 400, 600, and 800 µm, and polished using 0.5µm colloidal silica to a mirror finish. For AA6111 and AA7075 variants, electrolytic etching was done in sodium hydroxide (NaOH) and Barker's etchant (HBF) respectively.

4.1.2 Optical and Electron Optical Imaging

Metallography of all samples was carried out with a Zeiss® Axio metallurgical optical microscope at magnifications of 50x, 100x, and 200x. A polarized filter was used to take images for grain size measurement. Electron optical images were taken using Philips® XL30 S FEG-SEM at an operating voltage of 20 kV. For this purpose, the mounted and polished samples were carbon coated to have better conductivity and prevent charging of epoxy. An Oxford X-Max Energy-dispersive X Ray Spectroscopy (EDS) system was used to analyze the compositions of the constituent particles. The grain size was measured using the line interception method.

4.2 Mechanical testing

4.2.1 Room temperature tensile test

Uniaxial tensile test samples were CNC machined as per ASTM B557 standard with 2 inches gauge length and tested at room temperature on an Instron mechanical test system, Model #5500R, with a 25 kN load cell. Tensile tests were carried out in accordance to ASTM E8, at a displacement rate of 0.1 in/mm up to a tensile strain of 1.0%, followed by a displacement rate of 0.5 in/mm until fracture. The axial displacement of the gauge length was measured using an Instron AVE-1 video extensometer.

4.2.2 Elevated temperature tensile test

Warm tensile tests were also carried out at 300ºC with an Instron machine, model #4505, with the grip and specimen placed inside an environmental chamber set to 300ºC. A 50 kN load cell and an Instron AVE-2 video extensometer was used for strain measurement. The specimen was allowed to soak for 10 minutes to reach the target temperature. The

temperature was measured using a thermocouple attached to the specimen, before commencing the test.

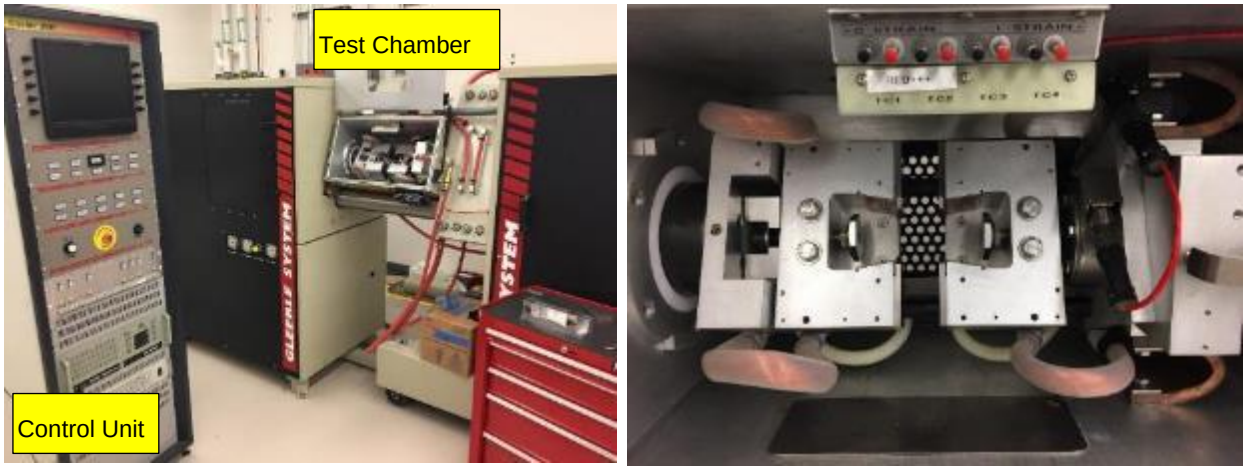

Figure 4-2. Gleeble thermo-mechanical test system for high temperature tensile test and overview of the Gleeble specimen.

Figure 4-3. A photograph of Gleeble tensile test specimen with a thermocouple welded for elevated temperature test.

High temperature tensile tests above 400ºC were carried out using Gleeble thermo-mechanical test system, model 3800-510 (see Figure 4-2). A sub-size F temper 7xxx Gleeble tensile specimen is shown in Figure 4-2. Gleeble thermo-mechanical test system for high temperature tensile test and overview of the Gleeble specimen was heated to 480ºC, and soaked for 5 minutes at temperature to allow full solutionising of the material. Subsequently, the specimen was cooled at 1.6ºC/sec to the target temperature and pulled to fracture at a strain rate of 1/sec.

4.2.3 Wrap bend test sample preparation and test apparatus

Wrap bend test samples were cut into 1 inch length x 3 inch width coupons with 3 inch dimension in the longitudinal (or rolling) direction. The coupons are tested in a custom designed wrap bend tester. The bends were carried out using a series of replaceable mandrels of different standard radii. During the test, a mandrel with a specific radius would be inserted into the wrap bend tester, then the sample would be wrapped over the mandrel using swing of the lever, fitted with a freely rotating roller, to fully bend the coupon (Figure 4-4). The sample surface was then examined with unaided eye for fissures or micro-cracks on the outer tensile surface. The mandrel with the smallest radius which the sample passed without any fissures or micro-cracks, was considered as the minimum bend radius of the material. This radius divided by the sample thickness, also called the r/t ratio, was taken as a measure of bendability of the sheet material. When the test was completed for each radius, the sample was retrieved from the tester to examine for cracks. For the 6xxx series aluminum sheet, the test was first carried out with 0.028 inch mandrel radius, followed by progressively decreasing radii of 0.024 inch, 0.020 inch, 0.016 inch and 0.012 inch. Triplicate tests at each mandrel radius were used to ensure consistency and repeatability.

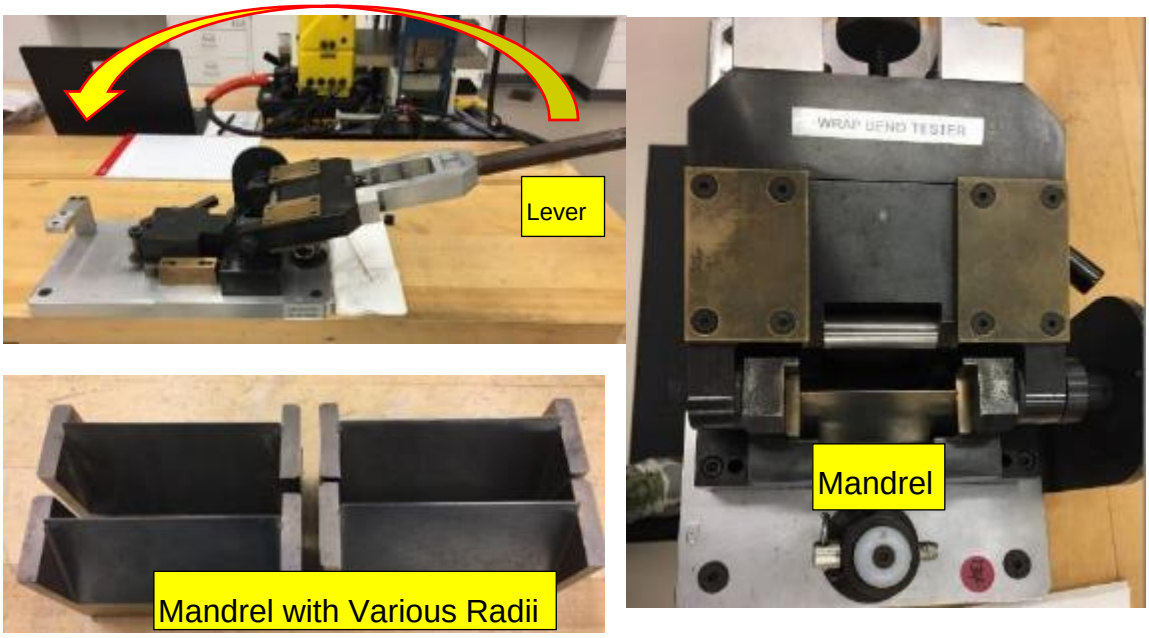

Figure 4-4. Photographs of the wrap bend tester and the mandrel region.

4.3 High temperature formability testing

4.3.1 Sample perpetration

Sample preparation involved specimen cutting, cleaning, and gridding for strain measurement after the material was rolled to final gauge. The sample panels were fist sheared to 6.5 inch x 6.5 inch squares. The sample panels were then degreased using ultrasonic cleaner by immersing in isopropanol alcohol for 5 minutes to remove any rolling lubricant and debris. Sample were wiped using clean paper towels. The samples were then electrochemically etched using a stencil with a periodic pattern of 1 mm diameter circular dots with 2 mm edge-to-edge spacing. In addition to the stencil, the process of electrolytic etching utilized a DC power source and a roller marker. Commercially available electrolyte LNC-5 manufactured by Electroetch company, formulated specially for etching aluminum sheet, was used as it provided good contrast of white dots against

the grey background of the original sheet surface. A good sample preparation was critical towards later analysis, especially for high temperature tests. An example of typical etched sample is shown below in Figure 4-5.

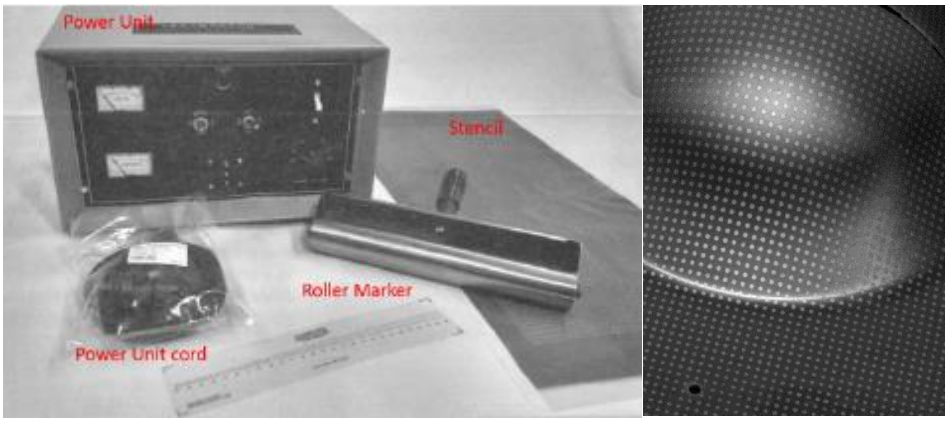

Figure 4-5. Photographs of electrochemical etching set-up (left) and an etched and deformed test sample (right).

4.3.2 High Temperature Forming Test

High temperature forming tests were carried out using a hot gas bulge tester at McMaster University. Figure 4-6 shows the schematic of the high temperature gas forming test jig that was part of the gas bulging system. The system consisted of an upper die supported by a long cylindrical component. This die had a circular opening and two circular rings connected through springs to provide cushioning. The bottom tooling was a flat plate to which a die of circular or elliptical opening was mounted. The entire set up was placed inside an environmental chamber. A square blank of size 6.5 in x 6.5 in was precisely located between the lower die (supported on four posts) and the upper die using guide pins located on the bottom die.

The upper die was controlled via a pneumatic cylinder to move up and down and apply clamping force to the sample. During the test, the sample was clamped between the upper and lower dies with a force of 178 kN to ensure full clamping. A shallow lock-bead was also utilized as part of the die design to ensure complete restraining (i.e., no draw-in) of the material outside the lock-bead region into the die material during bulging. For bulging, a gas line from a compressed cylinder was connected to a small opening in the lower die. The pressure was monitored by an in-line pressure valve. The clamping and bulging process is schematically illustrated in Figure 4-7.

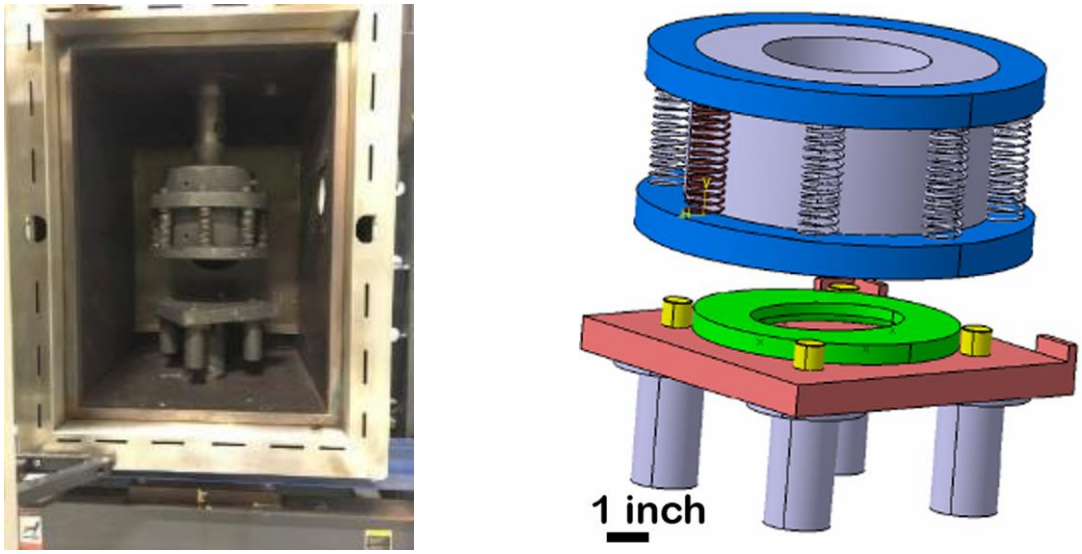

Figure 4-6. Photograph and a schematic of the hot gas bulge test system.

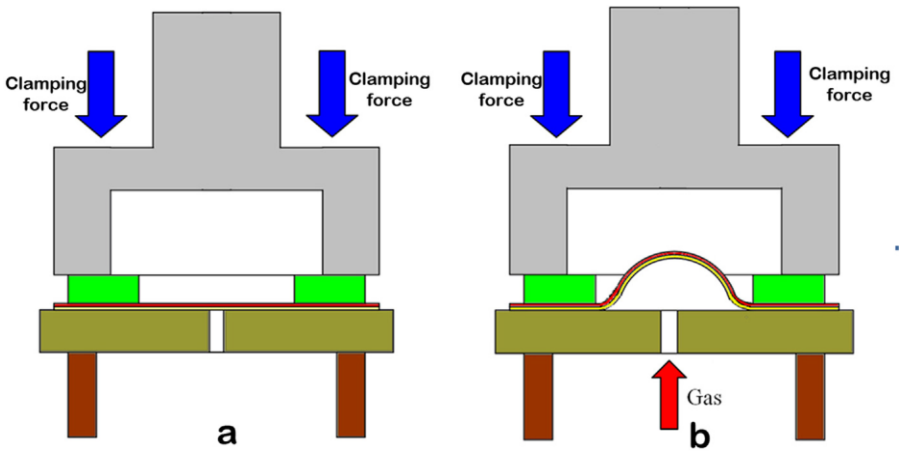

Figure 4-7. Schematics of the clamping and bulging process steps for a hot gas bulge specimen.

In order to achieve different strain paths on the right hand side of FLC, three dies with elliptically-shaped openings of different aspect ratios, in addition to a circular opening die, were used. The major versus minor axes for the elliptical openings were 4:3, 4:2 and 4:1 respectively. Four grooves on the outer edge of the die were used to place the die in between the four posts at the bottom to prevent any slippage (Figure 4-8).

Figure 4-8. Photographs of the dies with elliptical openings for hot gas bulge test.

The tests for 6xxx series sheet materials were started in T82 temper to simulate warm forming process. The samples with etched periodic grids were placed, one at a time, inside the furnace and soaked for 5 minutes to allow sample to reach target temperature

uniformly. Similarly, 7xxx series samples with etched periodic grids were introduced in to the furnace but in the as-fabricated (i.e., F temper) state. These samples were first brought to 480ºC and allowed to soak for a minimum of 10 minutes to ensure complete solutionising and attainment of uniform temperature. The furnace temperature was then lowered to the test temperatures of 470ºC and 425ºC. The blank were then placed in the die and bulged with a pressure rate of approximately 2 psi/sec. Once the sample fractured under pressure, the test was terminated manually and the burst pressure was recorded.

4.3.3 Sample imaging

The bulged sample with etched grids were imaged and analyzed for mapping surface strains using Argus system from GOM, Germany (GOM). For this purpose, the sample was first placed on a sample holder to provide 360º rotation. A total of 5 miniature sized Argus position markers were placed around the perimeter of the sample to provide coordinates (see Figure 4-9). A Nikon D60 DSLR with a tripod was used to take images of the sample using a 25 mm lens, a shutter speed of 1/250s and an aperture setting at 16. A white balanced flash was used to achieve the best image quality.

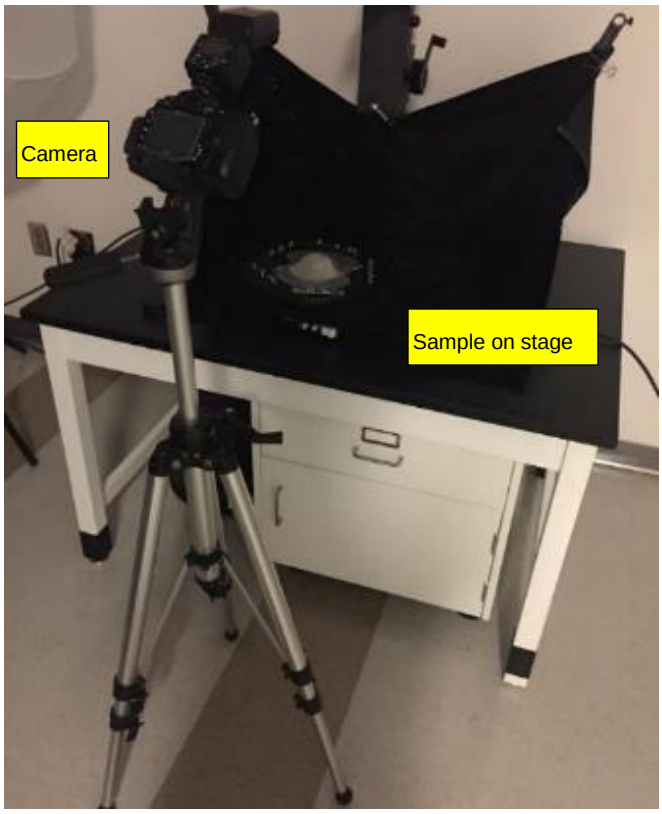

Figure 4-9. Hardware of Argus optical strain measurement system for surface strain mapping of bulge samples.

Two complete 360º rotations were made for each sample with different camera tilt angles of 30º and 60º (see Figure 4-10). With the aluminum sheet's shiny surface and in some cases faded/damaged circular grid, there were often certain areas of the sample where the image quality was poor and the information was unrecognizable by the Argus software during the analysis. Therefore, it was recommended to take one image for every 3-5 degrees rotation, i.e., about 100-120 images in total for each tilt, to capture as much pattern information as possible and avoid glare from external lighting at certain angles.

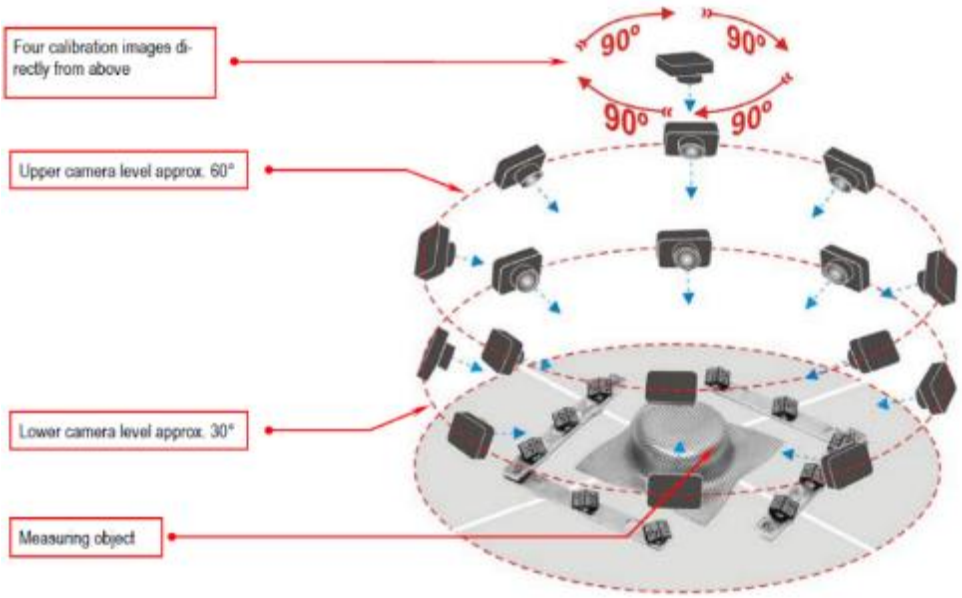

Figure 4-10. Schematic of the images taken with two 360ºC rotations and with two levels of tilt.

4.3.4 Image analysis with Argus

After images were taken, they were uploaded into the GOM Argus system software for analysis. A strain map was generated from the set of images taken to calculate 3D major and minor strains in formed specimen from each die geometry. A total of 5 lines sections were created across the apex (fractured area) of the sample, as shown in Figure 4-11. The FLC curve was determined in accordance to ISO 12004-2:2008 test standard. The photograph in Figure 4-11 shows an equi-biaxial sample and its corresponding strain map.

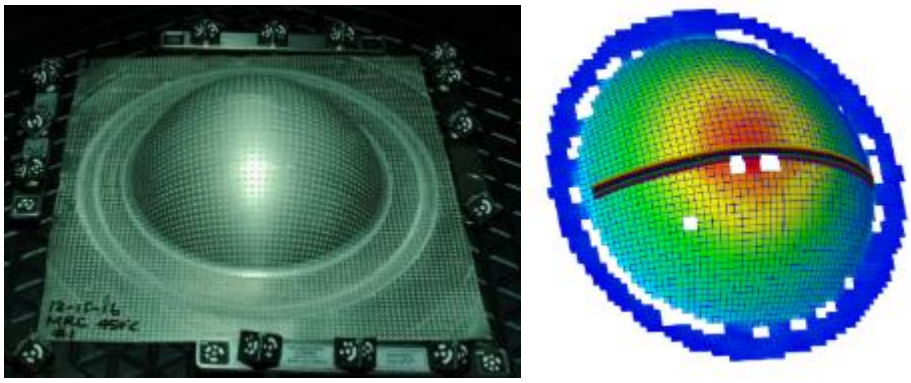

Figure 4-11. Strain mapping and limit strain determination proceure with Argus optical strain measurement system for bulged specimens.

4.4 Fractography

An equi-biaxial axial sample from each of the variants from 6xxx and 7xxx was selected after strain maps were developed using Argus. The sample was carefully cross-sectioned away from the fractured area using a diamond saw to avoid any damage to the fracture surface, as illustrated in Figure 4-12.

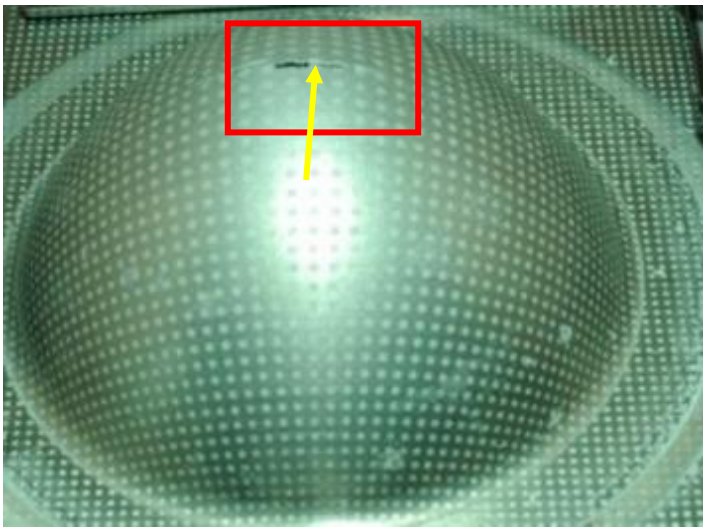

Figure 4-12. Schematic of sample location for fractography using SEM.

The sample was cut dry without any lubricant to avoid contamination of the metal surface (Figure 4-13). The fractured surface was then placed inside a Philips® XL30 S FEG-SEM operating at a voltage of 20 kV for observation and EDX measurement.

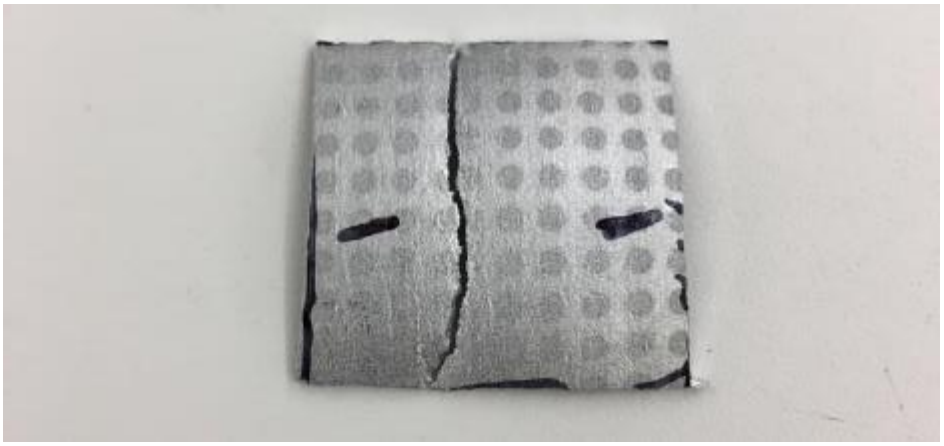

Figure 4-13. A photograph of the cut region of the test specimen.

The fractured sample was also cross-sectioned transverse to the fracture, mounted, ground and polished the same way as described in section 4.1.1 and examined under metallurgical microscope as well as a scanning electron microscope (SEM).

5.Sample casting and processing

5.1 6xxx

Two 6xxx aluminum sheet variants were cast by Novelis' Solatens group facilities in Spokane, WA, USA, using direct chill (or DC) casting method in a 3.5 inch x 9 inch mold. Subsequently, the head and tail of the ingots were sawn off and all ingots were scalped (an oxidized surface removal process) to 73 mm thickness. Ingot homogenization, carried out at Novelis' research center in Kennesaw, GA, USA, involved a 2-step process, with 50ºC/hr ramp up from room temperature to 560ºC in an enclosed furnace, then a soak for 6 hours followed by cooling to 540ºC and a final soak for 2 hours. The ingots were then air cooled to ambient temperature and cut to 6 inches in length and hot rolled at a pre-heat temperature of 500ºC. A rolling pass schedule (RPS) of 13 passes was used to roll the ingots from 73 mm to a hot band gauge of 8 mm (see Table 2).

Table 2. Hot Rolling Pass Schedule (RPS) of AA6111 variants.

Pass	1	2	3	4	5	6	7	8	9	10	11	12	13	14
Thickness (mm)	73	68	62	56	50	44	38.5	33.5	27.5	22.5	17.5	13.5	10.5	8
Reduction (%)		6.9%	8.8%	9.7%	10.7%	12.0%	12.5%	13.0%	17.9%	18.2%	22.2%	22.9%	22.2%	23.8%

The hot-rolled material was then sheared to remove the head and tail and cut to 10 inch sections (due to rolling table length constraint) prior to cold rolling. Cold rolling was carried out with a 12-14 pass RPS. Thickness reduction was fixed at 0.5 mm per pass. The final targeted gauge was 1.8 mm, with all final gauges measured to within ±0.03 mm.

Cold rolled samples were edge trimmed to remove edge cracks and cut to a 6.5 in x 6.5 in blank size for batch solution heat treatment and aging. The solution heat-treat (or SHT) was carried out using a box furnace. The peak metal temperature (PMT) was kept at 535ºC. In order to simulate the industrial continuous annealing and solution heat-treat (or CASH) process, the furnace was set at 700ºC to allow the samples to experience a fast heat up, with less than 2 minutes of heat up time to reach the PMT. The samples were then taken out of the furnace and immediately quenched in room temperature (25ºC) water. The samples were stored in ambient air to naturally age and tested within a 2 week period after water quenching. FLC samples and warm temperature tensile were artificial aged at 225ºC for 30 minutes to T82 temper.

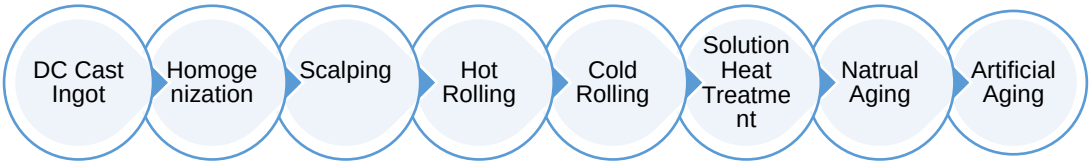

Figure 5-1. 6000 alloys' process flow of the ingot from DC cast to final gauge/temper.

5.2 7xxx

Similar to 6xxx series sheet materials, three variants were cast by Novelis' Solatens group using DC cast method in a 3.5 in x 9 in mold. All cast ingots were immediately put into a stress relieve furnace at 370ºC for 16 hours to prevent ingot cracking, then air cooled to room temperature. The head and butt of the ingots were sawn off to reduce the ingot length to 21 in. The rolling face of the ingots were scalped and left with 65 mm thickness. A 2-step homogenization process consisted of 50ºC/hr heating rate from room

temperature to 460ºC and soak time of 3 hours followed by a second ramp to 485ºC and soak for 6 hours. Ingots were then air cooled in ambient temperature and cut to 6 in length and hot rolled at a pre-heat temperature of 420ºC. A 13-pass RPS was used to roll the ingots from 65 mm to a hot band gauge of 8 mm (see Table 3). The targeted exit temperature was 350ºC or above to promote recrystallization. The head and tail of hot-band ingot were sheared off and some edge trimming was also required to remove the edge cracking. Hot bands were cut to 10 inches plates and cold rolled in a 14-pass RPS. Reduction was fixed at 0.5 mm per pass. The final gauge targeted was 1.5 mm, with all final gauges measured to within ±0.05 mm.

Table 3. Hot Rolling Pass Schedule (RPS) of 7075 and its variants.

Pass	1	2	3	4	5	6	7	8	9	10	11	12	13	14	15	16	17	18
Thickness (mm)	65	63.5	62	60	58	56	54	52	49	46	43	39	35	30	25	20	14	8
Reduction (%)		2.4 %	2.4%	3.3%	3.4%	3.6%	3.7%	3.8%	6.1%	6.5%	7.0%	10.3%	11.4%	16.7%	20.0%	25.0%	42.9%	75.0%

Figure 5-2. Photographs of an ingot sample and the resulting hot band plates from 4 ingots.

Cold rolled samples were edge trimmed to further remove edge cracking and cut into 6.5 in x 6.5 in rectangular samples and were solution heat treated in a box furnace. 7xxx samples were heated to 480ºC and soaked for 5 minutes followed by quenching in 55ºC warm water and artificially aged in a separate furnace at 125ºC for 24 hours to bring them to T6 temper.

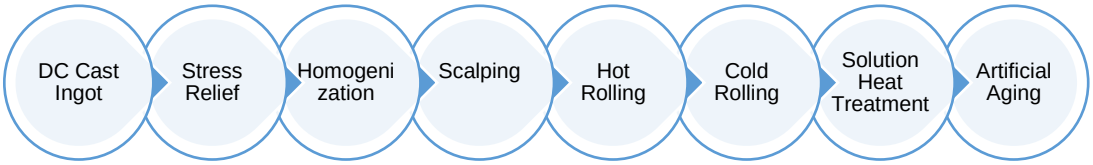

Figure 5-3. Process flow of 7075 alloys from ingot to final gauge/temper.

All 7075 variants, baseline 7075, MRC 7075 and HRC 7075 were lab cast, homogenized and rolled at the same time.

6. Results and Discussion

6.1 6xxx Series Alloys

The chemical compositions of the two AA6111 alloys are listed below in Table 4. In order to create compositions similar to the high recycle content (HRC) material, impurities such as Fe, Mn and Cr were all increased above the baseline levels to simulate mixed scrap stream going into the re-melt. It should also be noted that the Mg is lower than the typical AA6111 composition, therefore, the strength was expected to be reduced. However, the purpose of this research was to investigate the effect of the impurities on mechanical properties, and furthermore, to evaluate their warm formability at elevated temperature, Therefore, slightly lower magnesium content in the HRC material was not considered critical.

Table 4. Actual Compositions of Baseline 6111 and HRC 6111.

Alloy	Cu	Fe	Mg	Mn	Si	Ti	Zn	Cr	Al
Baseline 6111	0.51	**0.25**	0.55	**0.19**	0.52	0.009	0.04	**0.04**	Bal
HRC 6111	0.52	**0.37**	0.53	**0.34**	0.56	0.007	0.004	**0.07**	Bal

6.1.1 Microstructures

Before selection of the chemical composition of the HRC 6111 alloy, a phase diagram was generated using thermodynamic calculation software, JMet Pro, a thermodynamic calculation software. to compare the effect of different compositions on potential phase formation.

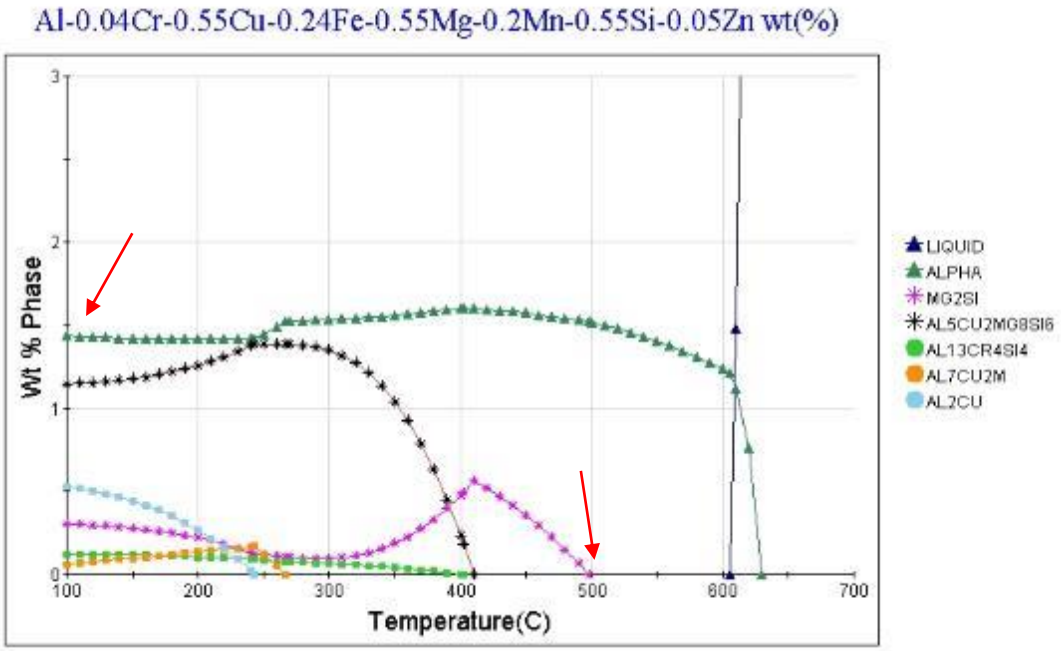

Figure 6-1. Phase predictions of baseline AA6111 alloy from JMet Pro.

As illustrated in Figure 6-1, the weight percentage of α particle was shown to increase significantly from AA6111 to HRC6111 due to the addition of minor amounts of Fe, Mn and Cr. In addition, the solvus temperature for Mg_2Si decreased and solidus temperature of the alloy increased slightly in the case of HRC6111 (see Figure 6-2). It is common knowledge that composition changes affect thermodynamics of the alloy. It is to be noted that phase predictions are based on equilibrium condition which are nearly impossible and impractical to achieve during a DC casting and in a production processing environment. The calculations only provide a general guidance as to what stable phases may exist at different temperatures. There could be additional metastable phases present such as the β particles from casting and homogenization. The diagram is still considered helpful in determining the solutionising temperature and weight fraction of some of the phases. Calculations confirmed that a slight decrease in the Mg_2Si particles solvus

temperature in the case of HRC 6111 was not significant enough to change the solutionising temperature during the SHT practice. The weight percent of α particles, in the case of HRC 6111, increased by almost 1% with the addition of the minor alloying elements identified in Figure 6-1 and Figure 6-2. Therefore, more constituent particles were expected for HRC6111 alloy. The diagram also revealed that constituent particles (α and β) will not be dissolved back into solution unless the temperature had reached above the solidus temperature. Based on the above predictions, the material was produced and processed. The microstructure of the two different chemistries were examined and compared in the as-cast, homogenized, T4 and T82 conditions. Since the constituent particles could not be dissolved in any of these steps, the thermal and thermo-mechanical processes were expected to trigger some phase transformation between the α and β particles.

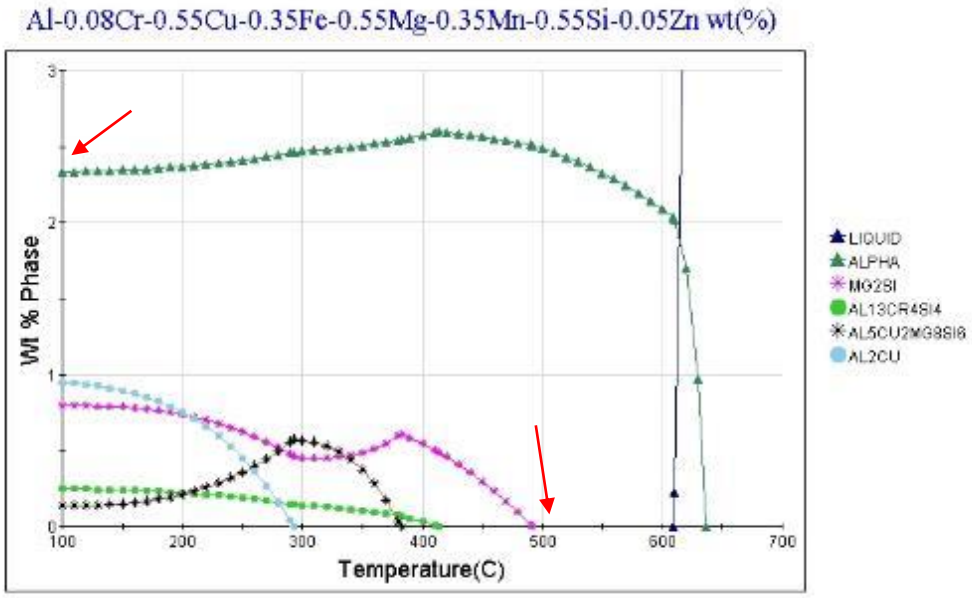

Figure 6-2. Phase predictions of HRC 6111 alloy from JMet Pro.

6.1.1.1 As-cast Microstructures

The quarter thickness location of both benchmark and HRC 6111 alloys was cross-sectioned, mounted, ground, polished and etched for comparison. Compared to the as-cast microstructure of benchmark AA6111 (Figure 6-3), the as-cast microstructure of HRC 6111 had much finer grains (Figure 6-4).

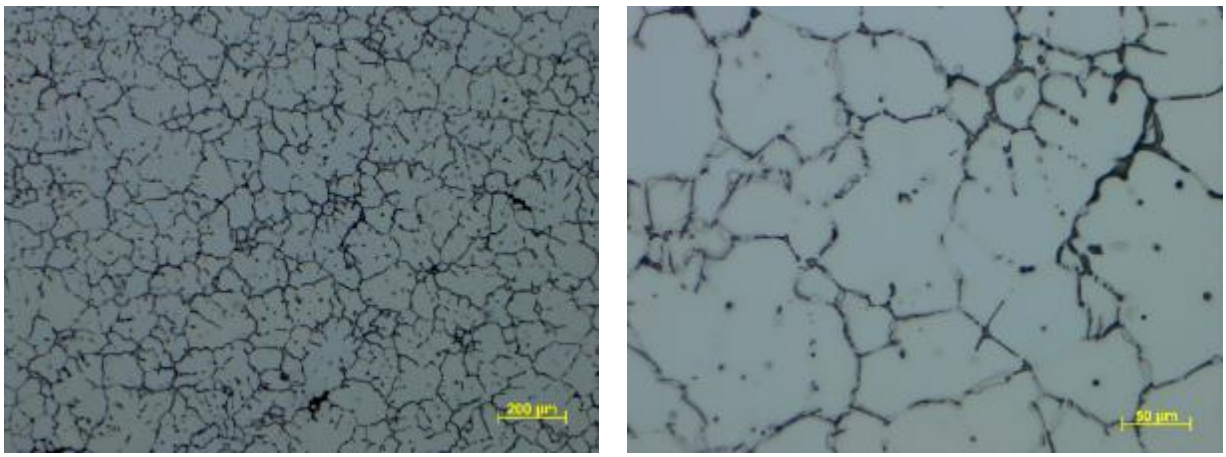

Figure 6-3. As cast microstructure of AA6111 from quarter location.

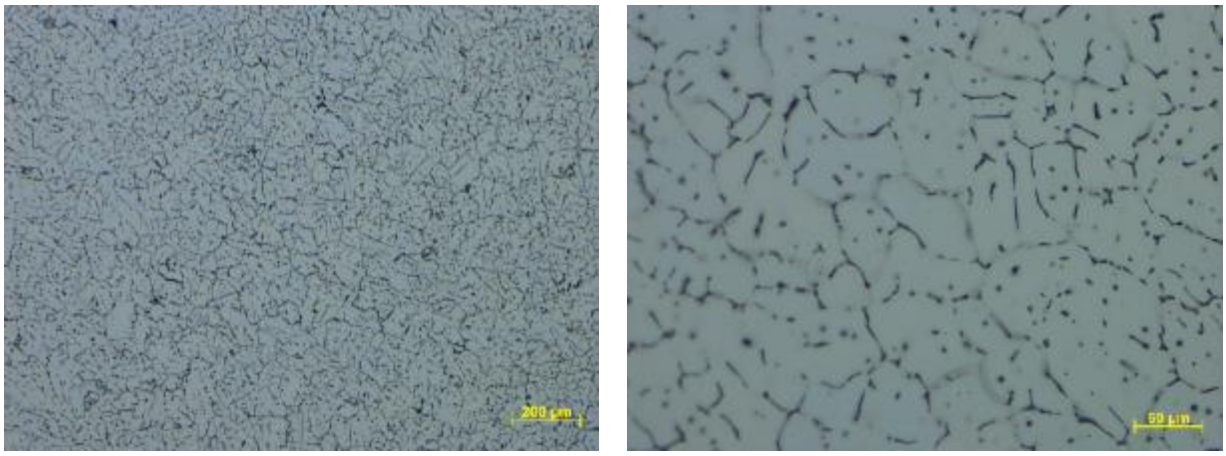

Figure 6-4. As cast microstructure of HRC6111 from quarter location.

The primary phase particles which would solidify first in liquid would act as a nucleation site during the solidification process. This reduced grain size in as-cast structure with

increasing transition metal content in AA6111. This is in agreement with finding of Jin Haiou et al. (Haiou, et al., 2005). Figure 6-5 and Figure 6-6 show SEM images of AA6111 and HRC6111 in as-cast condition, in the back scattered mode. Both alloys had similar matrix characteristics. Al-Fe-Mn-Si type constituent particles appear as light grey at the grain boundaries and Mg-Si-Cu precipitates as dark black. More constituent particles were observed in HRC 6111 alloy.

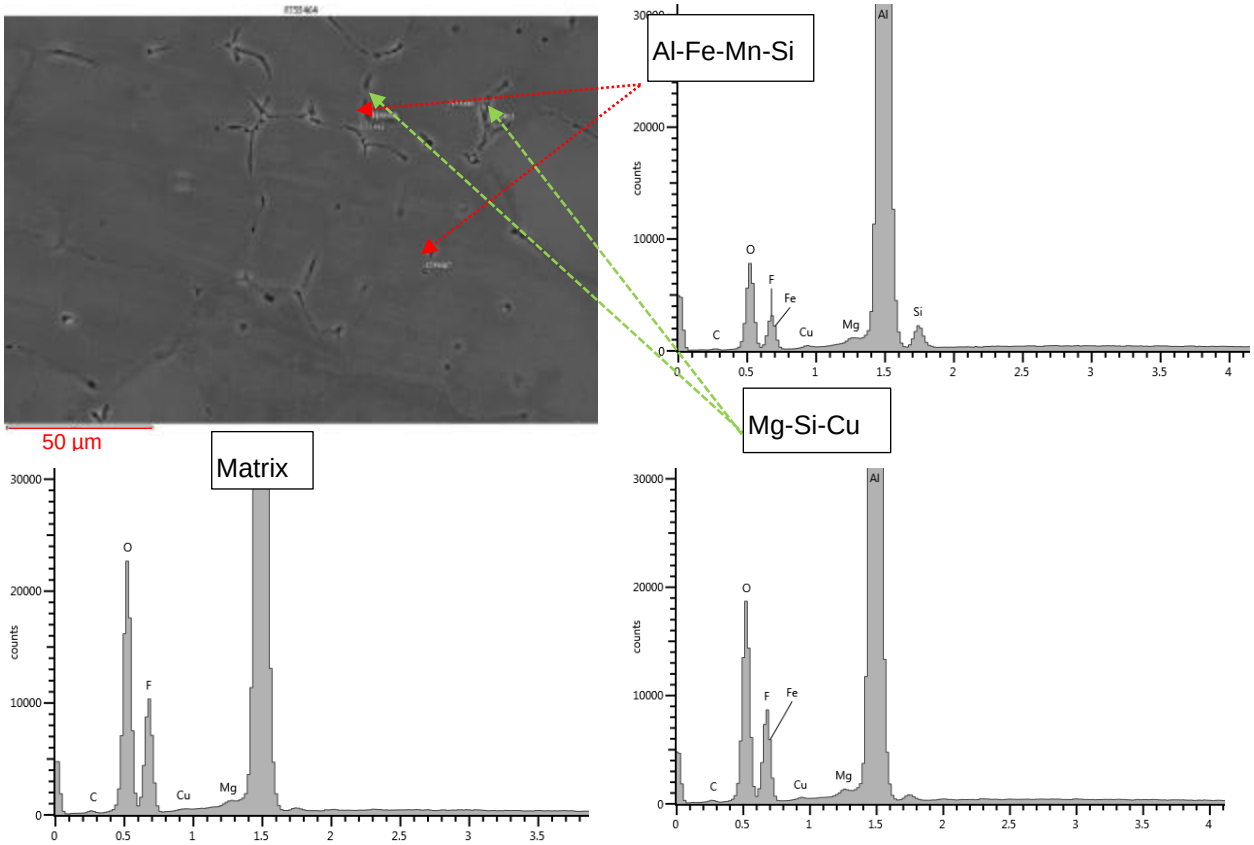

Figure 6-5. SEM (BSE) image of AA6111 alloy in the as-cast condition and various EDX plots showing matrix and two different constituent particles.

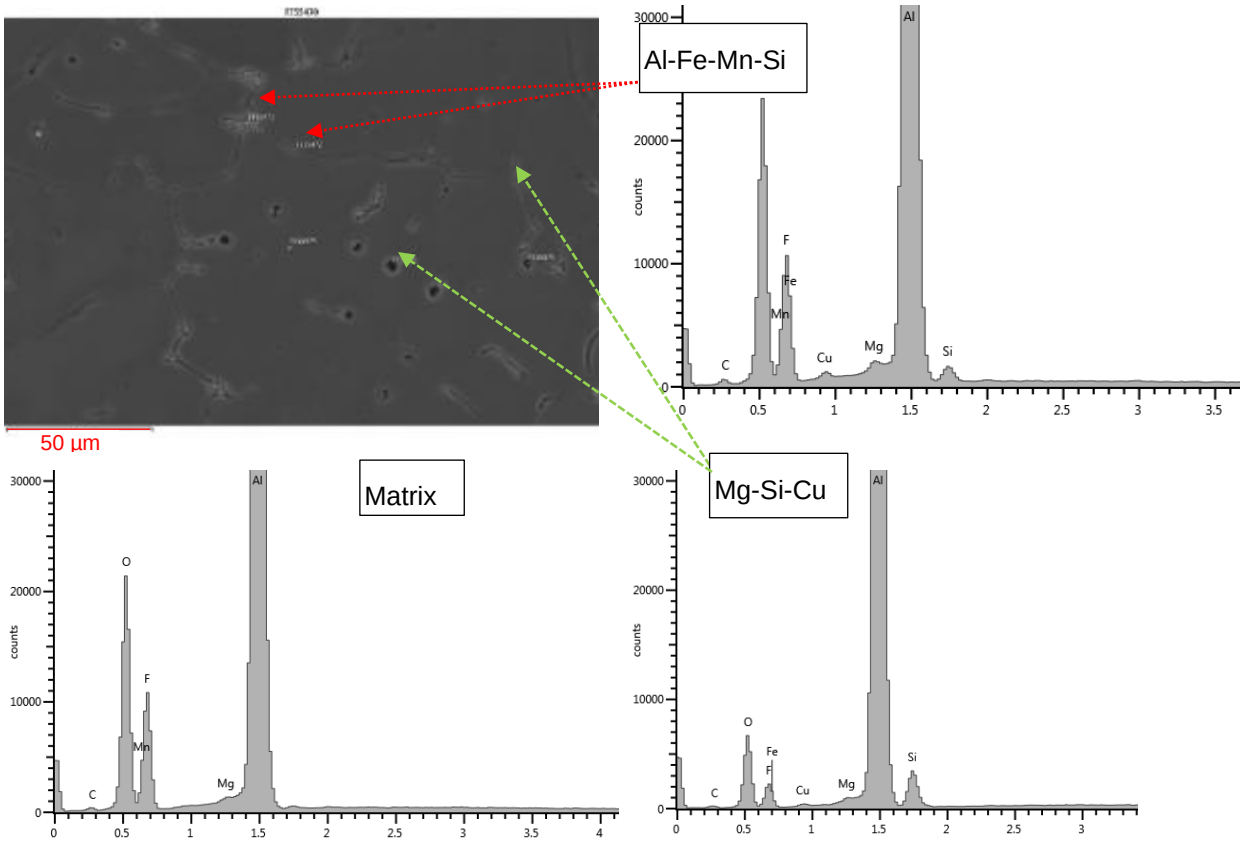

Figure 6-6. SEM (BSE) image of HRC 6111 in as cast condition and various EDX plots showing different constituent particles.

6.1.1.2 Homogenization and Homogenized Microstructures

Ingot homogenization process, a common practice in industry, is utilized to mitigate macro-segregation through solid state diffusion and dissolve the primary phases that could cause eutectic melting. The process also reduces the micro-segregation. Particles containing Fe, Mn, Cr and Si were transformed during the homogenization process. As indicated by the phase prediction from JMet Pro, the solvus temperature of Mg_2Si was about 500ºC, and thus, after the homogenization at 560ºC, the Mg_2Si phase was dissolved back into the solid solution. Figure 6-7 below shows the Differential Scanning Calorimetry (or DSC) traces of both alloys after homogenization where no evidence of eutectic melting such as a sharp peak in the trace is present.

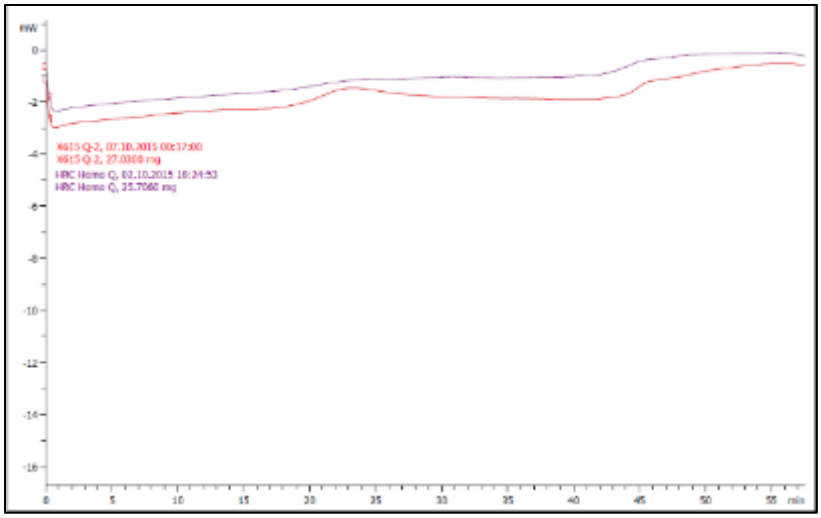

Figure 6-7. Differential Scanning Calorimetric (DSC) traces of both 6xxx alloys after homogenization showing no sign of eutectic melting.

Figure 6-8 and Figure 6-9 illustrate the microstructures of AA6111 and HRC 6111 respectively, after homogenization. As expected, when compared to the earlier as-cast microstructures, the micro-segregation was reduced and much cleaner grains were observed with some of the constituents dissolved back into solution. However, the homogenization practice was unable to dissolve some constituent particles (constituents appear black in optical micrographs). HRC 6111 alloy still exhibited finer grains compared to AA6111.

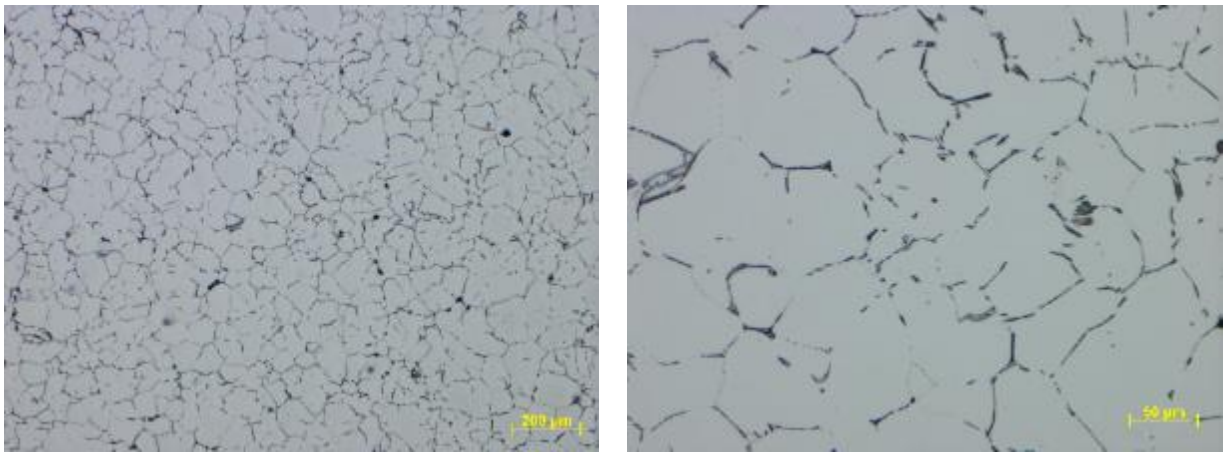

Figure 6-8. Microstructure of AA6111 after homogenization.

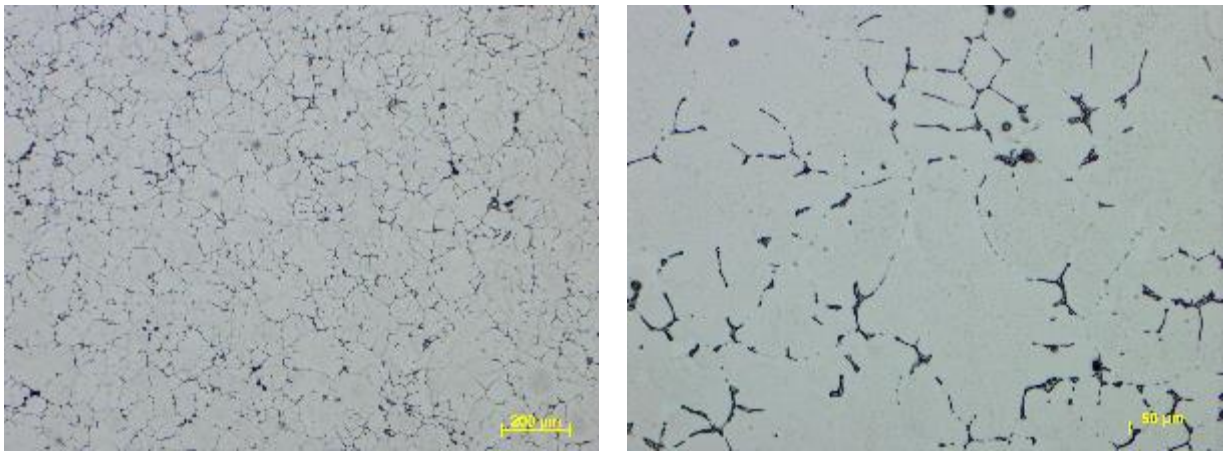

Figure 6-9. Microstructure of HRC 6111 after homogenization.

Figure 6-10 and Figure 6-11 show the SEM images of AA6111 and HRC6111 after homogenization. HRC 6111 again showed more Al-Fe-Mn-Si containing particles compared to AA6111 baseline. These particles had plate-like or spherical shapes and appeared light grey under the back-scattered electron (BSE) imaging mode. Both variants showed Mg-Si-Cu containing constituents represented by larger black particles in the BSE image.

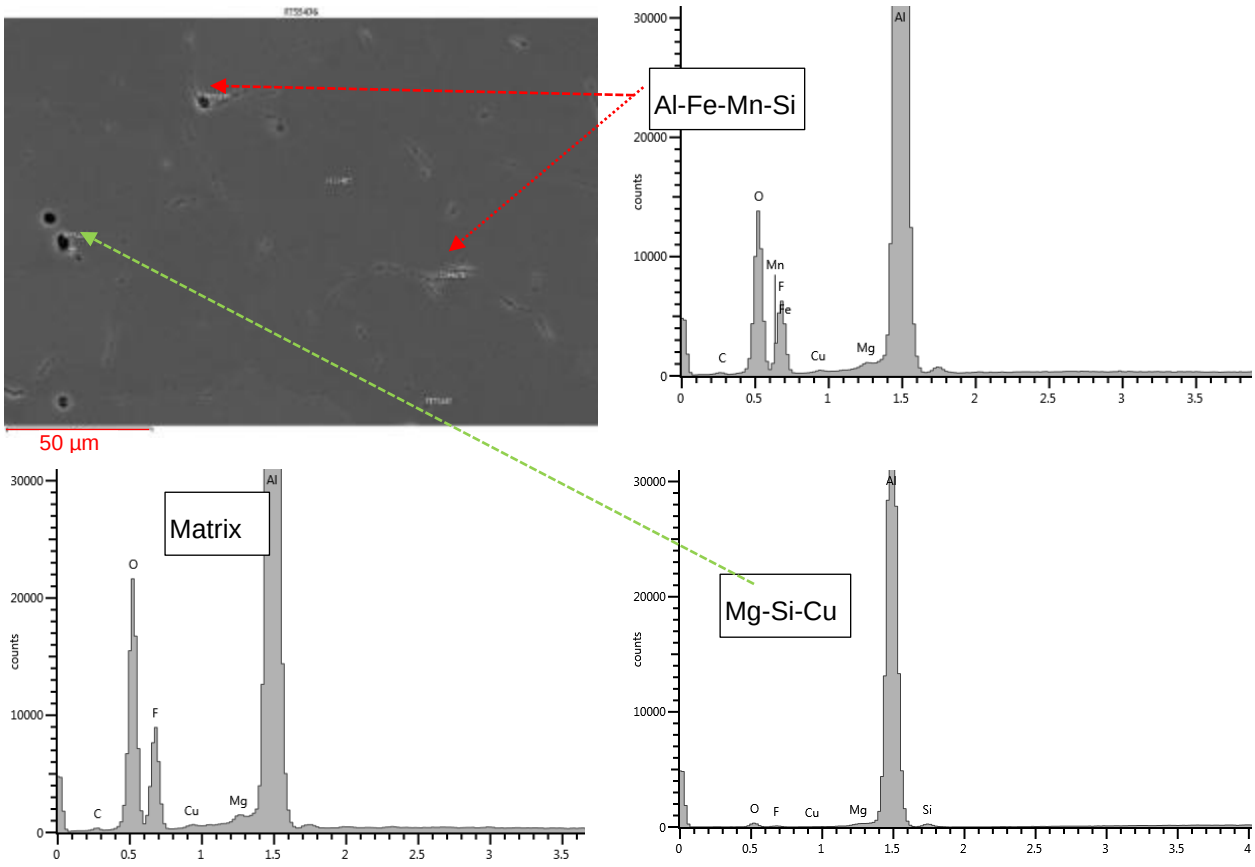

Figure 6-10. SEM (BSE) image of AA6111 in homogenized condition with EDX plots of different constituent particles.

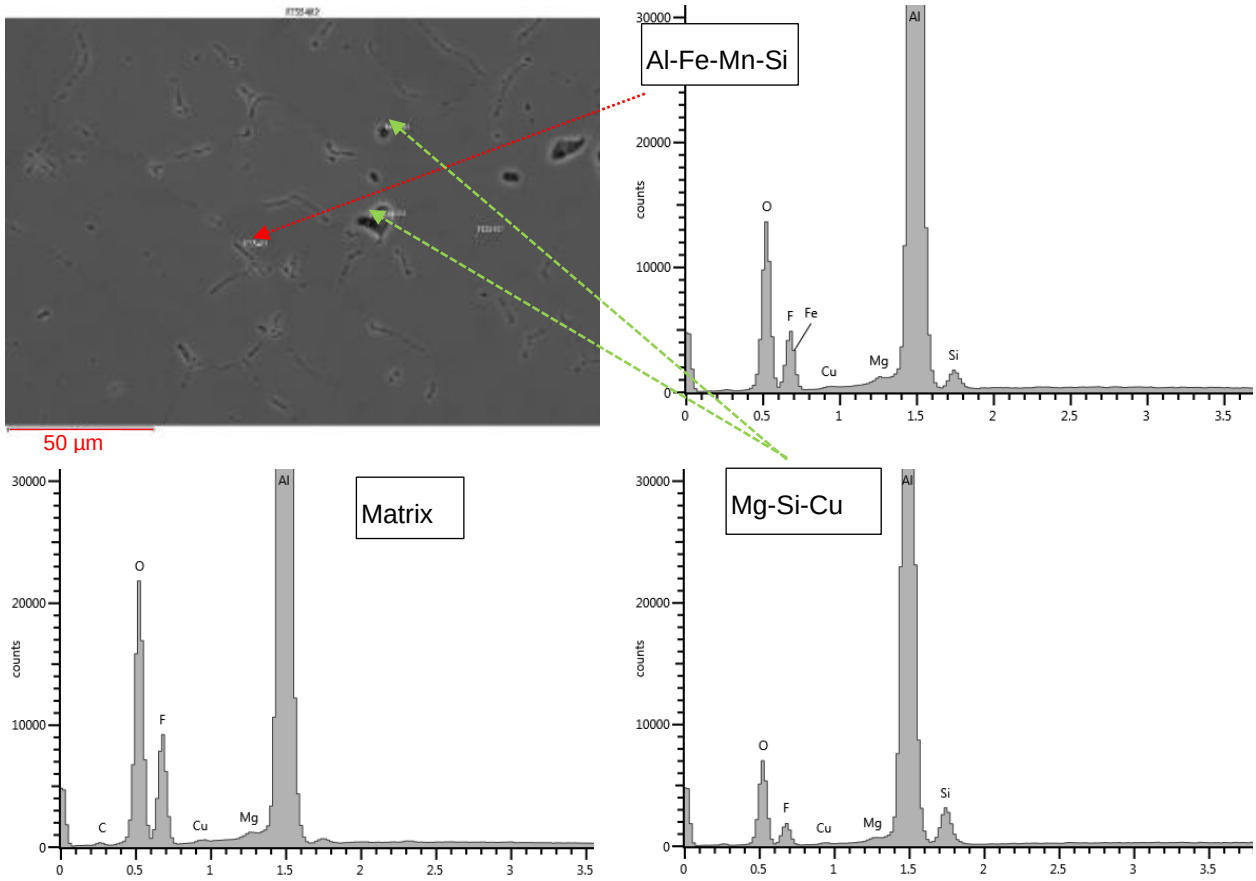

Figure 6-11. SEM (BSE) image of HRC6111 in homogenized condition with EDX plots of different constituent particles.

6.1.1.3 T4 Microstructures

Figure 6-12 to Figure 6-12 show optical micrographs of AA6111 and HRC 6111 at final gauge in T4 condition in the long transverse (or LT) direction. AA6111 appears to be cleaner compared to HRC 6111 with less constituent particles. This is consistent with Jmet Pro calculation, HRC version would have as much as 1% higher constituents than the baseline due to its higher alloying content.

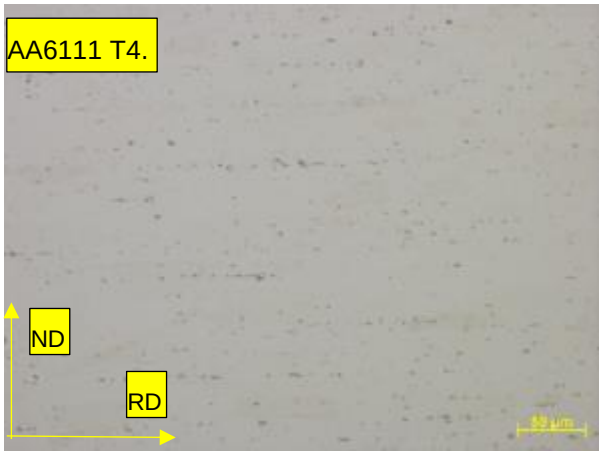

Figure 6-12. AA6111-T4 (200x).

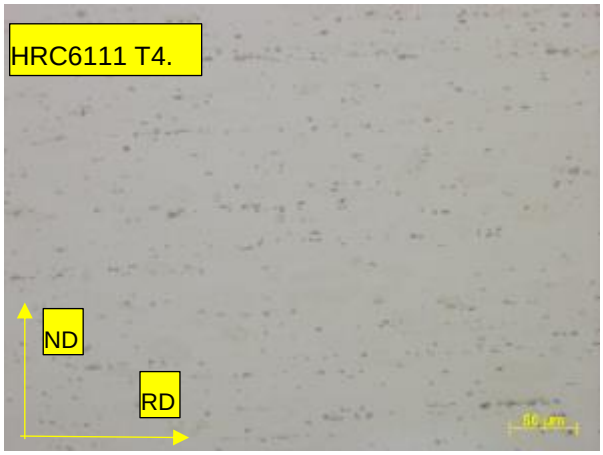

Figure 6-13. HRC AA6111-T4 (200x).

The constituent particles were identified as Al-Fe-Mn-Si particles using SEM and EDX as shown in Figure 6-14 and 6-15. Coarse Al-Fe-Mn-Si constituent particles were observed as lighter particles under back scattered mode. Also, since the alloy was rolled, the distribution of constituent particles was different from that of the as-cast/homogenized samples. Instead of distributing around the grain boundaries, the constituent particles were broken down and distributed along the rolling direction of the sample.

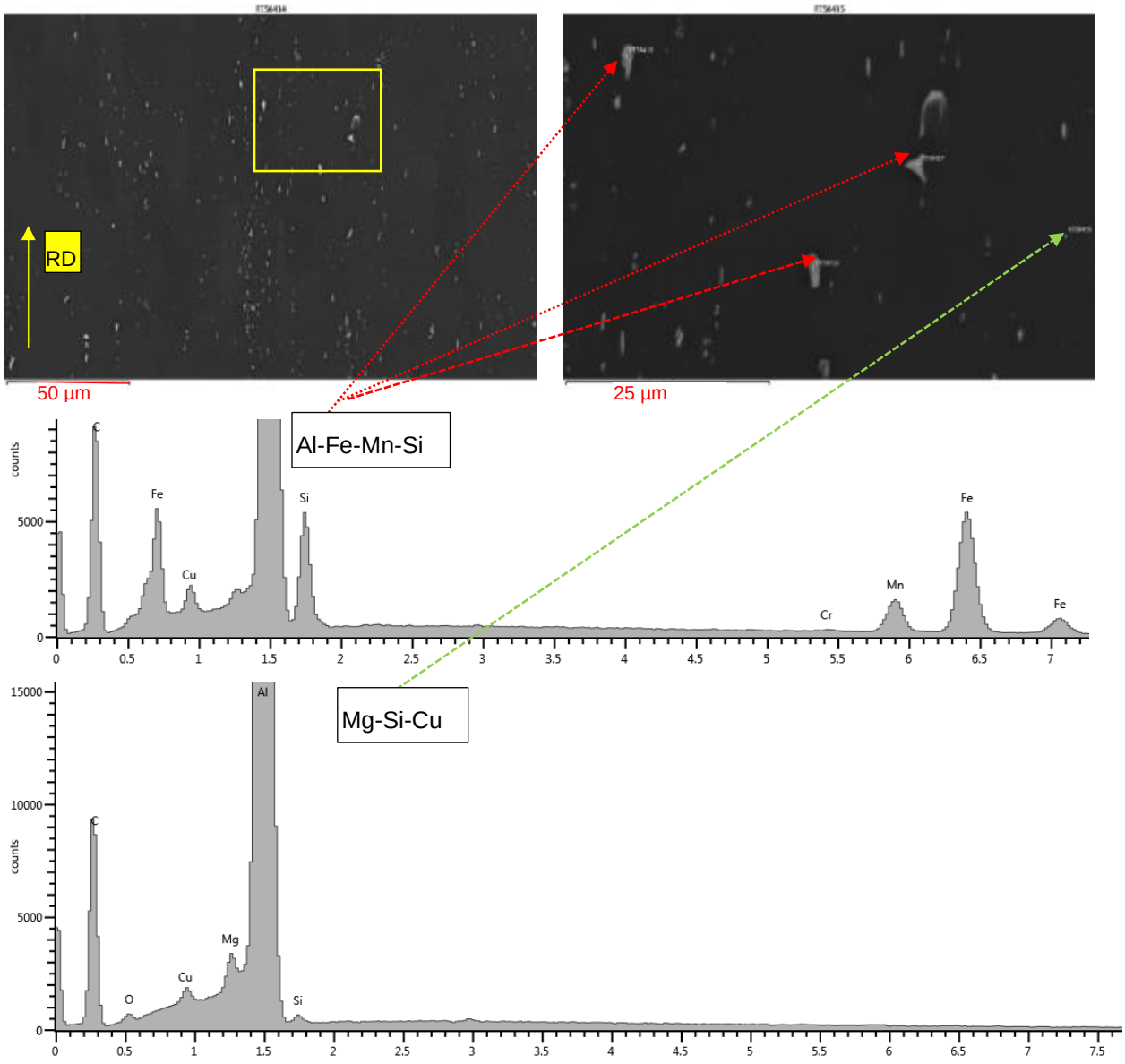

Figure 6-14. BSE image of AA6111-T4 sample with EDX plots of constituent particles.

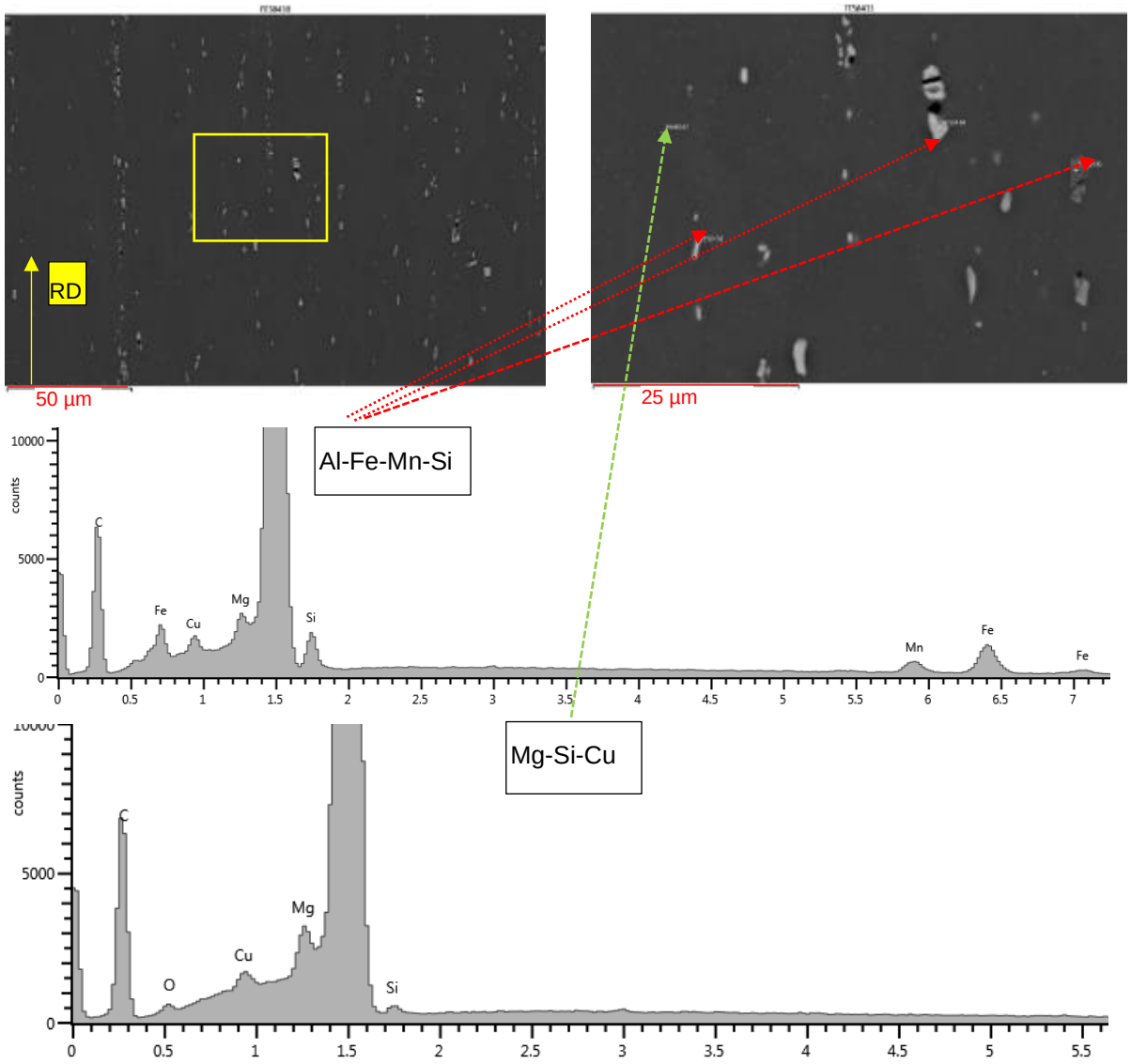

Figure 6-15. BSE image of HRC6111 T4 sample with EDX plots of particles.

6.1.1.4 T82 Microstructures

Figure 6-16 and Figure 6-17 show the microstructures of AA6111 and HRC6111 in T82 condition respectively viewed under polarized light. HRC 6111 has a smaller grain size compared to AA6111.

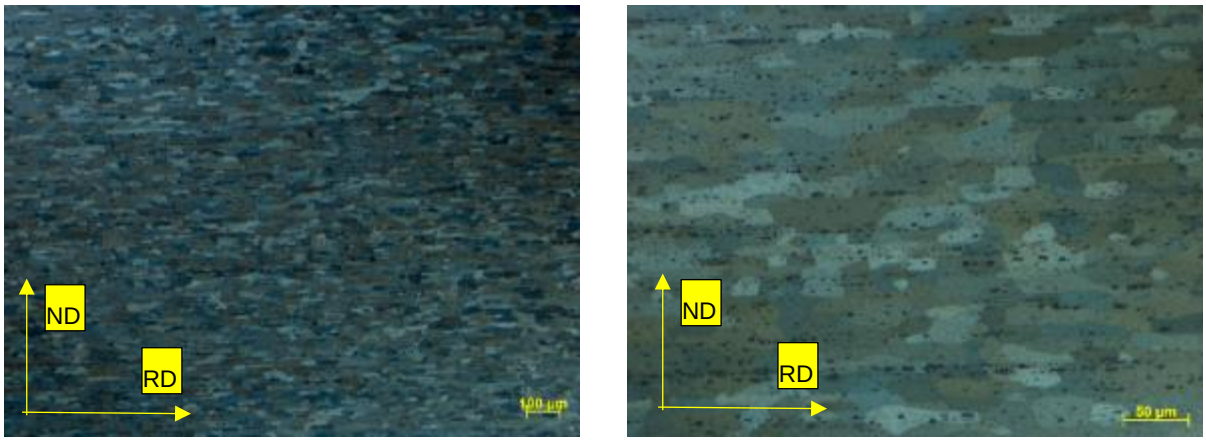

Figure 6-16. Microstructure of baseline AA6111 in T82 condition.

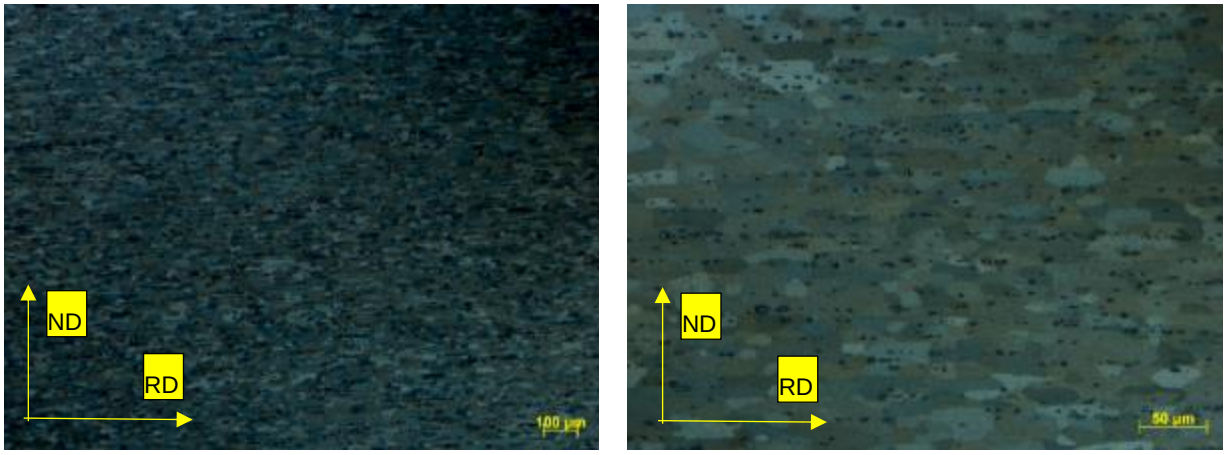

Figure 6-17. Microstructure of HRC AA6111 in T82 condition.

This was confirmed by the grain size measurement as shown in Figure 6-18. The grain size as well as the grain morphology between the two variants are different. HRC 6111

exhibits a finer and more equi-axed grains compared to slightly larger and more elongated grains of baseline AA6111 sheet.

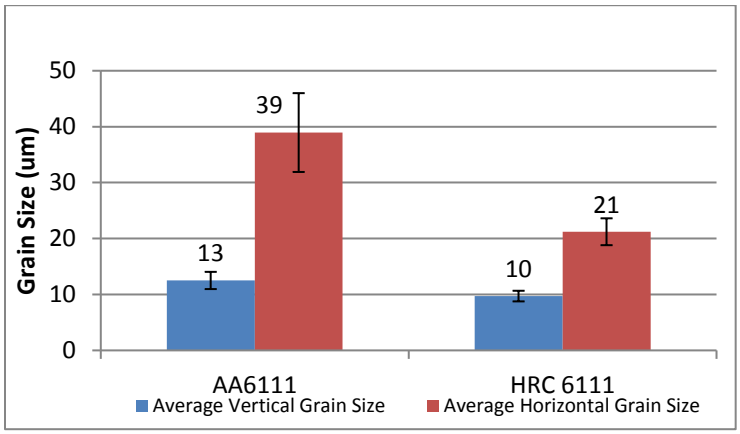

Figure 6-18. Grain size comparison between AA6111 and HRC 6111-T82 sheets.

Figure 6-19 and Figure 6-20 show the SEM images of AA6111 and HRC 6111 sheets respectively in T82 condition at final gauge, from the LT plane. The Al-Fe-Mn-Si constituent particles along the rolling direction were analyzed using EDX. Since the phase of the particle could change during the homogenization process and subsequent heat treatment, the identification of the particles was not carried out until the final temper, by using Feature Detection and Count (or FDC) to distinguish between α and β particles. This will be discussed later in Section 6.1.3.

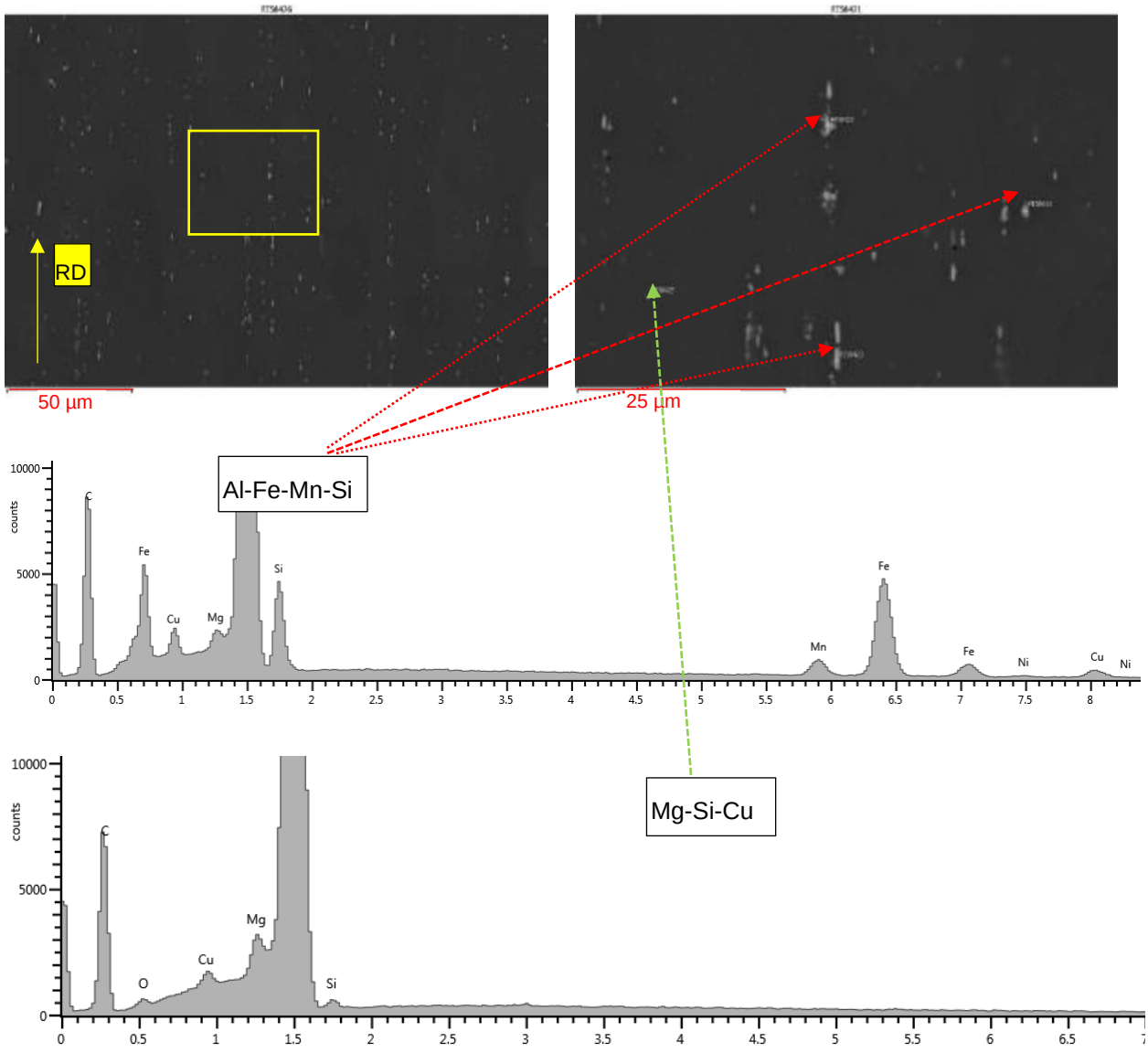

Figure 6-19. SEM (BSE) of AA6111-T82 sheet and EDX plots of the constituent particles.

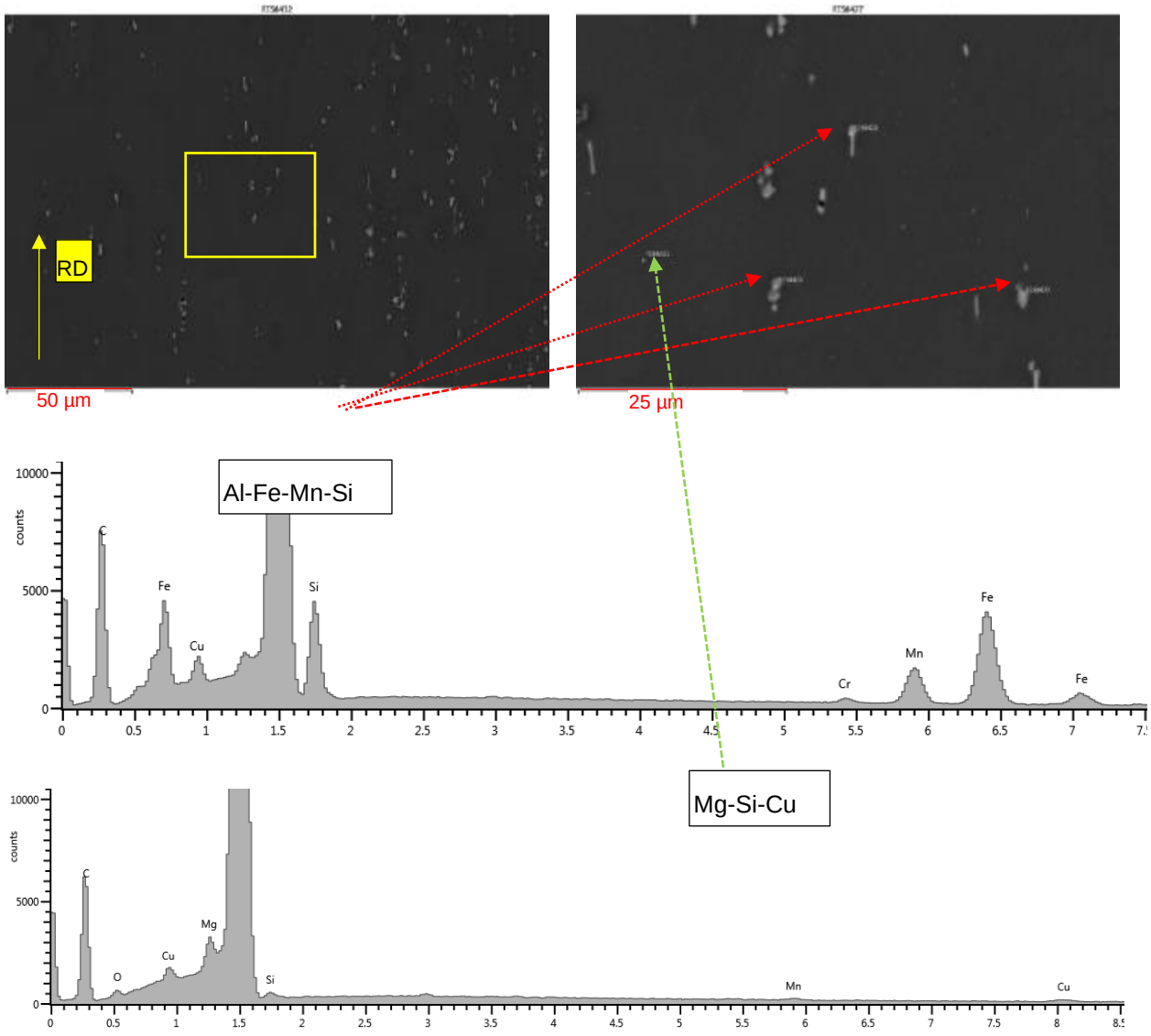

Figure 6-20. SEM (BSE) of HRC 6111-T82 sheet and EDX plots of particles.

6.1.2 Mechanical Properties

Mechanical properties are influenced by the chemical composition, subsequent processing during rolling and the aging process. Both materials were tested and compared in T4 and T82 temper conditions at room temperature. Only T82 properties were tested and compared at elevated temperature (300ºC) to investigate the warm forming behavior.

6.1.2.1 Room Temperature Tensile Properties

Figure 6-21 shows the typical stress-strain curve of HRC6111 and AA6111 in T4 and T82 conditions. Table 5 summarizes the uniaxial tensile properties of both variants of AA6111 alloy in T4 and T82 temper conditions.

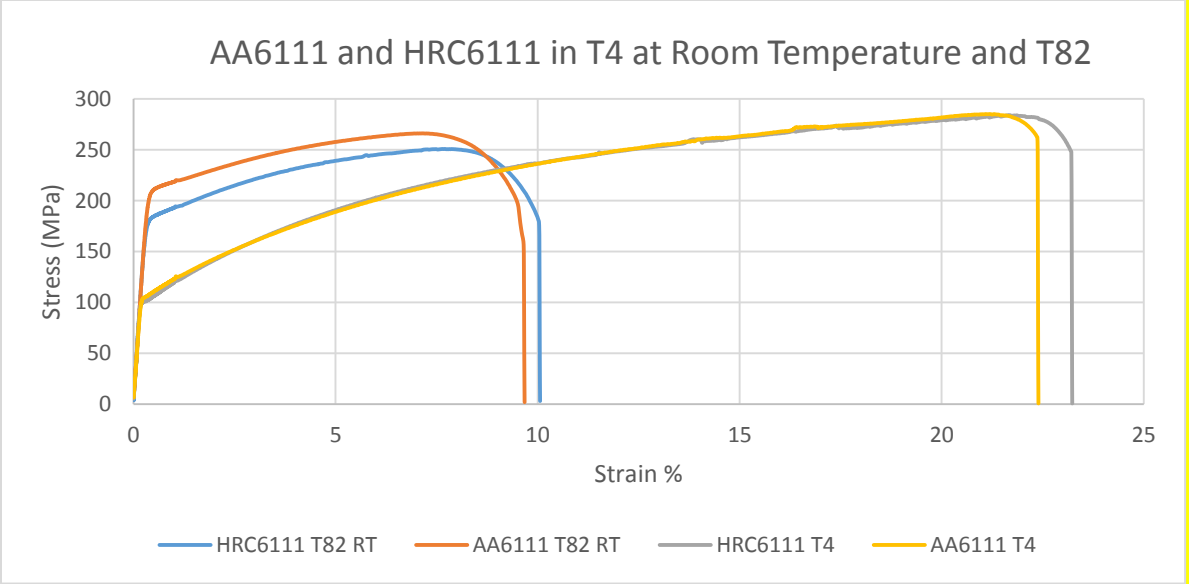

Figure 6-21 Stress Strain Curve of AA6111 and HRC6111 in T4 and T82.

Table 5. Room temperature mechanical properties of both variants of 6111 sheet in T4 and T82 conditions.

	Yield Strength (stdev) MPa	Maximum Tensile Stress (stdev) MPa	Uniform Elongation %	Strain at Break (%)	n-Value	r-Value
AA6111 T4	107 (0.7)	232 (1.9)	20.0	25.7	0.26	0.556
HRC 6111 T4	101 (2.3)	227 (3.6)	19.3	24.7	0.25	0.555
AA6111 T82	211 (10.8)	248 (9.2)	7.1	10.33		
HRC6111 T82	180 (7.1)	231 (5.6)	7.6	10.8		

As noted above, there was not a significant drop in the T4 strength and elongation for the HRC variants compared to the baseline 6111 sheet. The T82 strength of both alloys increased significantly while the elongation decreased, as expected. Since 6xxx alloy is a precipitation-hardenable alloy, the Mg_2Si to precipitated out during artificial aging and enhanced its strength. HRC variant of 6111, with the addition of Fe, Mn and Cr, had a higher number of constituent particles and many of them incorporated Si in their composition, as shown earlier in SEM and EDX analyses. Since both alloys were designed with similar Si level, when Si was combined with these constituent particles, it caused the Si to deplete and limit the amount of Si that was available to combine with Mg to form the strengthening precipitate later. Thus, the HRC 6111 sheet resulted in a much lower strength in T82 condition. This is reflected in the T4 properties where precipitation strengthening has not yet taken place. Despite the increase in constituent particles, the elongation of the HRC version was not severely affected and remained similar to the baseline 6111 sheet.

6.1.2.2 Wrap Bend Test of AA6111 Variant

Both variants of 6111 sheet in T4 temper were tested for bendability using the wrap bend test in the longitudinal direction. It is to be noted that T4 is the temper in which 6xxx sheets are typically formed in automotive stamping. Both variants resulted in very similar r/t values of slightly below 0.4. (see Table 6). This value is typically considered sufficient for many automotive bending applications. In fact, the experiment went further with smaller radius in order to distinguish the difference between the two alloys in the microscopic observations.

Table 6. Bendability in terms of r/t values from Wrap bend test. The symbols “r” and “t” refer to the bend mandrel radius and sheet thickness respectively.

Alloy	Rating	r/t value	Pass
AA6111	1	*r*	0.028
		t	0.07150
		r/t	0.392
HRC 6111	1	*r*	0.028
		t	0.07125
		r/t	0.393

Figure 6-22 presents optical micrographs from tensile region of through-thickness cross-section of a bent test sample of AA6111-T4 sheet bent to a radius of 0.020 in. Some surface undulation and early stage of void formation can be observed. The void typically formed around spherical α constituent particles. Similar results were observed for HRC 6111-T4 bent sample tested with r=0.024 in mandrel (see Figure 6-23).

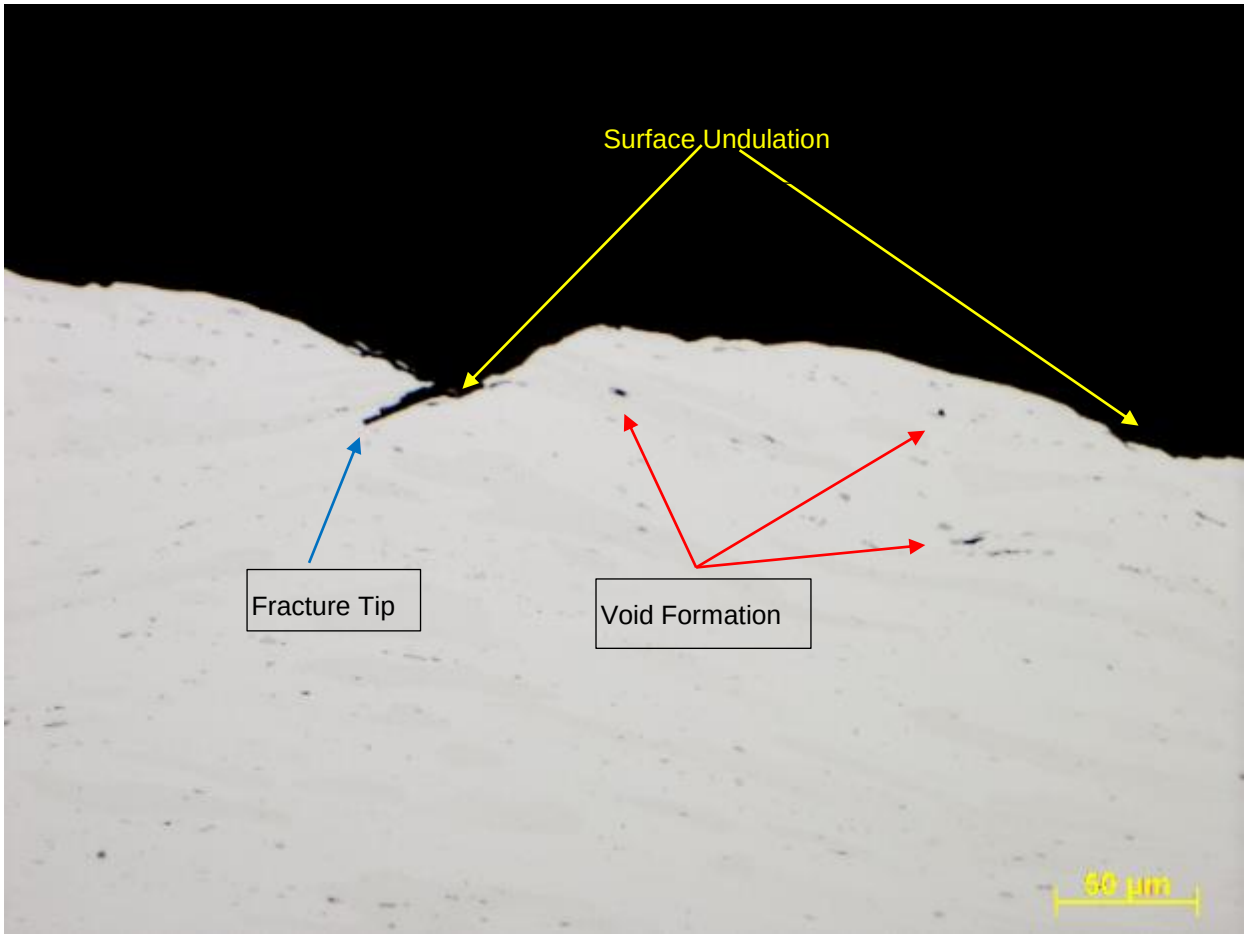

Figure 6-22. Optical micrograph of AA6111-T4 bent sample tested with r=0.02 in mandrel.

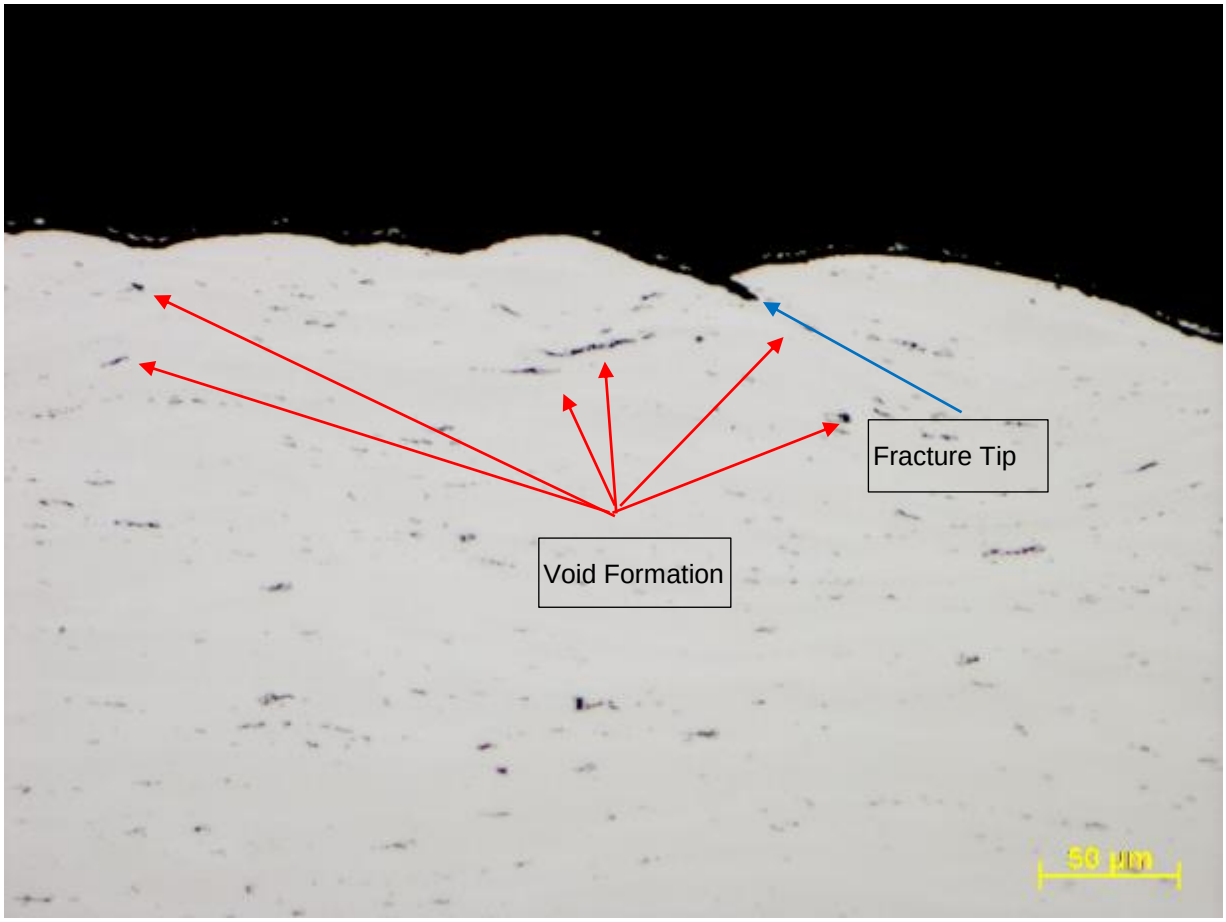

Figure 6-23. Optical micrograph of HRC 6111-T4 bent sample tested with r=0.024 in mandrel.

Figure 6-24 shows a micrograph of the same cross section in HRC 6111-T4 bend sample with r=0.24 in. Clearly, this material shows more constituent particles than the baseline 6111 and exhibits more extensive void formation around the constituents.

AA6111,r=0.024

HRC6111,r=0.024

AA6111,r=0.020

HRC6111,r=0.020

AA6111,r=0.016

HRC6111,r=0.016

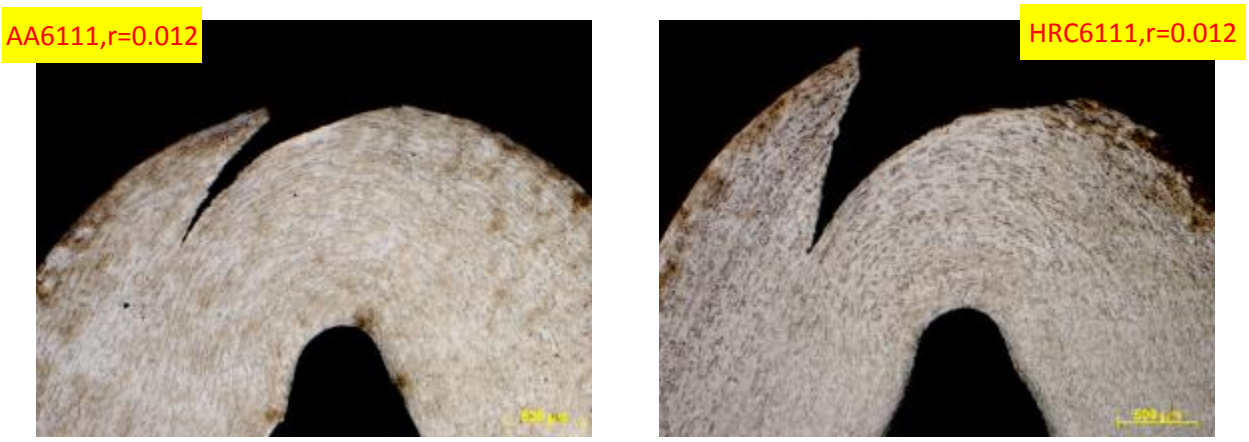

Figure 6-24. A comparison of microstructures of bend specimens of AA6111-T4 and HRC 6111-T4 from tests conducted with different bending mandrel radii.

In general, increased number of constituent particles were seen to increase the propensity towards void nucleation. Thus, increased Fe, Mn and Cr in HRC6111 sheet led to a decrease in its bendability. This was in agreement with data in the literature where increased Fe content was shown to increase void damage and macroscopic shear band formation in the earlier stages of the deformation and cause reduced bending performance in 6xxx alloys (Lievers, 2003). It is shown that HRC 6111-T4 developed fracture earlier than AA6111-T4 sheet at r=0.016 in, while AA6111-T4 sheet initiated fracture at a smaller radius of 0.012 in.

6.1.2.3 Elevated Temperature Tensile Test Results

Both variants of 6111 sheet were artificially aged to T82 temper and tested at 300ºC to simulate the warm forming process. Figure 6-25 shows the stress-strain curve of AA6111 and HRC6111 in T82 at room temperature and 300ºC respectively. Table 7 shows the average tensile properties of the two sheet materials.

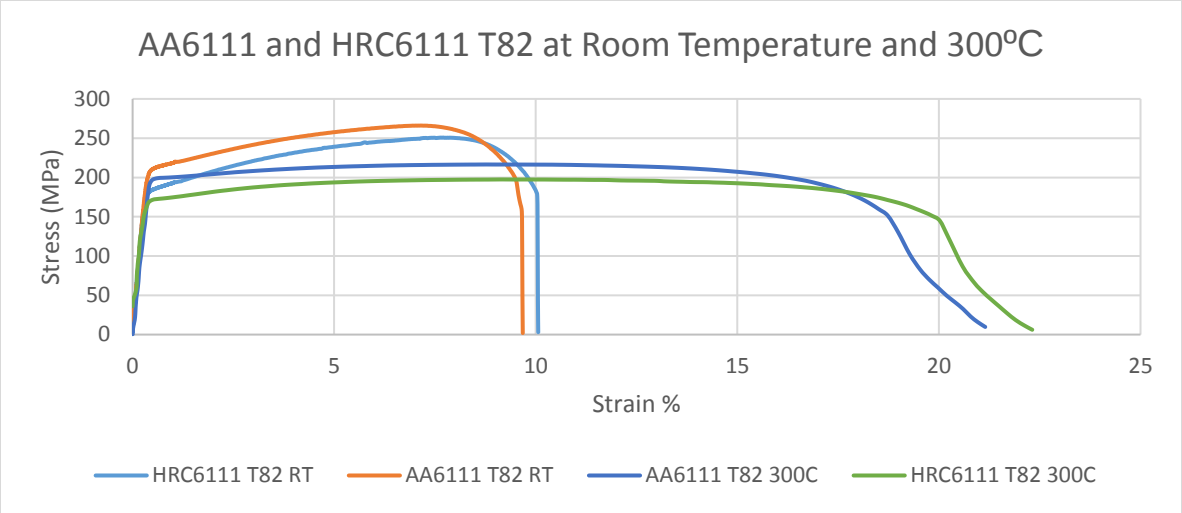

Figure 6-25. Stress-strain curves of AA6111-T82 and HRC 6111-T82 sheets at RT and 300ºC.

Similar to a published study (Li, 2003), both 6111 variants showed a marginal decrease in yield strength at 300ºC compared to room temperature while the elongation increased substantially. Also, for both variants, the elongation at this temperature was comparable to the elongation of AA6111 T4 temper at room temperature. These alloys exhibited significant higher elongations at 300ºC compared to the 10% elongation in T82 at room temperature.

Table 7. Uniaxial tensile properties of AA6111-T82 and HRC 6111-T82 at 300ºC.

Sample	Temperature	Yield Strength (stdev) MPa	Tensile Strength (stdev) MPa	Total Elongation (%)
AA6111	300^0C	194 (5.4)	199 (4.9)	22.4
HRC 6111	300^0C	175 (4.9)	186.9 (3.6)	19.3
AA6111	RT	211 (10.8)	248 (9.2)	7.1
HRC 6111	RT	180 (7.1)	231 (5.6)	7.6

6.1.3 Microstructural Characterization Using SEM Feature Detection and Count

During casting of 6xxx Al alloys, several Fe-Mn containing intermetallic phases such as Al-Fe, Al-Fe-Si and Al-Fe-Mn-Si phases were present in between the dendrites due to their low solubility in liquid phase. These intermetallic phases form during solidification as constituent particles, as discussed earlier. The α particles, as part of Al(FeMn)Si family of particles, are globular in shape and β particles in the AlFeSi family are more acicular or plate-like in geometry with a thickness of a few of a tenth of micrometer (see Figure 6-26).

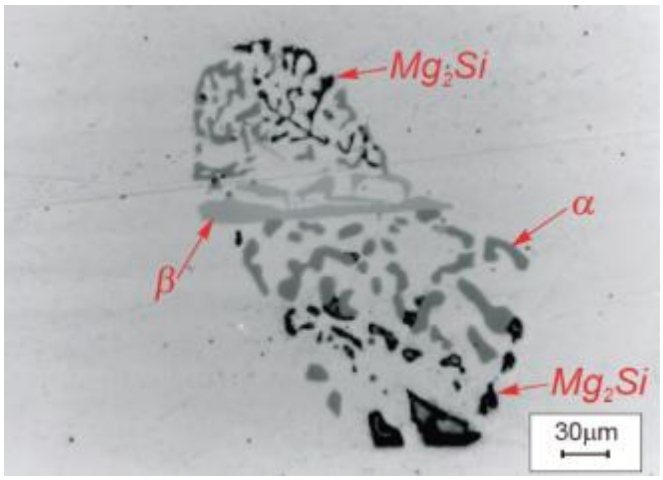

Figure 6-26. An SEM image of AA6111 alloy showing α and β particles and Mg_2Si precipitates. (G. Mrowka-Nowotnik, 2007)

The α particles were predominantly $Al_{16}(Fe,Mn)_4Si_3$, while the β particles were predominantly Al_5FeSi. It is commonly believed that α particles, due to their spherical geometry, have a reduced tendency to break into smaller particles during rolling process, whereas β particles, which have a plate-like or acicular geometry, are relatively easier to break (Mohamad, 2006). So it is more favorable to have β particles in the alloy than α particles. There are many ways that could be used to identify and differentiate the two types of constituents as discussed by Kuijpers et al. (Kuijpers, 2003). The method used

in the present work is called the “Feature Detection and count” (or FDC) method and utilizes the SEM to identify, measure and differentiate constituent particles (mainly α and β particles in 6xxx) based on their chemical composition and geometry.

The β particles are a meta-stable phase that can transform into α particles during homogenization. From the thermodynamic calculation, during the sheet heat-treat (SHT) and aging process, either of these two types of particles can dissolve back into solid solution. Also, the geometry and distribution of these particles can be changed during the rolling process (i.e. during their break down) but remain the same after cold rolling. Therefore, T82 samples were analyzed for FDC and the results are presented in Figures 6-27 and 6-28.

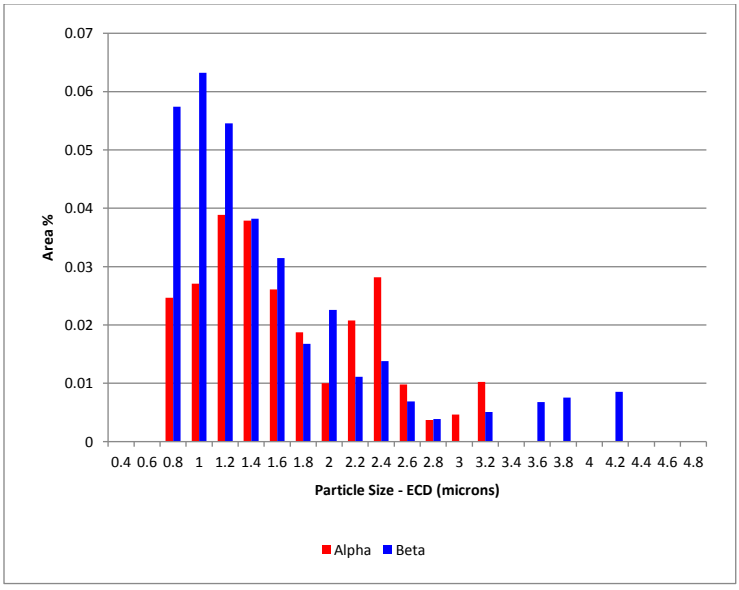

Figure 6-27. FDC plots of area fractions of α and β in AA6111.

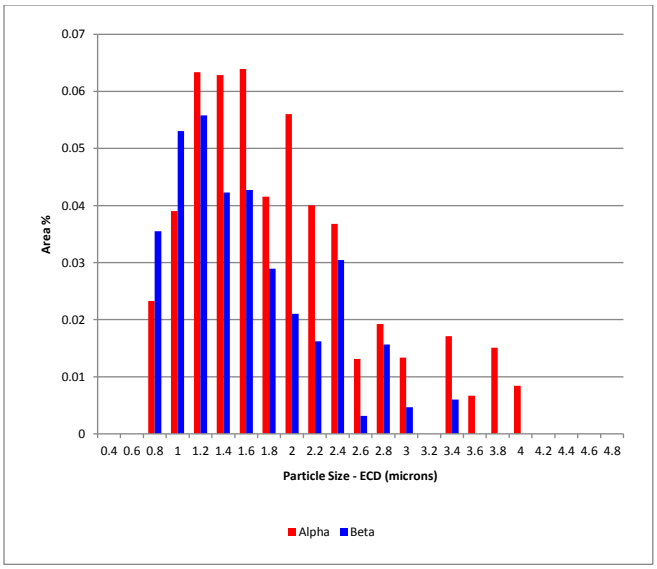

Figure 6-28. FDC plots of area fractions of α and β in HRC 6111.

Table 8 and

Table 9. Particle data for HRC 6111 T82.

Table 9 show the area fractions and number count of each particle in AA6111-T82 and HRC 6111-T82 respectively. In the case of HRC AA6111, the total number of particles were increased by 11% compared to AA6111. This was consistent with previous Jmet Pro calculation that showed that the HRC 6111 could have as much as 1% weight fraction increase compared to AA6111. This was also consistent with SEM/EDX observations of the homogenized and rolled samples.

Alpha		Beta	
Features	506.00	Features	486.00
% Total Feature	51.01	% Total Feature	48.99
Feature Area (sq. µm)	764.10	Feature Area (sq. µm)	522.55
% Total Area	0.52	% Total Area	0.36

Table 8. Particle data for AA6111-T82.

Alpha		Beta	
Features	328.00	Features	565.00
% Total Feature	36.73	% Total Feature	63.27
Feature Area (sq. µm)	383.13	Feature Area (sq. µm)	511.15
% Total Area	0.26	% Total Area	0.35

Table 9. Particle data for HRC 6111 T82.

Alpha		Beta	
Features	506.00	Features	486.00
% Total Feature	51.01	% Total Feature	48.99
Feature Area (sq. µm)	764.10	Feature Area (sq. µm)	522.55
% Total Area	0.52	% Total Area	0.36

6.1.4 Warm Forming Characteristics of AA6111 Sheet Materials

The high temperature forming tests were carried out on two 6111 variants in the T82 temper state using the hot gas bulge tester at McMaster University. The samples were bulged using different elliptical die openings, in the order of increasing ellipticity, as described earlier in section 4.5.2. Samples of both variants were first set inside the furnace for 10 minutes to ensure temperature uniformity across the sample. As the gas pressure increased, the sample would start to bulge and then neck, prior to fracture by bursting. The burst pressure of each alloy was recorded at the end of the test. As the sample geometry became narrower, i.e., strain path changed from balanced bi-axial tension towards plain strain, the burst pressure became larger (see Figure 6-29). The

trends were very similar for the 2 variants, with HRC variant showing a slightly higher burst pressure compared to AA6111 baseline.

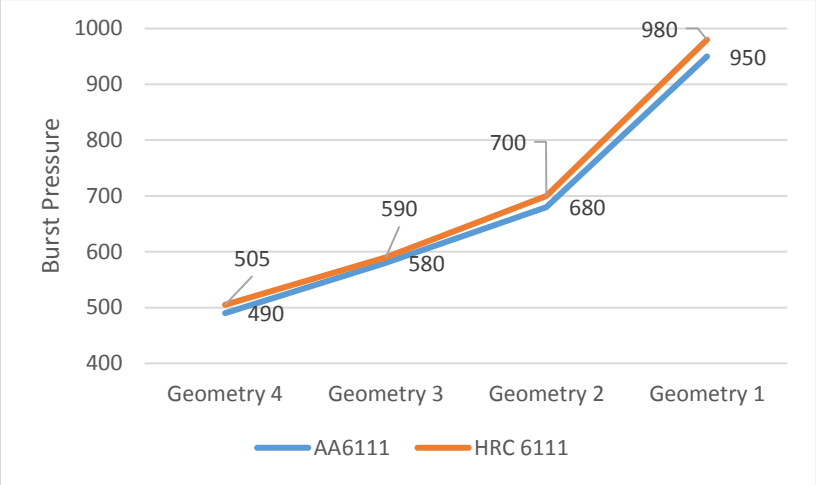

Figure 6-29. A comparison of burst pressures of AA6111-T82 and HRC 6111-T82 sheets.

An example of the formed sample and its respective strain map is provided in Figure 6-30. There are some areas with missing strain information in the strain map. This was due to fading of grids as the samples stayed in the furnace over extended period of time (>15 minutes total) as well as from subsequent stretching of the sample during bulging. The grids located at the apex were too close to the fracture region and became unrecognizable by the software during post-test analysis. However, a small area of missing data did not affect the measurements on the limit strains. Argus strain mapping software was utilized with points adjacent to fracture at the apex to fit the data and predict major and minor strains (see Figure 6-30)

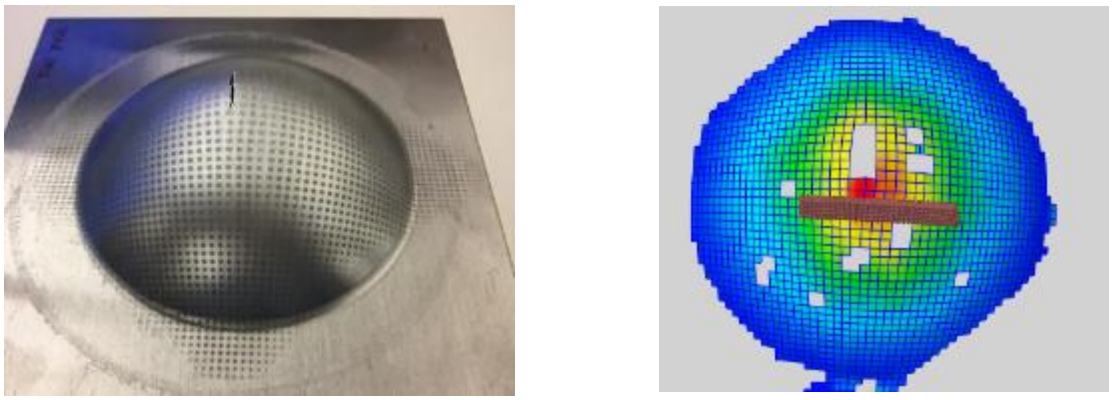

Figure 6-30. A typical AA6111-T82 balanced bi-axial tension bulge sample and strain map at 300ºC.

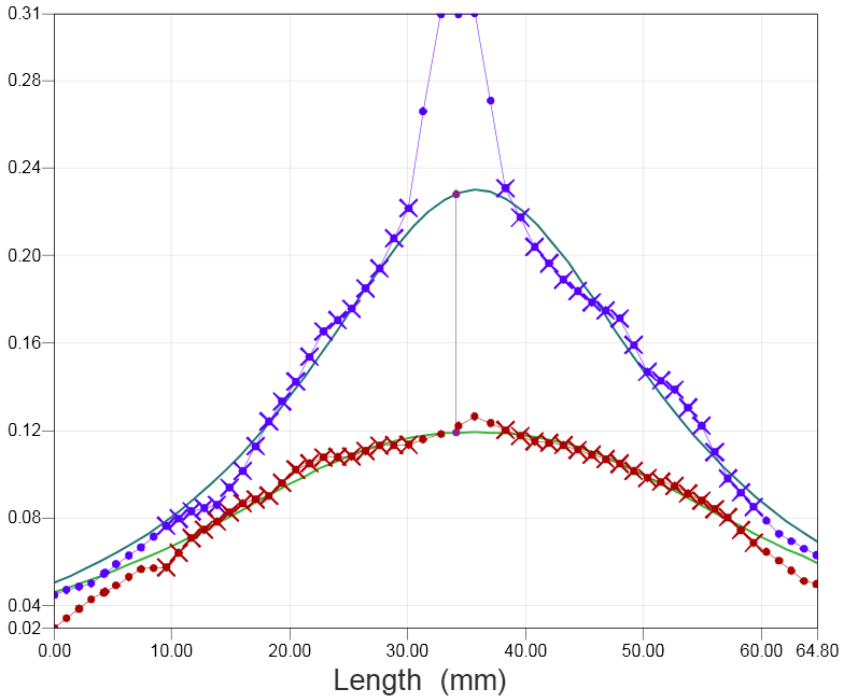

Figure 6-31. Major and minor forming limit strain measurement by Argus optical system.

In the case of geometry #1 (4:1 ratio, plane strain sample), the burst pressure was significantly higher with a value of around 1000 psi. These samples started to neck and fracture at the bottom radius (see Figure 6-32 below). This was because the gauge of the material was not quite appropriate for the radius of the die. It was quite a challenge to

have the necking to occur at the apex of the deformation (i.e., plain strain). Once the issue had been identified, the samples were gridded on both sides to specifically monitor the strain path at the bottom necked area. Interestingly, the geometry at the bottom necked area could also provide data point that were close to the plain strain limit.

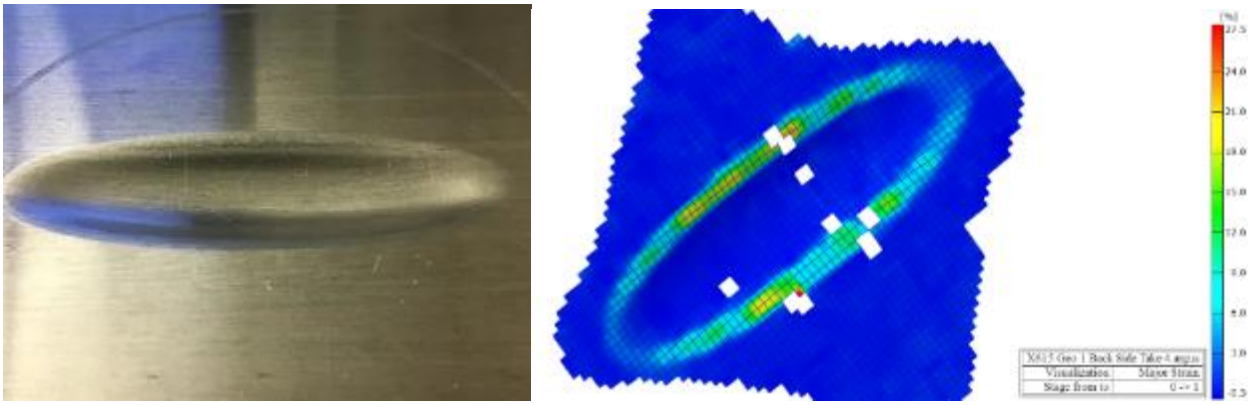

Figure 6-32. Necking observed at the bottom radius area in samples from Geometry 1 die and corresponding strain map.

The major and minor strains were calculated using Argus system and plotted on a graph to construct the right hand side of the FLC (see Figure 6-33). In general, AA6111 showed better formability than HRC 6111 at elevated temperature of 300ºC. The plain strain data point was from analyzing the bottom necked area from the narrowest (4:1 ratio) geometry, where the two alloys behaved similarly.

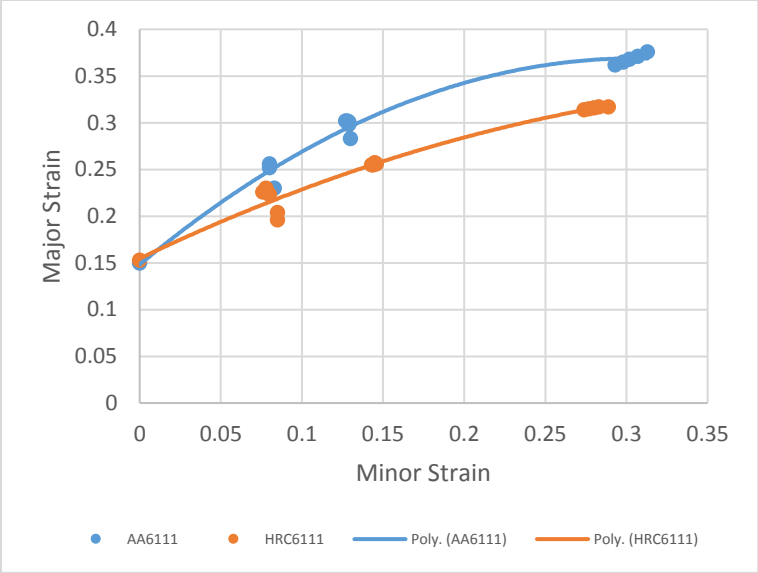

Figure 6-33. Experimentally determined biaxial tension side of FLC for AA6111-T82 and HRC 6111-T82 sheets at 300ºC.

The formability of these two alloys in T82 temper at 300ºC was comparable to the formability of AA6111 in T4 condition at room temperature from Graf et. al. (Graf, 1994), as shown in Figure 6-34. However, when comparing with the formability of AA6111 T4 at 300ºC, (Li, et al., 2004), the new alloys had lower forming limit. This is due to different temper used in the two experiments. In the current study, the material were tested in T82 condition, with higher strength and 50% lower elongation compared to T4. One of the goals was to determine if the warm formability of the AA6111 in T82 elevated temperature could be similar to that of the T4 material at room temperature, so that no additional heat treatment would be required after the part is formed. The result presented in Figure 6-33 established that the warm formability of AA6111 in T82 temper is indeed equivalent to the formability of T4 temper material at room temperature (see Figure 6-34).

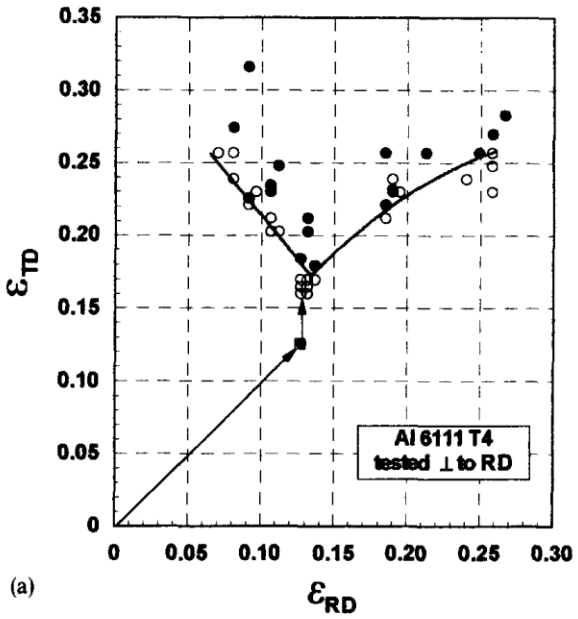

Figure 6-34. FLC of AA6111 T4 at room temperature.

6.1.5 Fractography of equi-biaxial bulge samples of AA6111 and HRC6111 tested at 300ºC

Equal-biaxial bulge samples from AA6111 and HRC6111 were cross-sectioned and examined under the SEM. The through-thickness fractographic results for AA6111-T82 sheet are shown in Figure 6-35 and Figure 6-36. Figure 6-35 is a lower magnification image that shows the top (bright region) and bottom (dark region) as well as the through-thickness fracture region. The fractograph shows dimpled rupture typically observed in ductile metallic materials at large plastic strains. Also, the fracture surface shows a depression at mid-thickness, similar to the cup and cone fracture of highly necked regions in cylindrical specimens of ductile metallic materials. The voids appear larger and more rounded in this region with sharp ridges, appearing as white lines around the grain boundaries.

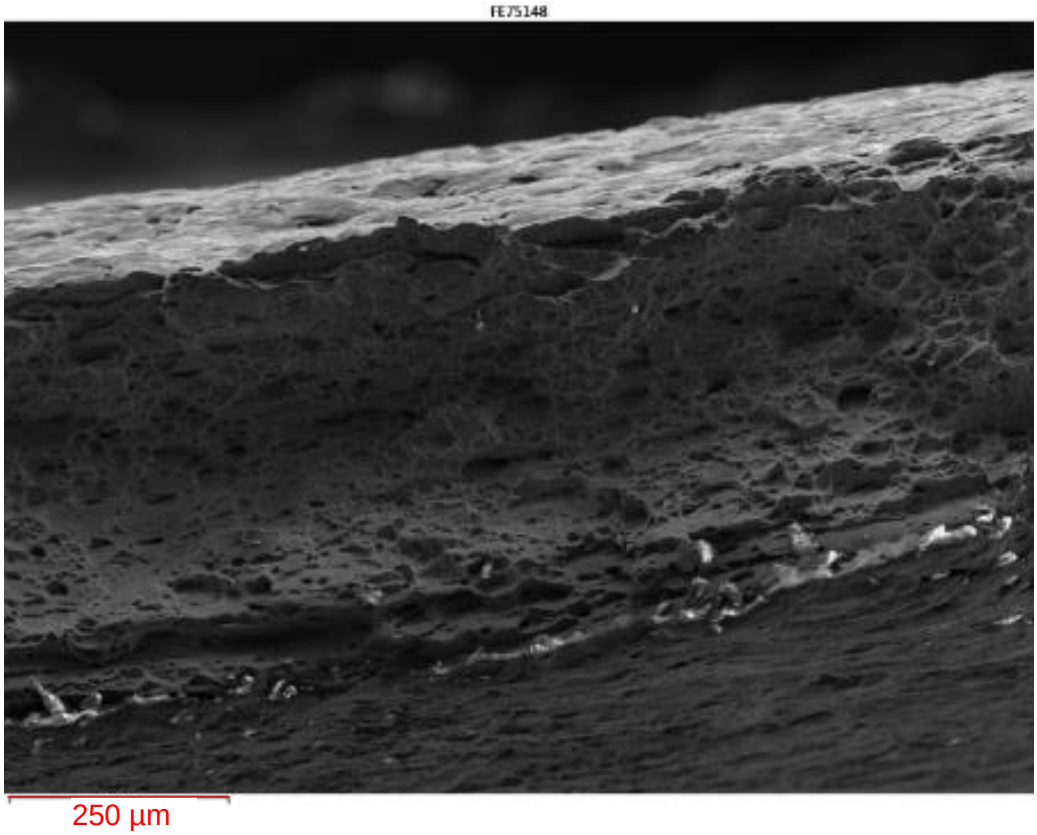

Figure 6-35. SEM image of equi-biaxial AA6111 T82 bulge specimen fracture surface showing ductile void damage.

Figure 6-36 is a larger magnification of the mid-thickness fracture region showing larger voids around the smaller constituent particles. The void ridges are now clearer as well as the presence of particles at the bottom of the voids. EDX spectrum of constituent particles found at the fractured surface is shown in Figure 6-36. This spectrum suggests that Fe-rich constituent particles are most predominant.

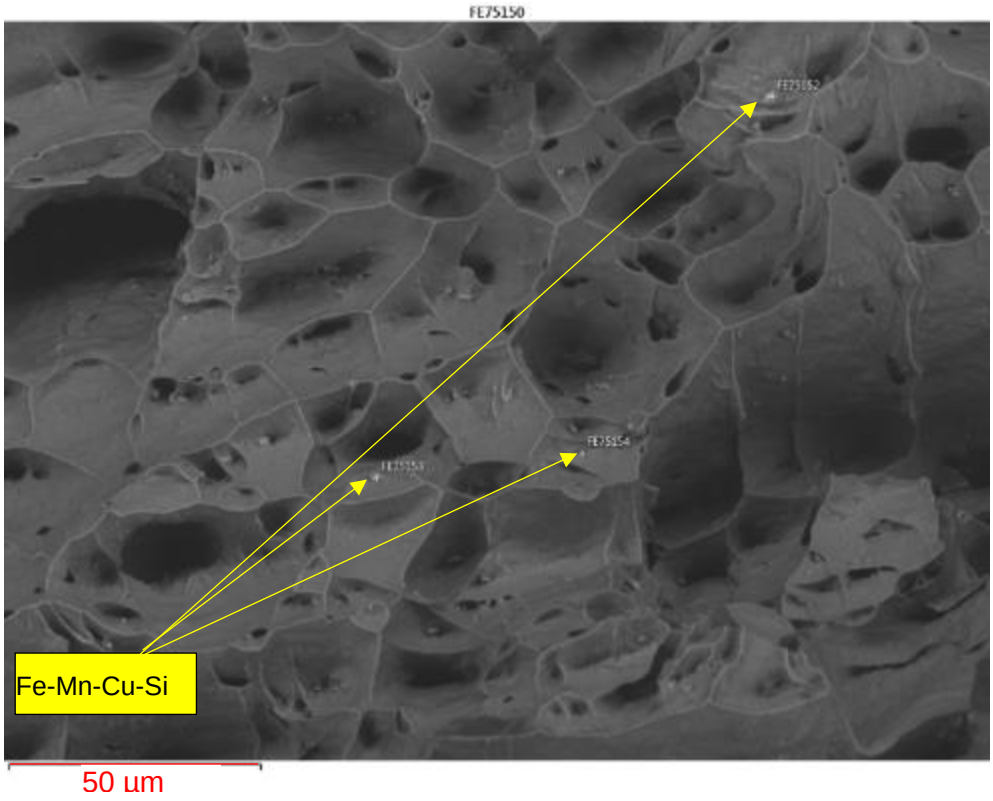

Figure 6-36. SEM image of the fractured surface of equi-biaxial AA6111 T82 sample fractured at 300ºC showing void formation around constituent particles.

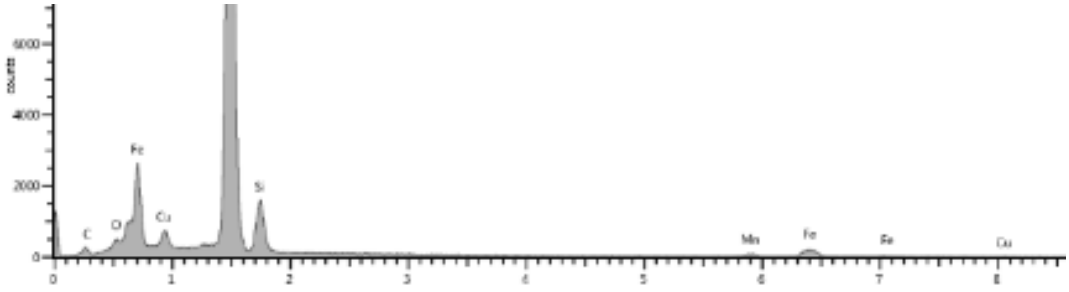

Figure 6-37. EDX spectrum of constituent particles found at the fractured surface of AA6111-T82 sheet.

Figure 6-38 and 6-39 show SEM image of fracture surface of HRC6111-T4 equi-biaxial bulge sample at low and high magnifications respectively. Clearly, the fracture surface of HRC6111 has a more faceted (or cleaved) in appearance unlike the deeper voids

observed in the benchmark AA6111-T4 sheet. Higher magnifications image in Figure 6-39 reveals clearer details of the faceted inter-void matrix region as well as more uniform and smaller void sizes compared to AA6111-T4. The difference in the number of constituent particles could not be quantified under the SEM. The qualitative observations, however, suggest that AA6111-T4 sheet exhibited a larger amount of void growth in the neck region prior to fracture. HRC6111-T4 sheet, on the other hand, exhibited less localized necking and a more precipitous ductile cleavage failure at the onset on necking. The observations are consistent with higher forming limit of benchmark AA6111-T4 compared to HRC6111-T4 sheet.

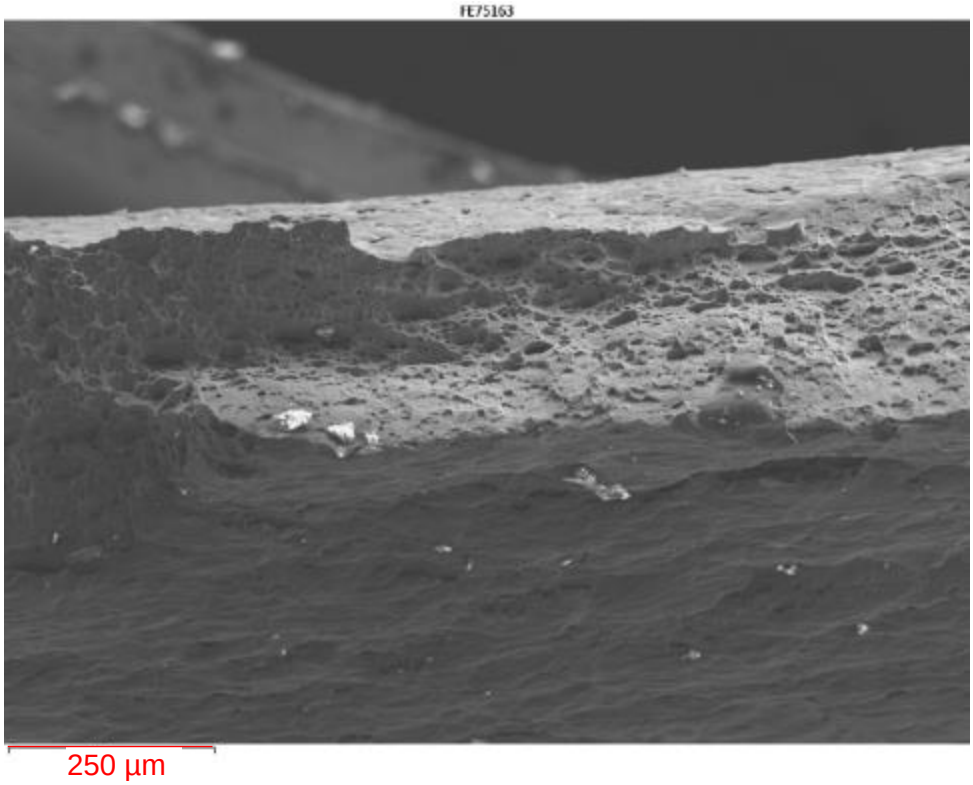

Figure 6-38. SEM image of Bi-axial HRC6111-T82 fractured surface.

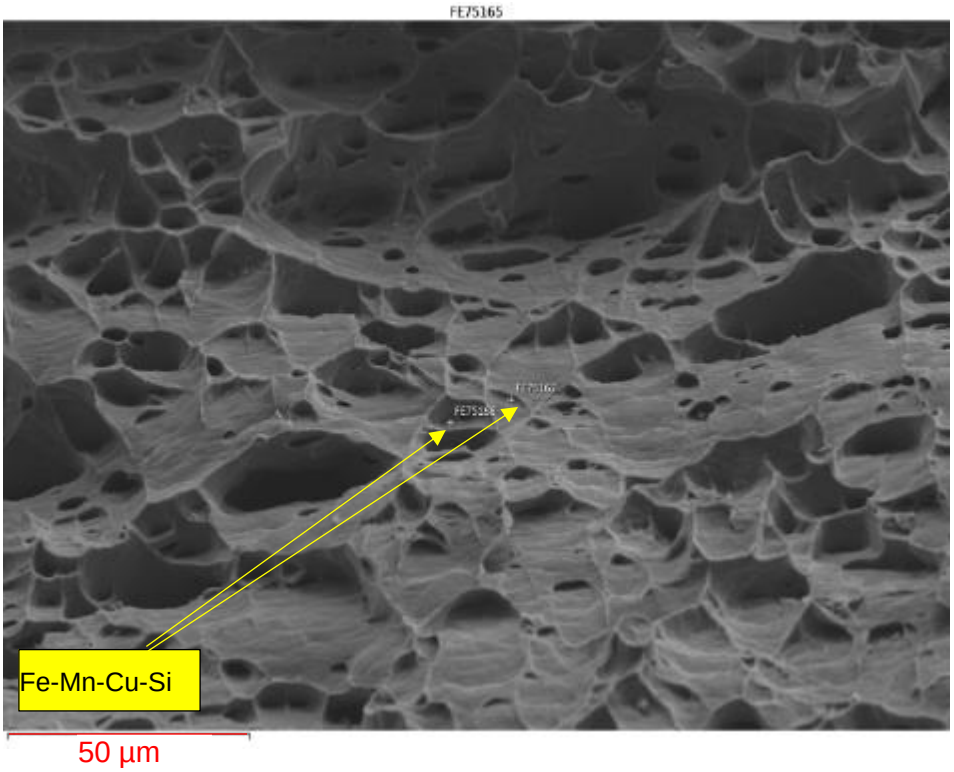

Figure 6-39. SEM image of fracture surface of equi-biaxial bulge sample of HRC6111-T82 sheet fractured at 300ºC.

The fractured samples observed by SEM were then cross-sectioned transversely and mounted for optical metallography and SEM/EDX characterization of the neck and fracture regions. Region in the vicinity of fracture revealed more void formation as indicated with red arrows in Figure 6-40. Void formed around constituent particles. In order to identify the particles, the same mount was subjected with SEM/EDS evaluation. Figure 6-41 to Figure 6-43 shows the back scatter image of the fractured area.

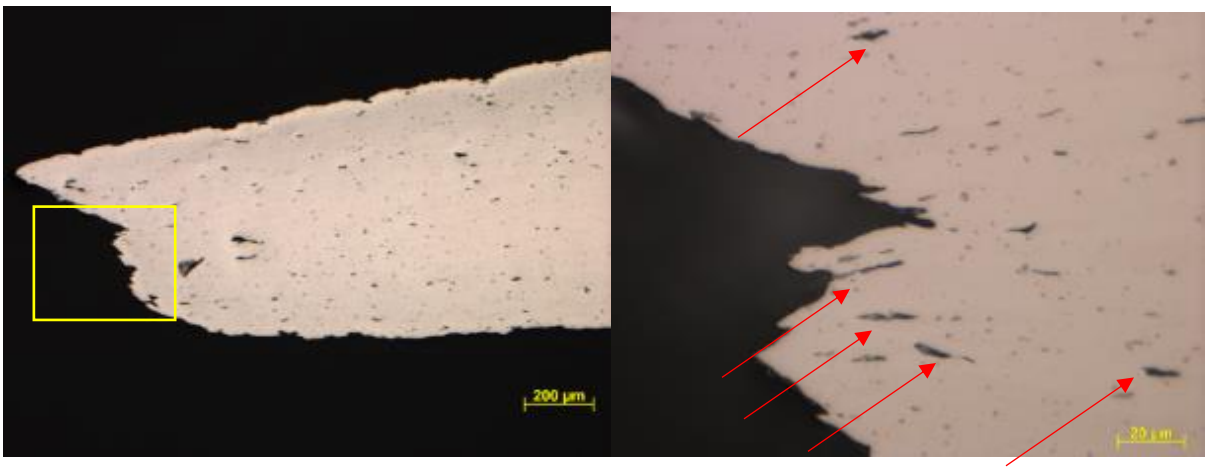

Figure 6-40. Optical micrographs of AA6111 T82 biaxial hot gas bulge sample fractured at 300ºC (50x and 200x).

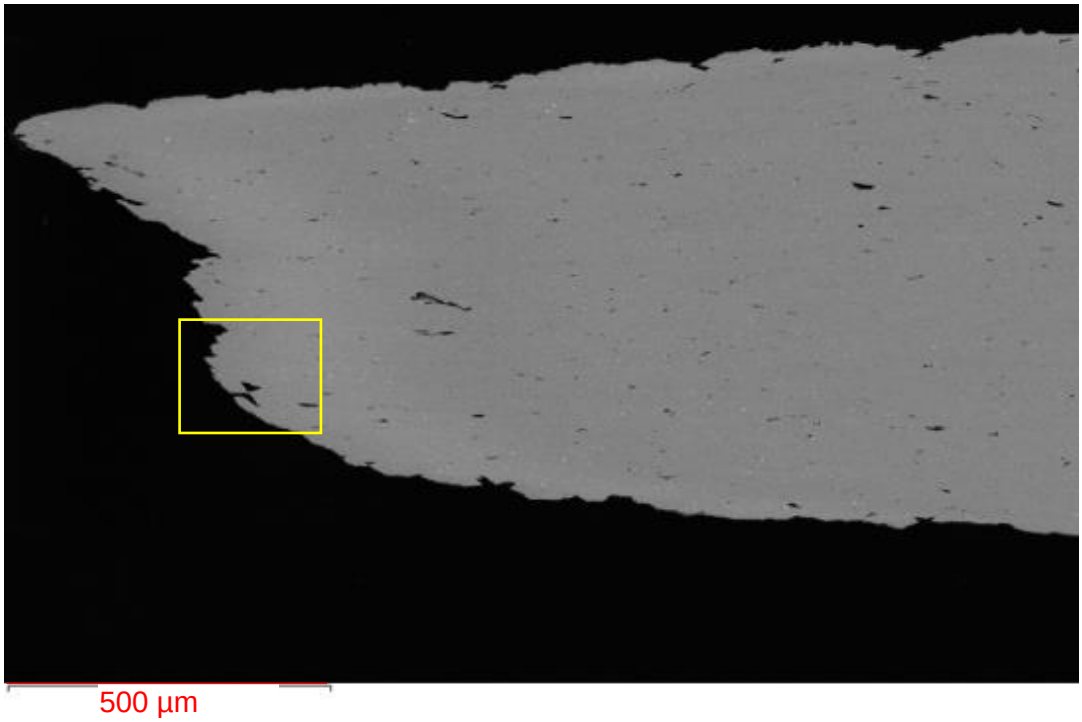

Figure 6-41. Back scattered SEM image of AA6111 T82 biaxial hot gas bulge sample fractured at 300ºC.

Figure 6-42. Back-scatterd SEM image of AA6111 hot gas bulge specimen fracture region at 300ºC.

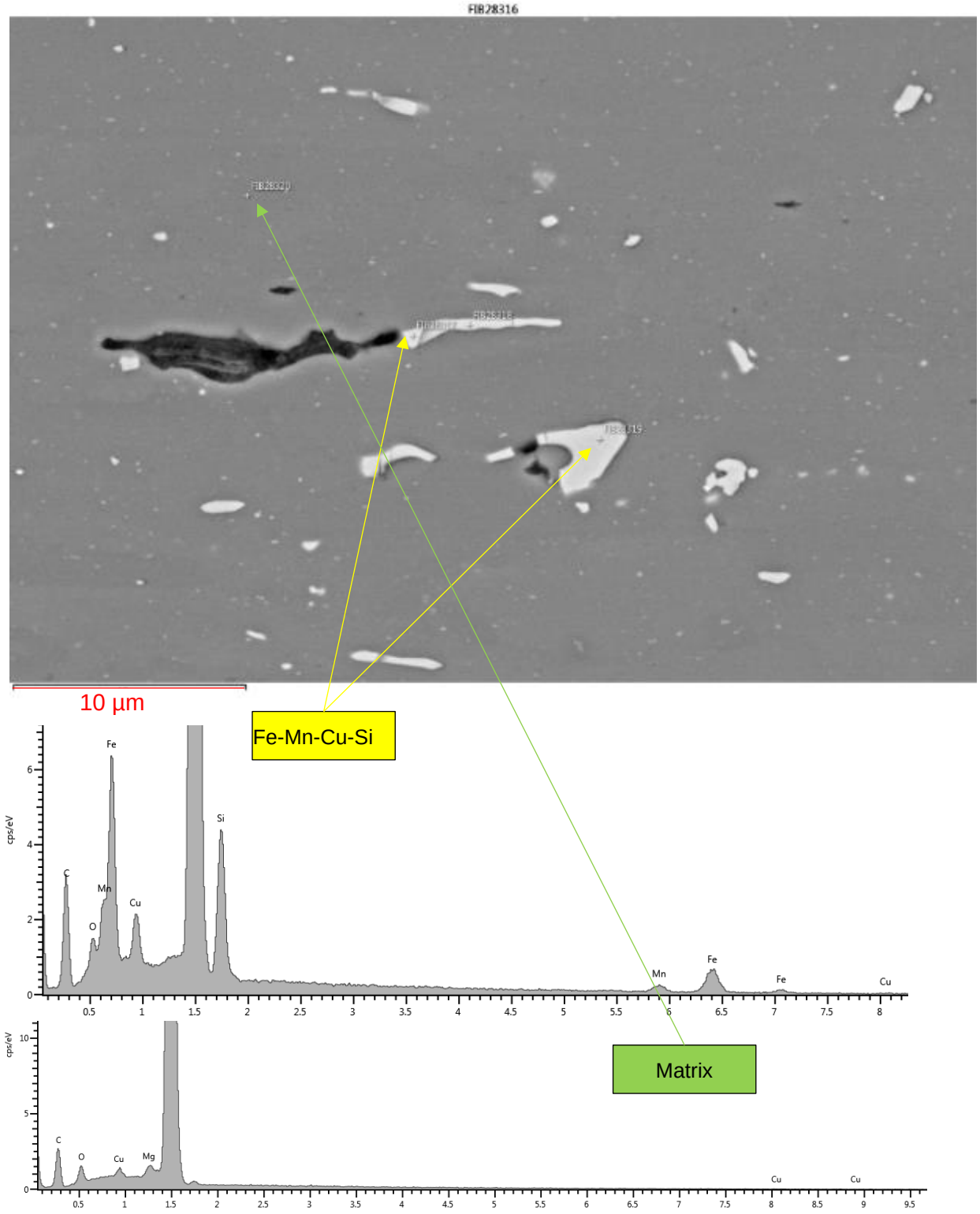

Figure 6-43. Higher magnification BSE image of AA6111 in the vicinity of fractured location showing void formmation adjacent to intermetallic particles.

Figure 6-44 shows a high magnification view of a nascent void, where the EDX indicates the void formed around the hard Fe-Mn-Cu-Si containing particles. This result is similar to previous observations made in Figure 6-36. The void would nucleate at the site of a constituent particle, then grow as illustrated in Figure 6-43, and finally coalesce and result in final fracture.

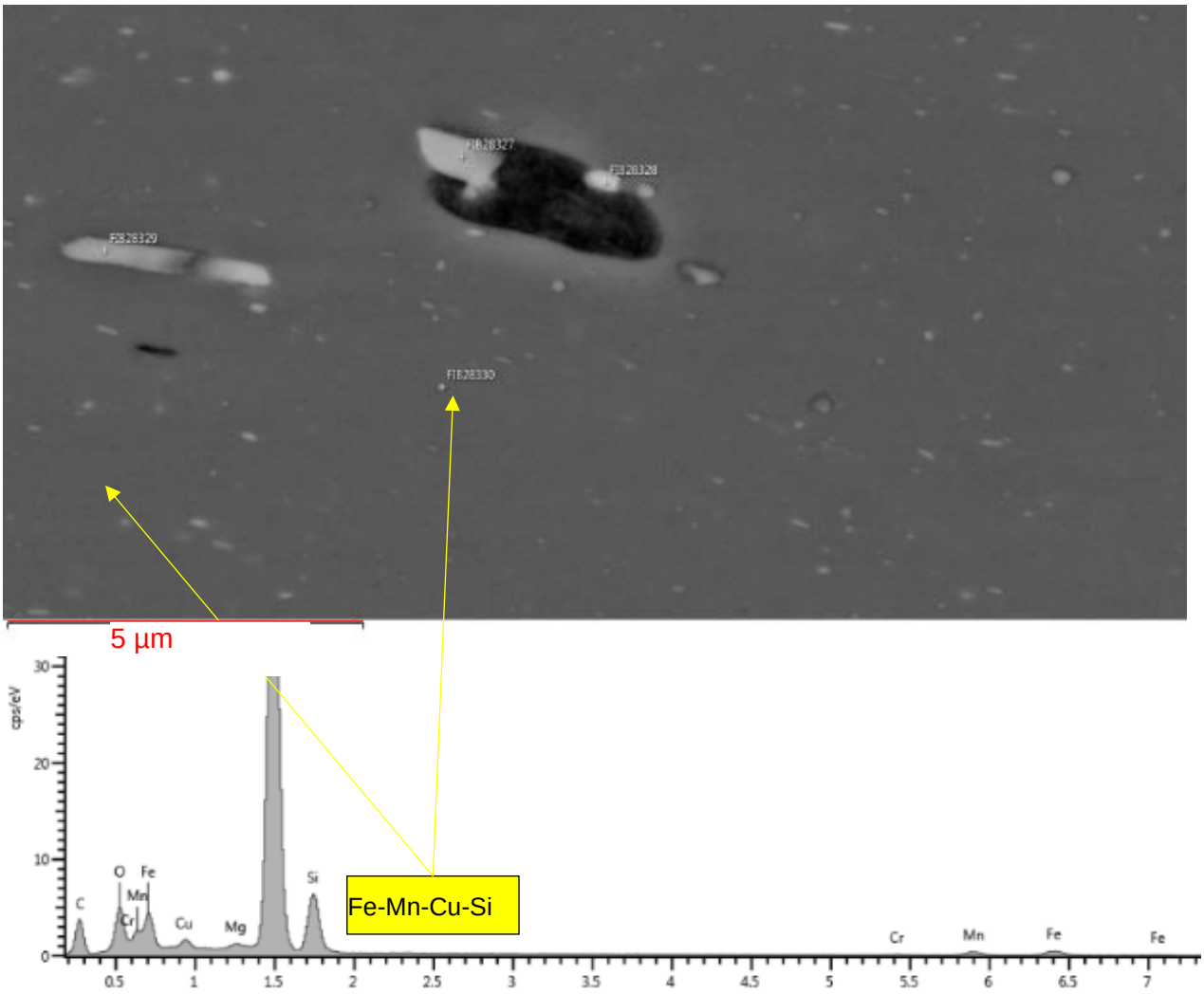

Figure 6-44. High magnification BSE of AA6111, showing nacent void formation in the matrix adjacent to the Fe and Mn containing intermetallic particles.

The same phenomenon was also observed in the HRC version of 6111 as illustrated in the optical micrographs of the fractured area in Figure 6-45. Void often formed adjacent to the fractured site. Figure 6-46 to Figure 6-49 shows the SEM/EDX analysis of the fractured location. EDX was able to identify and differentiates between the constituent particle and matrix. High magnification SEM image Figure 6-49 clearly shows the void nucleation around the constituent particles, subsequent void growth and coalescence leading to fracture.

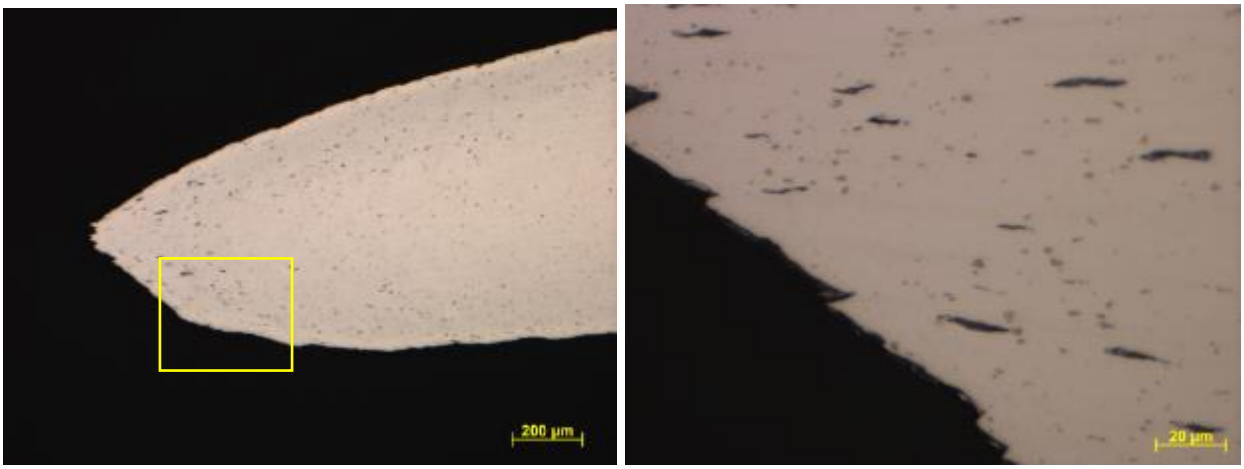

Figure 6-45. Optical mcrographs of HRC6111 biaxial bulge sample fractured at 300ºC (50x and 200x).

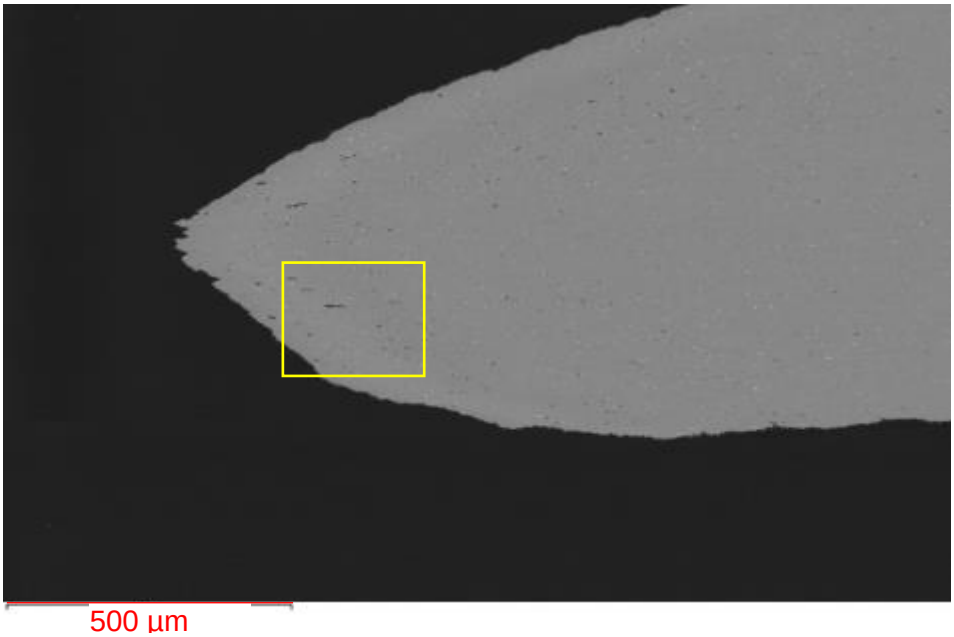

Figure 6-46. Back scattered SEM image of HRC6111 hot gas bulge specimen in the fracture region.

Figure 6-47. Back Scatterd SEM image of HRC6111 hot gas bulge specimen in the fractured region.

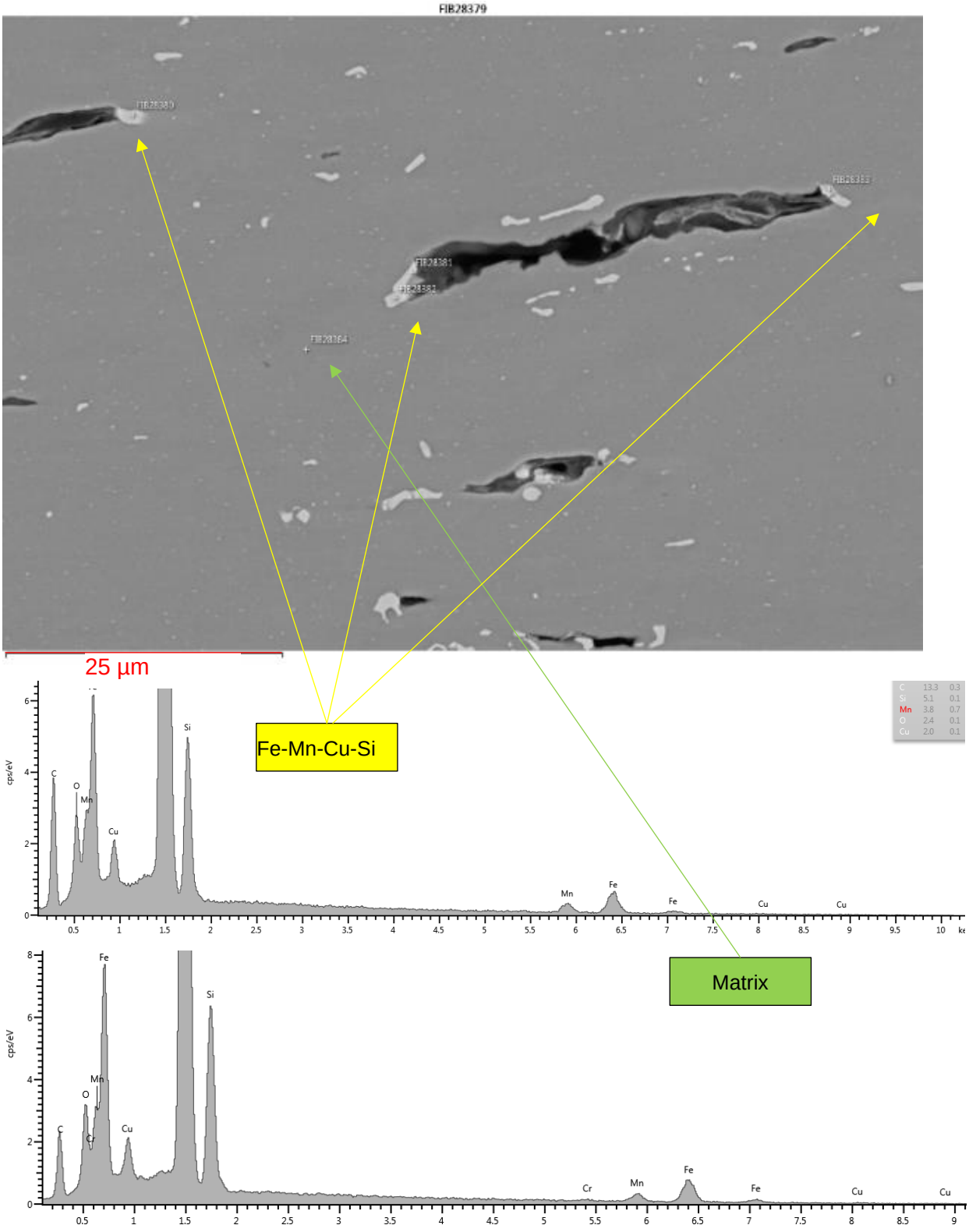

Figure 6-48. High magnification BSE image of HRCA6111 in the vicinity of fractured location showing void formmation adjacent to intermetallic particles.

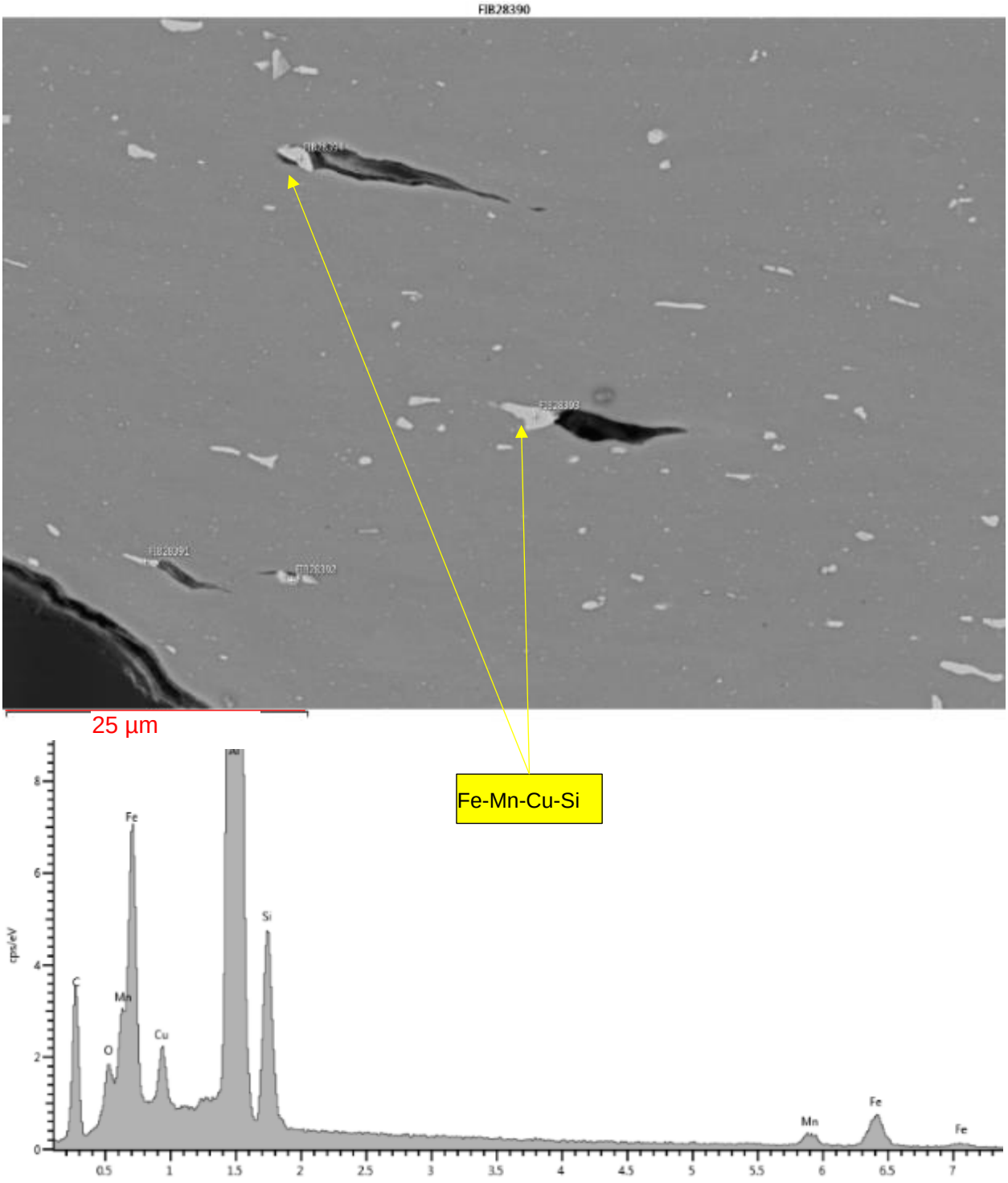

Figure 6-49 High magnification BSE of HRC6111, showing nacent void formation in the matrix adjacent to the Fe and Mn containing intermetallic particles.

6.2 7xxx Series Alloys

Three variants of AA7075 alloy were cast, of which two were similar in chemistry to that of recyclable 7075 sheet, as described earlier. Similar to 6xxx alloys, the objective was to investigate the effect of minor alloying elements on mechanical properties and elevated temperature forming limits of these 7xxx variants. The percentage of Fe, Mn and Cr were increased to two different levels, MRC 7075 and HRC 7075. MRC stands for 'Medium' Recycle Content 7075 where Fe, Mn and Cr contents were increased by 0.11, 0.13 and 0.06 respectively above the Baseline AA7075 alloy. Similarly, HRC 7075 stands for 'High' Recycle Content 7075 where Fe, Mn and Cr were increased further by 0.1, 0.15 and 0.05 compared to MRC variant of the alloy. Table 10 present the chemical compositions of the three 7075 alloys. The minor alloying elements are shown in bold letters.

Table 10. Chemical compositions of AA7075 baseline, MRC7075 and HRC 7075 alloys.

Alloy (wt%)	Cu	Fe	Mg	Mn	Si	Zn	Cr	Al
AA7075	1.47	**0.19**	2.48	**0.02**	0.09	5.43	**0.17**	Bal
MRC 7075	1.6	**0.3**	2.5	**0.15**	0.1	5.6	**0.23**	Bal
HRC 7075	1.6	**0.4**	2.5	**0.3**	0.1	5.6	**0.28**	Bal

6.2.1 Microstructures

Compared to the typical 6xxx series aluminum alloys, 7xxx series alloys are more complex, have more alloying elements, and therefore, involve more phases than the primarily θ (Mg_2Si) phase in the 6xxx series. The main phases that are present are η phase-$MgZn_2$ or M phase, $Mg(Zn,Al,Cu)_2$,T phase ($Al_2Mg_3Zn_3$), S phase (Al_2CuMg) and θ (Mg_2Si). In the case of 7xxx, only η phase ($MgZn_2$) is the desired strengthening phase. The S and θ phases, despite their strengthening effect in 2xxx and 6xxx series aluminum

respectively, are not desired since the chemical composition of 7xxx series alloys are not designed to optimize Mg-Si ratio of these elements. There are constituent particles such as Al_7Cr; Al_7Cu_2Fe and $Al_9Fe_2Si_2$ as well as meta-stable phases present in the 7075 alloys. Due to the higher alloying content of the 7xxx series, the solidus temperature of alloys is significantly lower than the 6xxx series alloys.

Similar to the earlier case of 6111 alloys, a phase calculation was carried out using ThermalCalc software to identify the potential phases in the 3 different variants of 7075 alloy. The reason to use ThermalCalc over JMetpro was because ThermalCalc computer program is able to deal better with aluminum alloys that have higher solute content and more phases involved. As noted earlier, calculation was in equilibrium condition and used as general guide for material casting and subsequent processing purposes. Figure 6-50 to Figure 6-52 show the predictions of the phases present in each of the three 7xxx alloys, baseline 7075, MRC 7075 and HRC 7075. With increasing alloying content, the solidus temperature of the alloy decreased slightly, resulting in melting temperature in the 490ºC-500ºC range. In other words, there was a limited window between the solvus temperature of S phase (470ºC) and solidus temperature (495ºC) for baseline 7075 alloy, as shown in Figure 6-50. These results were utilized as a guide for selecting the solutionising temperature for each of the alloys. The intent was to dissolve as much of these unwanted phases back into solid solution as possible to create maximum amount of η phase. It should also be noted that some of the phases such as Mg_2Si or constituents particles such as $Al_{13}Fe$ and Al_7Cr could not be dissolved since their solvus temperature was higher than the solidus temperature. Figure 6-51 shows the phase prediction of MRC 7075, the main phase $MgZn_2$ (marked as C14_LAVES in the figure legend) that dissolved around

370ºC, and a new phase Al_6Mn was also present. The fraction of Al_7Cr (identified as AL45V7 in the figure legend) increased due to the addition of minor alloying elements. The solidus temperature decreased resulting in even narrower solutionising window for this alloy.

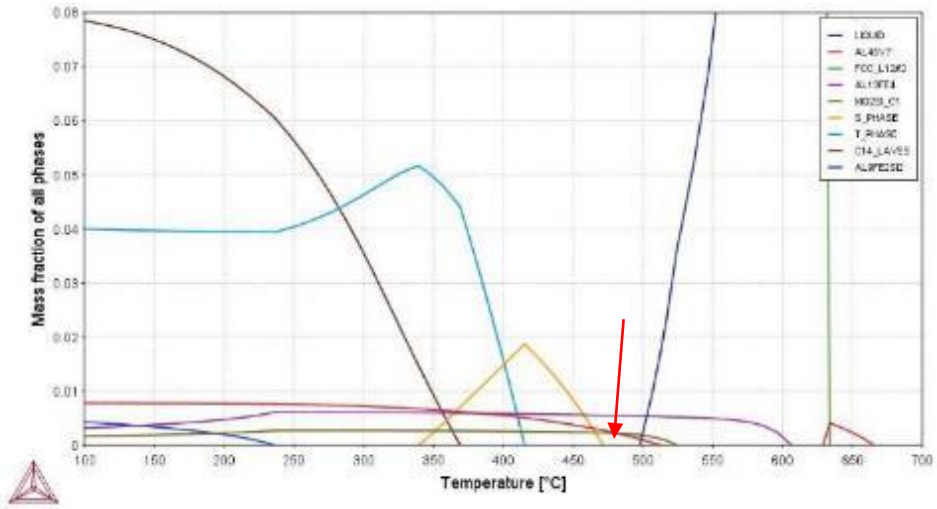

Figure 6-50. Baseline 7075 alloy phase predictions using ThermalCalc software.

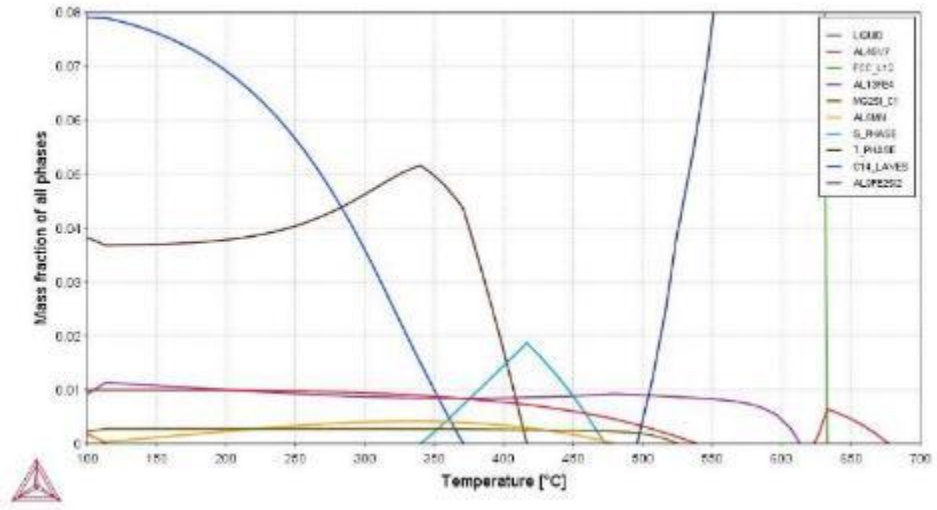

Figure 6-51. MRC 7075 alloy phase predictions using Thermal Calc software.

Figure 6-52 shows the phase prediction of HRC 7075 alloy. There are no additional phases generated, however, the mass fraction of Al_7Cr, Al_6Mn and $Al_{13}Fe_4$ increased further. Since these constituents were unable to dissolve during solution heat treatment, it was expected to have more constituent particles present in the final product. Since the solidus temperature was not significantly affected, the solutionising temperature was kept the same as for MRC 7075 alloy.

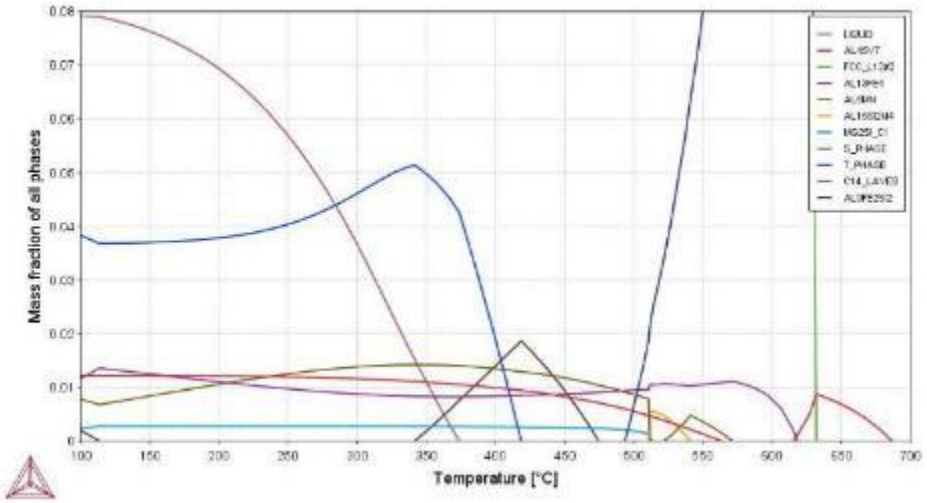

Figure 6-52. HRC 7075 phase predictions using ThermalCalc software.

6.2.1.1 As-cast Microstructures

The above noted compositions were cast using the same set-up as for AA6111 alloys. The quarter thickness location of each ingot was cross-sectioned, mounted and polished to obtain the as-cast microstructures. Figure 6-53 from left to right shows optical micrographs of baseline AA7075, MRC 7075 and HRC 7075 alloys respectively at two different magnifications. From the higher magnification, bottom row, it was revealed that

MRC and HRC had more secondary phase particles present compared to the baseline AA7075 alloy.

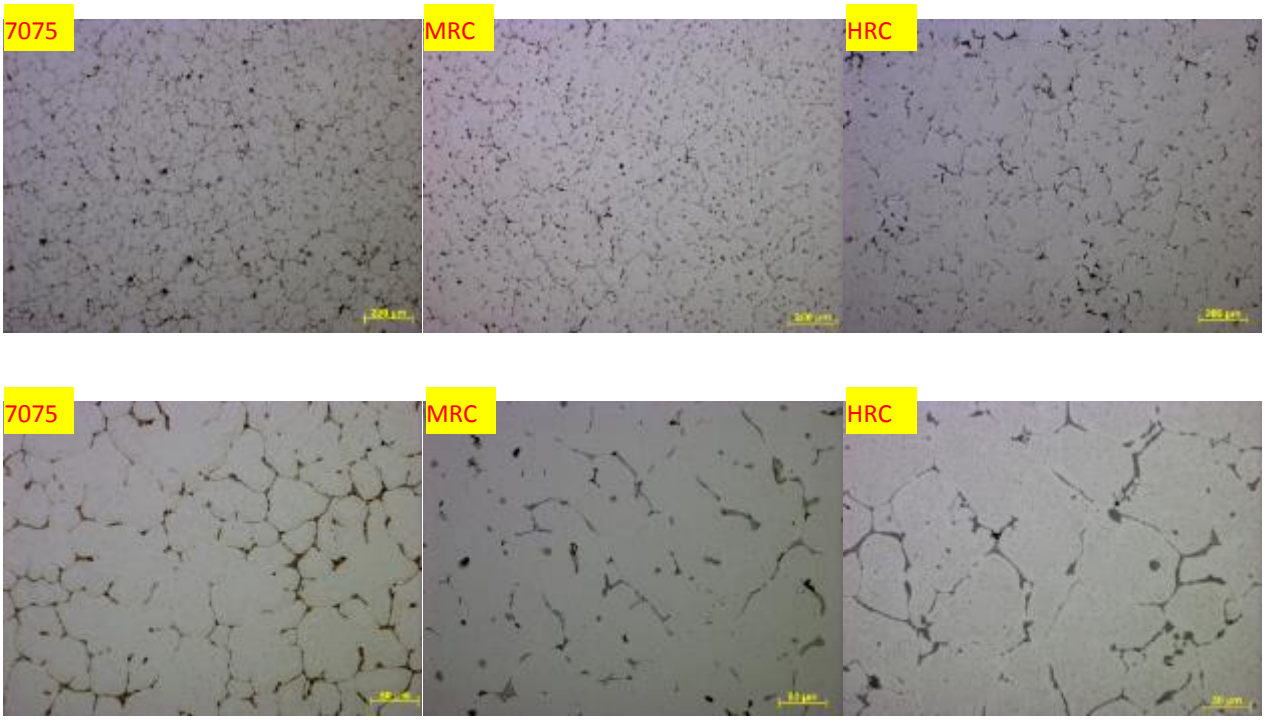

Figure 6-53. As-cast optical micrographs from quarter location of baseline 7075, MRC 7075 and HRC 7075 alloys.

6.2.1.2 Homogenization Process and Homogenized Microstructures

Due to higher solute levels, 7xxx alloys have lower melting temperature compared to 6xxx series aluminum. The phases also make 7xxx series alloy more prone to eutectic melting. Therefore, it was essential to perform the homogenization to ensure that eutectic phases were dissolved completely. Figure 6-54 shows the DSC scan of the alloys in the as-cast condition, from quarter thickness location of the ingots. All of the scans show eutectic melting in the range 480-490ºC.

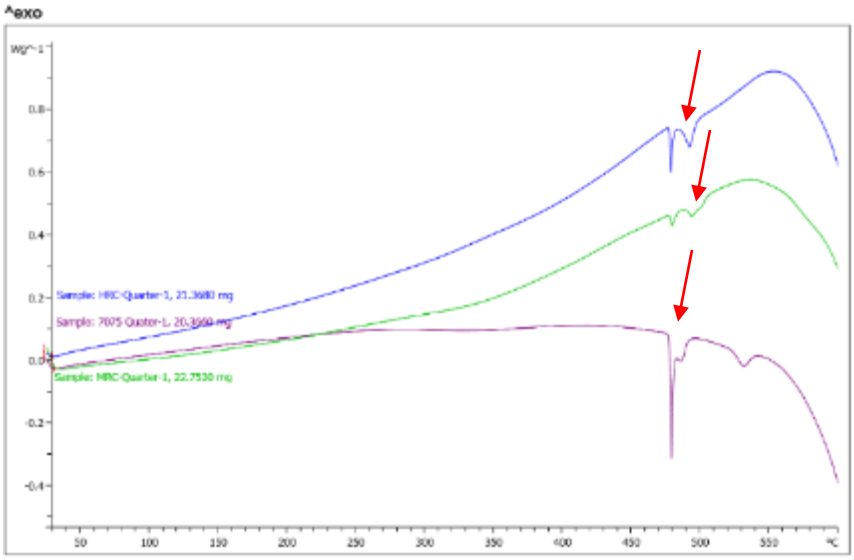

Figure 6-54. DSC scans of baseline 7075, MRC and HRC in as-cast condition showing eutectic melting.

Figure 6-55 below is a DSC scan of baseline and HRC ingot samples after homogenization. The curves show that the ingots had been successfully homogenized with no evidence of eutectic melting.

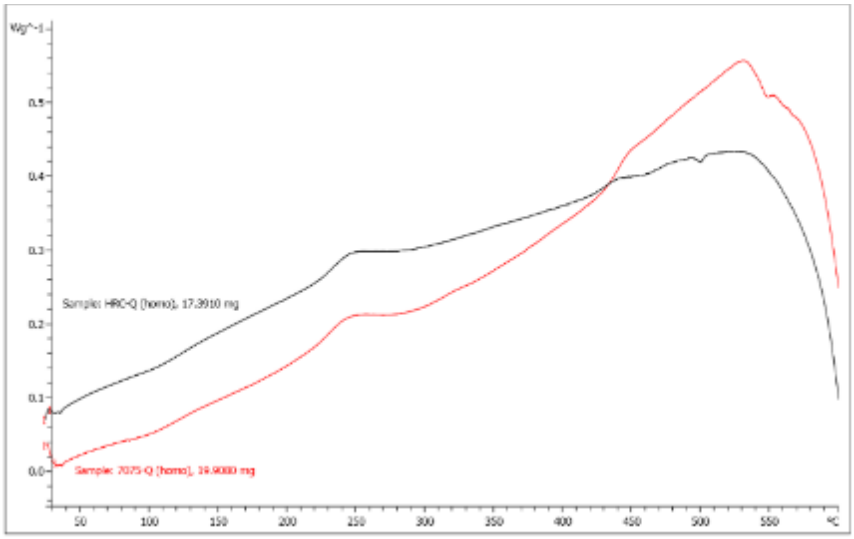

Figure 6-55. DSC scans of baseline and HRC Ingots after homogenization.

Figure 6-56 shows the optical micrographs of the ingots after homogenization. Most secondary phase particles were dissolved back into solid solution leaving very clean grains and only constituent particles were found at the grain boundaries. MRC and HRC version showed finer grains compared to the baseline 7075 (see bottom row in Figure 6-56).

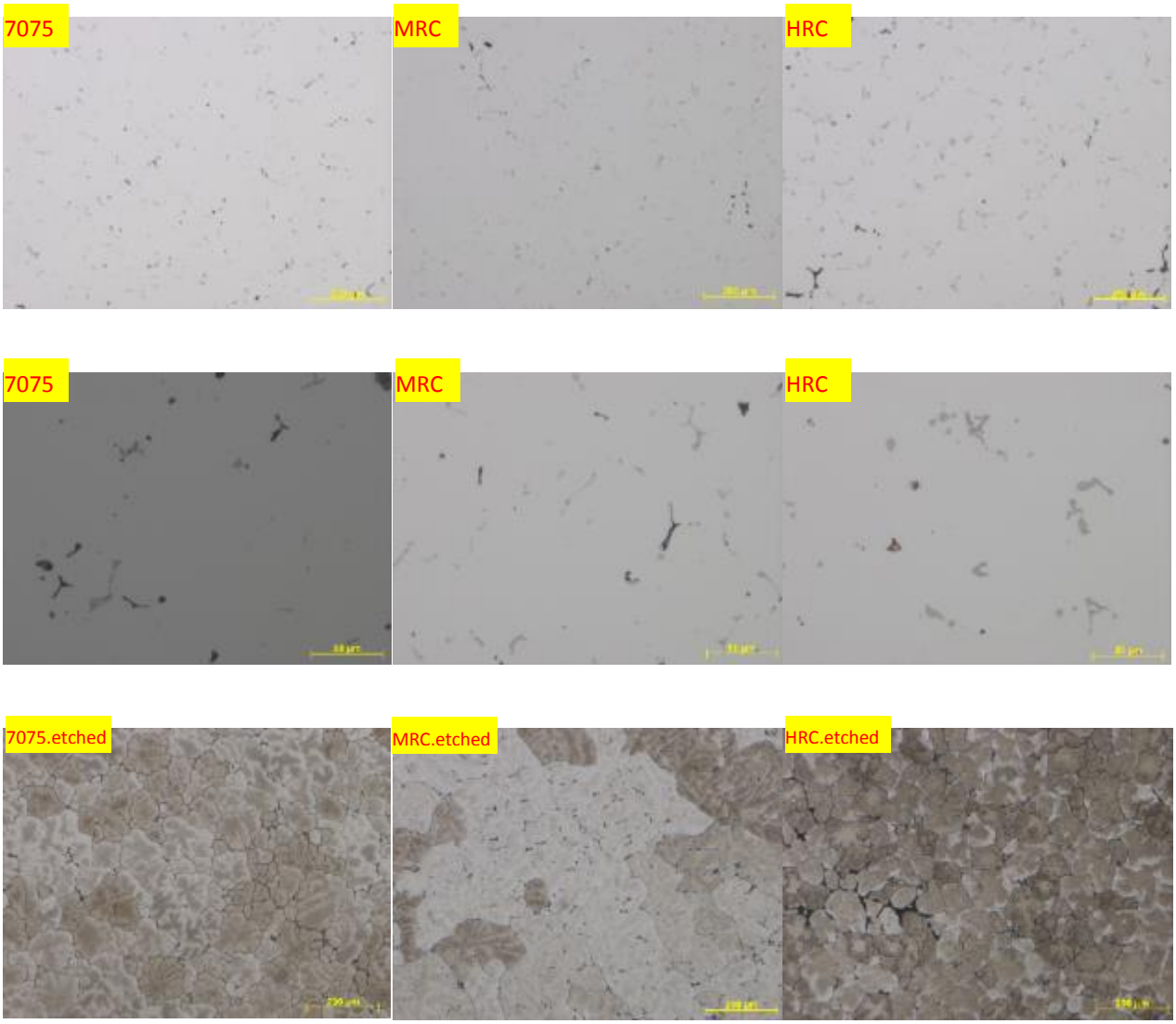

Figure 6-56. Optical micrographs of baseline 7075, MRC7075 and HRC 7075 after homogenization.

6.2.1.3 T6 Microstructures

Figure 6-57 shows the optical micrographs in T6 temper for all three 7075 alloys. As expected, baseline appeared to be cleaner, and MRC and HRC variants showed increased number density and larger constituent particles, which were Fe, Mn containing particles.

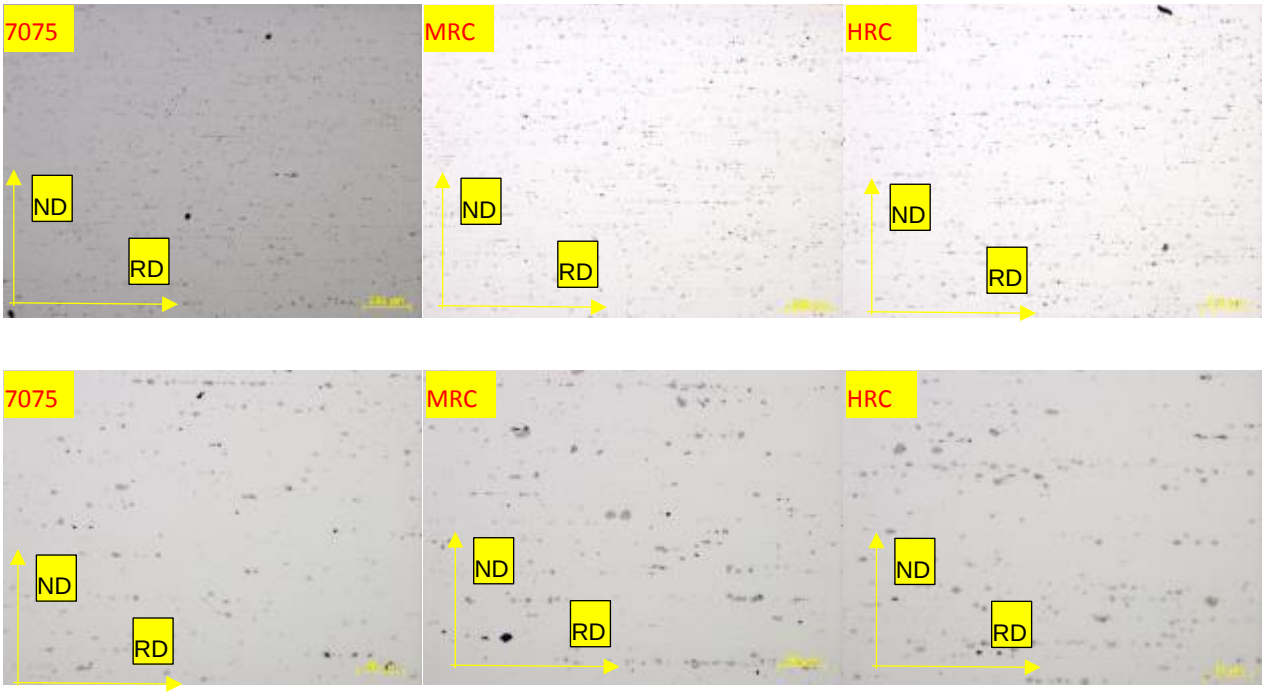

Figure 6-57. Optical micrographs in T6 condition of baseline 7075, MRC 7075 and HRC 7075 sheets.

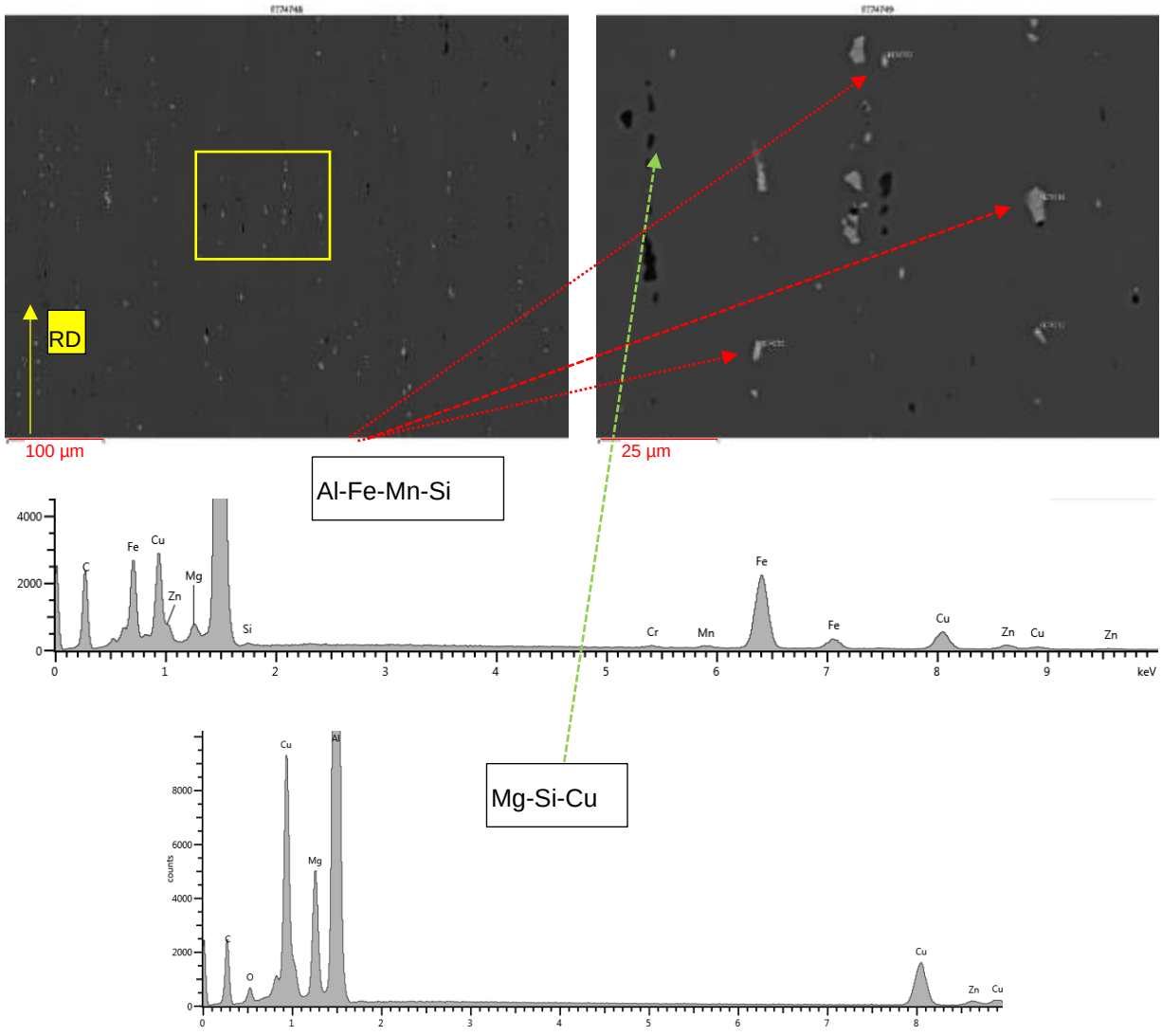

Figure 6-58. SEM (BSE) of AA7075-T6 sheet and EDX plots of the constituent particles.

Figure 6-58 to 6-60 show SEM images of AA7075, MRC7075 and HRC7075 final rolled surfaces respectively. AA7075 appears to have slightly lesser amount of constituents on the surface compared to MRC7075 alloy. HRC7075 alloy appears to have the most amount of constituent particles. The particles of all variants appears to distribute along the rolling direction of the sheet. There are two major types of constituents observed at the surface. Al-Fe-Mn-Si containing particles, which are the light grey features in the back scattered electron (BSE) mode and Mg-Si-Cu particles which are dark black phases.

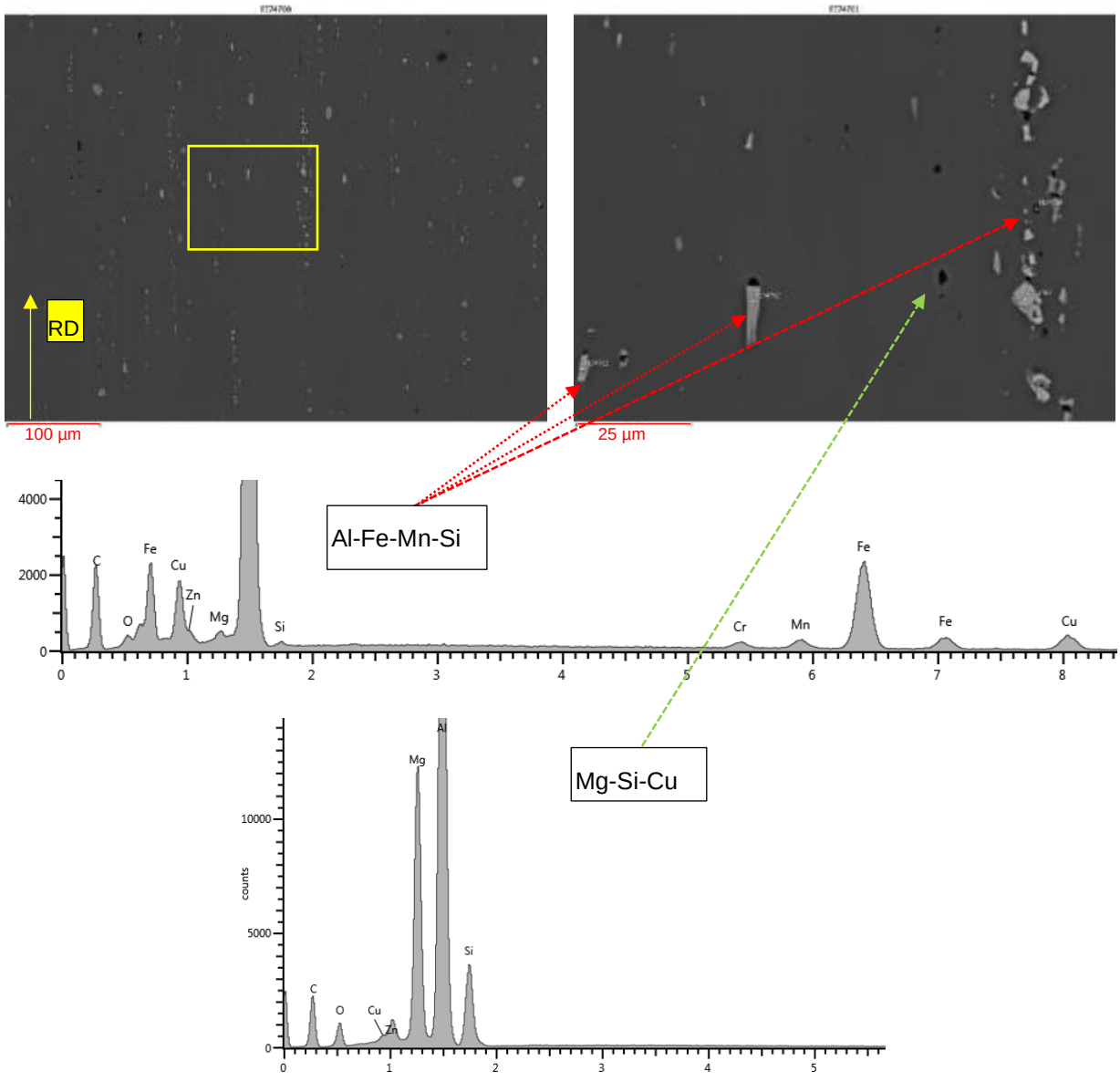

Figure 6-59. SEM (BSE) of MRC7075 sheet and EDX plots of the constituent particles.

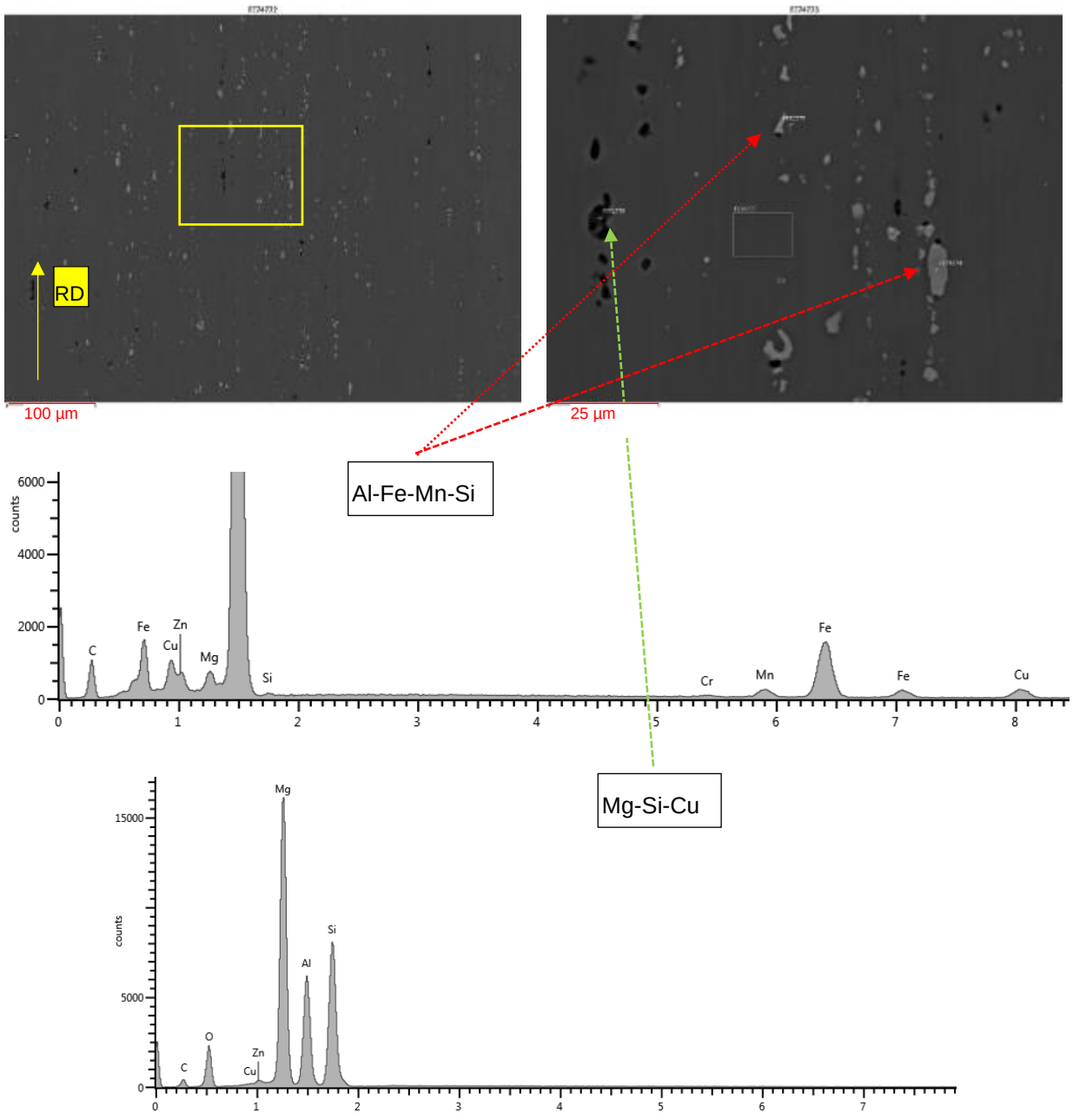

Figure 6-60. SEM (BSE) of HRC 7075 sheet and EDX plots of the constituent particles.

It is worth mentioning that in Figure 6-60, for the case of HRC7075, there is a very high density of constituent particles on the surface. These hard inter-metallic particles, during deformation, could become stress risers compared to the softer adjacent aluminum matrix and result in drop in strength and formability. This is discussed later in Section 6.2.4.

6.2.2 Mechanical Properties

6.2.2.1 Room Temperature Tensile Properties

Table 11 shows the mechanical properties of baseline AA7075, MRC and HRC sheet materials in T6 condition.

Table 11. Room temperature tensile test results for baseline 7075-T6, MRC 7075-T6 and HRC 7075-T6 sheets.

Sample	Yield Strength (Stdev) MPa	Tensile Strength (Stdev) MPa	Uniform Elongation (%)	Total Elongation (%)
Baseline	496 (3.0)	553 (2.6)	10.8	13.8
MRC	472 (0.6)	545 (1.4)	10.6	13.6
HRC	460 (4.3)	537 (2.1)	10.8	12.5

The baseline AA7075 showed the highest strength, and MRC variant showed a significant strength drop compared to the baseline alloy, and HRC showed further strength drop compared to the MRC alloy. Unlike the case of 6xxx, where there was limited Si available for forming the main strengthening phase Mg_2Si, from the ThermalCalc calculation, the mass fraction of the main strengthening phase $MgZn_2$ in 7075 alloys did not change. The loss in strength was caused by increased number and larger sizes of constituent particles. Voids tended to form around these hard constituents surrounded with soft aluminum matrix during deformation and resulted in lower strength and elongation. This is discussed in more detail later in Section 6.2.4.

6.2.2.2 High Temperature Tensile Test Results

At lower temperatures, the plastic deformation of 7075 sheet materials is primarily enabled by dislocation motion in the field of various constituent particles and phases that affect the work hardening behavior of the alloy and also initiate void formation in their

vicinity. At high temperature, however, the material experiences a 'quasi-superplastic' deformation where deformation is enabled by grain boundary sliding. Thus, grain size is an important factor in high temperature elongation, and chemical composition could also be a contributing factor. Unlike some studies (Weimin, et al., 2014) where researchers were largely focused on thermo-mechanical aspects of deformation, metallurgical changes such as dynamic grain growth should not be neglected, and in fact, play a more important role in high temperature deformation than dislocation kinetics. In the present work, the tensile stress-strain curves for baseline AA7075 exhibited early stress saturation and even softening with increasing test temperature at 400ºC and above. Also, a significant drop in tensile strain to fracture (or total elongation) with increase in temperature was observed. A trend towards lower elongation values at higher temperatures in the range 450°C – 480°C as shown in Figure 6-61. This was similar to the work of Weimin et al. (see Figure 6-62) (Weimin, et al., 2014).

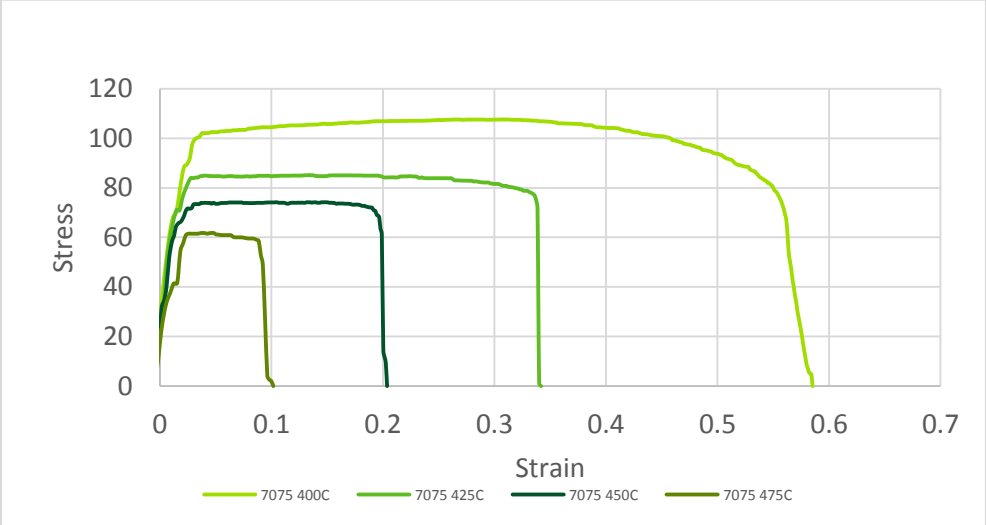

Figure 6-61. Elevated temperature tensile stress-strain curves of baseline 7075 at 400ºC, 425 ºC, 450 ºC and 475 ºC respectively.

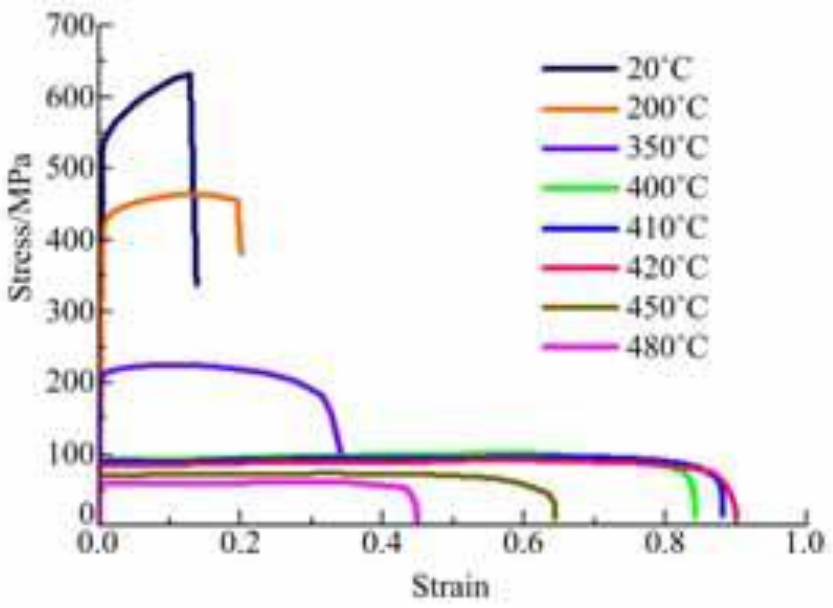

Figure 6-62. Tensile stress strain curves of AA7075 at elevated temperatures (Weimin, et al., 2014).

It is believed that the amount of decrease in elongation is grain size dependent, especially at higher temperatures. In addition to the grain size, the strain rate is also expected to a have significant effect on the elongation at high temperature. In the present experiment, the strain rate was controlled at 1/s, which is similar to strain rate observed during hot stamping. Lower strain rate would further increase the ductility of the material.

6.2.3 Hot Forming Characteristics of AA7075 Alloys

Figure 6-63 shows the burst pressure from hot gas bulge tests using circular and various elliptical die openings with different aspect ratios for AA7075, MRC7075 and HRC7075 sheets at 425ºC and 470ºC. The burst pressure of 7xxx alloy were much lower compared to the earlier 6xxx alloys due to (i) lower gauge of 1.5 mm for 7xxx alloys compared to 1.8 mm for 6xxx alloys, and (ii) considerably higher forming temperature than 6xxx.

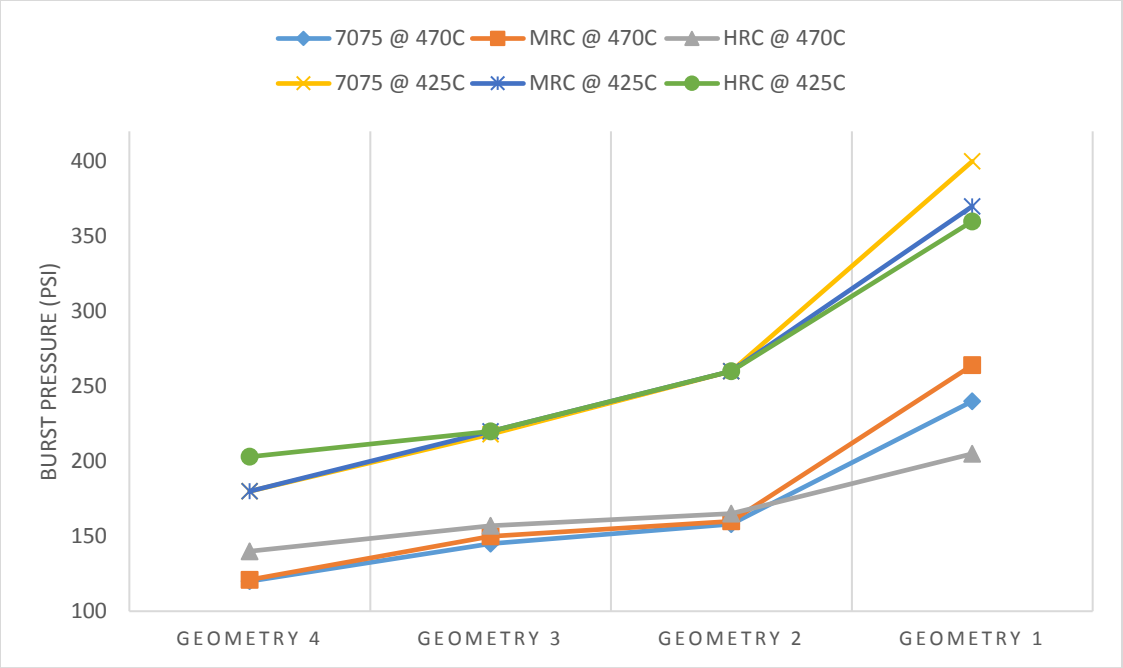

Figure 6-63. Burst pressures of 7xxx sheet materials at 425º and 470ºC.

Note that 'Geometry 1' refers to the largest die ellipticity and 'Geometry 4' refers to the lowest die ellipticity (i.e., circular die) cases.

It is to be noted that the burst pressure at 425ºC was higher than at 470ºC due to higher tensile strength at lower temperature for the 7xxx alloys, as shown earlier. The HRC and MRC variants showed no clear trends in terms of burst pressures as a function of strain path compared to the baseline AA7075 perhaps due to complex relationship of finer gain structure and increased damage development in recyclable variants.

6.2.3.1 FLC of AA7075 variants at 470ºC

All variants of the alloys deformed smoothly at 470ºC. Figure 6-64 shows an example of bulge specimen obtained from baseline7075 sheet using die geometry #4 (circular die opening) and the corresponding Argus surface strain map. For a more compact presentation of results in this section, the rest of sample images and corresponding strain

maps for all 7075, MRC7075 and HRC7075 at two different temperatures have been placed in the Appendix at the end of the thesis. Similar to that of 6xxx alloys, the strain measurement data of Argus accounted for the fracture width and utilized adjacent circular grids next to fracture to estimate the strain path at the apex to obtain the limit strains.

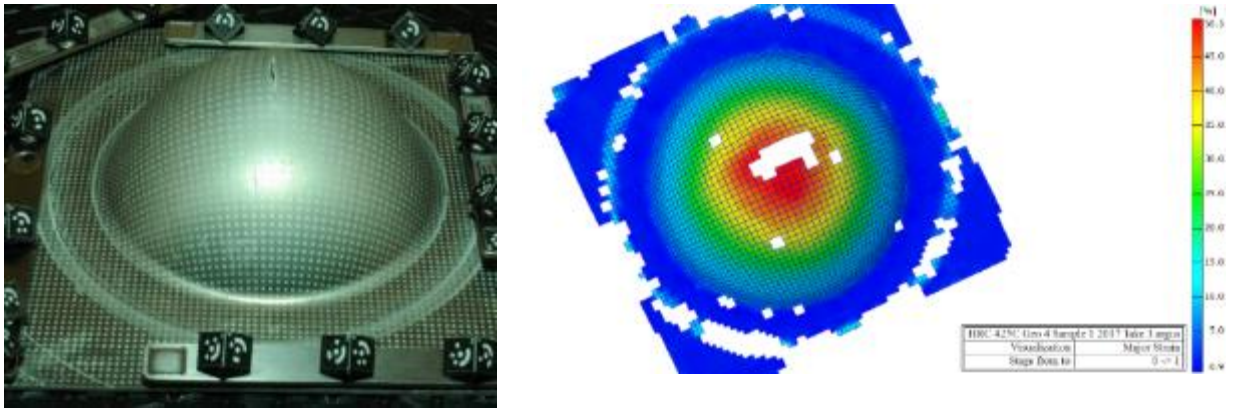

Figure 6-64. Baseline 7075 hot gas bulge samples and corresponding strain map at 470ºC.

Major and minor limit strains of all three 7xxx variants at 470ºC and different die geometries were obtained from analyzed grid strain data. Figure 6-65 shows the right side FLC curves for baseline AA7075, MRC 7075 and HRC 7075 at 470ºC. The baseline AA7075 shows the highest forming limits with MRC and HRC variants showing significant overall reduction in the forming limit. This is attributed largely to higher number of constituent particles present in MRC 7075 and HRC 7075 alloys, which triggered void initiation around the hard constituent during the deformation process, as discussed later. MRC version still exhibited forming limits relatively close to the baseline AA7075, which could potentially be considered for hot forming purposes.

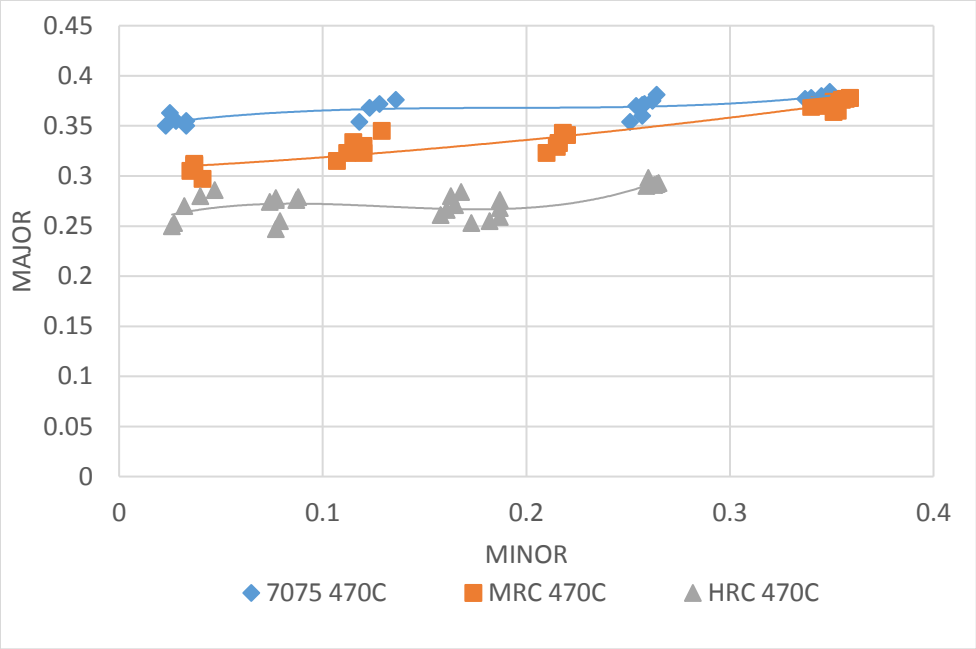

Figure 6-65. Right side of FLC for baseline 7075, MRC 7075 and HRC 7075 sheet materials at 470ºC.

6.2.3.2 FLC of AA7075 variants at 425ºC

All three variants were also bulged at 425ºC using different elliptical dies, and a circular die, to attain different biaxial tension strain paths. The resulting necking strain clusters and limit strains in the form of FLCs are shown in Figure 6-66 for the three 7xxx variants. Again, the baseline AA7075 FLC showed the best formability with MRC 7075 FLC exhibiting slightly lower values. However, HRC 7075 exhibited significantly reduced formability. A higher concentration of the constituent particles is the contributing factor resulting in void formation due to breakage of particles during the deformation process.

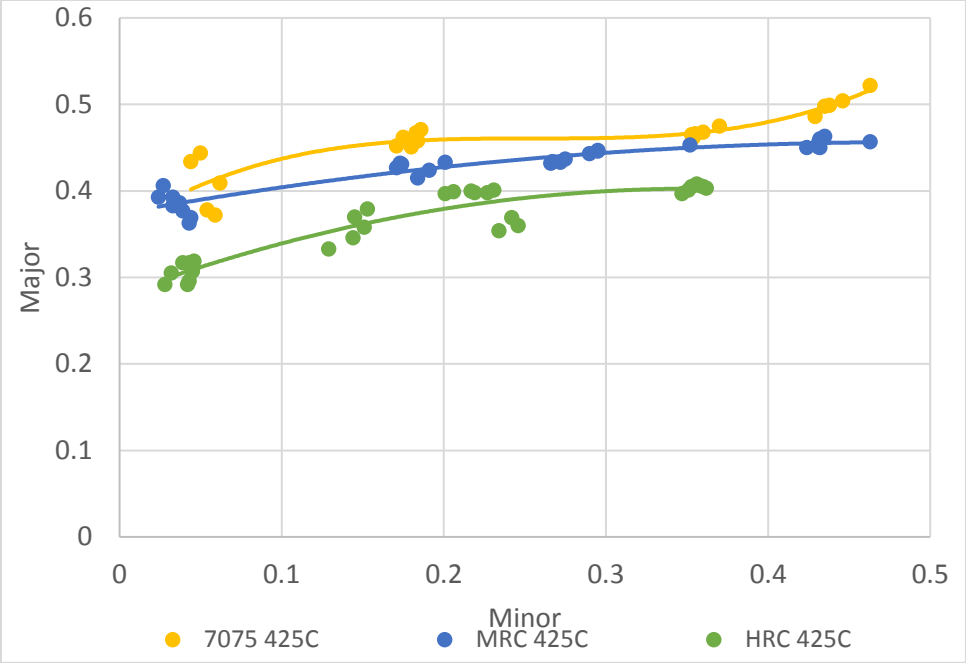

Figure 6-66. Right side of FLC for baseline 7075, MRC 7075 and HRC 7075 sheet materials at 425ºC.

It should be noted that the limit strains were significantly higher at 425ºC compared to 470ºC. This result is consistent with the results of elevated temperature tensile tests presented earlier. Some circular dot patterns at the apex of the dome that experienced larger deformation, and combined with the temperature effect, were difficult to detect using Argus (see Figure 6-67). Typically there was at least one good sample among the three replicates with limited missing information and Argus was able to extrapolate the information. The shape of the curve is dictated by the fitting method used in order to best fit the data points. Currently high degree polynomial function was used in order to create the best fit for only half (i.e. right hand side) of FLC.

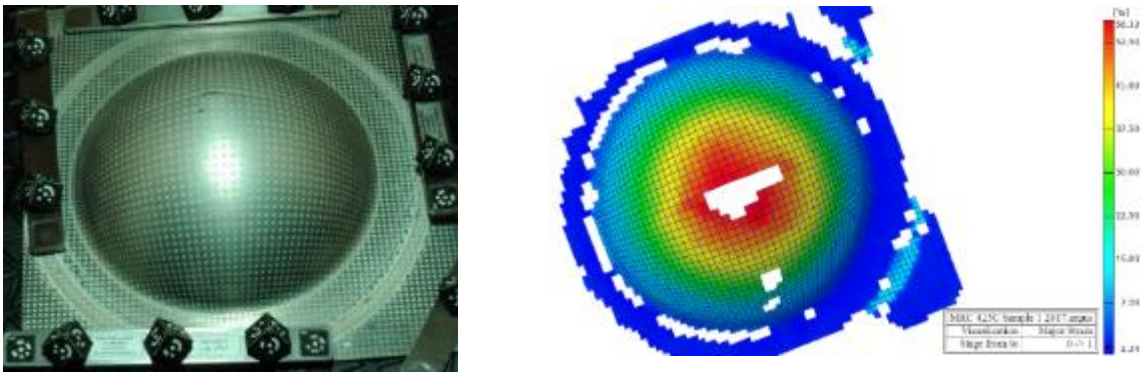

Figure 6-67. MRC 7075 hot gas bulge sample and corresponding major strain map at 425ºC.

6.2.4 Fractography of Equi-biaxial Bulge Test Samples of AA7075, MRC7075 and HRC7075 at 470ºC

Equi-biaxial sample tested at 470ºC were later cross-sectioned at the fractured location for AA7075, MRC7075 and HRC7075 and observed under the SEM. Figure 6-68 shows the through-thickness fractured surface of AA7075. The fracture in AA7075 appears to have more cleavage or brittle fracture as opposed to the cup and cone shaped ductile fracture in AA6111 sheet. When looking at the fracture surface at higher magnification, as illustrated in Figure 6-69, light grey particles could be observed at the fractured surface. EDX spectrum shown in Figure 6-70 indicates that the particles are Zn-Mg-Cu precipitates.

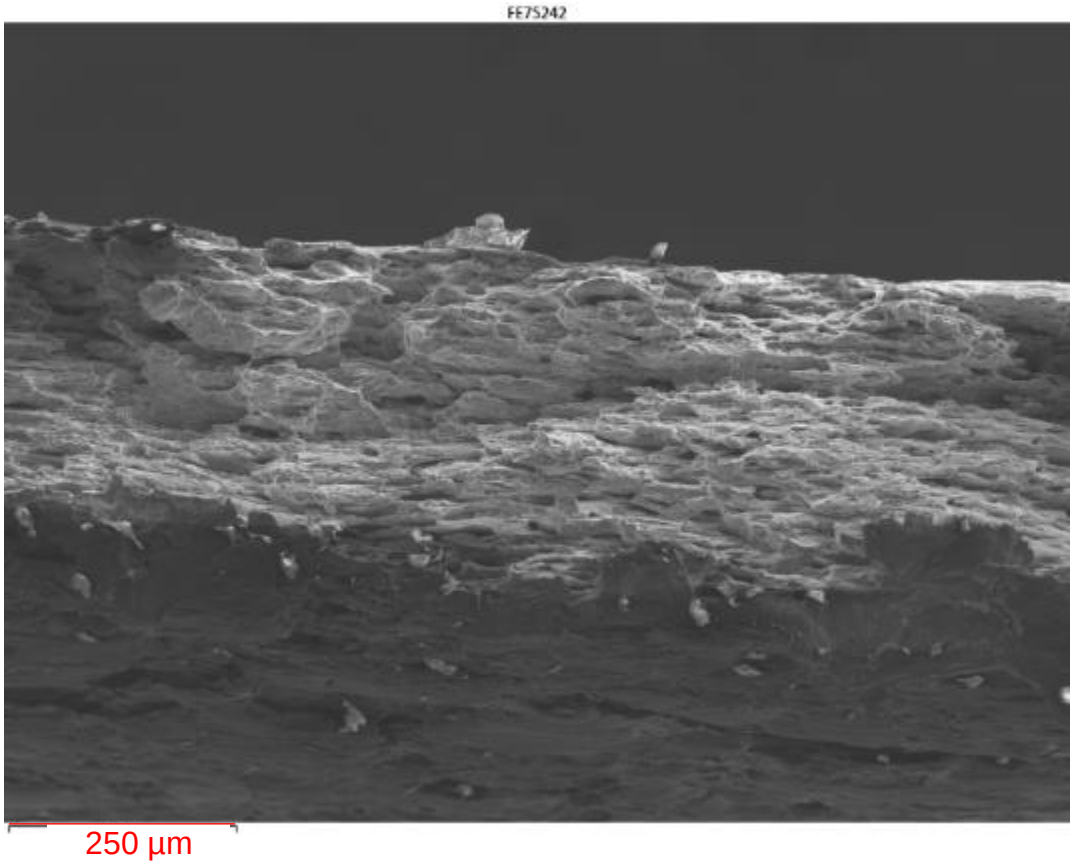

Figure 6-68. SEM image of equi-biaxial AA7075 fractured surface.

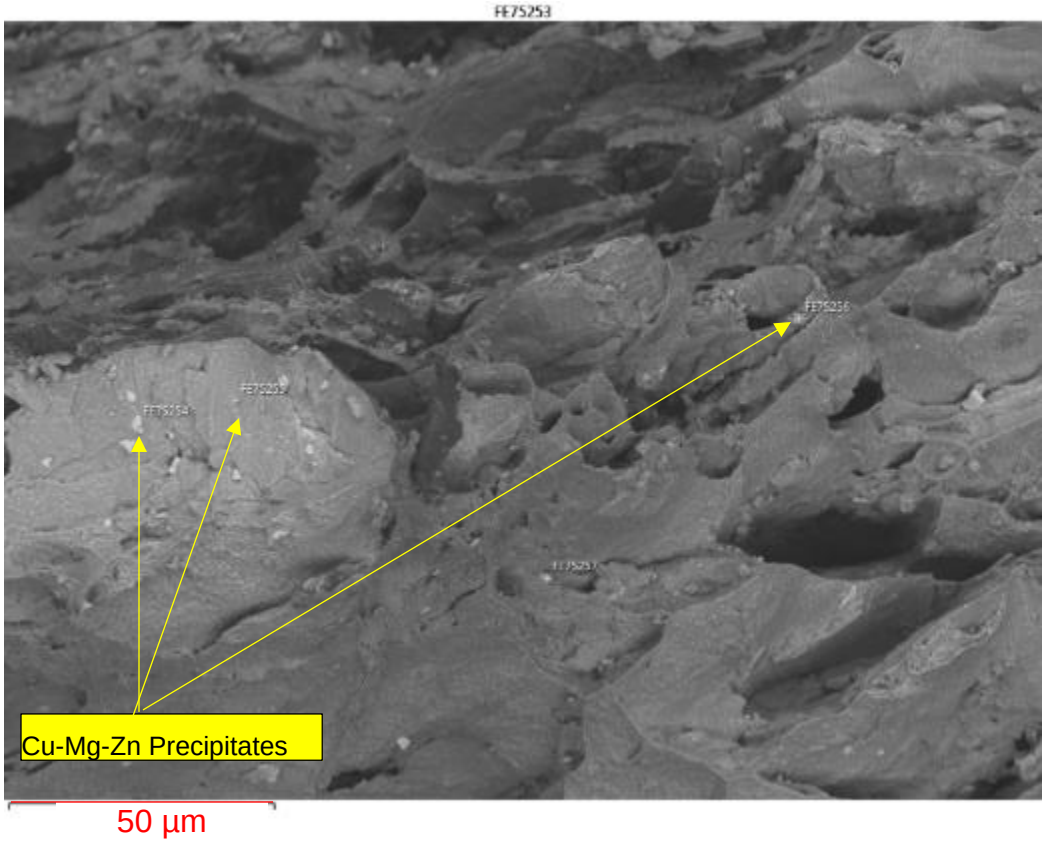

Figure 6-69. SEM image of equi-biaxial 7075 fractured surface.

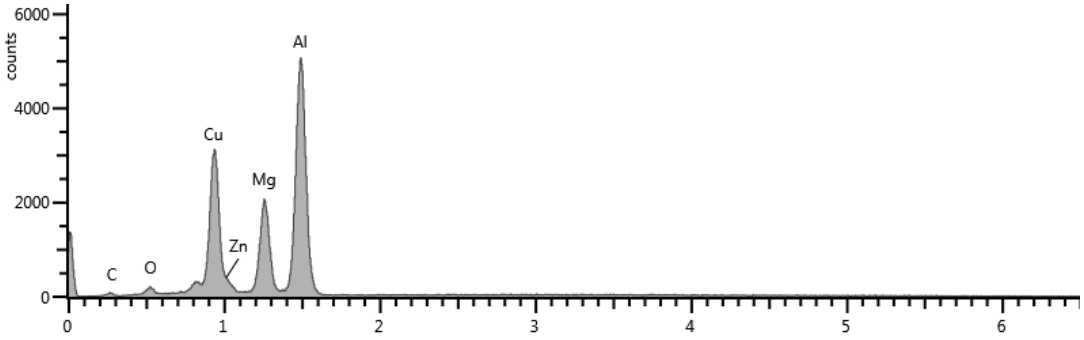

Figure 6-70. EDX spectrum showing composition of precipitates in 7075.

Figure 6-71 and Figure 6-72 show the fractured surface of MRC7075 equi-biaxial sample fractured at 470ºC at two different magnifications. Similar to the baseline AA7075 sample, the fractured surface has fewer ductile fracture features such as dimpled rupture. Once again, Mg-Cu-Zn precipitates were observed at the fractured surface. Moreover, there

were Fe containing particles observed at the fractured surface for MRC 7075, due to higher impurities present in this alloy compared to the baseline AA7075 sheet. EDX spectrum showing Fe containing particles found in MRC7075 is presented in Figure 6-73.

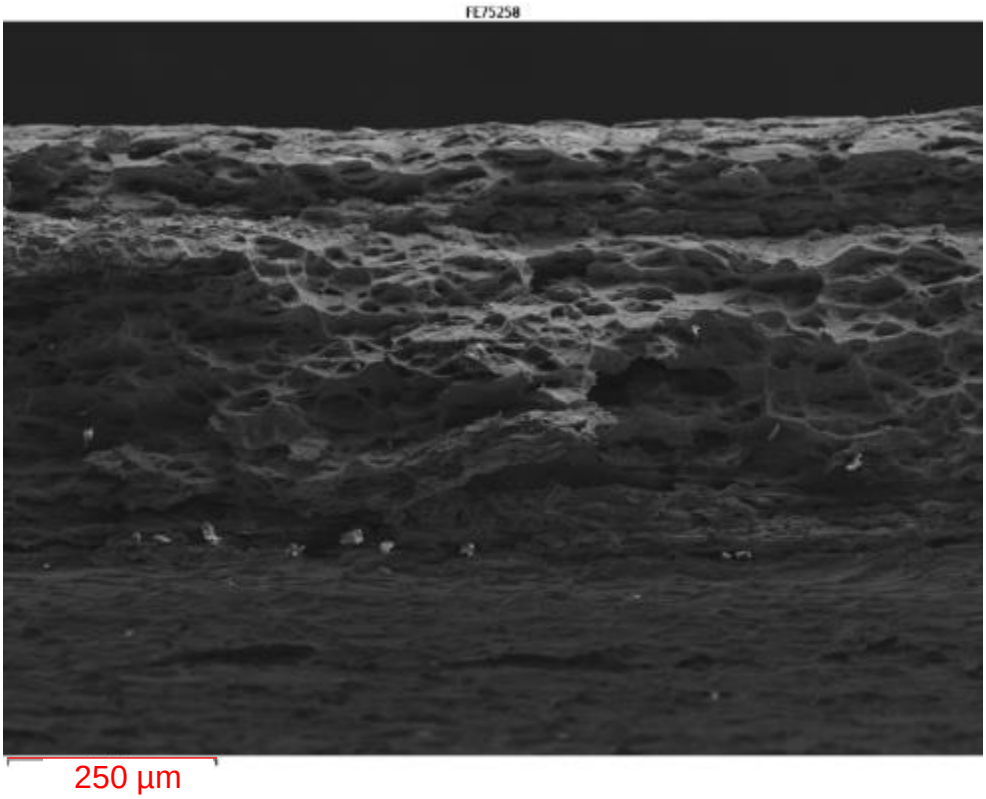

Figure 6-71. SEM image of fractured surface of an equi-biaxial bulge sample of MRC7075 sheet.

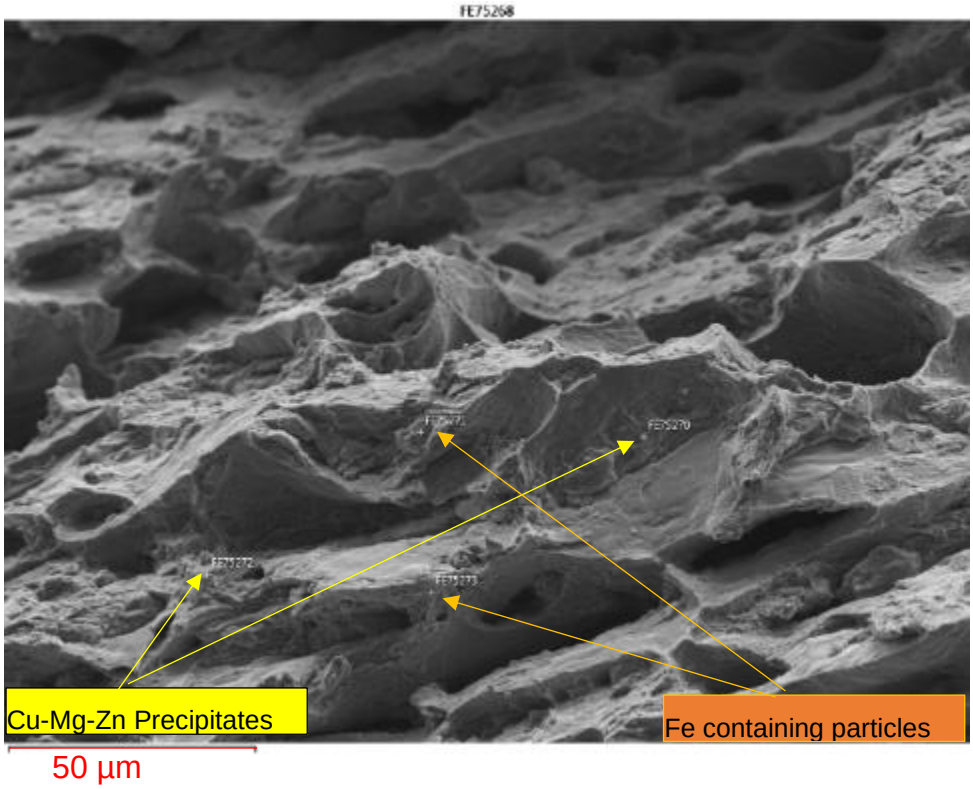

Figure 6-72. High mag SEM image of fractured surface of an equi-biaxial bulge sample of MRC7075 sheet.

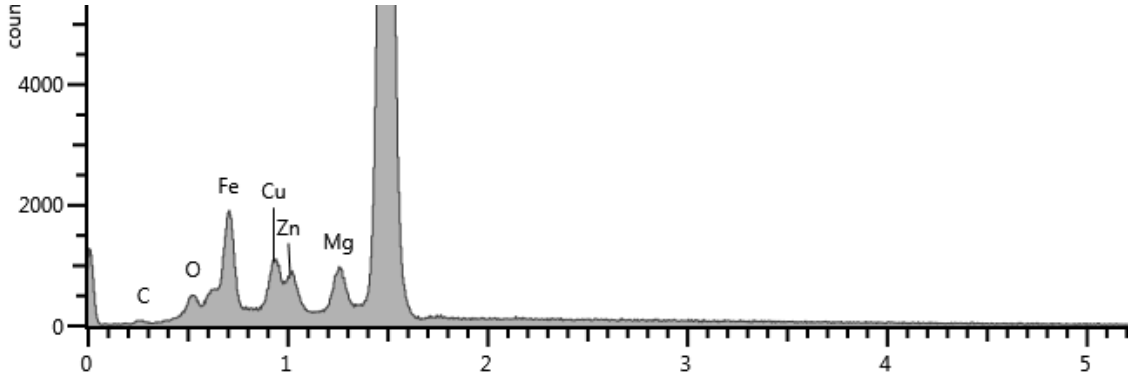

Figure 6-73. EDX spectrum showing Fe containing particles found in MRC7075.

Figure 6-74 and Figure 6-75 show the SEM images of fracture surface of equi-biaxial bulge samples of HRC7075 sheet. This variant of 7xxx sheet exhibited the least amount of ductile features compared to MRC7075 and Baseline AA7075 samples. More importantly, when looking at the fractured surface at higher magnification, Figure 6-75,

there are large micron sized intermetallic particles present at the fractured interface. Such a feature was not observed in the case of MRC7075 and baseline AA7075 sheet. EDX on the intermetallic particles, as shown in Figure 6-76, reveals the presence of Fe, Mn and Cr in the particles. Due to even higher additions of Fe, Mn and Cr compared to MRC7075 alloy, more intermetallic constituents were formed. Fractures appeared to be associated with these particles and resulted in reduced mechanical properties and formability, especially in the case of HRC7075.

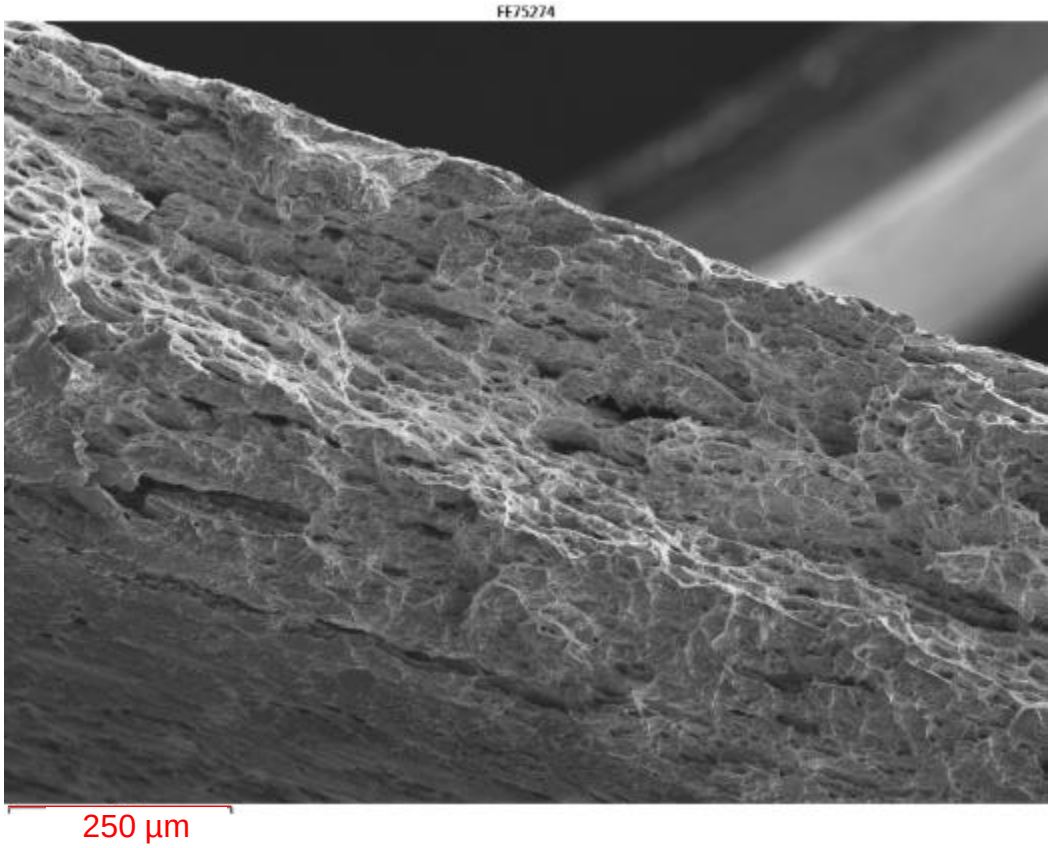

Figure 6-74. SEM image of fractured surface of equi-biaxial bulge specimen of HRC7075 sheet.

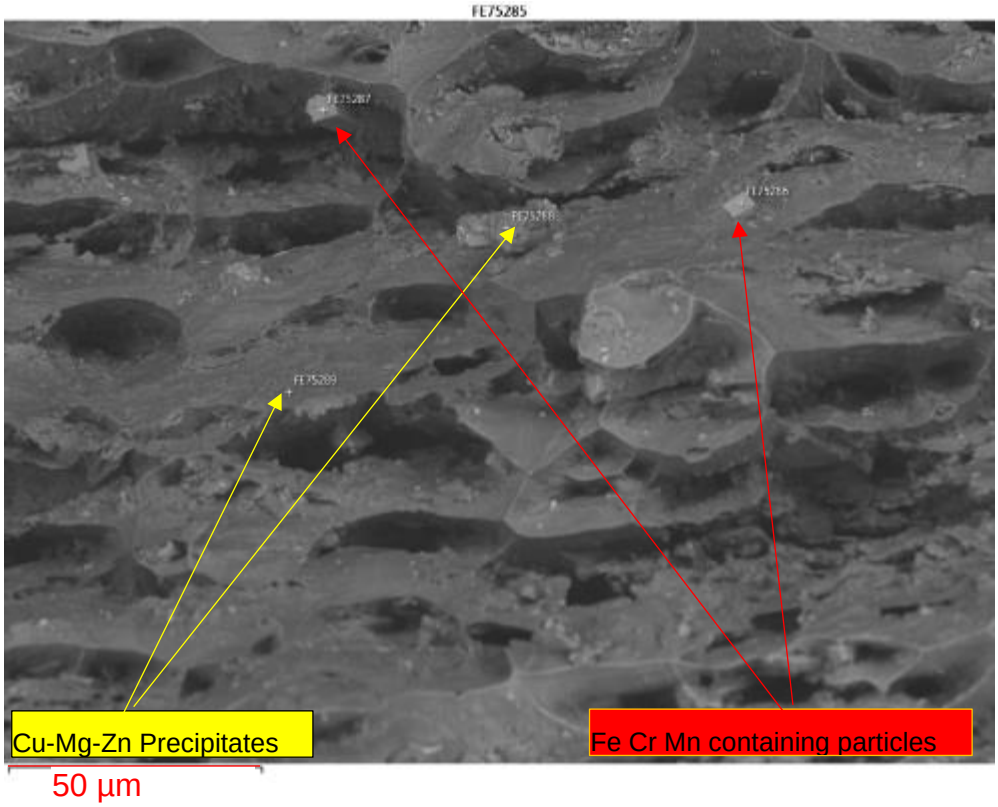

Figure 6-75. High mag SEM image of fractured surface of equi-biaxial bulge specimen of HRC7075 sheet.

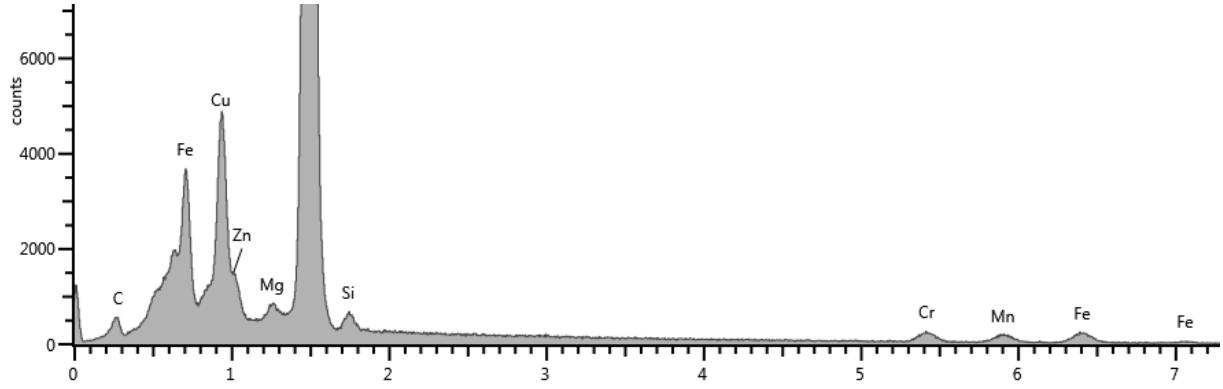

Figure 6-76. EDX spectrum from fractured surface of equi-biaxial bulge specimen of HRC7075 sheet showing Fe, Cr and Mn containing particles.

The fractured bulge samples were also cross-sectioned transversely across the fracture line, mounted, polished, and examined under optical microscope and SEM. Figure 6-77

shows the optical micrographs of AA7075 biaxial sample hot bulged to fracture at 470ºC. High magnification image shows that there are larger numbers of voids found in the sample. In addition to the tensile void formation, due to the relative slow strain rate, the sample sustained deformation at higher temperature for extended period of time, therefore, creep could have caused the voids to grow significantly.

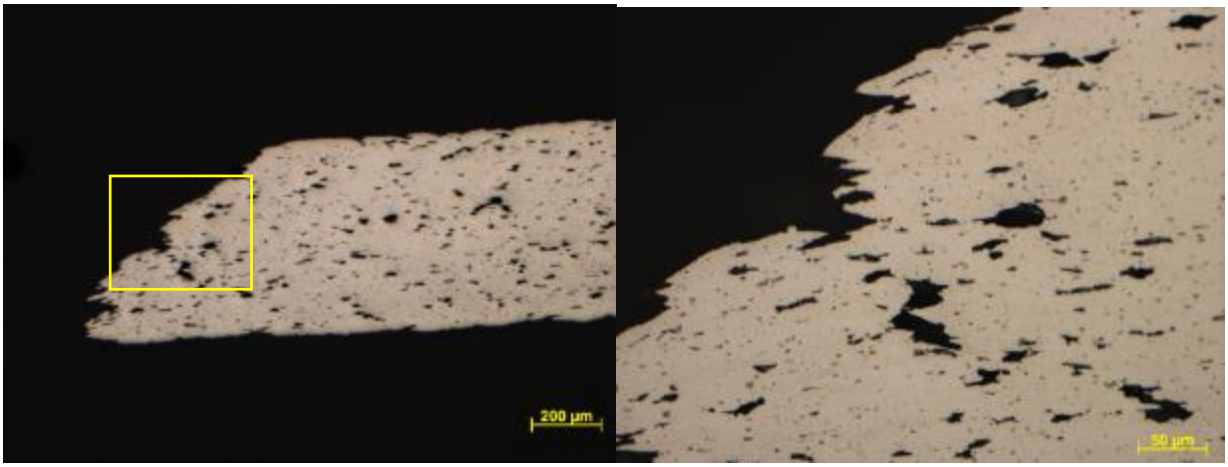

Figure 6-77. Through-thickness optical micrographs at two different magnifications of a AA7075 equi-biaxial hot gas bulge sample tested to fracture at 470ºC.

Figure 6-78 to Figure 6-80 show the BSE images of the same fractured location, further confirming a high density of voids formation. Figure 6-80 show high magnification image of the voids and EDX identifying different phases. It should be noted that the Cu-Mg-Zn precipitates are formed due to the slower air cooling of the sample from high temperature to the room temperature state. The T6 temper sample prepared in lab, on the other hand, was first transformed to super saturated solid solution (SSSS) state by a higher quench rate from water quenching and then subjected to artificial aging. Since the hot gas bulge sample was air cooled, one should assume the formation of precipitate was after the void had formed and did not contribute to the void formation as previously seen in the 6xxx

alloys. The void formation and growth is largely due to the Fe-Cu containing precipitates and a combination of biaxial tensile deformation and creep at elevated temperature.

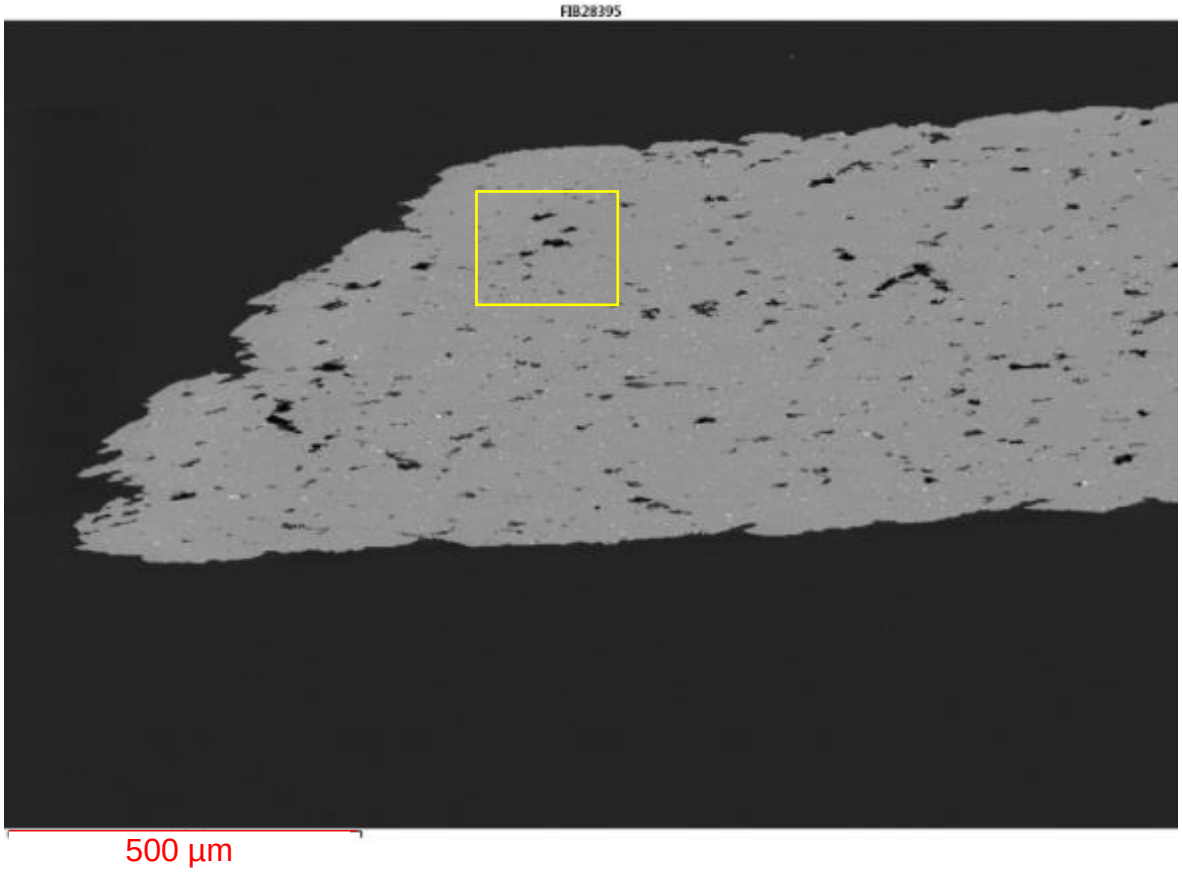

Figure 6-78: Lower magnification BSE Image of AA7075 biaxial hot gas bulge sample taken to fracture at 470ºC.

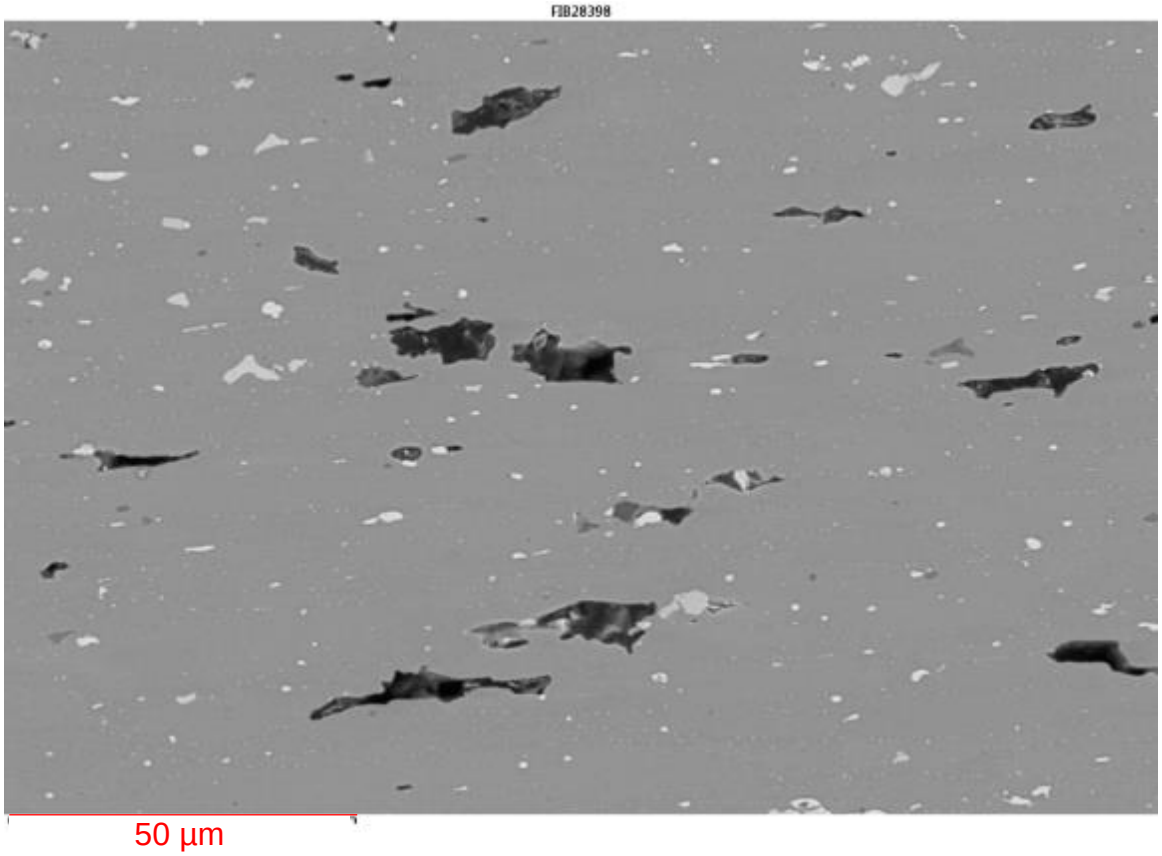

Figure 6-79. Higher magnification BSE image of AA7075 biaxial hot gas bulge sample taken to fracture at 470ºC.

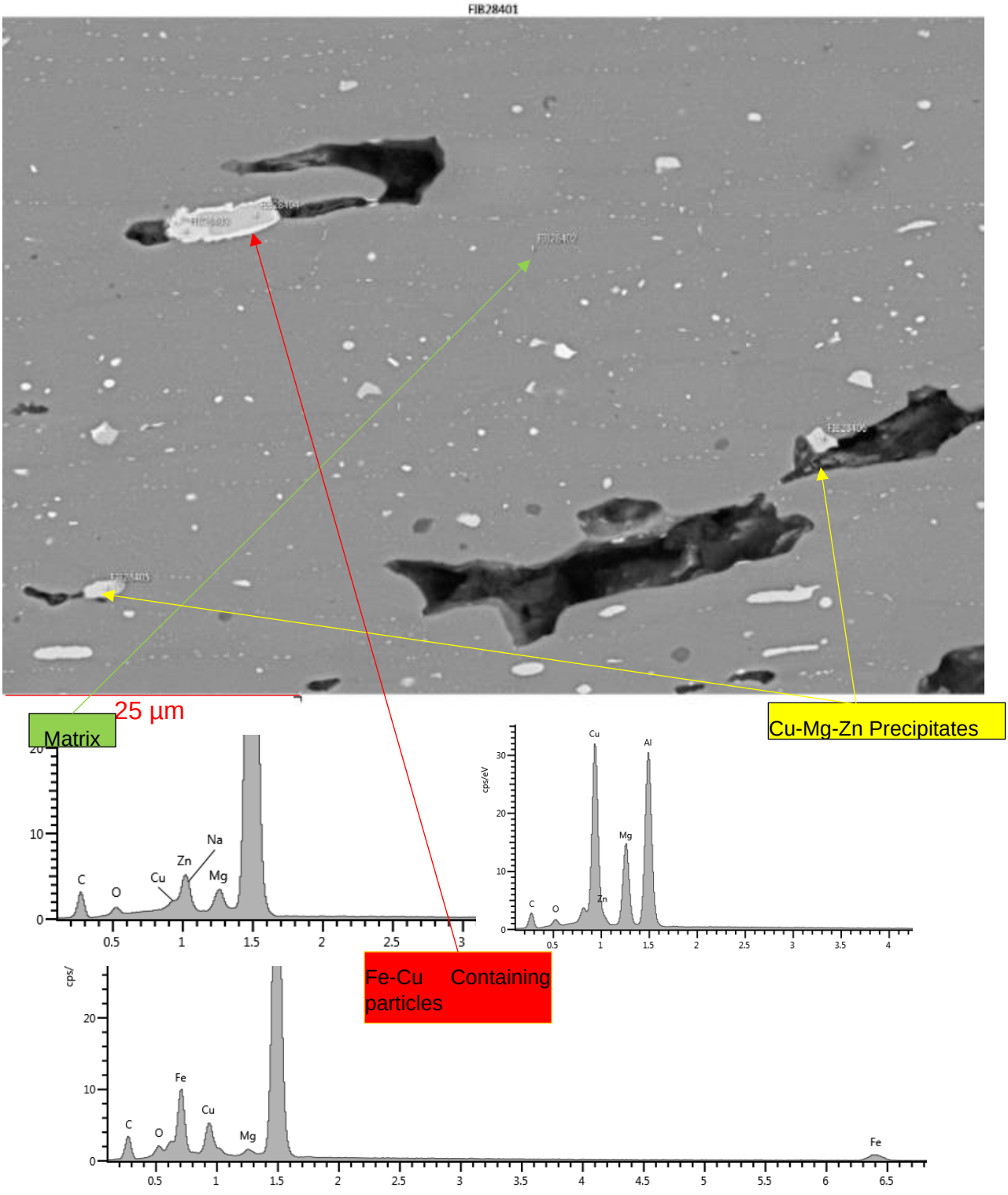

Figure 6-80. High magnification of AA7075 biaxial hot gas bulge sample fractured at 470ºC with EDX identification of the matrix and constituent phases.

Figure 6-81 shows the through-thickness optical micrographs from MRC hot gas bulge samples in the vicinity of fracture surface. Similar to AA7075, considerable void growth can be observed due to a combination of biaxial tensile deformation and high temperature creep. Figure 6-82 to Figure 6-84 shows the BSE images from the same region in the vicinity of fracture at increasingly larger magnifications respectively. As previous metallography have shown, particles containing Fe and Mn were present. The MRC7075 sheet metallography as shown in Figure 6-57 shows MRC version have higher number density of such particles, which would be detrimental to the alloy's strength and formability.

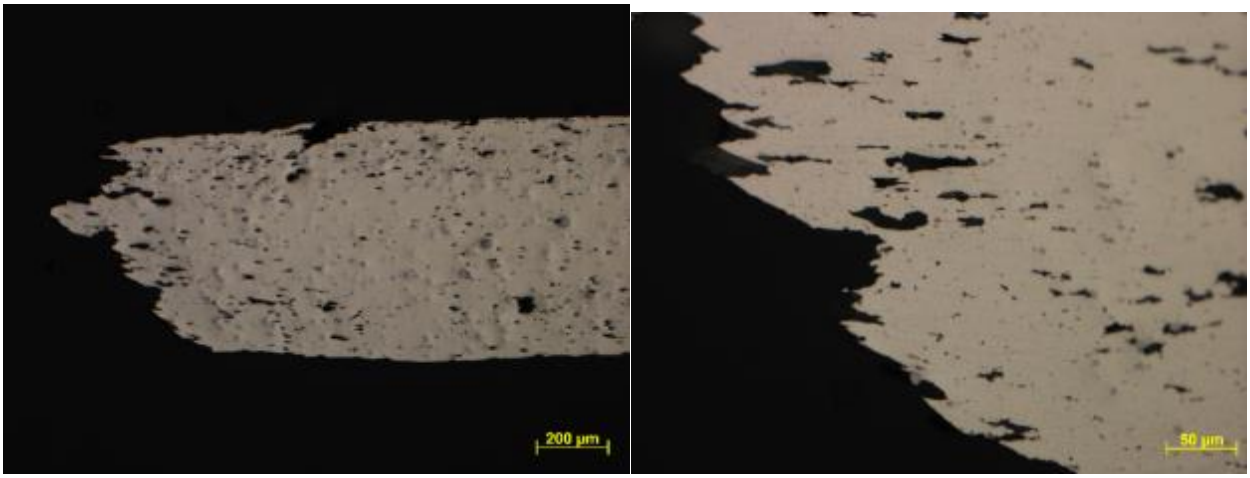

Figure 6-81. Through-thickness optical micrographs at two different magnifications of a MRC7075 equi-biaxial hot gas bulge sample tested to fracture at 470ºC.

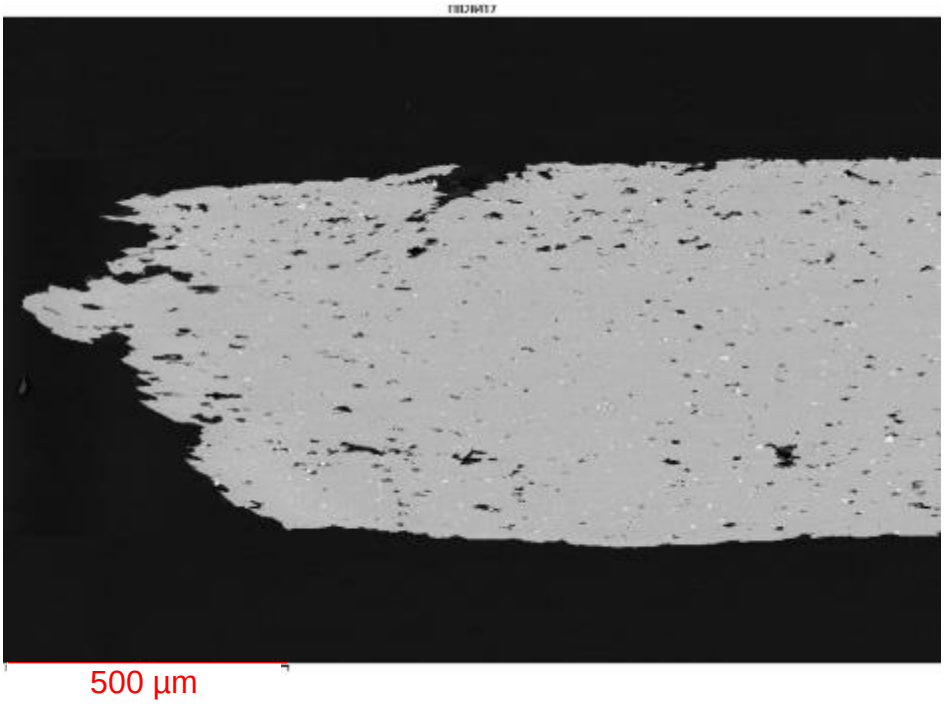

Figure 6-82. BSE Image of MRC7075 biaxial hot gas bulge sample tested to fracture at 470ºC.

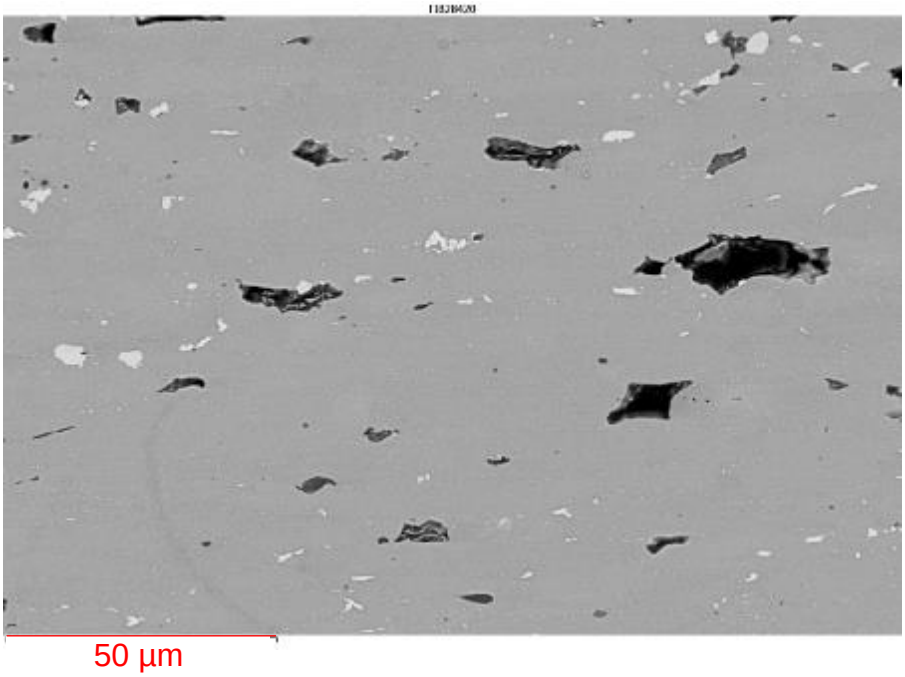

Figure 6-83. Higher magnification BSE image of MRC7075 biaxial hot gas bulge sample tested to fracture.

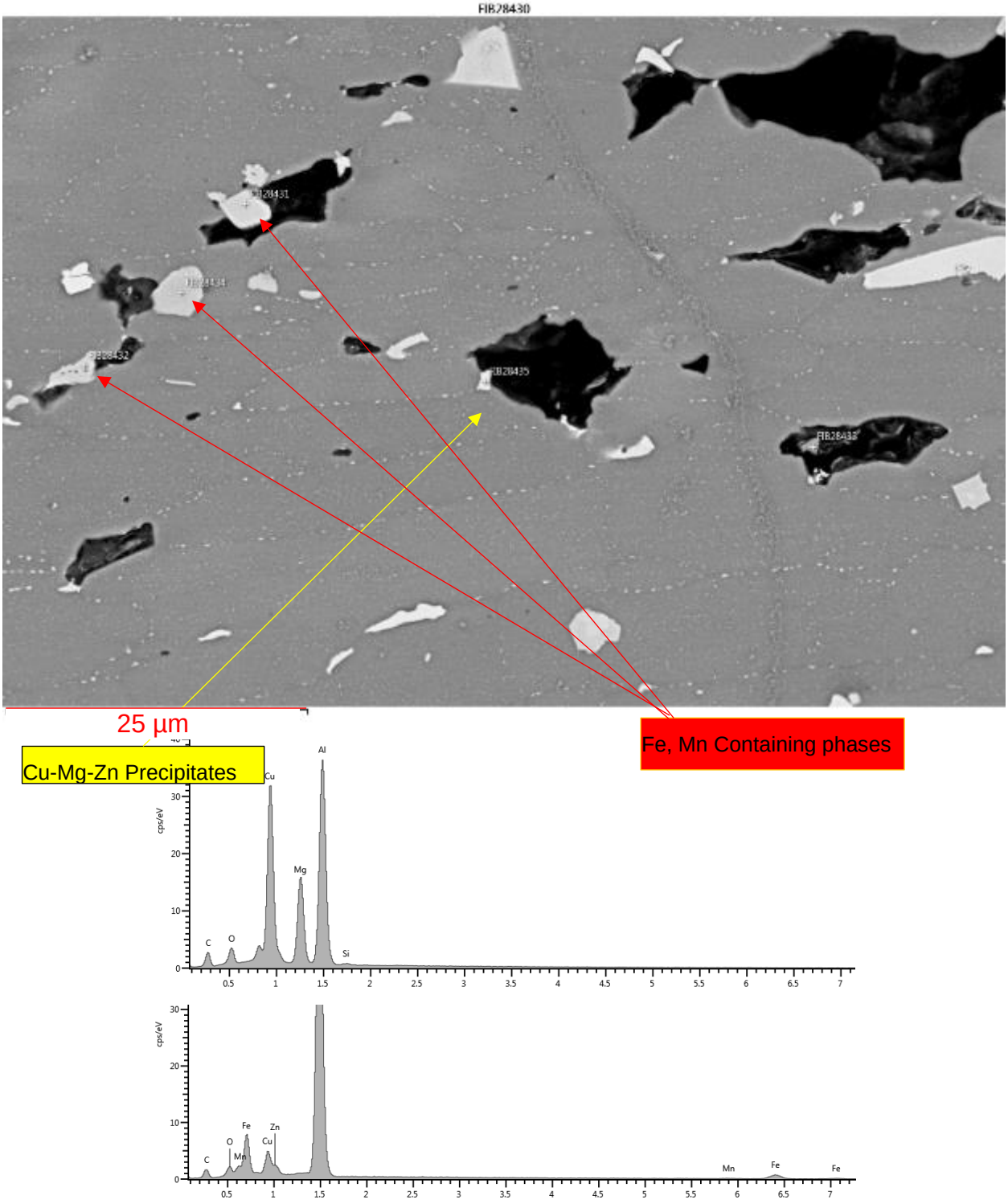

Figure 6-84. Higher magnification of MRC7075 biaxial hot gas bulge sample tested to fracture at 470ºC with EDX identification of the matrix and constituent phases.

Figure 6-85 to 6-87show the optical micrographs from a hot gas bulge sample of HRC7075 alloy taken to fracture at 470ºC. Similar to previous MRC7075 and AA7075, this bulge sample also showed a high density of void formation. EDX spectrum in Figure 6-88 indicates that HRC7075 has even higher numbers of Fe-Mn-Cr containing particles compared to MRC and baseline 7075 alloys.

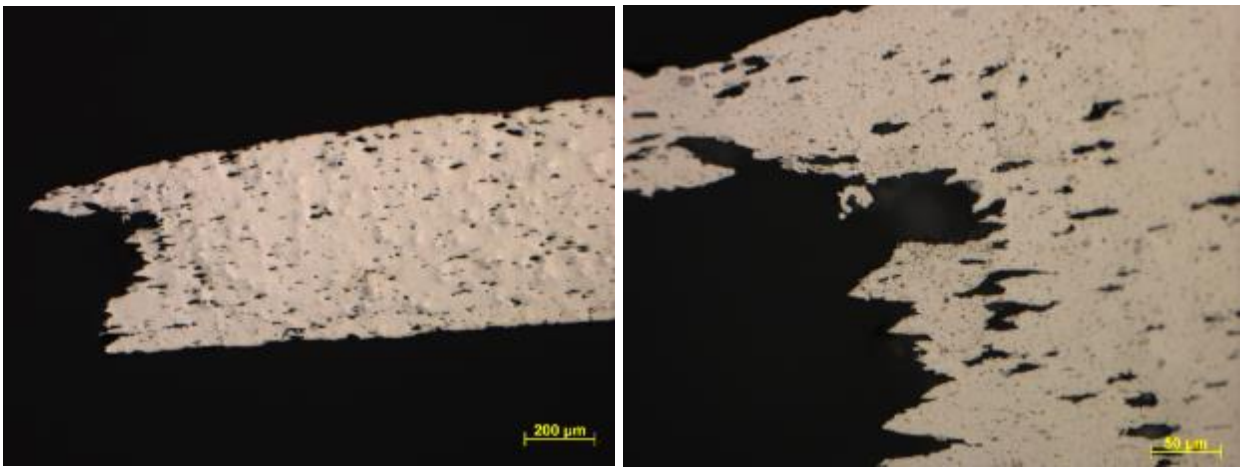

Figure 6-85. Through-thickness optical micrographs at two different magnifications of a HRC7075 equi-biaxial hot gas bulge sample tested to fracture at 470ºC.

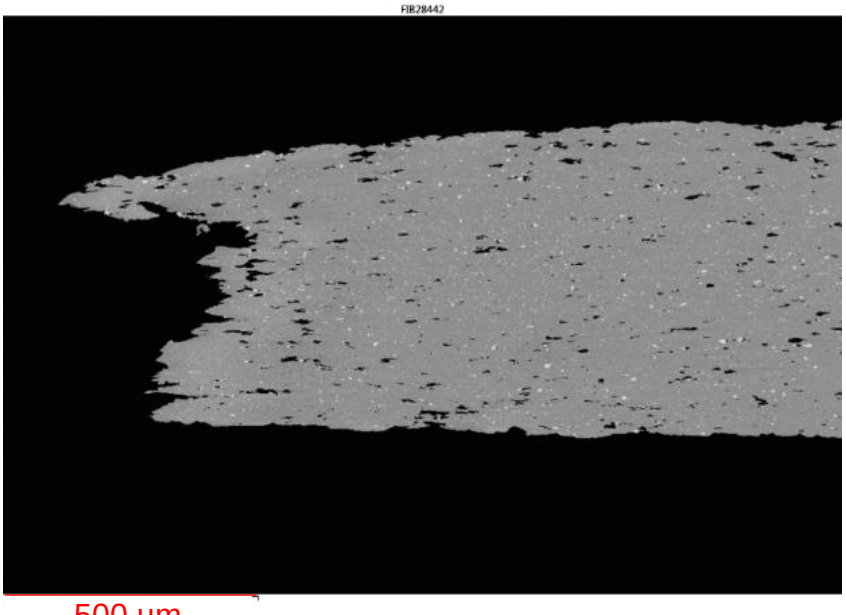

Figure 6-86. BSE image of a HRC7075 biaxial hot gas bulge sample taken to fracture at 470ºC.

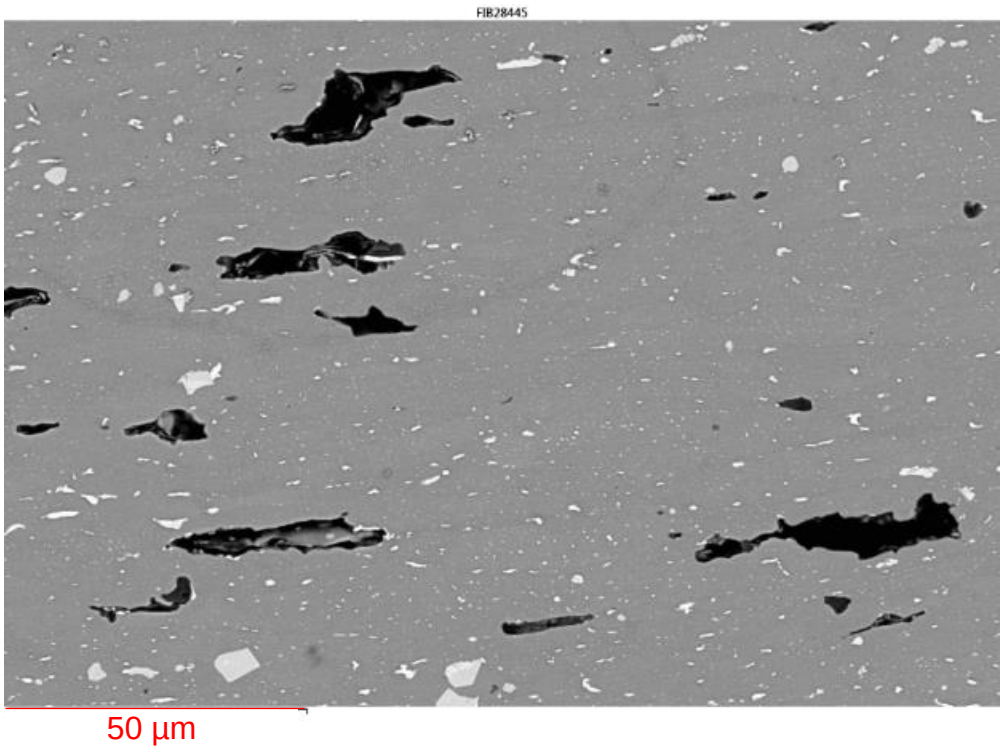

Figure 6-87. Large magnification BSE image of HRC7075 biaxial hot gas bulge sample taken to fracture at 470ºC.

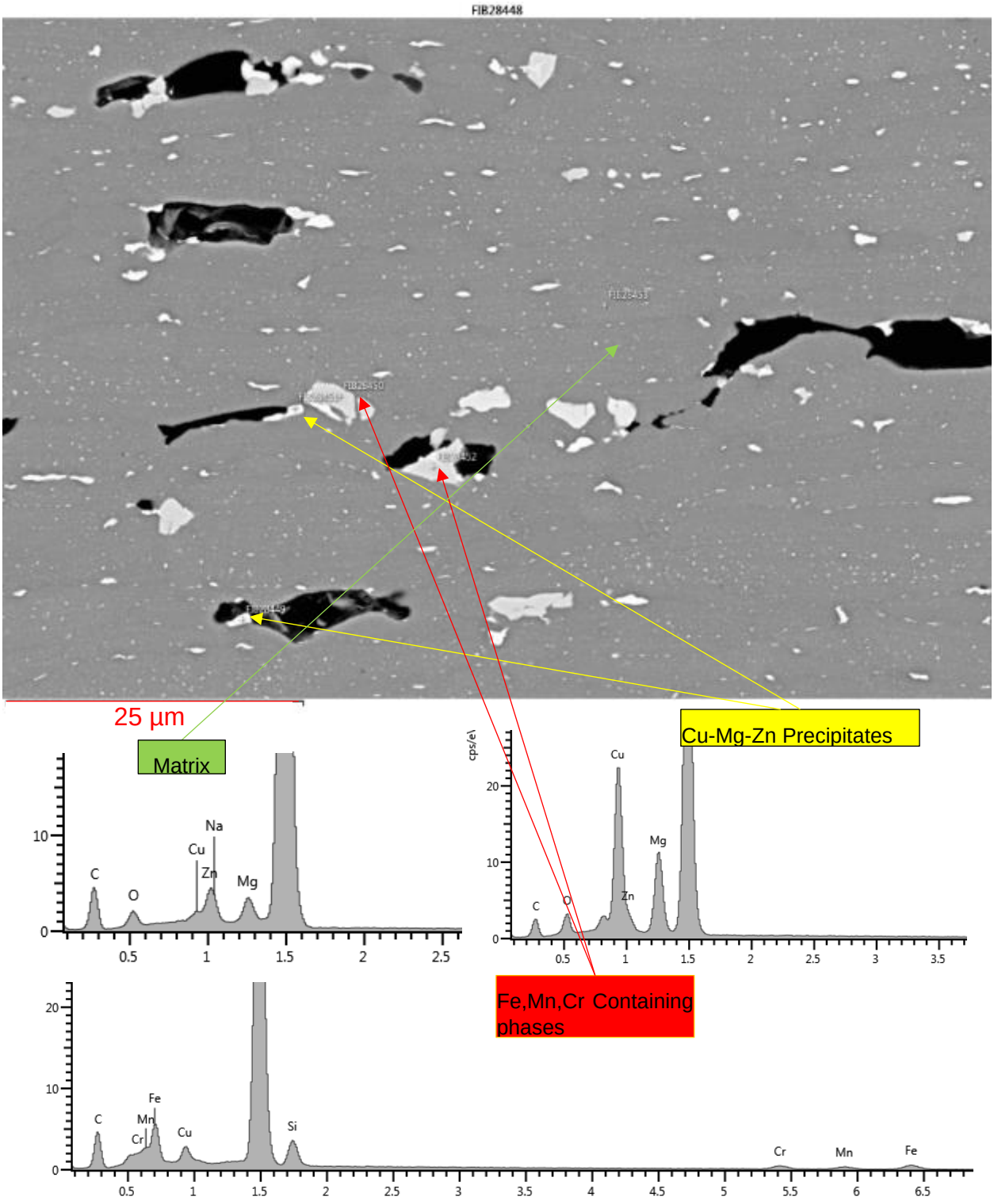

Figure 6-88. Still larger magnification of HRC7075 biaxial hot gas bulge sample taken to fracture at 470ºC with EDX identification of the matrix and constituent phases.

6.2.5 Elevated temperature FLCs using interrupted hot gas bulge tests

Interrupted bulge tests were conducted at 425ºC using baseline AA7075 by adding a pressure control valve to the bulge test system. The sample was spray painted with random (or speckle) pattern for strain measurement by more accurate DIC based Aramis full-field 3D strain measurement system. Partially formed bulge specimen was put into the gas bulge tester and subjected to incremental bulging to increased pressure levels. The sample was removed from the bulging unit after each incremental bulge for strain measurement. Once removed, the sample was placed in a fixed position and imaged using the Aramis system. The process was repeated until sample failure.

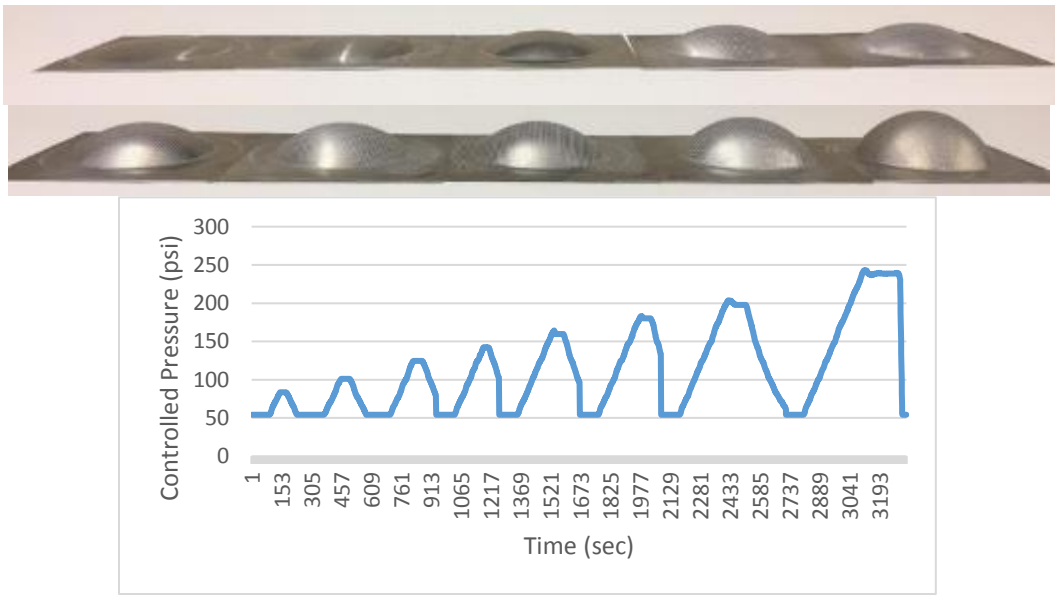

Figure 6-89. Photographs of a bulge test specimen and the pressure profile from interrupted bulge test.

Figure 6-89 presents the interrupted test scheme in the form of a set of photographs of some of the incremental bulges and the pressure profile from the test for demonstration purpose. There was only one sample used for the whole interrupted test. The stages of

the test were combined within the Aramis software to obtain a strain map and compared with the strain map obtained using Argus.

Figure 6-91 shows photographs of test specimens from continuous and final stage from interrupted tests. The two tests exhibit very similar shapes and strain characteristics. Figure 6-91 shows the sample strain maps in the final 2 stages which correspond to pressures of 240 psi and 245 psi. During the last few stages of interrupted test, the material experienced necking and had larger deformations compared to previous stages. Therefore, the pressure interval between the two interruptions was decreased to 10 psi. In the final stage, the sample was fractured, damaging the spray paint at the apex. Hence, there was a large area of missing information. With the limited information available from Aramis the major strain for fractured sample was between 52.5% and 61.47%. This result was compared with Argus test sample, which showed a major strain 56.3%. The two values thus were quite close to each other and hence validated the results obtained using the Argus system.

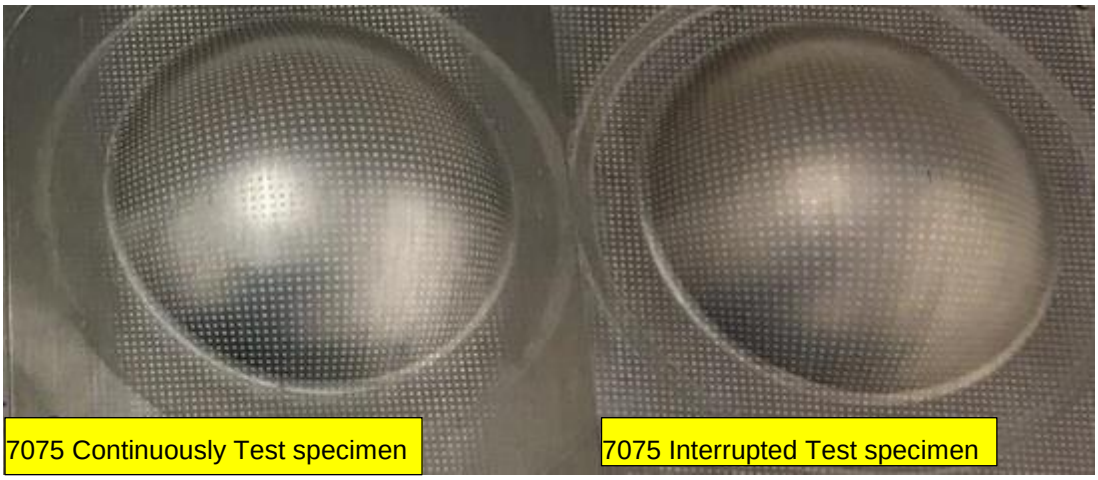

Figure 6-90. Comparison of baseline AA7075 equi-biaxial bulge specimens obtained using continuous and interrupted test methods.

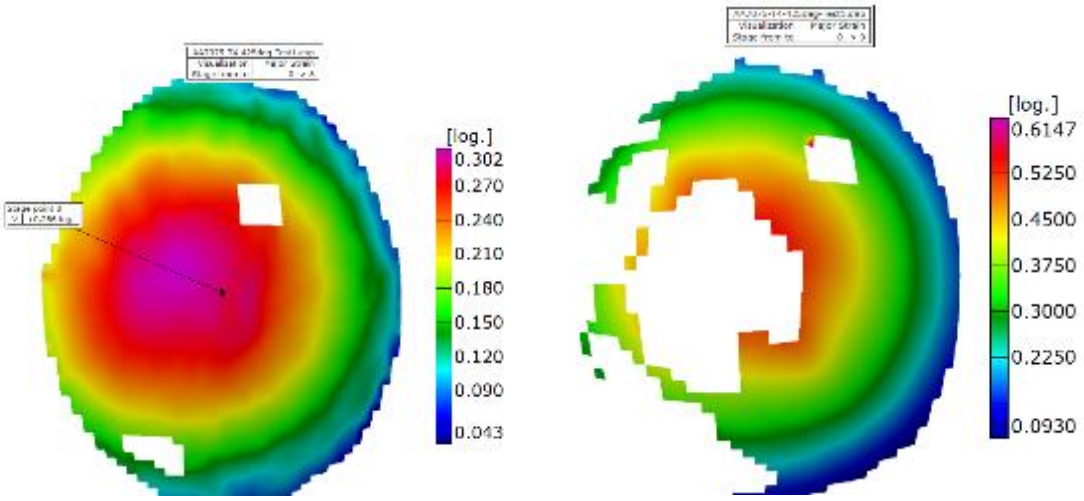

Figure 6-91. Comparison of major strain maps from last 2 images at the end of the test from baseline AA7075 equi-biaxial bulge specimen tested at 425ºC using the interrupted test method.

6.2.6 Hot Gas Forming FLC of AA7075 sheet at 425ºC with in-situ 2-Camera Aramis System

Continuous hot gas bulge test to fracture was also conducted on baseline AA7075 blank using the Macrodyne press. This system was equipped with a larger circular hot gas bulge die in an environmental chamber and an on-line 3-D (2-camera) Aramis DIC strain measurement system. Also, the system offered an accurate control of the gas pressure. Figure 6-92 shows speckle-patterned sample tested on Macrodyne press. The sample was tested to failure at ~180 psi.

Figure 6-92. Photographs of two bulged samples of baseline 7075 sheet tested at 425ºC using Macrodyne press.

The strain map of various stages during the deformation was captured using Aramis and illustrated by step in Figure 6-93. The strain prior to fracture had a major strain of 0.474 which was similar to the strain map obtained using the CGA based post-test strain measurement in Argus. The minor differences could be caused by strain rate difference between the two testing apparatus and variation between samples.

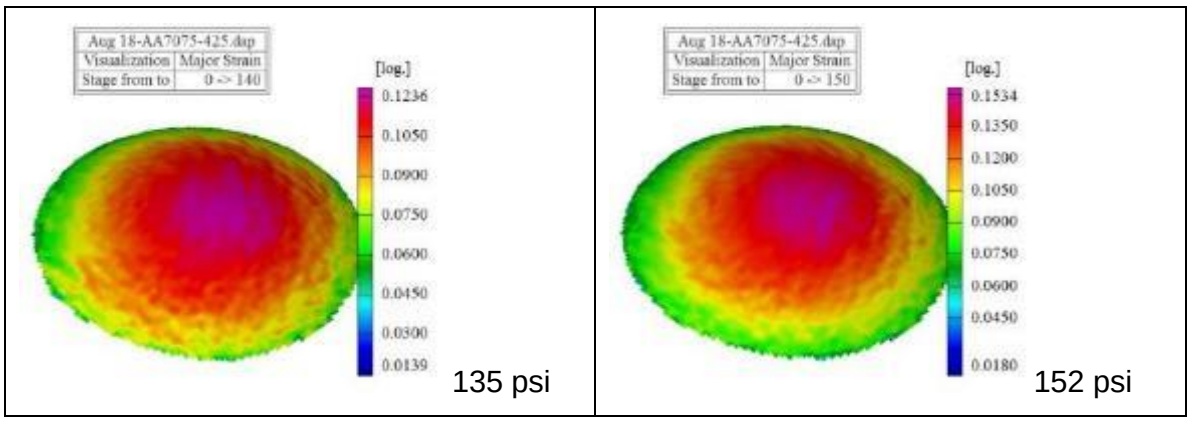

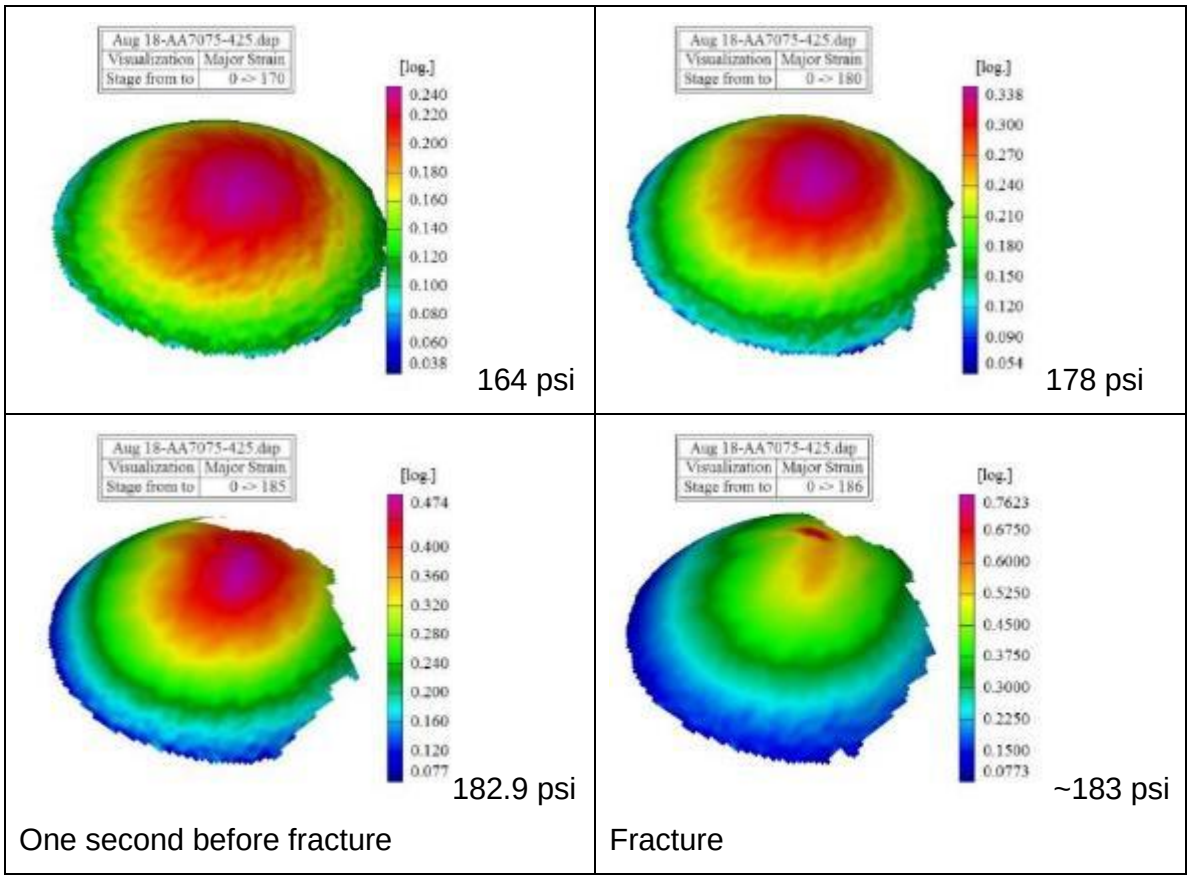

Figure 6-93. Major strain maps of baseline 7075 bulged samples from Macrodyne press at 425ºC.

After conducting the hot gas bulging tests, the average value of effective stress can be calculated on the basis of the force equilibrium of a small circular element at the center of a membrane from:

$$\sigma_{eff} = \frac{p \cdot R}{2 \cdot t}$$

where p is the bulging pressure, and R and t are the radius of curvature and the thickness of the pole of the dome, respectively. The corresponding thickness strain or biaxial strain can be evaluated by implementing the principal of volume constancy as

$$\varepsilon_{maj} + \varepsilon_{\min} + \varepsilon_t = 0$$

$$\varepsilon_t = -(\varepsilon_{maj} + \varepsilon_{\min})$$

$$\varepsilon_{eff} = -\varepsilon_t = \ln\left(\frac{t_0}{t}\right)$$

Where ε_{maj}, ε_{min} and ε_{eff} are major, minor and effective strains respectively at the pole of the dome. With this information, one could calculate the effective stress and strain of the samples.

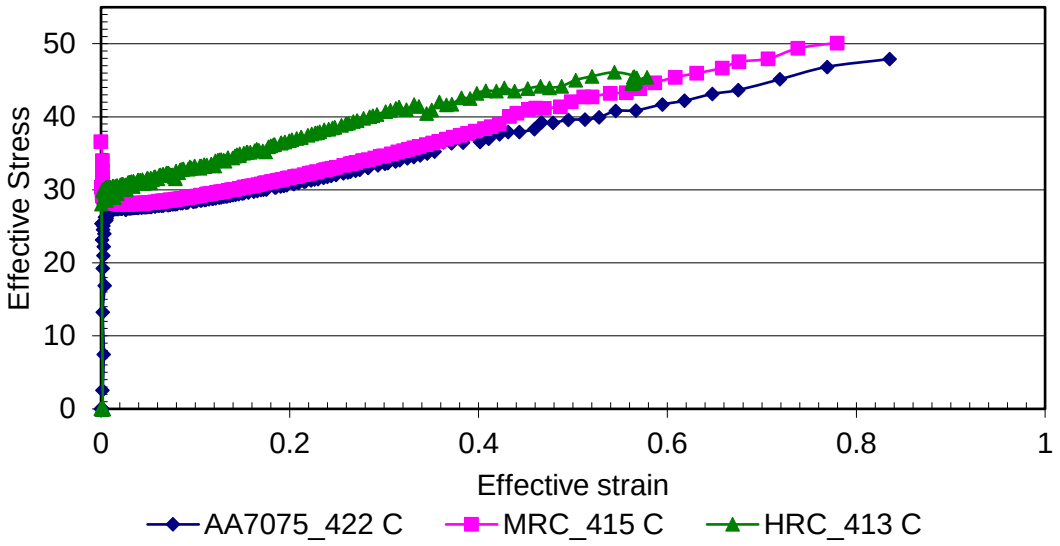

Figure 6-94 Effective stress and strain calculated for AA7075, MRC7075 and HRC7075.

Figure 6-94 shows the effective stress and strain curve for AA7075, MRC7075 and HRC 7075 respectively. Though the temperature was slightly off for MRC and HRC, which were lower than the target forming temperature of 425ºC. The effective stress between the three alloys were comparable, the minor deviation could be caused by the temperature difference. But one should assume the trend for these alloys is consistent with previous mechanical property results as well as their FLC. Which AA7075, had the highest formability (i.e. effective strain) followed by MRC7075 and HRC7075 showed the worst in terms of formability.

6.2.7 Comparison of FLCs of different AA7075 sheets at 425ºC and 470ºC

The FLCs of three 7075 sheet materials from previous sub-sections are re-plotted in Figure 71 for comparison purposes. The FLCs were consistently higher at 425ºC (i.e., lower test temperature) compared to those at 470ºC for all 3 variants of 7075 sheet in this study. It is to be noted that the trend in decreased limit strain as a function of increased test temperature was similar to the trend in decreased uniaxial tensile elongation with increased temperature for 7xxx for the three 7xxx variants.

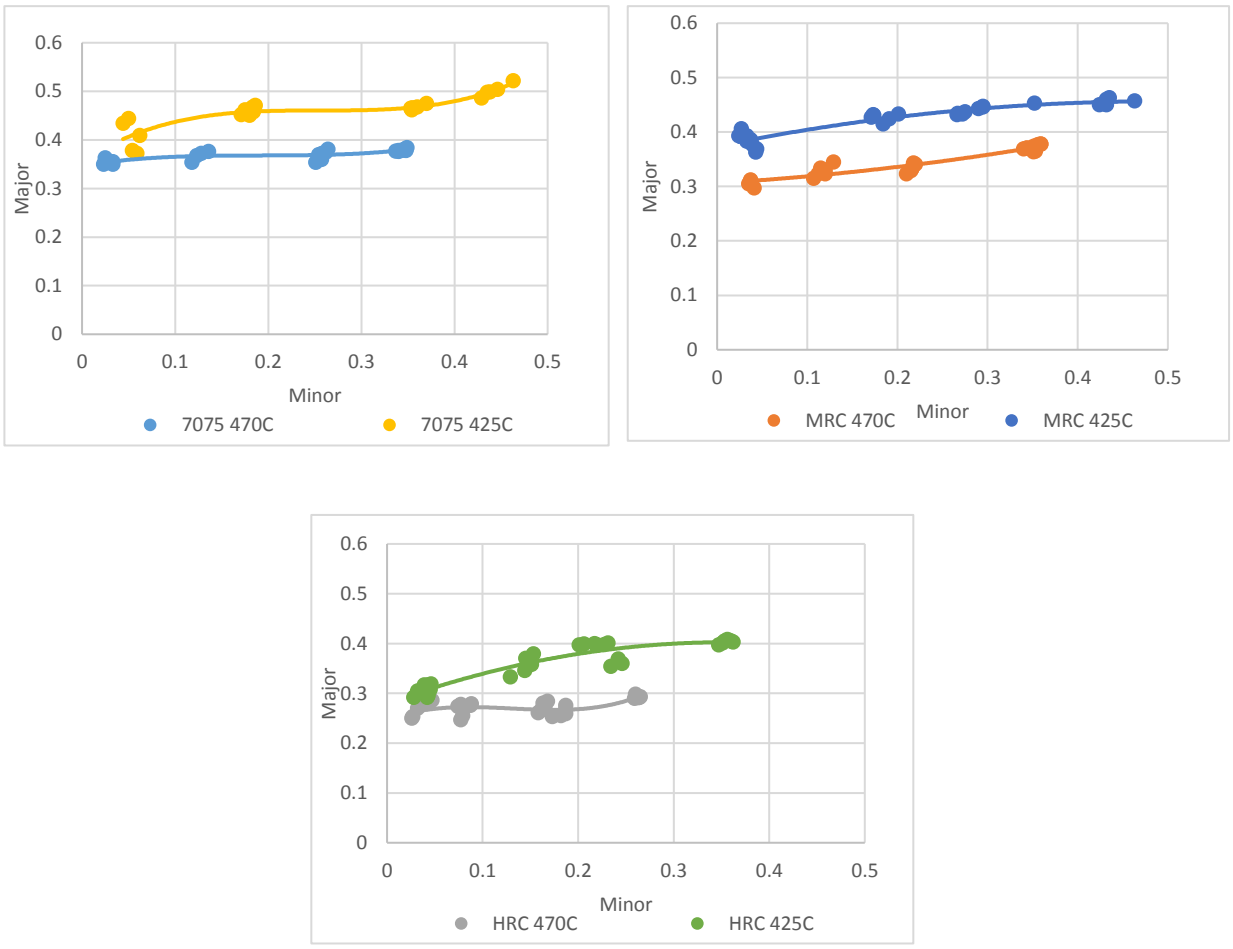

Figure 6-95. Comparison of FLCs of baseline 7075, MRC 7075 and HRC 7075 FLC at 425ºC and 470ºC.

6.3 Comparison of 7xxx and 6xxx series aluminum alloys.

The precipitation hardening aluminum alloys from 6xxx and 7xxx series have different chemical compositions, precipitation phases, uniaxial tensile properties. Also, their formability differs significantly at room temperature. In the present study, it was shown that:

- Both alloys including their recyclable variants showed improved formability at elevated temperature making them suitable for elevated temperature forming process.
- In both alloys, increasing impurity content increased the number of constituent particles that were present in the alloy, which led to lower strength and decreased formability.
- Based on their respective FLCs, recyclable variants at lower levels of impurity can be effectively used to produce warm formed automotive components.

7. Summary and Conclusions

Automotive alloys, AA6111 alloy with its one recyclable variant, and AA7075 alloy with its two levels of recyclable variants, were cast, homogenized, hot and cold rolled, and subsequently heat-treated to produce sheets in the T82 and T6 temper states. The material microstructure was characterized extensively during different stages of processing via various experimental techniques involving composition analysis, phase characterization, grain size measurements. Mechanical properties of benchmark AA6111 and AA7075 were evaluated at different temper and elevated temperature formability as well as those of recycle content variants were investigated and compared. Elevated temperature biaxial tensile FLDs were obtained using hot gas bulging experiment and a range of dies with elliptical and circular opening to attain different strain paths. The fracture surface of bulge specimens for the AA6111 and AA7075 sheets (and their variants) was examined by SEM fractography. In addition, SEM imaging and EDX analysis of polished through-thickness sections in the vicinity of fracture was carried out to further investigate the nature of void initiation, growth and fracture. Tensile elongations were also correlated with the biaxial tensile FLDs. The following conclusions can be drawn from this study.

[1]. Recyclable variant of AA6111 with increased Fe, Mn and Cr had finer as cast grain size and T82 grain size compared to the baseline AA6111. The average grain size for AA6111 and HRC6111 were 39 and 21µm respectively.

[2]. Increasing Fe, Mn and Cr content in AA6111 led to lower mechanical properties in T4, T82 as well as at elevated temperature in T82. Yield strength was 6% lower in T4 and

15% lower in T82. The strength drop in T82 is more prominent due to the fact more Si was taken to form the intermetallic particles containing Fe, Mn, Cr. The amount of Si that is available becomes limited to form the strengthening Mg_2Si.

[3]. Even though the bendability of HRC6111 sheet was lower than the bendability AA6111 sheet, both variants met the target r/t value of 0.4 typically requested by Automotive companies. The decrease in bendability was largely due to presences of more constituent particles and transformation from β to α type particles.

[4]. The elevated temperature elongations of baseline AA6111 and HRC6111 T82 sheet were comparable to the room temperature tensile elongations in T4 condition and significantly increase compared that of T82 in room temperature, making these alloy capable of warm forming automotive components in their final temper.

[5]. Elevated warm forming temperature FLDs were determined for baseline AA 6111 and its recyclable variant. The FLD at 300ºC was higher than the room temperature formability in T4 temper condition typically used in automotive stamping. The FLD could be used for future simulation work when designing 6xxx alloys for warm forming.

[6]. Increased amounts of Fe, Mn and Cr in the alloy composition of MRC and HRC variants of 7075 ally compared to the baseline 7075 alloy led to increase in number of constituent particles and reduced mechanical properties. Yield strength in T6 were dropped by 4.8% and 7.3% compared with AA7075 for MRC7075 and HRC7075 respectively. The higher recycle content form more secondary constituent phases, these phases are unable to be dissolved during the Solution heat treat practice and hence cause more void nucleation and resulted in the strength drop.

[7]. Currently, it is not possible to stamp automotive parts at room temperature in the T6 temper state due to the high strength and low elongation (~10% total). Baseline AA7075 and its two recyclable variants exhibited increased formability at elevated temperatures then at room temperature. This will enable production of higher strength parts at elevated temperatures in the F temper state, i.e., via a hot forming process. Forming at elevated temperature dramatically increases the formability to 0.3-0.35% in the plain strain state.

[8]. Baseline AA7075 and its two recyclable variants (MRC and HRC) showed decreased forming limits at 470ºC compared to 425ºC. The formability of AA7075 was hinder by grain boundary sliding at higher temperature. This phenomenon was observed in high temperature tensile test and by other researchers (Weimin, et al., 2014).

[9]. The elevated temperature forming limits of recyclable variants of baseline AA7075 sheet decreased progressively with increased content of minor alloying elements. Thus, MRC7075 sheet exhibited higher forming limits compared to the HRC 7075 sheet. However, the forming limits of MRC7075 were only slightly lower than the baseline AA7075 sheet. The results were consistent with the elevated temperature tensile properties. MRC7075 offers a good recyclable material for elevated temperature automotive part forming to obtain higher strength automotive parts.

[10]. Elevated temperature forming limits using two different approaches were compared; (i) continuous bulge tests to necking or fracture and post-test strain measurements with the Argus system using period grids and (ii) interrupted tests and DIC based strain measurement using 2-camera Aramis system were compared. Similar limit strains were achieved from these two approaches, confirming the applicability of both methods for

elevated temperature FLD determination, depending upon the availability and cost of the forming equipment.

8. Future Work

The present work focused on role of the microstructure in terms of constituent particle characteristics and the damage arising from them during the elevated temperature plastic deformation and forming processes in high strength automotive alloys from 6xxx and 7xxx series and their recycling variants. The forming limit was determined from elevated temperature uniaxial tensile testing (a single tension-compression strain path in the forming limit diagram space) as well as plane strain and biaxial tension testing (i.e., right side of the FLD). Following suggestions are made for future studies on elevated temperature forming of high strength automotive aluminum alloys.

[1]. Complete left hand side (i.e., tension-compression region of the FLD) should be obtained in the future to ensure that the conclusions are valid for this important forming region as well, so that the new alloys become more acceptable to stamping industry for elevated temperature part forming.

[2]. There is a need for a more exhaustive quantitative study to relate microstructure to elevated temperature formability of the various alloys and their recyclable variants explored in the future. Such a study will help develop a family of recyclable high strength alloys in a more systematic manner rather than somewhat arbitrary selection of desirable alloy compositions.

[3]. There is a need for developing a suitable mathematically model that can relate experimentally observed qualitative and quantitative microstructural data and observations to elevated temperature uniaxial tensile deformation and forming limits of high strength automotive aluminum alloys. Such a model can help with prediction of

elevated forming limits based on microstructural characteristics of the alloys to guide alloy development and forming process development for such alloys.

[4]. Uniaxial tensile tests as well as hot gas bulge forming experiments were conducted at rather slow test speeds and gas pressurization rates respectively. The effect of test speed and gas pressurization rate on uniaxial tensile test results and FLDs respectively should be studied in the future.

[5]. Determination of FLDs at elevated temperature has been a challenge in the present work. The forming test methods that have been refined for room temperature FLD determination over the years should be more efficiently adapted to elevated temperature FLD determination to reduce cost and time in the future. Development of an international standard for elevated temperature FLD determination will be a good first step.

9.References

Anderson David Forming Limit Curve Measurement, Detection, Representation [Report]. - Kennesaw : Novelis Inc, 2016.

Association Aluminum International Alloy Designations and Chemical Composition Limits for Wrought Aluminum and Wrought Aluminum Alloys [Report]. - Arlington : The Aluminum Association, 2009.

Beckermann C. [Book Section] // Encyclopedia of Materials: Science and Technology. - [s.l.] : Elsevier Science Ltd., 2001.

Beckermann C. Encyclopedia of Materials Science and Technology 1st Edition [Book Section] // Macrosegregation / book auth. Buschow K. H. Jürgen [et al.]. - [s.l.] : Pergamon, 2001. - Vols. 4733-4738.

C.W.Fulton Effect of Small Amounts of Impurities in Alcan Alloys [Report]. - Kingston : Alcan, 1968.

Chemin Aline [et al.] Influence of Al7Cu2Fe intermetallic particles on the localized corrosion of high strength aluminum alloys [Journal]. - Sao Carlos : Materials and Design, 2014. - 118-123 : Vol. 53.

Cikmis A. Talic, Pepelnjak T. and Hasanbegovic S. Experimental determination of forming limit diagram [Conference] // 14th International Research/Expert Conference. - [s.l.] : TMT 2010, 2010.

Cui Jirang and Roven Hans J. Recycling of automotive aluminum [Journal]. - Trondheim : Trans. Nonferrous Met. Soc. China, 2010. - 2057-2063 : Vol. 20.

Ducker Aluminum in Cars [Report]. - [s.l.] : EAA Brochure, 2012.

G. Mrowka-Nowotnik J. Sieniawski, M. Wierzbinska Intermetallic Phase Particles in 6082 Aluminum Alloy [Journal]. - Rzeszow : Materials Science and Engineering, 2007. - 2 : Vol. 28.

GOM GOM Home Page [Online] // http://www.gom.com/3d-software.html.

Graf Alejandro and Hosford William The Influence of Stain-Path changes on Forming Limi Diagrams of AA6111 T4 [Journal]. - Ann Arbor : International Journal Mechanical Science, 1993. - 10 : Vol. 36.

Graf Alejandro The Influence of Strain-Path Changes on Forming Limit Diagrams of Al 6111 T4 [Journal] // Int. J. Mech Sci. - 1994. - pp. 897-910.

Haiou Jin and D.J.Lloyd Roping in 6111 Aluminum alloys with arious iron contents [Journal]. - Kingston : Materials Science and Engineering A, 2005. - 403 : Vols. 112-119.

Hirsch Jurgen Recent development in aluminum for automotive applications [Journal]. - Bonn : Transactions of Nonferrous Metals Society of China, 2014. - Vol. 24.

Hua Huang, Dayong Li and Yinghong Peng Experimental study on the forming limit diagrams (FLD) of 7075-T6 aluminum alloy sheet at warm state [Journal]. - Shanghai : Journal of Plasticity Engineering, 2010. - 1 : Vol. 17.

Keeler S. and Backhofen W. Plastic instability and fracture in sheet stretched over rigid punches [Journal]. - [s.l.] : ASM Transactions Quarterly, 1964. - 25-48 : Vol. 56.

Kuijpers N.C.W. Assessment of different techniques for quantification of a-Al(MfMn)Si and b-AlFeSi intermetallics in AA 6xxx alloys [Journal] // Materials Charaterization. - 2003. - pp. 409-420.

Li Daoming and Ghosh Amit K. Biaxial warm forming behavior of aluminum sheet alloys [Journal] // Journal of Materials Processing Technology. - 2004. - pp. 281-293.

Li Daoming Tensile deformation behavior of aluminum alloys at warm forming temperatures [Journal] // Materials Science and Engineering. - 2003. - pp. 279-286.

Lievers W.B. The influence of iron content on the bendability of AA6111 sheet [Journal] // Materials Science & Engineering A. - 2003. - pp. 312-320.

M. Kumar N. Sotirov, C.M. Chimani Investigations on warm forming of AW-7020-T6 alloy sheet [Journal]. - Ranshofen : Journal of Materials Processing Technology, 2014. - Vol. 214.

Marciniak Z. and Kuczynski K. Limit strains in the processes of stretch forming sheet metal [Journal]. - [s.l.] : International Journal of Mechanical Sciences, 1967. - 609-620 : Vol. 9.

Mitukiewicz G. [et al.] A new method of determining forming limit diagram for sheet materials by gas blow forming [Journal]. - Hamilton : Journal of Materials Processing Technology, 2014. - 2960-2970 : Vol. 2014.

Mohamad On the thermodynamic stability of intermetallic phases in the AA6111 aluminum alloy [Journal] // Computer Coupling of Phase Diagrams and Thermochemistry. - 2006. - pp. 159-170.

Nakazima K., Kikuma T. and K Hasuka Study on the formability of steel sheets [Journal]. - [s.l.] : Yawata Technical Report , 1968. - 8517-8530 : Vol. 264.

NHTSA NHTSA CAFE Standard [Online] // NHTSA. - Environmental protection agency, 2016. - June 19th, 2017. - https://www.nhtsa.gov/laws-regulations/corporate-average-fuel-economy.

Rombach Integrated assessment of primary and secondary aluminum production [Journal]. - Surrey : DMG Business Media Ltd, 1998.

Rometsch Paul A., Zhang Yong and Knight Steven Heat treatment of 7xxx series aluminum alloys- Some recent developments [Journal]. - Clayton : Transactions of Nonferrous Metals Society of China, 2013. - 2003-2017 : Vol. 24.

S. Mahabunphachai M. Koc Investigations on forming of aluminum 5052 and 6061 sheet alloys at warm temperatures [Journal]. - Richmond : Materials and Design, 2010. - Vol. 2010.

Sarkar J. [et al.] Tensile properties and bendability of T4 Treated AA6111 Aluminum Alloys [Journal]. - Hamilton : Materials Science and Engineering A, 2004. - 258-266 : Vol. A369.

Shumei Wang Shanshan Chen, Kenji Matsuda, Tokimasa Kawabata, Junya Nakamura, Susumu Ikeno, Koji Kawakita, Hidetoshi Takagi and Tomokazu Yamashita Effect of Mn or Fe Addition on Age-Hardening Behaviour of Al-Mg2Si Alloys [Journal]. - [s.l.] : Materials Transactions, 2012. - 8 : Vol. 53.

W.B.Lievers, Pilkey A.K. and Lloyd D.J. The influence of iron content on the bendability of AA6111 Sheet [Journal]. - Kingston : Materials Science and Engineering, 2003. - 312-320 : Vol. A361.

Wang Hui Luo Yingbing, Peter Priedman, Chen Minghe, Gao Lin Warm Forming Behavior of High Strength Aluminum Alloy AA7075 [Journal]. - [s.l.] : Trans. Nonferrous Met. Soc. China, 2012. - Vol. 22.

Wang Shumei [et al.] Effect of TM-Addition on the Aging Behaviour of Al-Mg-Si Alloys [Journal]. - Toyama : Materials Transactions, 2011. - 2 : Vol. 52.

WARDSAUTO 2014 WARDSAUTO, Dupont Automotive Trends Benchmark Study [Report]. - Troy, MI : [s.n.], 2014.

WARDSAUTO 2015 WARDSAUTO Survey [Report]. - [s.l.] : Dupont, 2015.

Weimin Zhuang, Dechuang Cao and Hui Ye Prediction of FLC for AA7075 under hot stamping based on continuum damage mechanics [Journal]. - [s.l.] : Jornal of Jilin University, 2014. - 2 : Vol. 44.

10. Appendix

Strain Measurement Data from hot gas bulge tests for the different sheet materials, bulge geometries and temperatures from Argus and Aramis systems.

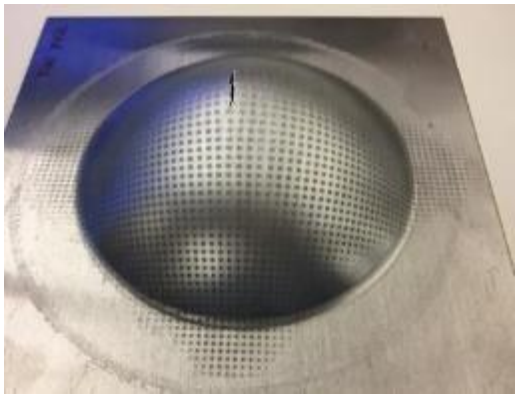

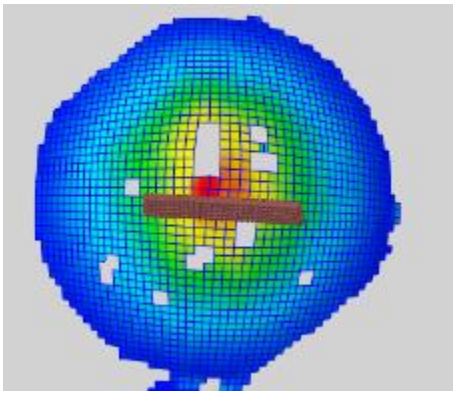

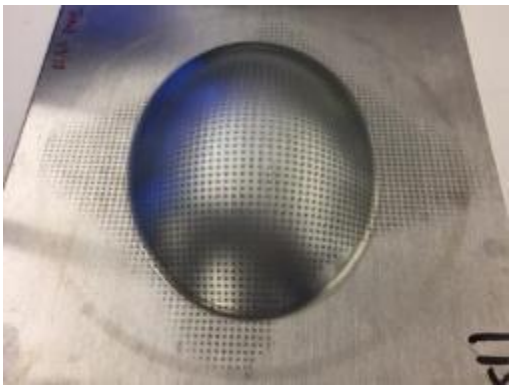

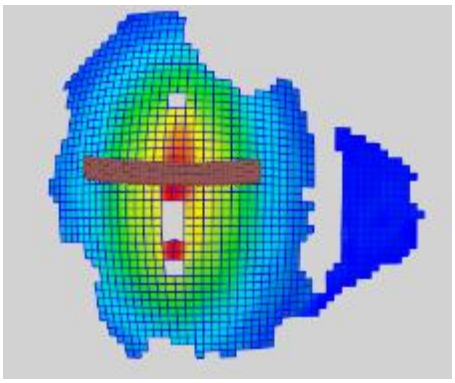

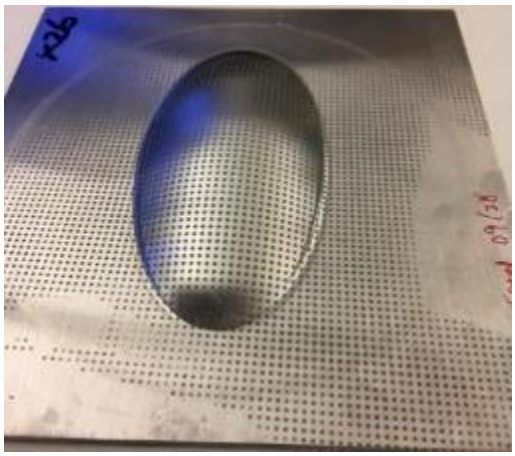

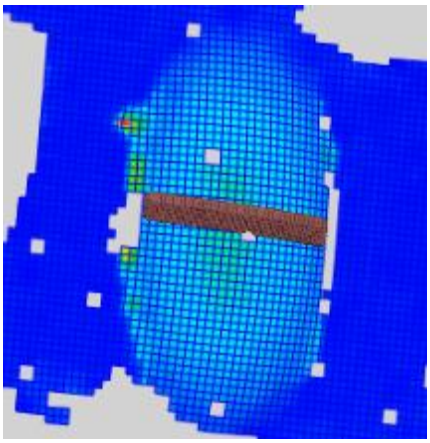

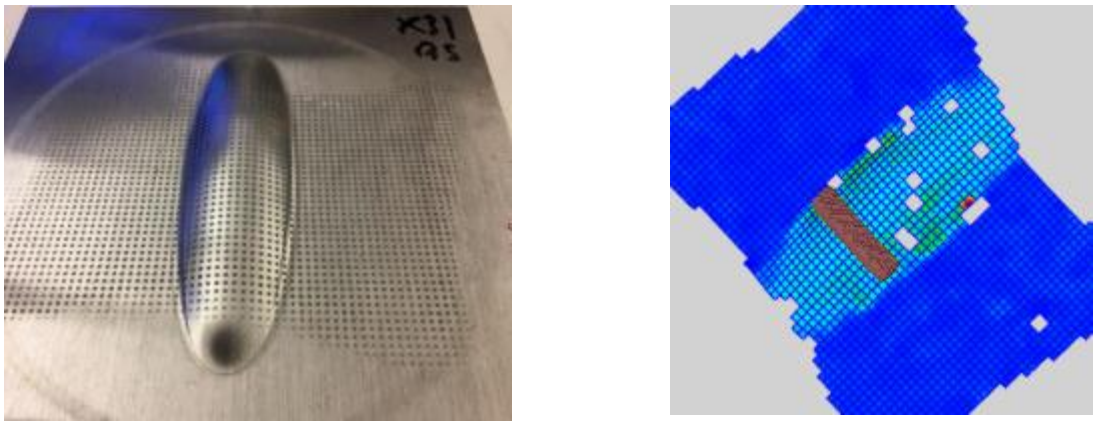

Figure 10-1. Photographs and corresponding Argus major strain maps of various hot as bulge sample of baseline AA6111 sheet.

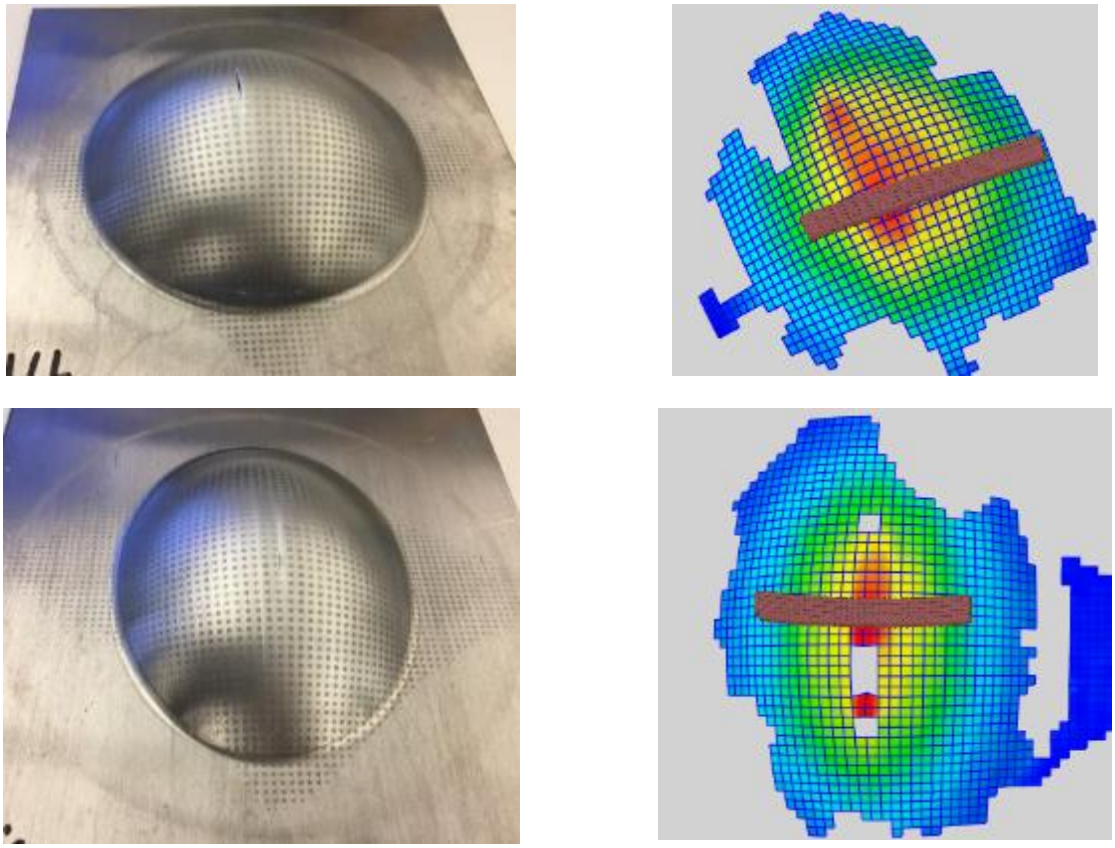

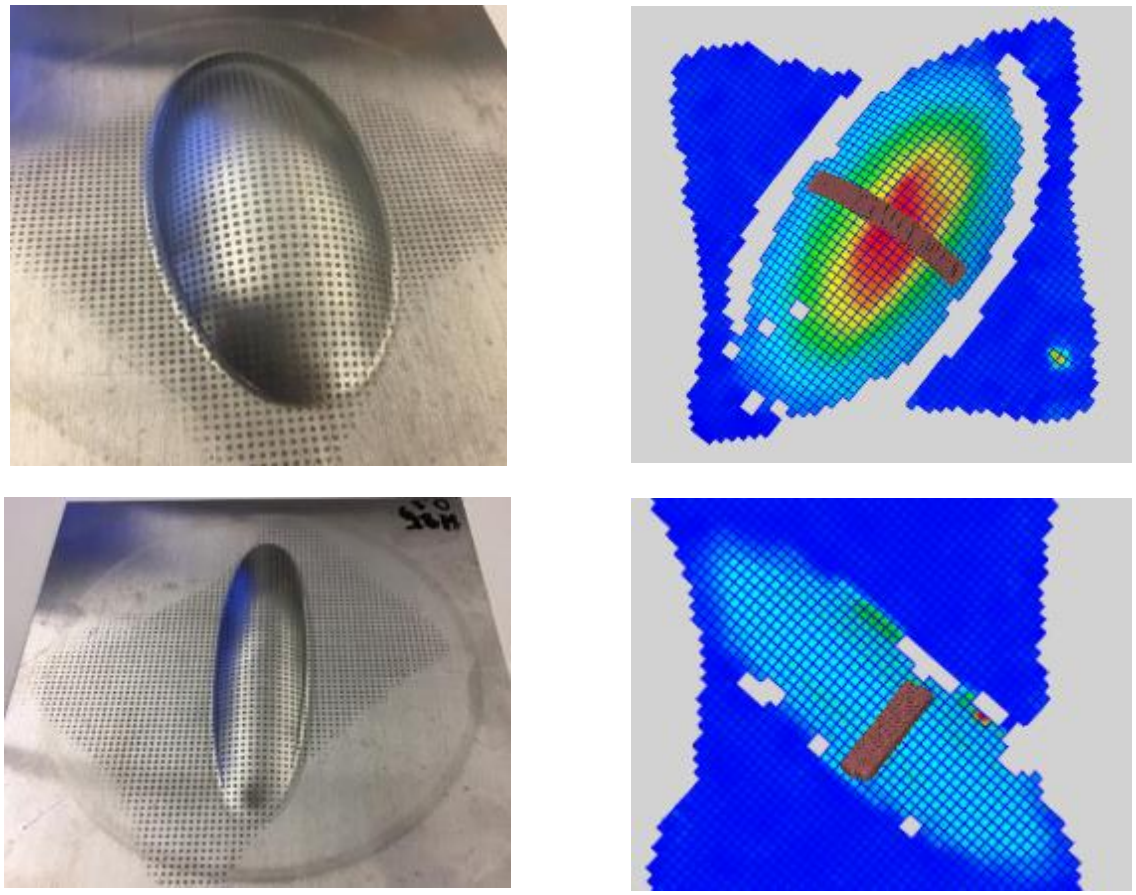

Figure 10-2. Photographs and corresponding Argus major strain maps of various hot as bulge sample of baseline HRC6111 sheet.

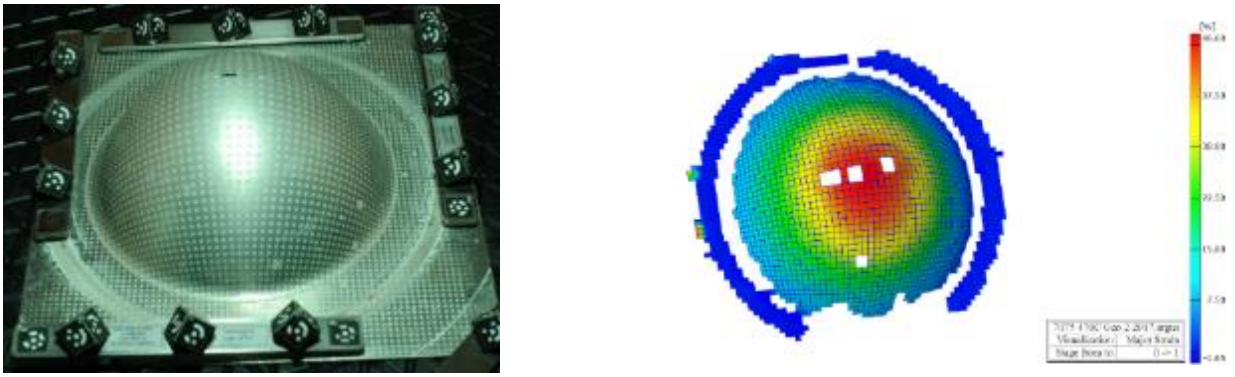

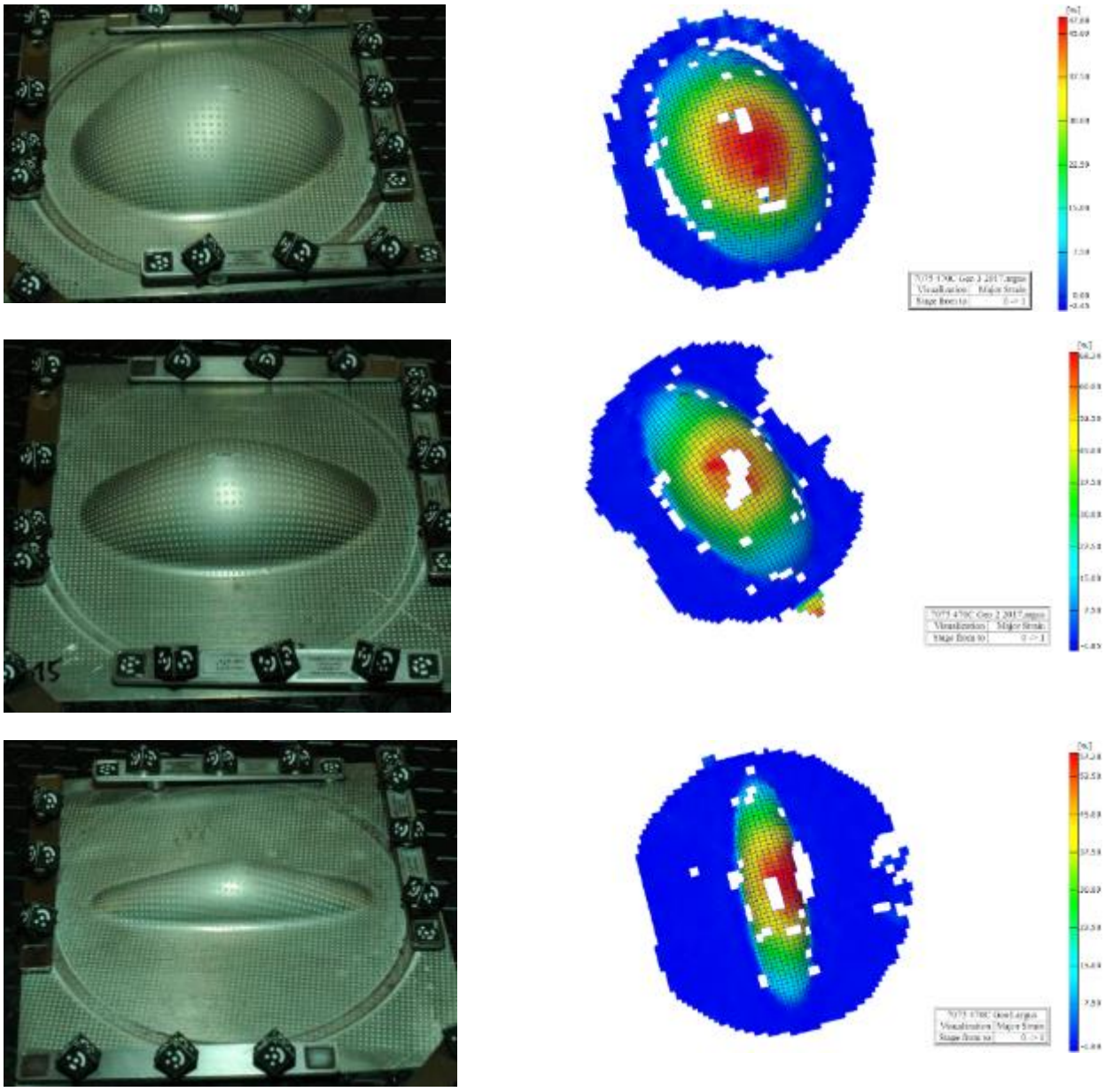

Figure 10-3. Photographs and corresponding Argus major strain maps of various hot as bulge sample of baseline AA7075 sheet at 470ºC.

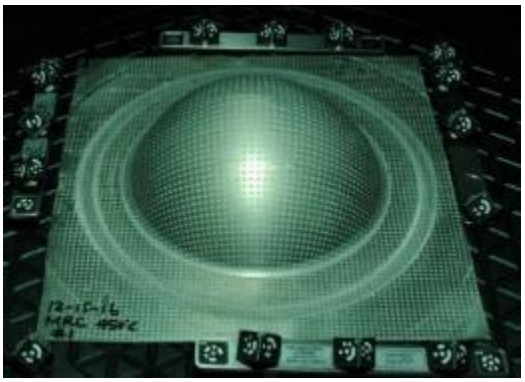

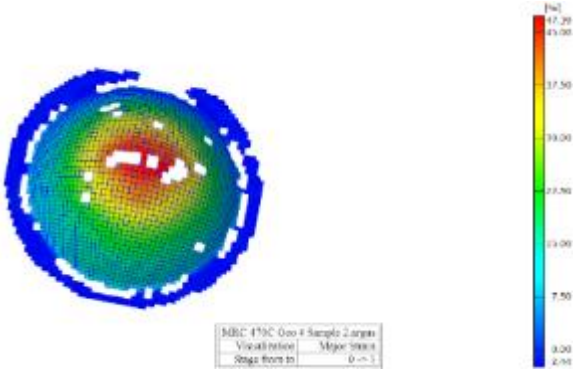

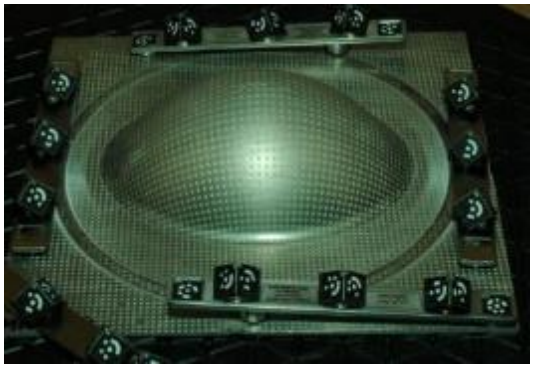

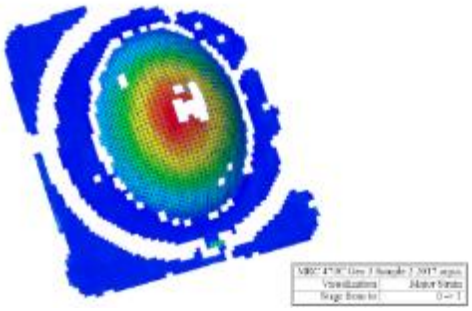

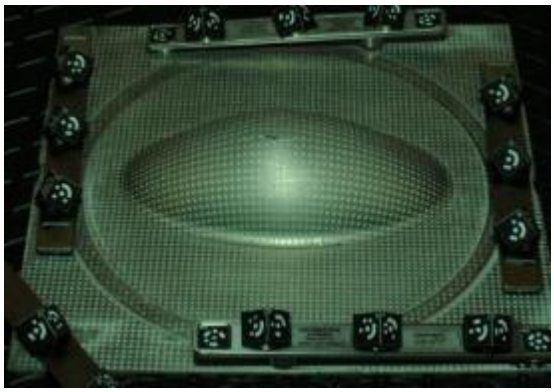

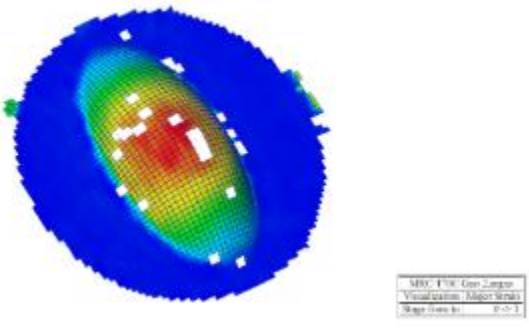

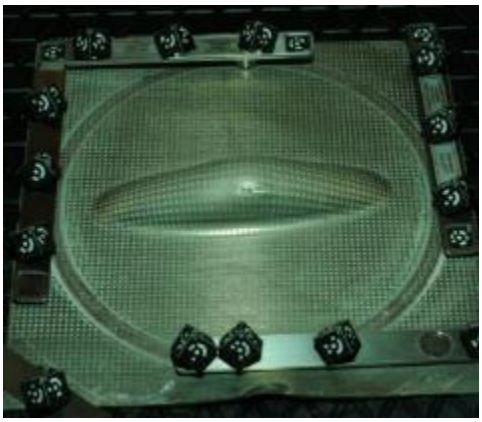

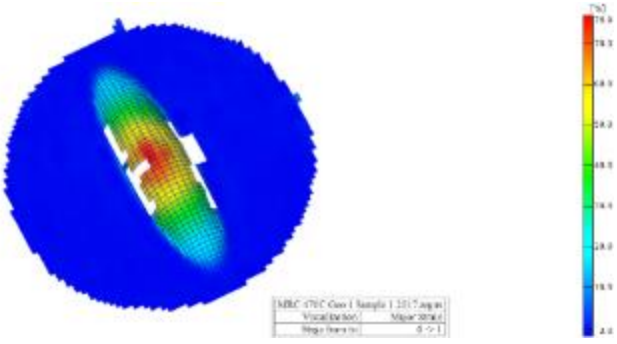

Figure 10-4. Photographs and corresponding Argus major strain maps of various hot as bulge sample of MRC 7075 sheet at 470ºC.

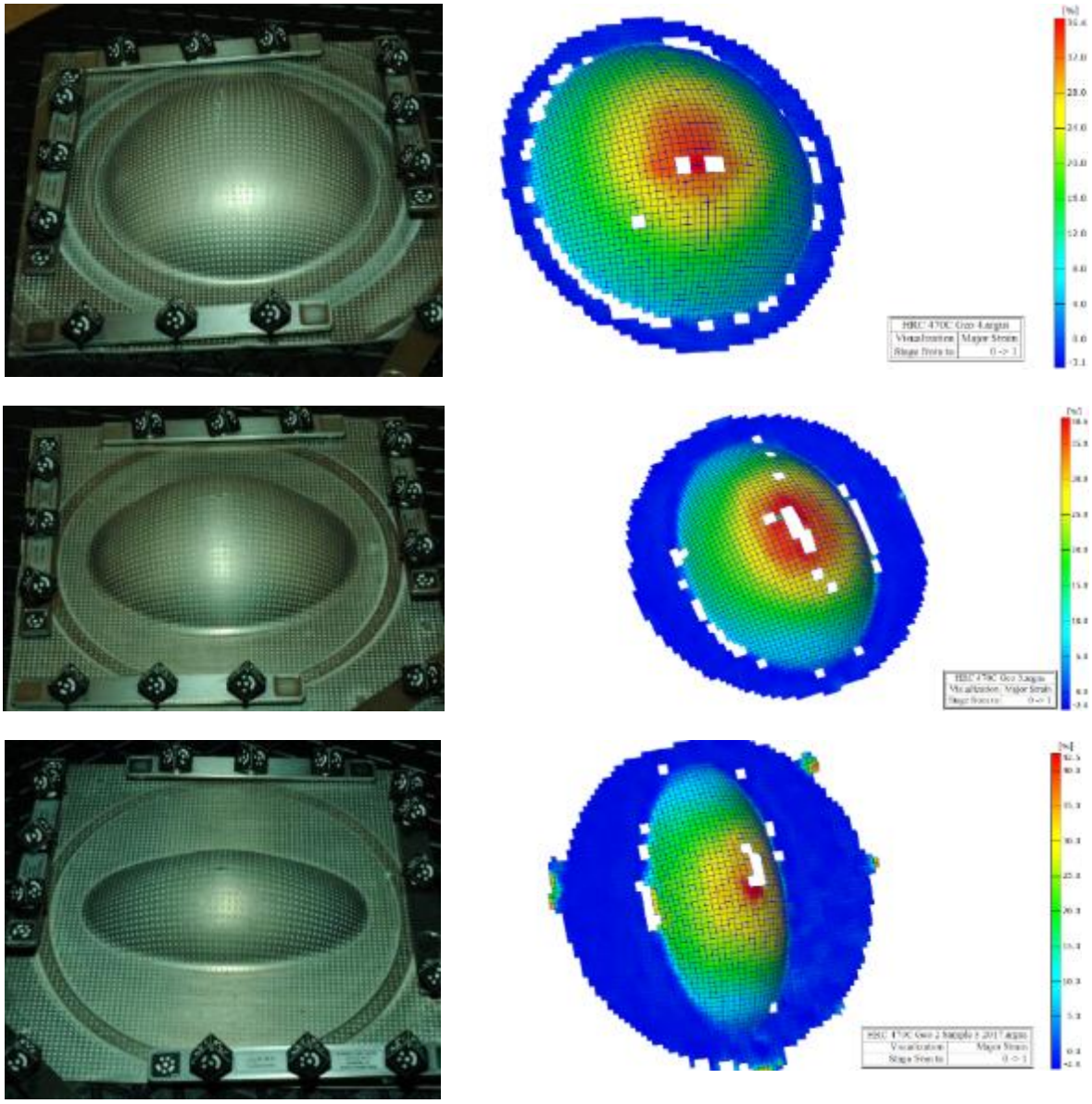

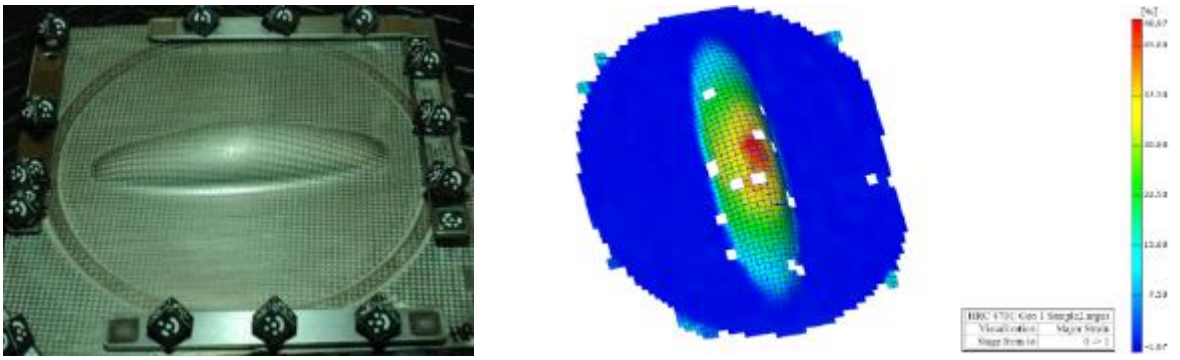

Figure 10-5. Photographs and corresponding Argus major strain maps of various hot as bulge sample of HRC 7075 sheet at 470ºC.

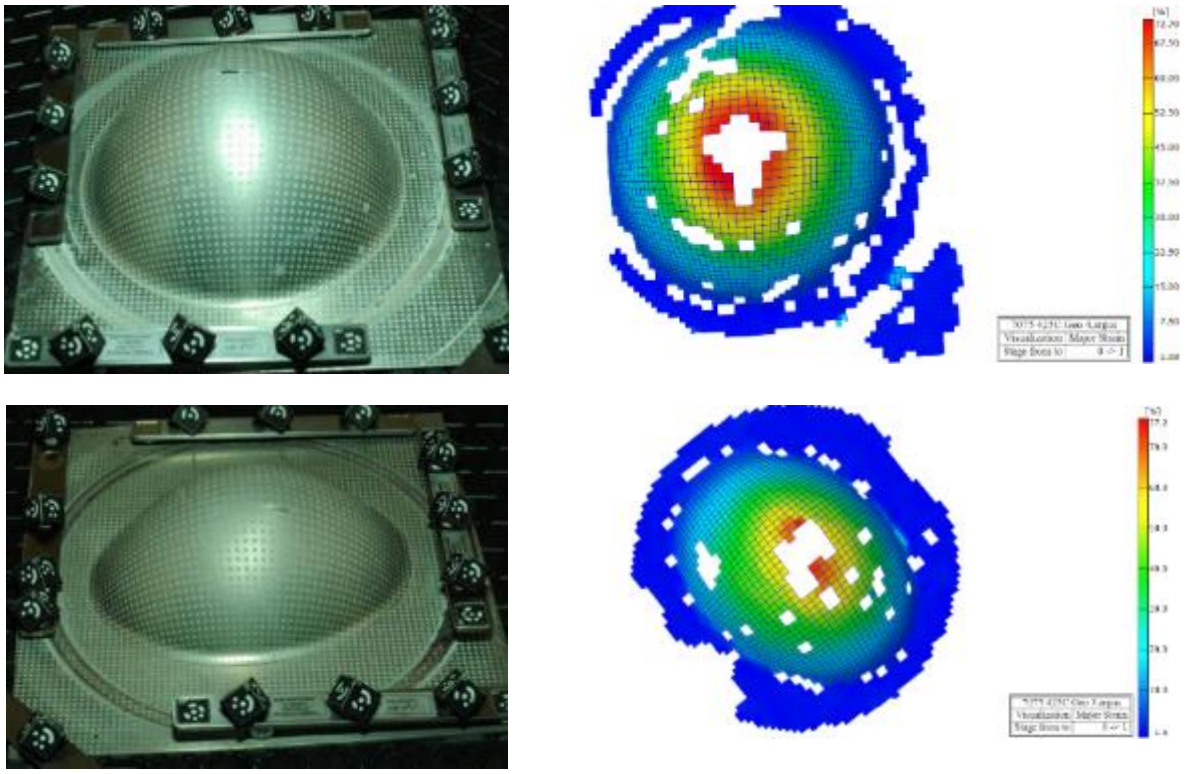

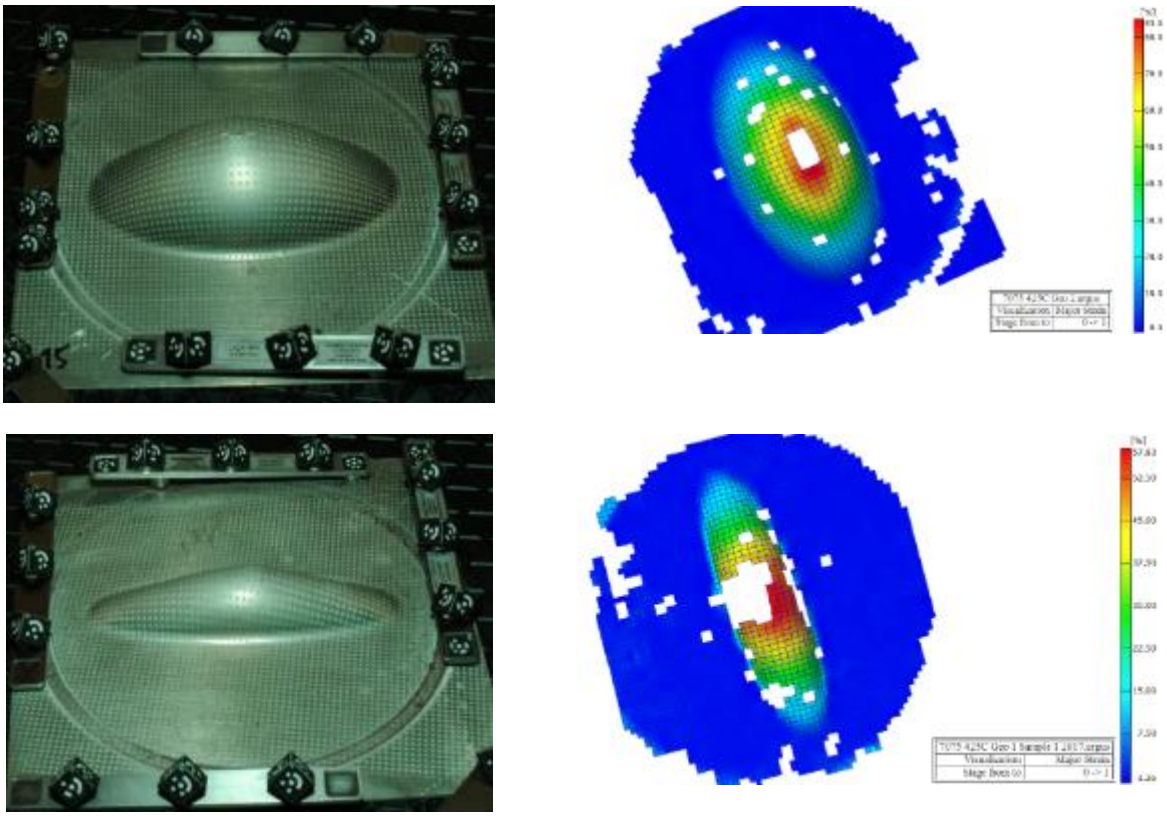

Figure 10-6. Photographs and corresponding Argus major strain maps of various hot as bulge sample of baseline AA7075 sheet at 425ºC.

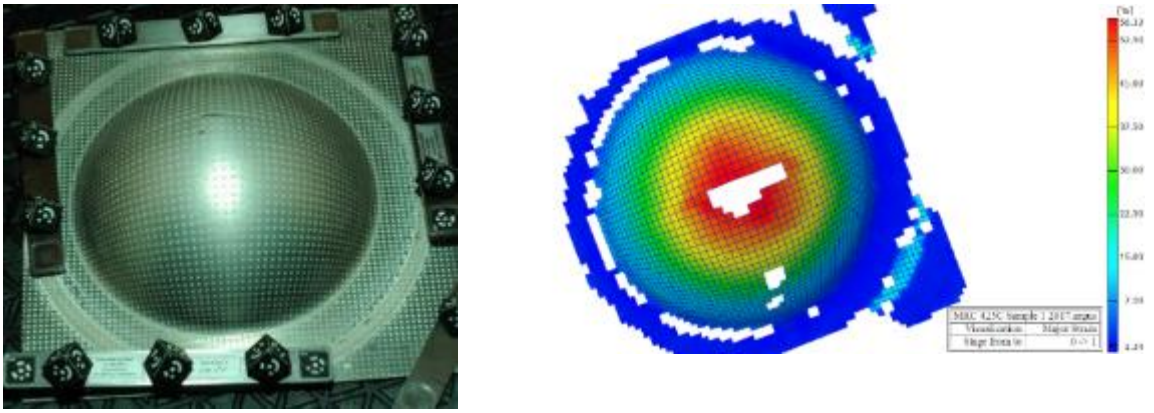

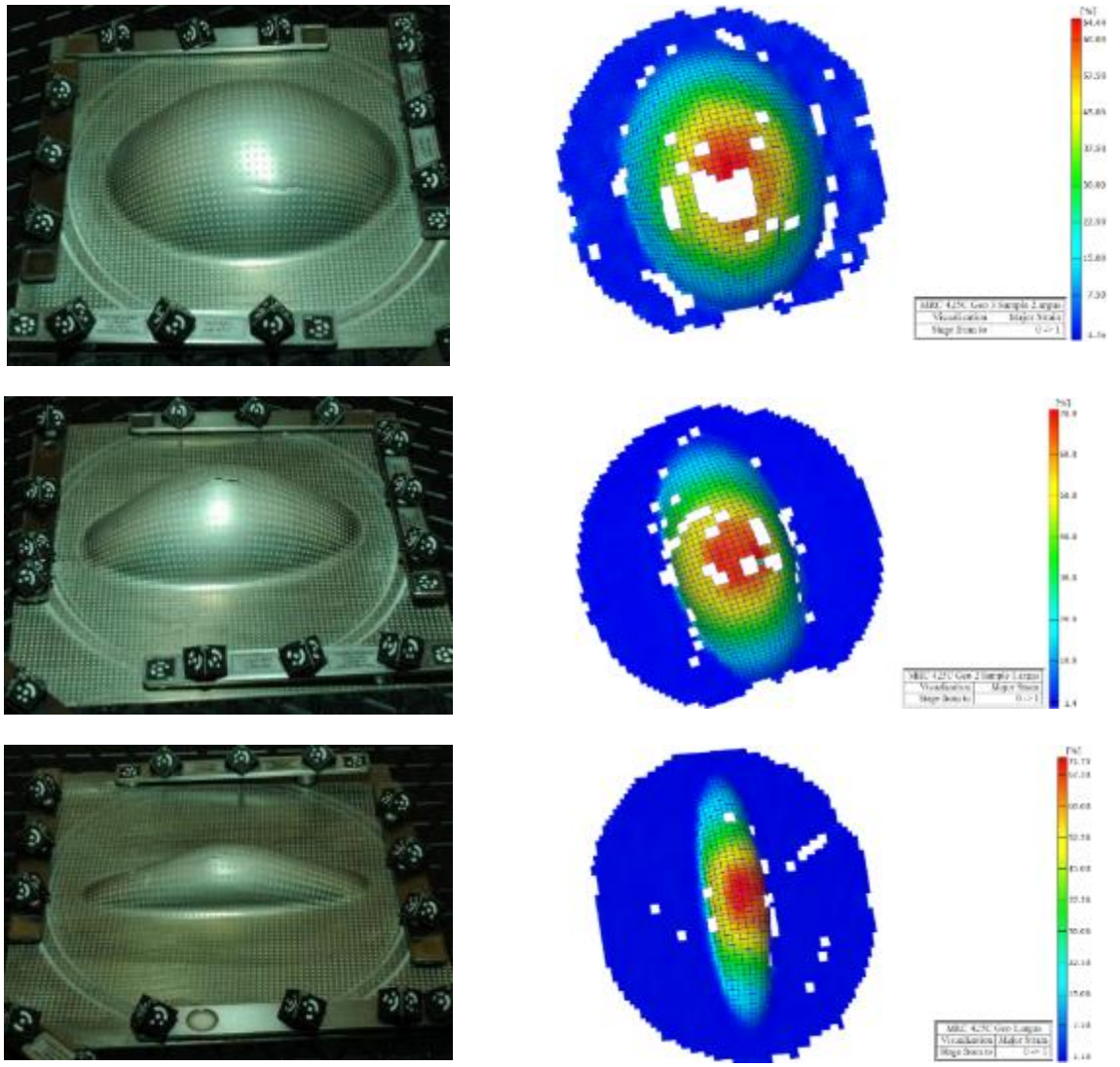

Figure 10-7. Photographs and corresponding Argus strain maps of various hot as bulge sample of MRC 7075 sheet at 425ºC.

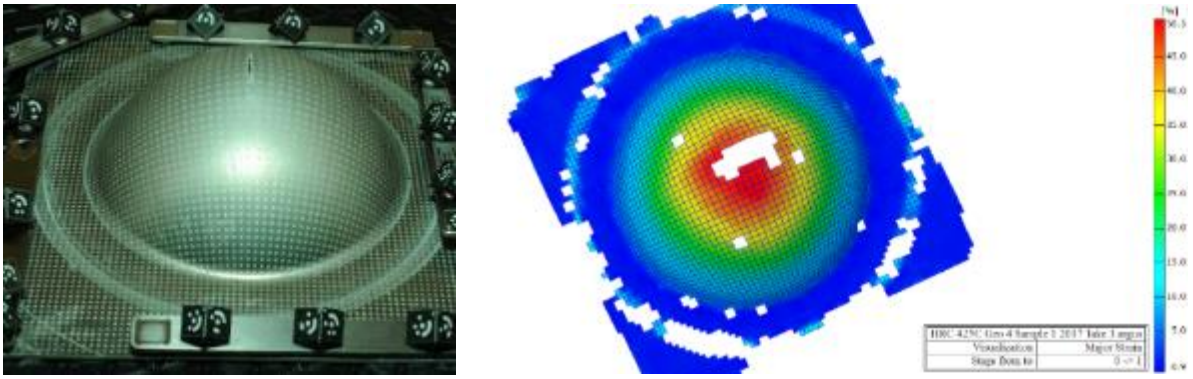

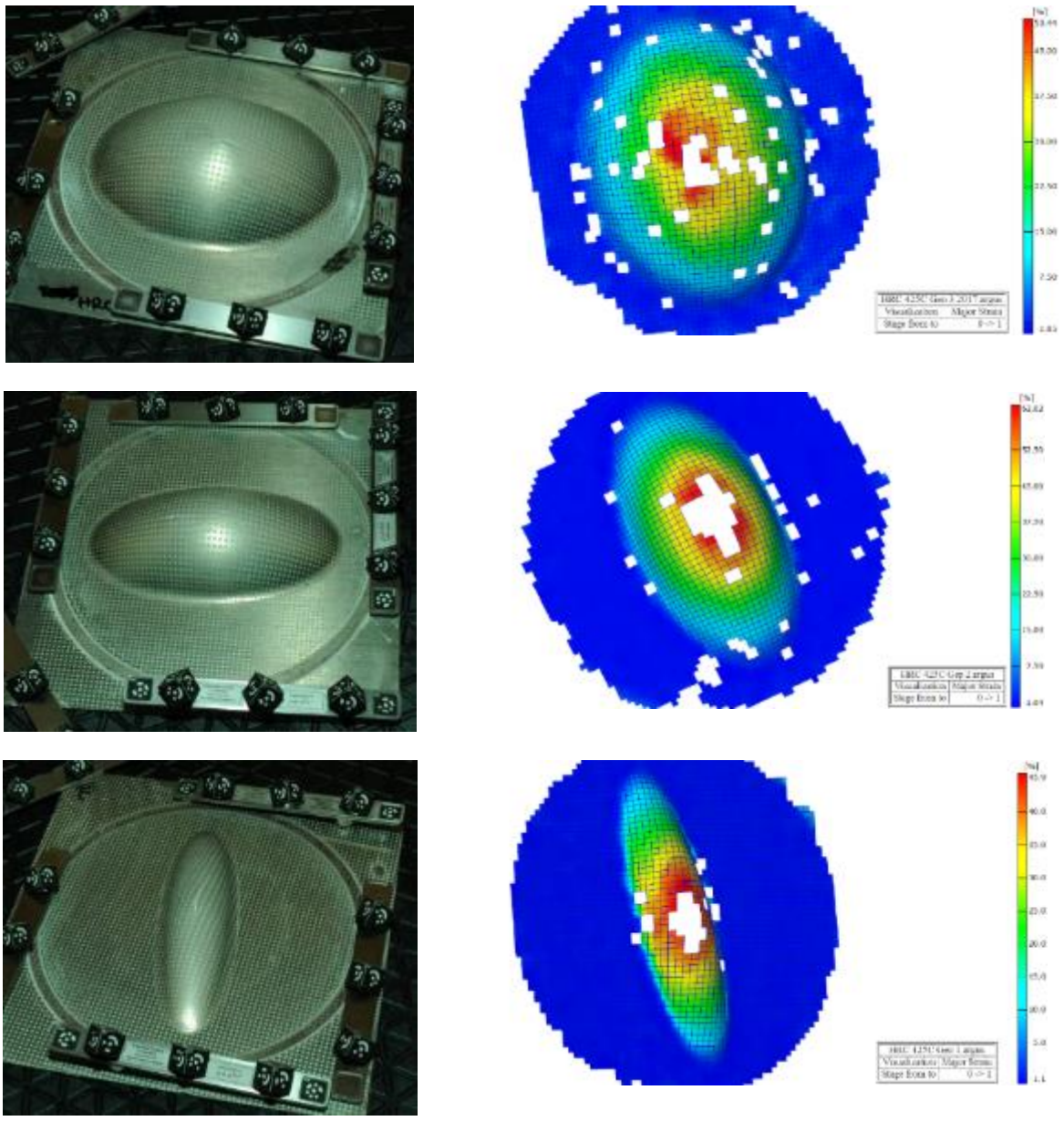

Figure 10-8. Photographs and corresponding Argus strain maps of various hot as bulge sample of HRC 7075 sheet at 425ºC.

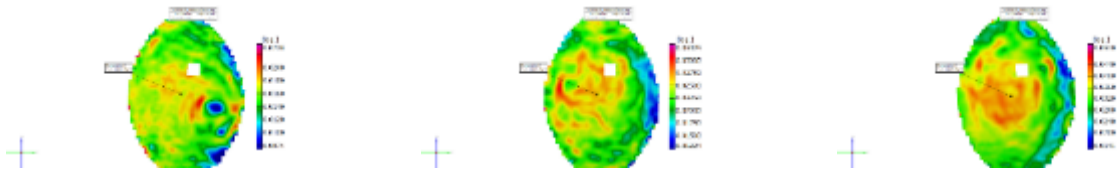

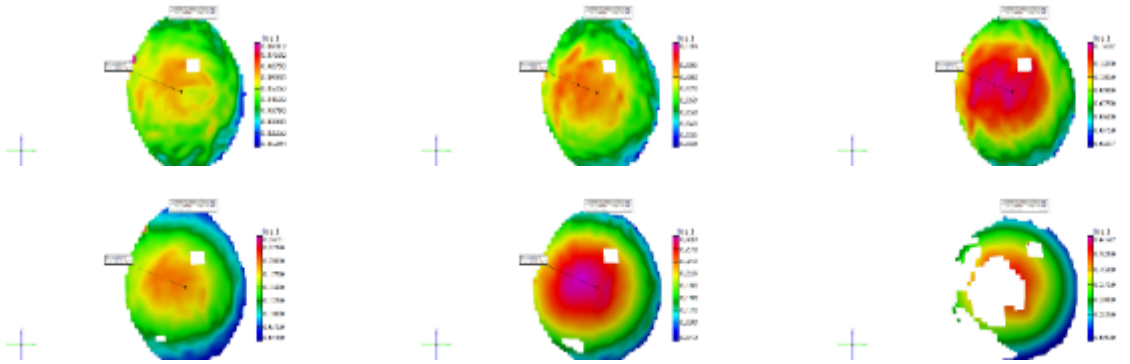

Figure 10-9. A sequence of Aramis major strain maps from interrupted hot gas bulge tests showing the development of strain at the pole of the bulge up to fracture.